

**APPLICATION OF ELECTROSPUN CARBON NANOFIBRES
FOR BATTERIES AND SUPERCAPACITORS**

by

Nicole Ying-Ju Lee

B.Sc., The University of British Columbia, 2008

**A THESIS SUBMITTED IN PARTIAL FULFILLMENT OF
THE REQUIREMENTS FOR THE DEGREE OF**

MASTER OF SCIENCE

in

**The Faculty of Graduate Studies
(Materials Engineering)**

THE UNIVERSITY OF BRITISH COLUMBIA

(Vancouver)

October 2011

© Nicole Ying-Ju Lee, 2011

Abstract

With the great demand for energy storage devices with much higher energy density, better power performance, and longer cycle life, researchers are looking into nano-structured battery and supercapacitor electrodes due to the higher accessibility of ions to electrodes, improved specific capacitance, and reduced chance of mechanical degradation compared to bulk materials. In this study, a composite system of conductive carbon nanofibres with active materials (polypyrrole and silicon nanoparticles) are fabricated for supercapacitor and lithium ion battery electrode applications. The aim is to use carbon as a strong mechanical and electrical support and the high energy storage capability of active materials to develop new generation electrode systems.

Carbon nanofibres with $3.9\pm0.5\times10^2$ nm in diameter are fabricated from a copolymer precursor, poly(acrylonitrile-co-acrylamide), through electrospinning and carbonization. The mild exothermic heat reaction of this copolymer and the enhanced heat flow into nano-scaled fibres during stabilization permits fabrication of high quality and large-scale carbon nanofibre mats with reasonable conductivity (18 ± 1 S/cm), high porosity, and high accessible surface area to solutions.

Carbon nanofibres are subsequently deposited on electrochemically with polypyrrole for 4 and 8 hours for use as a supercapacitor electrode. Capacity is compared with that of a bulk polypyrrole film. Both systems possess a gravimetric capacity of ca. 150 F/g, but an enhanced volumetric capacity in the nanofibrous electrode ($9\pm1\times10^7$ F/m³ for nanofibres vs. $6.0\pm0.5\times10^7$ F/m³ for film) at greater amount of polypyrrole deposition (8 hour deposition) is observed. The porous nanofibrous system also reduces the ionic resistance

from that of the pure polypyrrole film, which is at least $1.9 \pm 0.8 \times 10^2 \Omega$, to just 2 – 3 Ω at the highly reduced state.

In lithium ion battery applications, a core-shell electrospinning method is used to fabricate carbon nanofibres containing silicon nanoparticles in the core. The core-shell structural advantage over non-core-shell structure observed to be in the prevention of silicon particle fusion and reduced breakage after interacting with lithium ions. At 30 wt% nanoparticle loading, both systems can reach over 1000 mAh/g initial capacity at 100 – 600 mA/g cycle rates. After 20 cycles, the capacity retention of Si in most core-shell systems are significantly higher than that of the non-core-shell system by ca. 10 – 20 %. Further optimization is required to improve the cycle life and electrode stability.

Table of Contents

Abstract.....	ii
Table of Contents	iv
List of Tables	vii
List of Figures.....	viii
Acknowledgements	xiii
1 Introduction.....	1
1.1 Nanofibre Energy Storage	1
1.2 Objective.....	2
2 Carbon Nanofibres.....	5
2.1 Introduction to Carbon Nanofibre	5
2.1.1 Precursor Selection	6
2.1.2 Electrospinning	6
2.1.3 High Temperature Treatment	9
2.1.4 Role of Nanotechnology	16
2.2 Experimental.....	17
2.2.1 Copolymer Synthesis	17
2.2.2 Electrospinning	18
2.2.3 Carbonization.....	19
2.2.4 Characterization.....	21
2.3 Results and Discussions.....	22
2.3.1 Copolymer Characterization.....	22
2.3.2 Electrospun Nanofibres	28
2.3.3 Carbonization.....	31
2.3.4 Raman Spectroscopy	35
2.3.5 Conductivity Measurement.....	38
2.3.6 Flexural Rigidity.....	39
2.4 Conclusion	42

3	Supercapacitor	43
3.1	Introduction to Supercapacitor	43
3.1.1	Principles of Supercapacitors	44
3.1.2	Electrolyte Solution	47
3.1.3	Electrode Materials.....	49
3.1.4	Polypyrrole	50
3.1.5	ECP/Carbon Composite Electrodes.....	53
3.2	Experimental.....	53
3.2.1	Polypyrrole Synthesis.....	54
3.2.2	Characterization.....	54
3.3	Results and Discussions.....	55
3.3.1	CNF/PPy Characterization.....	55
3.3.2	GC/PPy Characterization.....	65
3.3.3	Resistance Analysis	71
3.4	Conclusion	81
4	Rechargeable Lithium Ion Batteries (LIB).....	82
4.1	Introduction to LIB.....	82
4.1.1	Principles of LIB.....	84
4.1.2	Role of Carbon in LIB Anode	86
4.1.3	Solid Electrolyte Interface	88
4.1.4	Carbon Structure vs. Capacity	91
4.1.5	Role of Silicon in LIB Anode.....	93
4.2	Experimental.....	97
4.2.1	Determination of Optimum Processing Parameters for Core-Shell Electrospinning Using PAN/SiNP Composite Nanofibres.....	97
4.2.2	Preparation of Core-Shell CNF/SiNP Composite Electrode with Different Concentrations of SiNP Using PANAM as Carbon Precursor.....	99
4.3	Results and Discussions.....	102
4.3.1	Determination of Solution Properties Using PAN/SiNP Prior to Core-Shell Electrospinning.....	102
4.3.2	Core-Shell Electrospinning.....	108
4.3.3	Electrochemical Cycling Characterization	127

4.3.4	Comparison with Published Results	166
4.4	Summary	173
5	Conclusion	175
6	Future Work.....	176
	References	178

List of Tables

Table 2-1 Methods of using sample holders during carbonization.....	33
Table 2-2 D and G peak positions and their intensity ratios from CNF pyrolyzed from different polymer precursors.	38
Table 2-3 Conductivities of CNF pyrolyzed from different polymer precursors.	39
Table 3-1 Resistance summary of CNF/PPy.	73
Table 3-2 Table summary of D_{eff} , τ (ionic), C_v , σ_{ionic} , and R_{ionic} of GC/PPy-4 and GC/PPy-8.....	78
Table 3-3 Table summary of R_{sol} , C , and RC (solution) of GC/PPy-4 and GC/PPy-8.....	78
Table 4-1. Properties of common rechargeable batteries [95, 103].	83
Table 4-2 Discharge capacity summary of CNF/SiNP carbonized at 700 (a), 900 (b), and 1100°C (c).	106
Table 4-3 Atomic concentrations of CNF/SiNP carbonized at 700, 900, and 1100°C.	108
Table 4-4. Atomic concentrations of core-shell CNF/SiNP.	117
Table 4-5 Raman peak positions and I_D/I_G ratio summary of pure carbon and core-shell carbon samples.	121
Table 4-6 Polymer precursor weight loss, conductivity, and volume density of core-shell CNF/SiNP.....	122

List of Figures

Fig. 1-1 Summary diagram of polymer nanofibre applications [9]. Reproduced with permission from Elsevier Science Ltd.	2
Fig. 2-1 Schematic representation of the basic setup of electrospinner with the SEM image of non-woven nanofibres collected on the metal ground (a) [3]. Reproduced with permission from John Wiley and Sons. Taylor cone formation during spinning process: 1-Formation of a Taylor cone 2-Ejection of a polymer jet 3-Relaxation of the cone by surface tension (b), adapted from [8].	8
Fig. 2-2 Coaxial electrospinning setup (a). Hollow nanofibres after the removal of core material (b). The shell is consisted of PVP and TiO ₂ [25]. Reproduced with permission from ACS Publications.	9
Fig. 2-3 Ladder structure produced by the intramolecular cyclization of CN groups, adapted from [26, 27].	10
Fig. 2-4 Intermolecular cyclization of CN groups as a result of dipole-dipole interaction, adapted from [20].	10
Fig. 2-5 Free radical cyclization (a) and ionic cyclization (b) mechanisms, adapted from [29, 30].	12
Fig. 2-6 Proposed chemical structures of PAN after oxidation. Carbonyl groups (a), lone pair donation of nitrogen to oxygen atom (b), bridged ether linkage (c), and hydroxyl and carbonyl groups (d), adapted from [31, 32].	13
Fig. 2-7 Cyclization and dehydrogenation of PAN precursor, adapted from [33].	14
Fig. 2-8 Chemical pathway on the formation of carbon structure during carbonization, adapted from [35].	15
Fig. 2-9 Free radical polymerization mechanism of PANAM.	18
Fig. 2-10 Schematics of the PAN (a) and PANAM (b) heating programs, and different methods of applying tensions during carbonization (c).	21
Fig. 2-11 Oven dried PANAM.	23
Fig. 2-12 NMR spectra of PANAM with 0.9 wt% AM (a) and 1.8 wt% AM (b).	24
Fig. 2-13 NMR spectrum of PANBAM.	25
Fig. 2-14 DSC comparison of PAN vs. PANAM (a) and PANAM with different AM concentrations (b).	27
Fig. 2-15 SEM figures of PAN (a), PANAM (0.9 wt% AM) (c), and PANAM (1.8 wt% AM) (e) electrospun nanofibres. Fibre diameter distribution of PAN (b), PANAM (0.9 wt% AM) (d), and PANAM (1.8 wt% AM) (f).	31
Fig. 2-16 SEM of carbon nanofibres pyrolyzed from PAN (a), PANAM (0.9 wt% AM) (b), and PANAM (1.8 wt% AM) (c).	35
Fig. 2-17 Representative Raman spectra of CNF pyrolyzed from PAN (a), PANAM (0.9 wt% AM) (b), and PANAM (1.8 wt% AM) (c).	37
Fig. 2-18 Stabilized electrospun PAN (a) and PANAM (0.9 wt% AM) (b).	41

Fig. 2-19 Carbonized electrospun PANAM (0.9 wt% AM) sample.....	41
Fig. 2-20 Side view indicating angle $\alpha = 41.5^\circ$ (a) and top view (b) of the home-made cantilever bending tester with the carbonized electrospun PANAM (0.9 wt% AM).....	42
Fig. 3-1 Ragone plot of various energy storage devices [59]. Reproduced with permission from Elsevier Science Ltd.	43
Fig. 3-2 Schematic representation of EDLC and the charge accumulation at the electrode/electrolyte interface upon charging the electrode [11]. Reproduced with permission from Elsevier Science Ltd.	45
Fig. 3-3 Plot of specific energy vs. operating voltage by using aqueous, organic, and ionic liquid electrolytes [69]. Reproduced with permission from Elsevier Science Ltd.	48
Fig. 3-4 Chemical Structure of PPy.	51
Fig. 3-5 The conductivity of the as-grown PPy film vs. potentials (circle) and the conductivity of the PPy film after cycled twice with a potentiostatic square wave (triangle) [77].	51
Fig. 3-6 Electrochemical redox reactions of PPy with the insertion and extraction of counterions. A^- is the counterion and e^- is the electron [78].	52
Fig. 3-7 SEM images of CNF/PPy-4 (a) and CNF/PPy-8 (b).	56
Fig. 3-8 CV curves of pure CNF (a) vs. CNF/PPy-4 (b) at 1 mV/s cycle rate.	58
Fig. 3-9 CV of CNF/PPy capacitance at 4 (a) and 8 (b) hours of PPy deposition.	60
Fig. 3-10 Galvanostatic cycling of CNF/PPy-4 (a), its charge/discharge capacitance (b), and Coulombic efficiency (c) at different current densities.	63
Fig. 3-11 Galvanostatic cycling of CNF/PPy-8 (a), its charge/discharge capacitance (b), and Coulombic efficiency (c) at different current densities.	64
Fig. 3-12 CV of GC/PPy-4 (a) and GC/PPy-8 (b).	66
Fig. 3-13 Galvanostatic cycling of GC/PPy-4 (a), its charge/discharge capacitance (b), and Coulombic efficiency (c) at different current densities.	69
Fig. 3-14 Galvanostatic cycling of GC/PPy-8 (a), its charge/discharge capacitance (b), and Coulombic efficiency (c) at different current densities	70
Fig. 3-15 Equivalent circuit model of ion diffusion into the PPy electrode, adapted from [93].	72
Fig. 3-16 The effect of R_{sol} at different RE positions. The effect is demonstrated using CV at 1 mV/s cycle rate (a) and galvanostatic charge/discharge at 0.67 A/g cycle rate (b) on the CNF/PPy-4 sample.	75
Fig. 3-17 R_{sol} of GC/PPy-4 and GC/PPy-8 at different charge and discharge current densities.	78
Fig. 3-18 Discharge capacitance comparison between CNF/PPy-4 and GC/PPy-4 (a) and CNF/PPy-8 and GC/PPy-8 (b).	80

Fig. 4-1 Volumetric and gravimetric energy density summary of common rechargeable batteries. PLiON is a type of flexible LIB developed by Bellcore [98]. Reproduced with permission from Nature Publishing Group.	83
Fig. 4-2 Schematic representation of a conventional rechargeable Li-ion battery [105]. Reproduced with permission from John Wiley and Sons.	85
Fig. 4-3 Charge/discharge profile of graphite (a), soft carbon (b), and hard carbon (c) [106]. Reproduced with permission from the American Association for the Advancement of Science.	86
Fig. 4-4 Discharge profile of hard carbon and graphite, adapted from [110].	88
Fig. 4-5 Schematic view of various types of SEI and their effect on the electrode capacity: (a) high reversible capacity (b) low reversible capacity, and (c) no reversible capacity[118]. Reproduced with permission from Springer.	90
Fig. 4-6 Schematic representation of lithium intercalation into layered graphite (a) and single-layered hard carbon (b) [134]. Reproduced with permission from Elsevier Science Ltd.	93
Fig. 4-7 Schematic representation of the three electrode cell setup for CNF/SiNP electrode testing.	99
Fig. 4-8 Schematic representation of fabricating CNF/SiNP composite electrode through core-shell electrospinning.	102
Fig. 4-9 TEM (a) and SEM (b) of PAN/SiNP using TX100 as the surfactant.	103
Fig. 4-10 TEM (a) and SEM (b) of PAN/SiNP using PVP as the surfactant.	104
Fig. 4-11 XRD of CNF/SiNP carbonized at 700, 900, and 1100°C (a) and pure SiNP (b).	107
Fig. 4-12 SEM of core-shell PANAM/Si-15 at $\times 600$ (a) and $\times 5k$ (b) magnification, PANAM/Si-30 at $\times 600$ (c) and $\times 5k$ (d) magnification, PANAM/SiNP-50 at $\times 600$ (e) and $\times 5k$ (f) magnification, and PANAM/SiNP-80 at $\times 600$ (g) and $\times 5k$ (h) magnification.	111
Fig. 4-13 TEM of core-shell PANAM/SiNP-15 (a), PANAM/SiNP-30 (b), PANAM/SiNP-50 (c), and PANAM/SiNP-80 (d) at $\times 30k$ magnification.	112
Fig. 4-14 Viscosity measurement of pure PANAM and PANAM/SiNP solutions with various SiNP concentrations.	113
Fig. 4-15 SEM of core-shell CNF/Si-15 at $\times 600$ (a) and $\times 5k$ (b) magnification, CNF/Si-30 at $\times 600$ (c) and $\times 5k$ (d) magnification, CNF/Si-50 at $\times 600$ (e) and $\times 5k$ (f) magnification, and CNF/Si-80 at $\times 600$ (g) and $\times 5k$ (h) magnification.	115
Fig. 4-16 TEM of core-shell CNF/Si-15 (a), CNF/Si-30 (b), CNF/Si-50 (c), and CNF/Si-80 (d) at $\times 50k$ magnification.	116
Fig. 4-17 XRD of pure carbon (a), core-shell CNF/Si-15 (b), CNF/Si-30 (c), CNF/Si-50 (d), and CNF/Si-80 (e).	118
Fig. 4-18 Plot of SiNP concentration in CNF vs. SiNP concentration in the core solution during core-shell electrospinning.	118

Fig. 4-19 Raman I_D/I_G ratios for core-shell CNF/SiNP samples with different SiNP concentration in the final CNF product.	121
Fig. 4-20 SEM of n-PANAM/Si at $\times 600$ (a) and $\times 5k$ magnification (b), and TEM of n-PANAM/Si at $\times 30k$ magnification (c).....	123
Fig. 4-21 SEM of n-CNF/Si at $\times 600$ (a) and $\times 5k$ magnification (b), and TEM of n-CNF/Si at $\times 50k$ magnification (c).	124
Fig. 4-22 Stress-strain curves of CNF/Si-80.....	125
Fig. 4-23 Stress-strain curves of n-CNF/Si.....	126
Fig. 4-24 Average stress-strain of CNF/Si-80 and n-CNF/Si.	127
Fig. 4-25 Charge/discharge voltage profile of core-shell CNF/Si-80 cycled at 100 (a), 200 (c), 400 (e), and 600 (g) mA/g; charge/discharge capacity summary of core-shell CNF/Si-80 cycled at 100 (b), 200 (d), 400 (f), and 600 (h) mA/g; the Coulombic efficiency (i) of the sample at each cycling rate.	133
Fig. 4-26 Charge/discharge voltage profile of n-CNF/Si cycled at 100 (a), 200 (c), 400 (e), and 600 (g) mA/g; charge/discharge capacity summary of n-CNF/Si cycled at 100 (b), 200 (d), 400 (f), and 600 (h) mA/g; the Coulombic efficiency (i) of the sample at each cycling rate.	139
Fig. 4-27 Charge/discharge voltage profile of pure CNF cycled at 100 (a), 200 (c), 400 (e), and 600 (g) mA/g; charge/discharge capacity summary of pure CNF cycled at 100 (b), 200 (d), 400 (f), and 600 (h) mA/g; the Coulombic efficiency (i) of the sample at each cycling rate.	145
Fig. 4-28 Discharge capacity summary of CNF/Si-80 (a), n-CNF/Si (b), and pure CNF (c) cycled at 100, 200, 400, and 600 mA/g.	147
Fig. 4-29 Discharge capacity comparison between CNF/Si-80, n-CNF/Si, and pure CNF cycled at 100 mA/g (a) and the pure SiNP capacity in different nanofibre composite after the subtraction of pure CNF capacity (b).....	150
Fig. 4-30 Schematic representation of the SEI film thickening upon cycling [174].	151
Fig. 4-31 Discharge capacity comparison between core-shell CNF/Si, non-core-shell CNF/Si, and pure CNF cycled at 200 mA/g (a) and the pure SiNP capacity after the subtraction of pure CNF capacity (b).....	153
Fig. 4-32 Discharge capacity comparison between CNF/Si-80, n-CNF/Si, and pure CNF cycled at 400 mA/g (a) and the pure SiNP capacity for both samples after the subtraction of pure CNF capacity (b).	155
Fig. 4-33 Discharge capacity comparison between CNF/Si-80, n-CNF/Si, and pure CNF cycled at 600 mA/g (a) and the pure SiNP capacity for both samples after the subtraction of pure CNF capacity (b).	158
Fig. 4-34 SEM of CNF/Si-80 after cycled at 100 mA/g with $\times 600$ (a) and $\times 3k$ (b) magnifications, after cycled at 200 mA/g with $\times 600$ (c) and $\times 3k$ (d) magnifications, after cycled at 400 mA/g with $\times 600$ (e) and $\times 3k$ (f)	

magnifications, and after cycled at 600 mA/g with $\times 600$ (g) and $\times 3k$ (h) magnifications.....	160
Fig. 4-35 SEM of n-CNF/Si after cycled at 100 mA/g with $\times 600$ (a) and $\times 3k$ (b) magnifications, after cycled at 200 mA/g with $\times 600$ (c) and $\times 3k$ (d) magnifications, after cycled at 400 mA/g with $\times 600$ (e) and $\times 3k$ (f) magnifications, and after cycled at 600 mA/g with $\times 600$ (g) and $\times 3k$ (h) magnifications.....	161
Fig. 4-36 SEM of pure CNF after cycled at 100 mA/g with $\times 600$ (a) and $\times 3k$ (b) magnifications, after cycled at 200 mA/g with $\times 600$ (c) and $\times 3k$ (d) magnifications, after cycled at 400 mA/g with $\times 600$ (e) and $\times 3k$ (f) magnifications, and after cycled at 600 mA/g with $\times 600$ (g) and $\times 3k$ (h) magnifications.....	165
Fig. 4-37 Curves (a), (b), and (c) are Al-treated natural graphite cycled at 0.2, 0.5, and 1.0 C rate, respectively, and curves (d), (e), and (f) are natural graphite cycled at 0.2, 0.5, and 1.0C rate, respectively [175]. Reproduced with permission from the Electrochemical Society.	165
Fig. 4-38 Curve a, b, and c are the 15, 30, and 50 wt% SiNP loading, respectively, in PAN CNF cycled at 100 mA/g in (a) and curve a, b, and c are the 15, 30, and 50 wt% SiNP loading, respectively, in PAN CNF cycled at 200 mA/g in (b). Curve b in both figures are comparable to our CNF/SiNP samples [13]. Reproduced with permission from Elsevier Science Ltd.....	168
Fig. 4-39 Schematic of Si film and micron-sized particle pulverization after cycling (a) and the preservation of SiNW morphology after cycling (nanowires grown directly on the current collector) (b) [180]. Reproduced with permission from Nature Publishing Group.	170
Fig. 4-40 Potential profile of the first two cycles for SiNW cycled at C/20 rate (a) and the charge/discharge capacity (squared and circled dots) of SiNW cycled at C/20 rate (b) [180]. Reproduced with permission from Nature Publishing Group. .	171
Fig. 4-41 Capacity of Sony's Sn-Co-C alloy anode (a) and the percentage capacity retention upon cycling. The 100 % capacity is 543 mAh/g (b) [183]. Reproduced with permission from the Electrochemical Society.....	172
Fig. 4-42 Capacity performance of 3M's Si-alloy anode (upper) and its Coulombic efficiency after cycling (lower) [184]. Reproduced with permission from the Electrochemical Society.	173

Acknowledgements

This project was kindly supported by the NSERC Discovery Grant and British Columbia Innovation Council. Some equipment used in this study were funded by a CFI grant.

I would like to express my gratitude and appreciation for the many people that have guided me throughout my Master's study. I would like to thank Dr. Michael Wolf for getting me interested in the field of materials chemistry. Most importantly, my supervisor, Dr. Frank Ko, provided me the greatest interdisciplinary research opportunity in fabricating nanofibrous electronics. This project cannot be completed successfully without the guidance and assistance from both Dr. Frank Ko and my co-supervisor, Dr. John Madden. I would also like to thank Dr. Eddie Fok and Dr. Heejae Yang, who have always patiently answered my questions, helped me solve technical issues, and provided many suggestions for this project.

I am also very thankful to Dr. Xavier Roy, who helped me greatly in copolymer synthesis. The technician, Mary Fletcher, provided me much assistance in operating SEM, TEM, and XRD. Ryan Thorpe from Dr. Göran Fernlund's group and Dr. Reza Korehei from Dr. John Kadla's group also helped me much in using DSC and TGA machines. I also appreciate all the valuable discussions with my colleagues and all the support from my close friends.

I would like to dedicate this thesis work to my mother, who has continuously provided me with love and support.

1 Introduction

1.1 Nanofibre Energy Storage

Fossil fuels are known as the primary global energy source in the 20th century. It supplies at least 86 % of the total energy today and the demand is expected to grow by at least 44 % in the next 24 years. However, with the increased fuel price and the heavy environmental pollution contributed from using fossil fuels, alternative energies, specifically clean and sustainable energies, have been constantly researched and developed. Among all, supercapacitors, lithium ion batteries, solar cells, and fuel cells are promising candidates for energy conserving devices. However, a breakthrough in device lifetime, power/energy performance, and energy efficiency is necessary to completely displace fossil fuels [1, 2].

The discovery of nanotechnology greatly benefits and accelerates the development of these clean energy devices. Many nano-sized materials in general possess different mechanical, thermal, electrical, and thermal properties than bulk materials, such as enhanced surface area to volume ratio, quantum confinement effect, photocatalytic, and greater flexibility. Nanomaterials with different morphologies, including nanoparticles, nanotubes, nanowires, and nanofibres have been synthesized through chemical synthesis, template synthesis, phase separation, self-assembly, or electrospinning [3-7]. Electrospinning is one of the most cost effective, simple, versatile, and efficient method to fabricate continuous nanofibres with high surface area and porosity. It has been researched in various areas including biomedical, electronics, filtration, and protective clothing [8], as shown in the summary diagram of Fig. 1-1 [9].

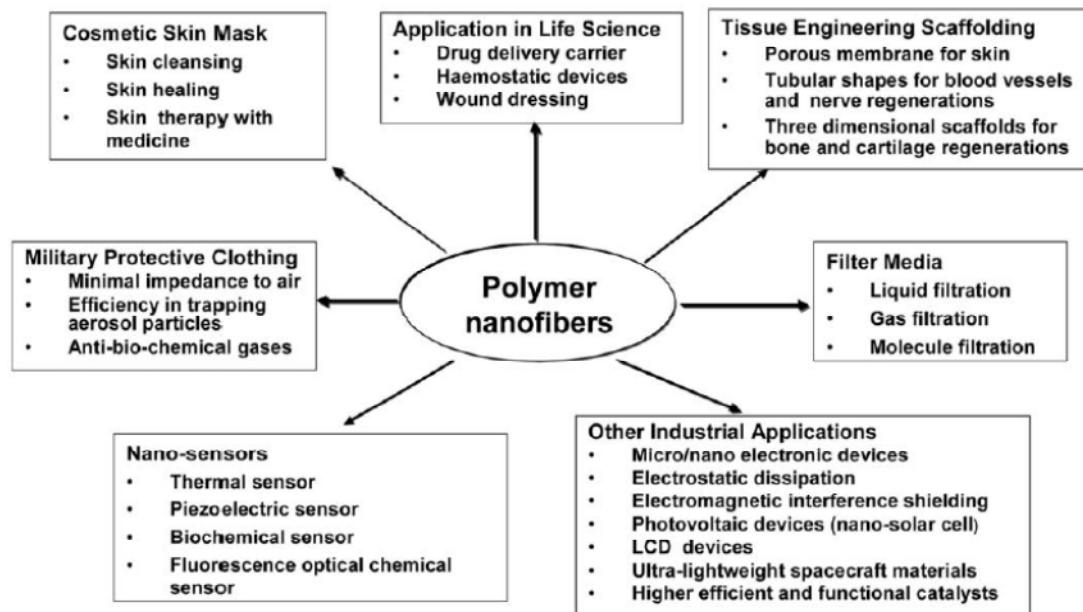


Fig. 1-1 Summary diagram of polymer nanofibre applications [9]. Reproduced with permission from Elsevier Science Ltd.

1.2 Objective

Among the four clean energy devices mentioned above, the objective of this work focuses on developing high performance supercapacitor and battery electrodes using electrospun carbon nanofibre (CNF) as a structural backbone for the active materials. Supercapacitors are known for providing bursts of power and possessing much higher energy density than conventional capacitors. This feature compensates for the high energy but low power density of batteries. A combination of both high power density from supercapacitors and high energy density from batteries could greatly improve the multifunctional demand of portable electronics and high performance electric vehicles [10, 11].

Electrospun CNF possess the advantage of good conductivity and high mechanical stability. The highly porous CNF film also permits fast ion transport throughout the structure. However, its energy storage capability is limited due to the limited amount of charge storage on the surface. New materials, including conducting polymers and inorganic nanoparticles, are often investigated to improve the amount of energy storage comparing to traditionally used carbon. In this study, supercapacitor electrode is fabricated using electrospun CNF as a supporting backbone for the conducting polymer, polypyrrole (PPy), coating (nm scale) on the surface. PPy is chosen for this study due its good conductivity, high specific capacitance [12], and our familiarity with this material. A thin-layered and nanofibrous PPy structure is expected to improve the rate of ion transport and volumetric capacitance.

A core-shell structured CNF with silicon nanoparticle (SiNP) in the core of CNF is fabricated from core-shell electrospinning for lithium ion battery electrode. Core-shell electrospinning permits co-electrospun and generation of nanofibres with core and shell consisted of two different materials. The inclusion of silicon nanoparticles in the carbon core is intended to prevent particle fusion and breakage during its expansion and shrinkage after interacting with lithium ions. SiNP is chosen due to its superior theoretical capacity (4200 mAh/g) than most known materials (372 mAh/g for graphite used in commercial devices) [13]. The high porosity and accessible surface area of CNF to electrolyte solutions provide advantages for high energy storage and fast ion transfer.

In Chapter 2, a brief discussion of carbon fibre precursor is summarized, which explains the background of precursor selection for this study. The selected precursor is synthesized, electrospun, and carbonized into CNF. Its mechanical and electrical

properties are compared with CNF fabricated from commercially available polymer precursor. In Chapter 3, a brief background of supercapacitor is reviewed, followed by the description of the fabrication process of CNF/PPy composite electrode and its electrochemical characterization. In Chapter 4, the application of CNF/SiNP composite for lithium ion battery is presented with a brief introduction of lithium ion battery, followed by electrochemical characterizations of CNF/SiNP electrode. The overall works are summarized in a general conclusion, followed by some suggested future works to improve the performance of CNF and CNF composite electrodes.

2 Carbon Nanofibres

2.1 Introduction to Carbon Nanofibre

Carbon fibres are major reinforcement fibres being used for aerospace composites and many advanced structural applications. The three major types of carbon fibre precursors being used in industry for large-scale productions are rayon, pitch, and acrylic fibres [14]. Rayons are synthetic fibres regenerated from cellulose and were originally carbonized mainly for defence applications back in 1950s. Pitches are mixtures of aromatic hydrocarbons with three- to eight-membered rings. They can be derived from sources such as petroleum, coal, asphalt, and poly(vinylchloride). Acrylic fibres are defined as fibres with acrylonitrile (AN) content greater than 85% [15]. Among all, acrylic fibres possess the advantage of higher carbon yield, lower cost, simpler fabrication, and enhanced mechanical properties. The linear carbon backbone and high carbon content of this polymer precursor allows easier conversion into carbons. The discovery of polyacrylonitrile (PAN)-based precursor has been known as one of the most important technology breakthrough in the carbon fibre production. The carbon yield from acrylic fibres are on average 50% as compared to the 30% yield from rayon. Expensive processing and purifying procedures used for pitch are often avoided for acrylic fibre. Most importantly, acrylic fibres have been demonstrated to be excellent precursors for high performance carbon fibres with high tensile strength, stiffness, compressibility, and light weight, which can be applied to aerospace, transportation, reinforcement, and many other engineering sectors [14-19].

2.1.1 Precursor Selection

PAN homopolymer is generally not used in industry for carbon fibre production due to difficulties in exothermic heat control during stabilization. Because PAN is a poor heat conductor, the rapid and surge of heat generation could potentially cause chain breakage or fusion, which results in carbon fibres with poor properties. Small amount of comonomer ($< 4\text{wt}\%$) is often added to optimize the stabilization process by increasing the polymer segment mobility, reducing the stabilization temperature, and generating a milder reaction environment. Comonomers can also disrupt the strong attraction between nitrile groups in PAN to enhance solubility and spinnability [15, 20].

Possible comonomers that could be incorporated into PAN include acids, vinyl esters, vinyl amides, or ammonium salts of vinyl compounds, etc. Most of them act as plastisizers and introduce additional cyclization mechanisms during low temperature stabilization, which will be discussed in section 2.1.3. Acrylamide (AM) comonomer was chosen for this study due to its superior tensile strength in the resulting carbon fibres and the significant reduction in the exothermic heat generation [19, 21].

2.1.2 Electrospinning

Acrylic precursors with a molecular weight between 70 k to 260 k g/mol are often spun into fibres followed by post treatment before converted into carbon fibres [22]. Common spinning methods include wet spinning, dry spinning, and air gap spinning. The general procedure is to first dissolve 10-30 wt% of the polymer precursor in a suitable organic solvent. The polymer solution is then spun into a coagulation bath or a cell for solvent removal or evaporation, respectively. Washing is applied subsequently for complete

removal of solvents. Post treatment such as stretching is often conducted to align the polymer chain and to reduce the fibre diameter. Stretching can produce a high degree of molecular order, which has been shown to improve the mechanical properties of carbon fibres. Reducing the fibre diameter can increase the rate of heat flow within the fibre, which improves the carbonization efficiency and minimizes the skin-core formation [15, 20, 23].

In contrast to those complicated spinning processes, electrospinning has become one of the most promising technique to generate continuous carbon fibres. Its unique capability of spinning nano-scaled fibres has attracted much attention, along with the rising importance of nanotechnology. With its simple setup and consistency in massive production of continuous nanofibres, it is superior to many conventional fibre production methods and have been applied to over 50 polymers in the fields of tissue engineering, life science, electronics, filtration, cosmetics, and nanosensors [8].

Fig. 2-1(a) is a simple schematic representation of a typical electrospinning setup[3]. It is mainly composed of a spinneret with a metallic needle, a high voltage power supply, and a metallic ground. When the needle is subjected to high voltage, charges are induced and evenly distributed on the surface of the polymer solution at the nozzle. Polymer drop at the nozzle tip experience interactions between electrostatic repulsion and the external electric field. A Taylor cone, known as a liquid droplet with a conical shape, is produced (Fig. 2-1(a) and Fig. 2-1(b)-1) [8]. When the electrostatic force overcomes the surface tension of the solution, the cone becomes unstable and a polymer jet is ejected (Fig. 2-1(b)-2). Surface tension subsequently causes the Taylor cone to relax again (Fig. 2-1(b)-3) with a steady ejection of the polymer jet. The jet then undergoes whipping and

stretching motions with the evaporation of solvents at the same time. This elongation process allows the reduction in fibre diameter to as small as nanometer scale. Fibres are collected on a metal ground with random orientation, known as non-woven mat, as shown in Fig. 2-1(a) [3, 8, 24].

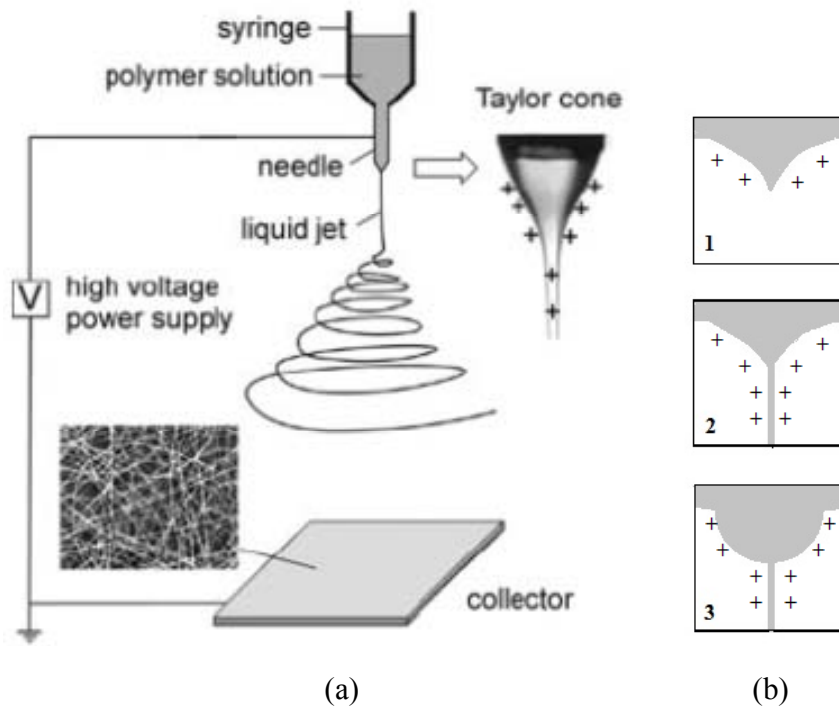


Fig. 2-1 Schematic representation of the basic setup of electrospinner with the SEM image of non-woven nanofibres collected on the metal ground (a) [3]. Reproduced with permission from John Wiley and Sons.

Taylor cone formation during spinning process: 1-Formation of a Taylor cone 2-Ejection of a polymer jet 3-Relaxation of the cone by surface tension (b), adapted from [8].

Fibres with different morphologies and orientations can be prepared by slightly modifying the spinning setup and the preparation method. Aligned nanofibres, nanofibres with core-shell structures, hollow nanofibres, and porous nanofibres have been made for various purposes. In this study, a core-shell nanofibre was demonstrated by coaxial electrospinning on two polymer solutions with different compositions for lithium

ion battery application in Chapter 4. Fig. 2-2(a) is a schematic representation of the coaxial spinning setup. Fig. 2-2(b) is some hollow nanofibres generated from coaxial spinning with the removal of core material through post-spinning treatment.



Fig. 2-2 Coaxial electrospinning setup (a).

Hollow nanofibres after the removal of core material (b). The shell is consisted of PVP and TiO_2 [25]. Reproduced with permission from ACS Publications.

2.1.3 High Temperature Treatment

The demand for PAN-based carbon fibres has increased significantly since its discovery in 1961[22]. Thermal treatment is essential to transform acrylic fibres into carbon and the processing conditions play a major role in producing high performance carbon fibres. The thermal treatment is mainly consisted of three stages: oxidative stabilization in air, carbonization in nitrogen, and high temperature carbonization in argon if above 2000°C [16].

i. Oxidative Stabilization

Stabilization reactions usually occur in between 200 – 300 °C in air and various structures have been proposed. Grassie [26, 27] stated that cyclization of nitrile groups produce a ladder structure as shown in Fig. 2-3:

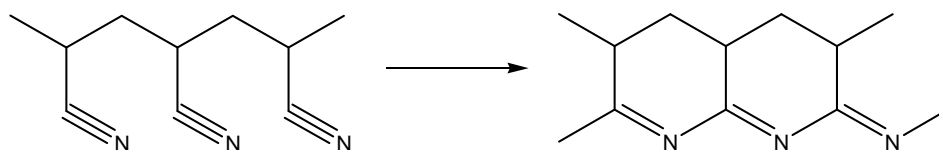


Fig. 2-3 Ladder structure produced by the intramolecular cyclization of CN groups, adapted from [26, 27].

Henrici-Olive [20] believed that intermolecular crosslinking of CN groups also occurs as a result of dipole-dipole interaction between neighbouring CN groups, as shown in Fig. 2-4:

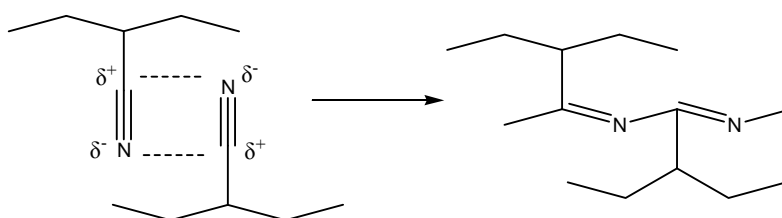


Fig. 2-4 Intermolecular cyclization of CN groups as a result of dipole-dipole interaction, adapted from [20].

Cyclization causes the chemical shrinkage of the acrylic fibre. Tension must be applied during stabilization to maintain the molecular order and reduce the amount of shrinkage [28]. It was observed that carbon fibres produced without tension

during pyrolysis could not be obtained with high tensile strength [23]. Such free-radical initiated oligomerization of CN triple bond is highly exothermic. If uncontrolled, the surge of heat could cause fibre fusion, chain scission, and poor carbon fibre properties. If the fibres were stabilized under optimum time and temperature regime, they would become thermally stable, infusible, and possess higher stiffness.

During stabilization, acrylic fibres gradually change their color from white to yellow and finally to brown, indicating the complete stabilization of the fibres and resistance to the flame [20]. Stabilization is thought to be the most complicated and most important part of the carbonization process.

As mentioned earlier, adding small amount of comonomers to PAN can significantly reduce the amount and the sharpness of the exothermic heat profile. Comonomers also disrupt the strong dipole-dipole interactions of CN groups, which permits faster oxygen diffusion and homogeneous stabilization. Different comonomers introduce different cyclization mechanisms. Since AM comonomer is used for this experiment, cyclization mechanisms introduced by the addition of AM is discussed here.

Both ionic and radical initiation mechanisms have been proposed for AM by Grassie and Sivy [29, 30], as shown in Fig. 2-5. It has been widely accepted that ionic mechanism initiates cyclization at lower temperature and slower rate, which reduces the overall reaction rate and surge of heat generation. However, too much comonomer addition will result in a slow oxidation and introduce more structural

defects to the resulting carbon fibre. A small and optimum amount of comonomer addition is crucial for the stabilization process.

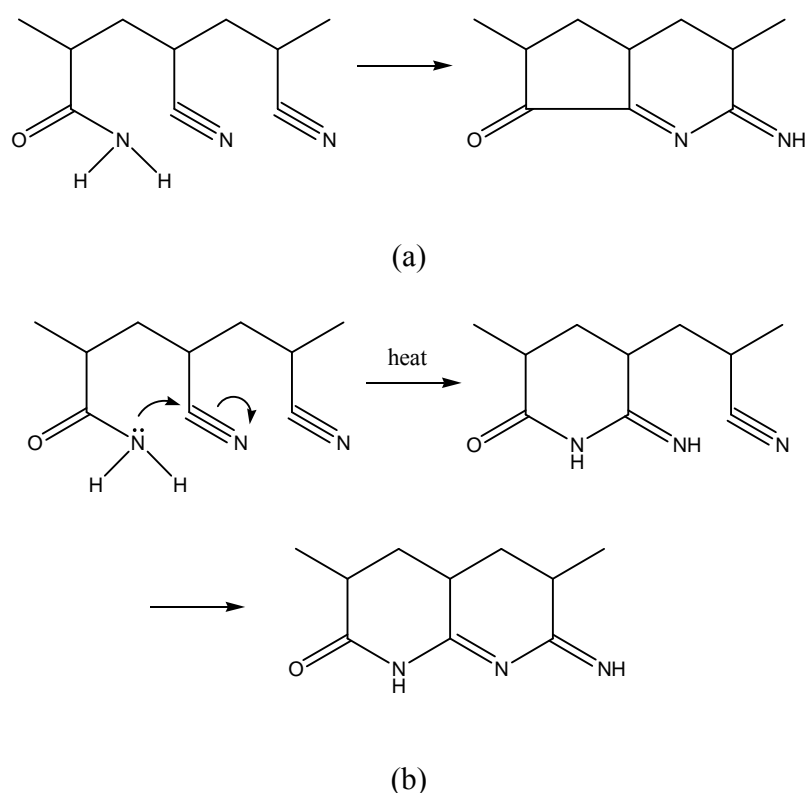


Fig. 2-5 Free radical cyclization (a) and ionic cyclization (b) mechanisms, adapted from [29, 30].

Cyclization reaction proceeds in both inert and oxygenated atmosphere but faster in the latter case. Donnet and Riggs believe that the presence of oxygen produces polar groups, as shown in Fig. 2-6, which facilitates cyclization and ring condensation [31, 32]. It has also been shown that fibres reacted with oxygen possess higher stability upon thermal treatment.

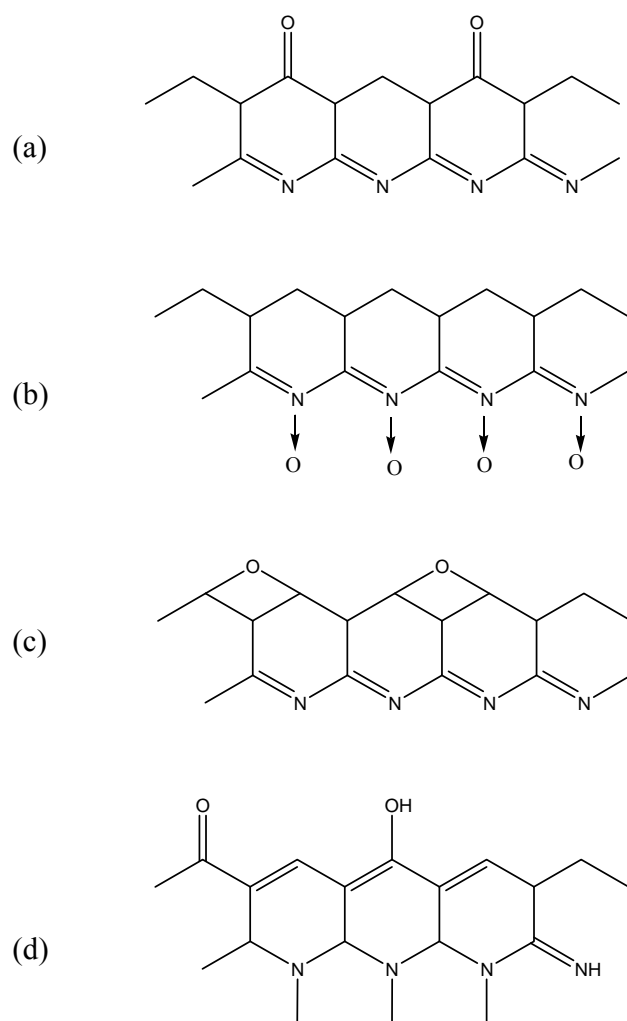


Fig. 2-6 Proposed chemical structures of PAN after oxidation. Carbonyl groups (a), lone pair donation of nitrogen to oxygen atom (b), bridged ether linkage (c), and hydroxyl and carbonyl groups (d), adapted from [31, 32].

On the other hand, a cyclized and dehydrogenated structure was proposed by Houtz [33], as shown in Fig. 2-7. The double bond formation on the carbon backbone was proposed to significantly improve the thermal stability of the polymer chain by preventing chain scission at elevated temperatures.

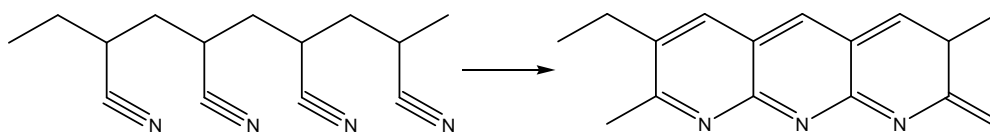


Fig. 2-7 Cyclization and dehydrogenation of PAN precursor, adapted from [33].

ii. Carbonization

After stabilization and ring cyclization, acrylic fibres can be heated up at a faster rate to the desired carbonization temperature without structural deterioration. Tension applied during carbonization shows little or no improvement on the mechanical properties of carbon fibres [34]. At this stage, dehydrogenation continues to occur at 400-600°C and denitrogenation, with the release of N_2 , is often observed at temperatures above 700°C, as shown in Fig. 2-8 proposed by Goodhew [35]. The cyclized rings are linked together laterally with the expulsion of gases (HCN , N_2 , CO , NH_3 , CO_2 , and CH_4) to produce turbostratic carbon [36, 37], which is known as high strength carbon fibres. A higher carbon content can be achieved with higher carbonization temperature. However, the maximum tensile strength of 7 GPa is only observed with carbonization temperature at around 1500°C [38]. The increase of the carbonization temperature improves the modulus but reduces tensile strength. An inert N_2 environment is mostly used at carbonization temperatures below 2000°C. At above 2000°C, argon is used instead to prevent N_2 from reacting with carbon [39].

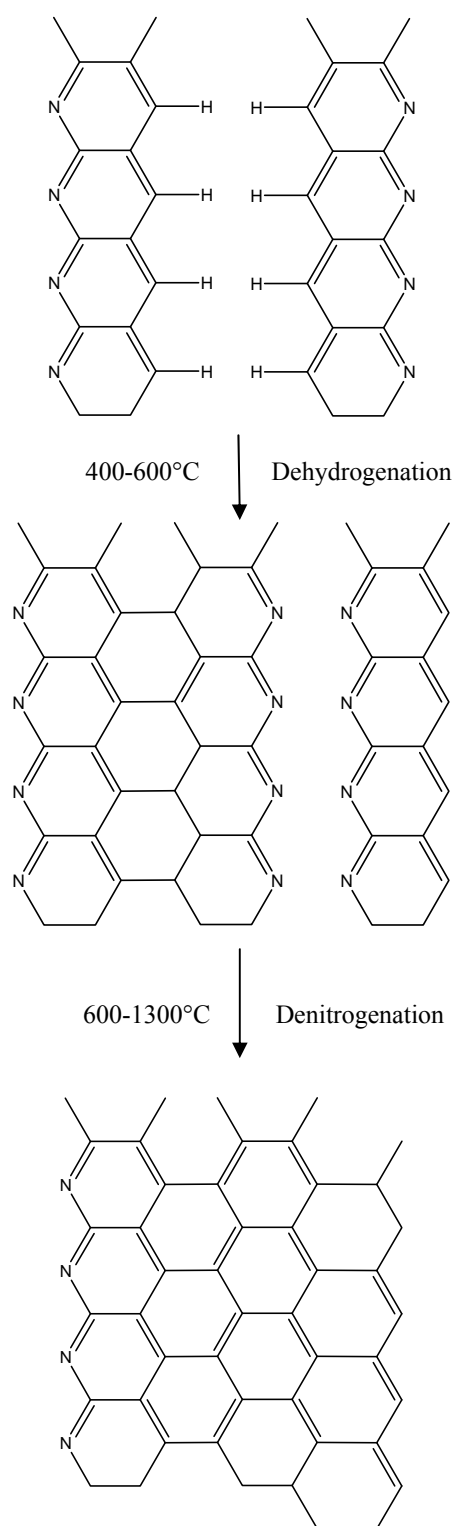


Fig. 2-8 Chemical pathway on the formation of carbon structure during carbonization, adapted from [35].

2.1.4 Role of Nanotechnology

“Nanotechnology” is the application and commercialization of nanoscience through the integration of chemistry, physics, biology, materials science, and engineering. In academia, “nanoscience” strictly refers to scientific methods dealing with materials with at least one dimension that is 1-100 nm. In industry, the “nano” range for materials broadens to 1-1000 nm [40]. Nanotechnology is known for enabling quality control of materials at molecular level [41]. One unique property of nano-materials is their size-dependent characteristics. For instance, gold is inert at macroscopic level but exhibits catalytic effect as nanoparticles. Wires below certain thickness at nano-level is able to conduct more current, namely higher conductivity, because electrons are more spatially confined [42, 43]. The enhanced surface area to volume ratio, surface reactivity, electrical conductivity, surface coverage, and mechanical property permits the development of nanofibres with advanced applications ranging from medical field, filtration, to electronic purposes.

With the growing research in the area of nanotechnology, nanofibres have also been intensely investigated in the past decade. As the fibre diameter is reduced to nano-meter scale, the specific surface area increases dramatically. For example, the reduction of fibre diameter from 1 μm to 100 nm increases the surface area from 3 m^2/cc to 30 m^2/cc . Nanofibres are therefore suitable for applications that require large surface area. They can further be modified with various functional groups or served as carriers for nanoparticles for multiple purposes in the areas of biotechnology and electronics. Many fabrication methods, including electrospinning, melt blown spinning, chemical synthesis, template synthesis, phase separation, and self-assembly, have been applied to synthesize

polymeric, inorganic, or composite nanotubular structures. Among all, electrospinning is most effective in producing high-aspect-ratio nanofibres (length/diameter > 100) [44, 45]. Carbon nanofibres generated from electrospinning have been applied to various areas including supercapacitors and battery electrodes [13, 46]. The small diameter permits thin film formation and the continuous fibre morphology with high aspect ratio develops a conductive network. The alignment of the nanofibre mat can also be controlled through electrospinning if necessary [3].

2.2 Experimental

The development of CNF mainly consists of three parts: synthesis of the copolymer precursor, electrospinning of the nanofibre from copolymers, and carbonization of the polymer nanofibre into CNF. The surface morphology, electrical conductivity, and flexural rigidity of CNF synthesized from copolymer are compared with that fabricated from commercially available PAN.

2.2.1 Copolymer Synthesis

AN, AM, and 4,4'-Azobis(4-cyanovaleric acid) (ACVA) were purchased from Sigma-Aldrich. Dimethylsulfoxide (DMSO) and neutral alumina were used as received. The inhibitor of AN was first removed by neutral alumina column. PANAM with two AM concentrations were synthesized through free radical polymerization as shown in Fig. 2-9. AN (4.5 M), AM (0.034 M or 0.068 M), and ACVA (0.0052 M) in DMSO were refluxed at 60°C overnight in nitrogen atmosphere. The copolymer was precipitated from large amount of methanol and was dried under vacuum at 50°C for 5 hours. The total amount of PANAM synthesized was ca. 20 g.

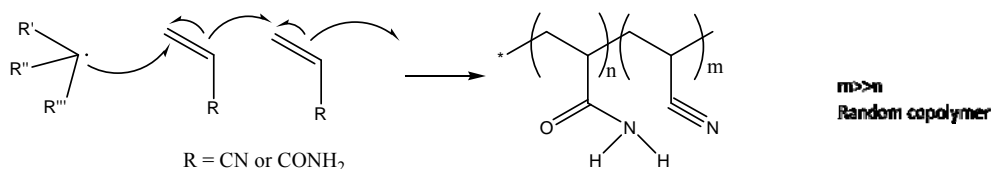


Fig. 2-9 Free radical polymerization mechanism of PANAM.

The copolymer poly(acrylonitrile-co-(N-*tert*-butyl)acrylamide) (PANBAM) was also synthesized to verify the approximate amount incorporation of AM. The monomer (N-*tert*-butyl)acrylamide (NTBAM) was purchased from Sigma-Aldrich and was used as received without further purification. AN (4.5 M), NTBAM (0.034 M), and ACVA (0.0052 M) in DMSO were refluxed at 60°C overnight in nitrogen atmosphere. PANBAM was also precipitated from large amount of methanol and was dried under vacuum at 50°C for 5 hours. The total amount of PANBAM synthesized was ca. 10 g.

2.2.2 Electrospinning

Solutions with 10 wt% PANAM and 10 wt% PAN in N,N-dimethylformamide (DMF) were prepared. PAN with a molecular weight of 150,000 was purchased from Scientific Polymers Inc. and was used as received. Syringes filled with these polymer solutions were placed in a Nanofibre Electrospinning Unit (NEU) from Kato Tech Ltd. The needles of PANAM and PAN solutions were supplied with a potential of 10 kV and 17 kV, respectively. The spinning distance (the distance between the needle tip and the collector ground) was 17 cm and the polymer flow rate was 0.03 – 0.04 mm/min.

Nanofibres generated from each solution were then collected onto grounded aluminium foil.

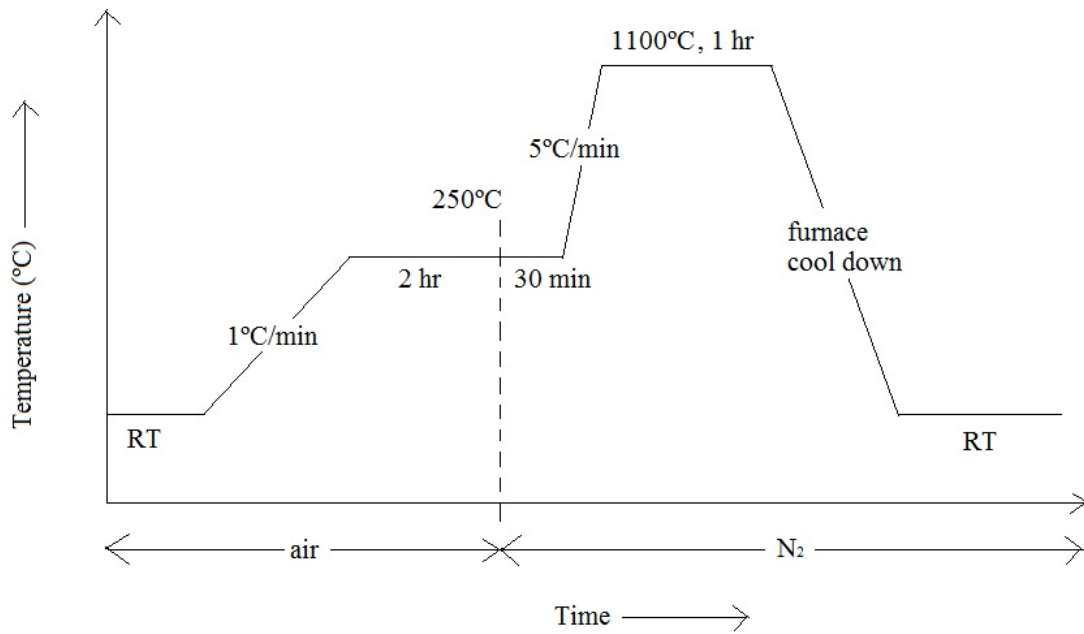
2.2.3 Carbonization

A Thermolyne 79400 tube furnace was used to carbonize nanofibre films. The film was sandwiched between two pieces of stainless steel holders with clamps to maintain tension during high temperature treatment. PAN nanofibre film was first heated at 1°C/min to 250°C in air. Sample holders were removed after the film was stabilized at 250°C in air for 2 hours. The sample was further stabilized at 250°C in nitrogen for 30 minutes before heated to 1100°C at 5°C/min ramp rate. The film was carbonized at 1100°C for 1 hour. A schematic of the heating program is shown in Fig. 2-10(a).

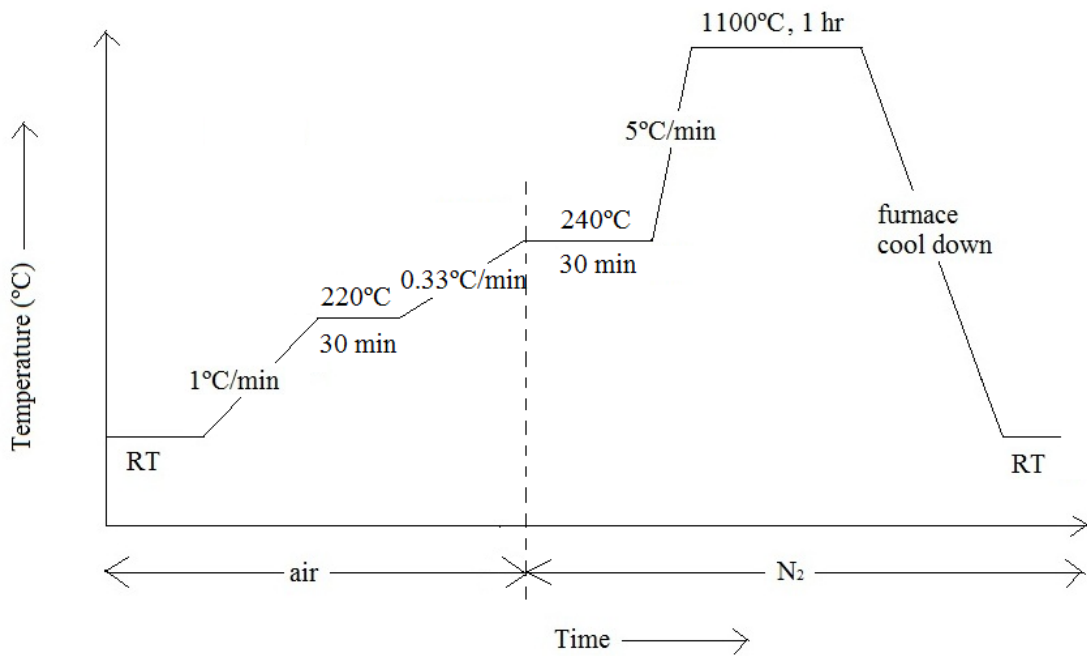
PANAM nanofibre film was sandwiched between sample holders with clamps and heated at 1°C/min to 220°C in air. After stabilized at 220°C in air for 30 minutes, it was heated to 240°C in air at 0.33°C/min ramp rate. Sample holders were then removed and the film was stabilized at 240°C for 30 minutes in nitrogen. Nanofibre film was heated to 1100°C at 5°C/min ramp rate with carbonization time of 1 hour. A schematic of the heating program is shown in Fig. 2-10(b).

Other methods of keeping sample holders on during pyrolysis were also investigated. The first method was to keep sample holders on without clamps throughout the whole carbonization process. The second method was to keep sample holders on with stainless steel screws throughout the whole process to provide more tensions. The third method was to use sample holders with clamps during oxidation in air, followed by removing

clamps but with holder on for the later process. A schematic of different tension applications is shown in Fig. 2-10(c).



(a)



(b)

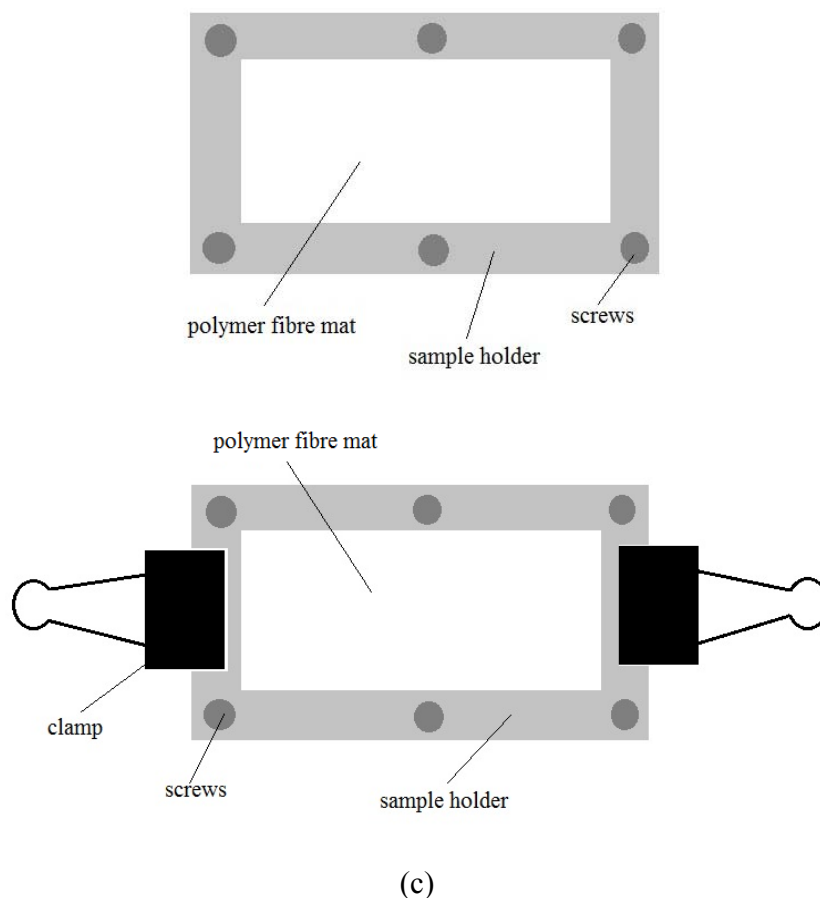


Fig. 2-10 Schematics of the PAN (a) and PANAM (b) heating programs, and different methods of applying tensions during carbonization (c).

2.2.4 Characterization

The intrinsic viscosity ($[\eta]$) method was used to characterize the viscosity molecular weight (M_v) of the copolymer. A Ubbelohde viscometer was used at 20°C with the copolymer in DMF solution. M_v was derived from the relationship of $[\eta] = 1.77 \times 10^{-4} M_v^{0.78}$ [47]. The weight percent of AM and NTBAM in PANAM and PANBAM, respectively, was characterized by ^1H nuclear magnetic resonance (NMR) experiment, which was carried out on a Bruker AV600. A TA Instrument Q1000 was used for DSC analyses on both PANAM and PAN nanofibres. DSC analyses were carried out with a

heating rate of 2.5°C/min from room temperature to 350°C in nitrogen. The nanofibre samples were encapsulated in a tightly sealed Hermetic pan. A Hitachi S-3000 Scanning Electron Microscopy (SEM) was used to characterize the surface morphology. The working distance was set at ca. 6 mm with an accelerating voltage of 20 kV. Energy dispersive X-ray spectroscopy (EDX) was done on the same SEM to measure the composition of CNF. The working distance was set at 15 mm with an accelerating voltage of 20 kV. The data was collected after 100 second scan. The average fibre diameters of the polymer precursor and CNF were calculated from 50 fibers in SEM images using ImageJ Program [48]. CNF film was also characterized in the backscattering mode of the Renishaw Raman spectrometer (RM 1000) excited by the diode laser with 785 nm wavelength. The data was collected after eight scans within the wavenumber range of 800 – 1800 cm⁻¹. The spectrometer was linked to a Leica DMLB microscope for focusing the sample. The conductivities of the CNF films were measured using a 4-point probe instrumented in the laboratory. The flexural rigidity of the CNF film was measured by the ASTM Standard Test Method for Stiffness of Fabrics (D1388-08) using a home-made cantilever bending tester.

2.3 Results and Discussions

2.3.1 Copolymer Characterization

The yield for PANAM was approximately 80 %. The M_v of PANAM synthesized from lower AM concentration was 1.98×10^5 g/mol and the amount of AM incorporated into the copolymer was 0.9 wt%. The M_v of PANAM synthesized from higher AM concentration was 1.72×10^5 g/mol and the amount of AM incorporated into the copolymer was 1.8 wt%. The M_v of PAN characterized from intrinsic viscosity was

1.57×10^5 g/mol. The oven dried PANAM is shown in Fig. 2-11. Fig. 2-12 shows the NMR spectra of both copolymers. Peak **a** and peak **b** are the $-\text{CH}_2$ and $-\text{CH}$ stretches, respectively, from the copolymer backbone. Peaks **c** and **d** are the $-\text{NH}_2$ stretches from the AM units [49]. The wt% of AM was calculated from the ratio of $-\text{NH}_2$ and $-\text{CH}_2$ stretches.

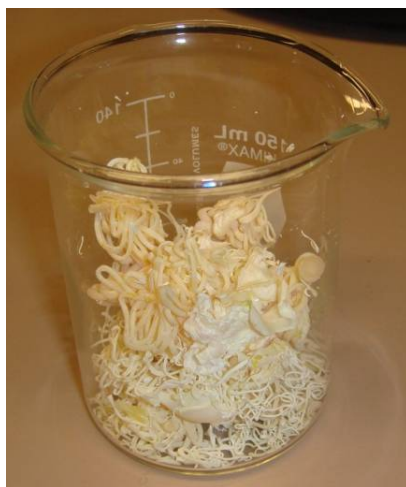
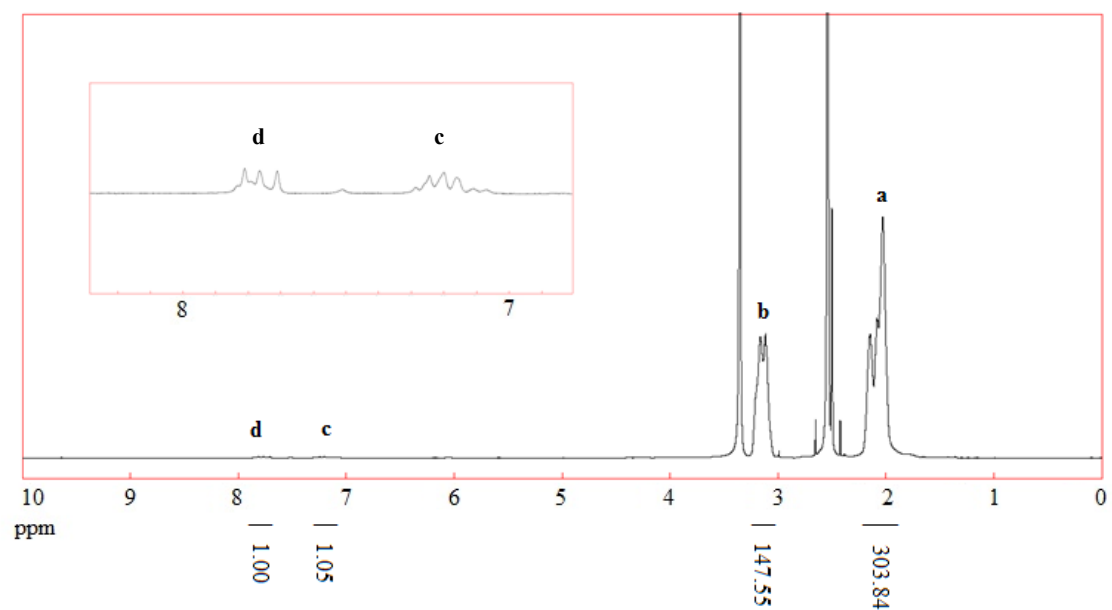
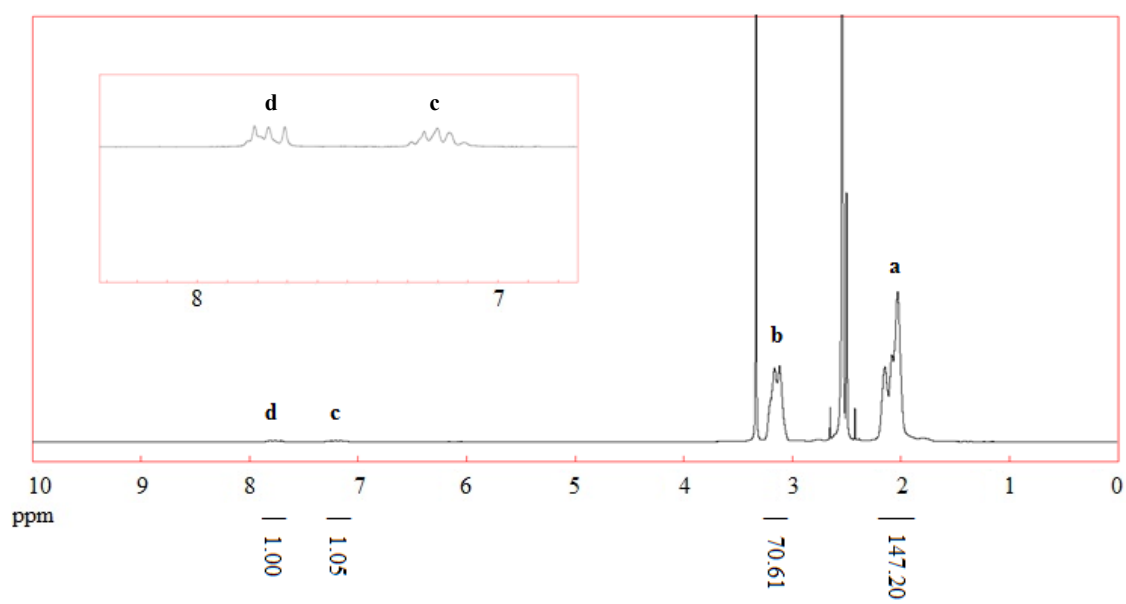


Fig. 2-11 Oven dried PANAM.



(a)



(b)

Fig. 2-12 NMR spectra of PANAM with 0.9 wt% AM (a) and 1.8 wt% AM (b).

In the mean time, the copolymer PANBAM was synthesized and characterized by ^1H NMR in order to verify the incorporation of AM since peaks **c** and **d** in Fig. 2-12 are very small. Fig. 2-13 is the NMR spectrum of PANBAM. As shown, peak **d** is the $-\text{CH}_3$ stretch from NTBAM, which is nine times larger than peak **c**, the $-\text{NH}$ stretch from NTBAM. This confirmed that the calculation method used for determining AM concentration is valid.

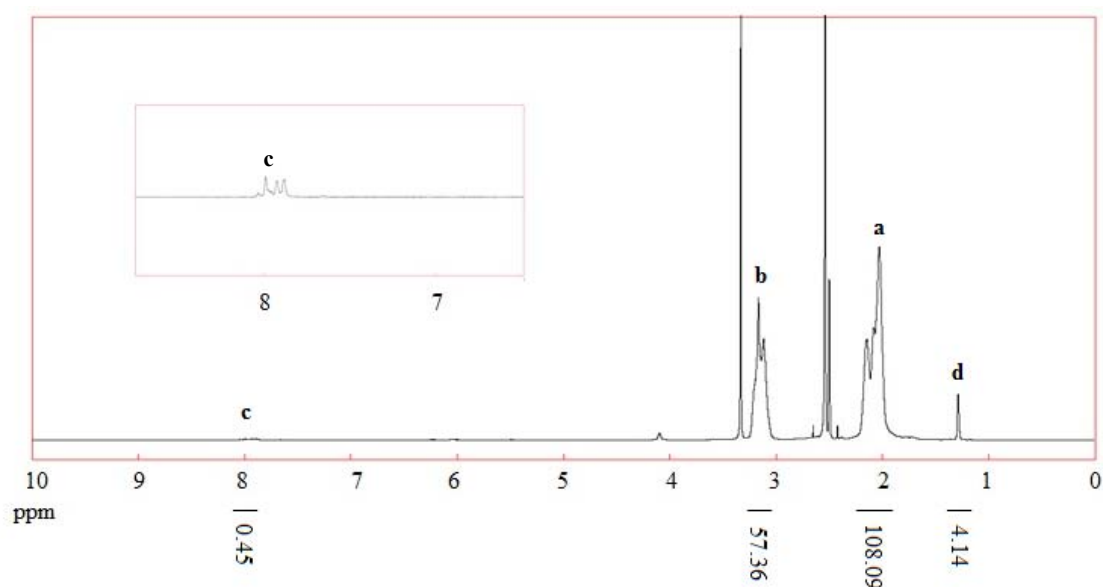
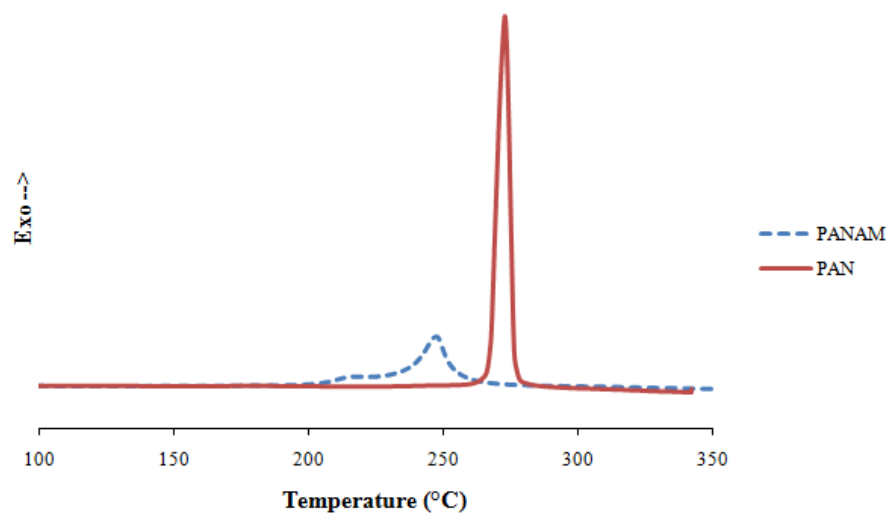


Fig. 2-13 NMR spectrum of PANBAM.

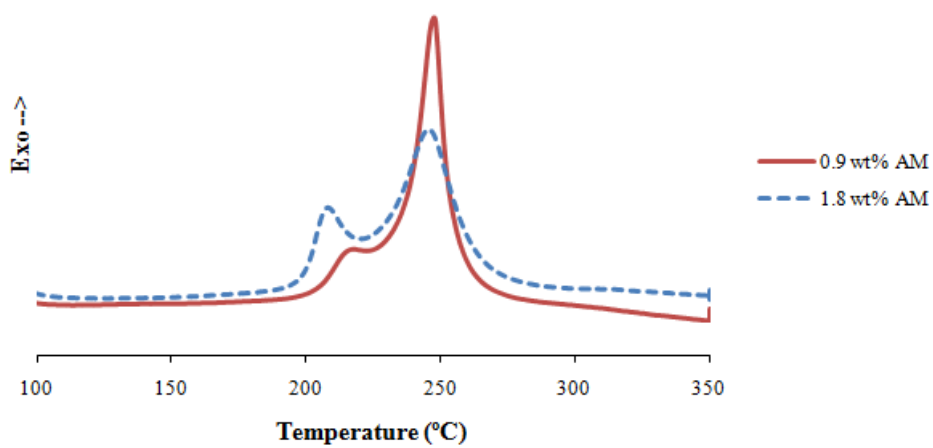
The purpose of adding a small amount of copolymer (usually less than 4 wt%) is to reduce the amount of exothermic heat generation between 200 – 300°C during pyrolysis. The surge amount of heat generated in a high temperature and a narrow temperature range could potentially cause polymer chain scission, fibre fusion, or fibre breakage, which is detrimental to the mechanical properties of the resulting carbon fibre [20]. As shown in the DSC curve of Fig. 2-14(a), the violent and sharp exothermic heat profile at

270°C generated from pure PAN is undesirable for stabilization. Adding a small amount of comonomer, in this case AM, significantly reduces the amount of heat and broadens the temperature range of the heat profile, which began at 200°C and ended at 275°C. The heat profile from the DSC curves are useful in selecting stabilization temperature parameters since the presence of exothermic heat indicates the onset of polymer chain cyclization. For pure PAN, temperature at 250°C, which is slightly below the exothermic heat peak, was selected to avoid the violent heat generation. For PANAM, a more complicated heating ramp was designed to accommodate the broad chain cyclization temperature according to Fig. 2-14(a).

Different ratios of AM also affect the exothermic heat performance of the copolymer, as shown in the DSC curves of Fig. 2-14(b). Adding more AM reduces the peak height at ca. 250°C and increases the peak height at ca. 200°C. This often generates an even milder reaction, but the polymer could suffer from slower and inefficient reaction rate [19]. Carbonization and subsequent CNF characterizations were conducted to verify the optimum amount of AM incorporation for the carbon fibre production.



(a)

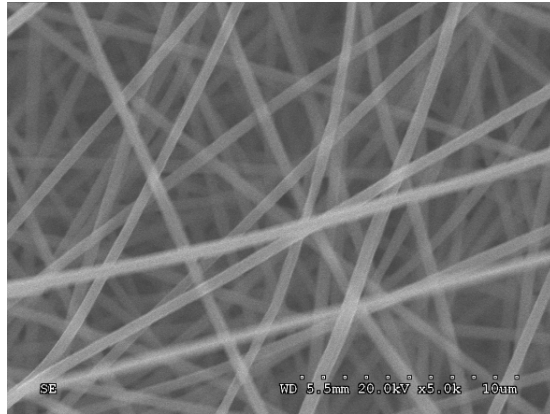


(b)

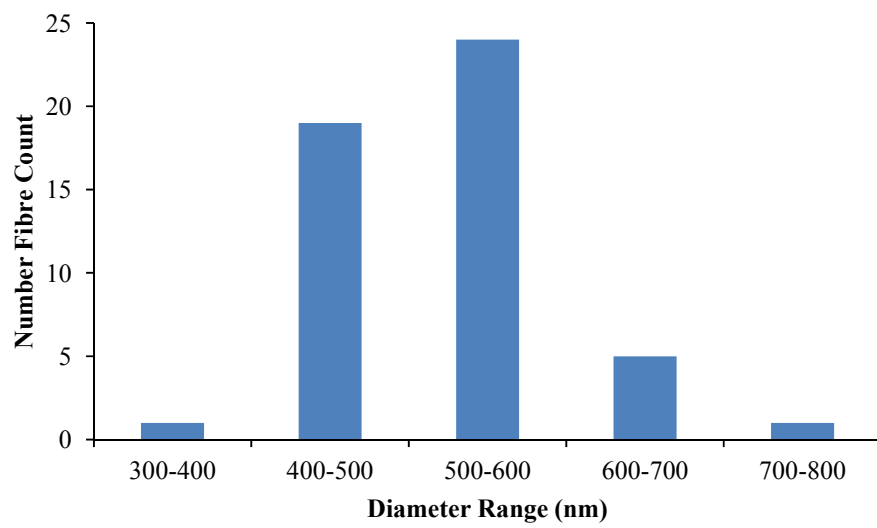
Fig. 2-14 DSC comparison of PAN vs. PANAM (a) and PANAM with different AM concentrations (b).

2.3.2 Electrospun Nanofibres

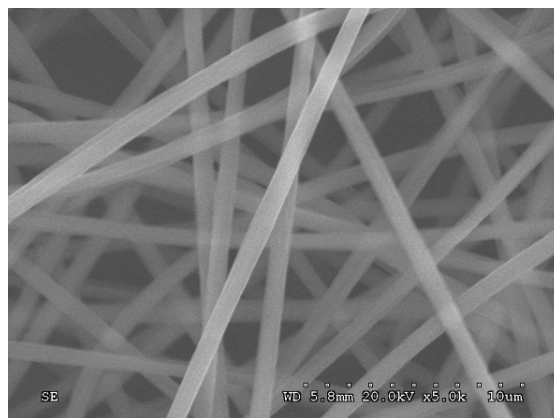
Introducing small amount of copolymer, in this case AM, can disrupt the strong dipole-dipole interactions of PAN nitrile groups. Polymer chains therefore possess better stretching ability and spinnability [15]. A lower spinning voltage was used for PANAM comparing to that for PAN. Fig. 2-15(a), (c), and (e) are the SEM figures of nanofibers electrospun from PAN and two types of PANAM. Average diameters vary with molecular weight and are $5.2 \pm 0.7 \times 10^2$ nm, $8 \pm 1 \times 10^2$ nm, and $8 \pm 1 \times 10^2$ nm for PAN, PANAM (0.9 wt% AM), and PANAM (1.8 wt% AM), respectively. Fig. 2-15(b), (d), and (f) are the diameter distribution of 50 fibres selected from each polymer that is used to calculate the average diameter. Uniform nanofibres were generated from all three types of polymers with a narrow window of diameter distribution.



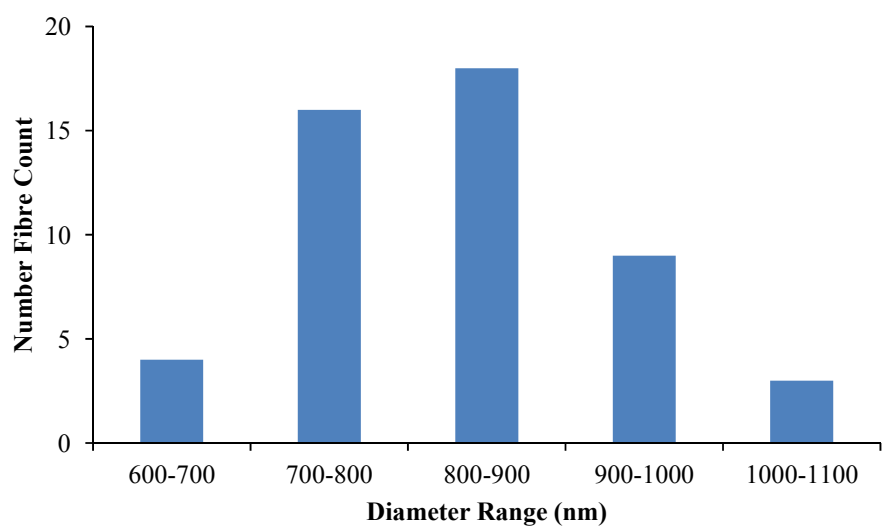
(a)



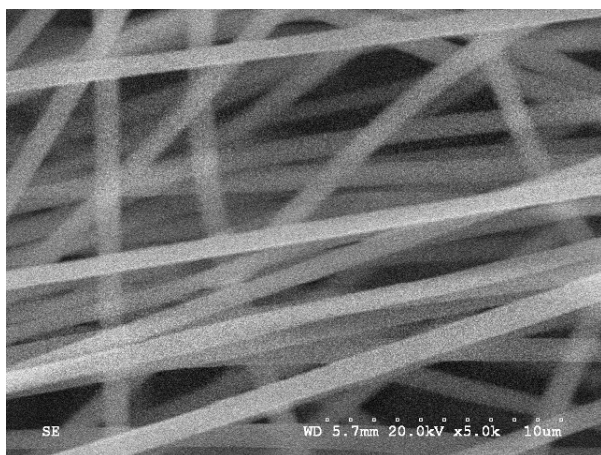
(b)



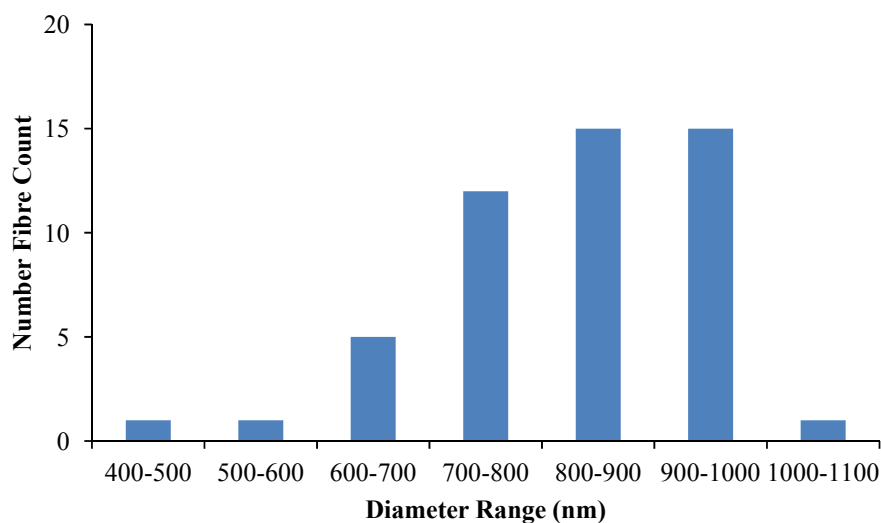
(c)



(d)



(e)



(f)

Fig. 2-15 SEM figures of PAN (a), PANAM (0.9 wt% AM) (c), and PANAM (1.8 wt% AM) (e) electrospun nanofibres. Fibre diameter distribution of PAN (b), PANAM (0.9 wt% AM) (d), and PANAM (1.8 wt% AM) (f).


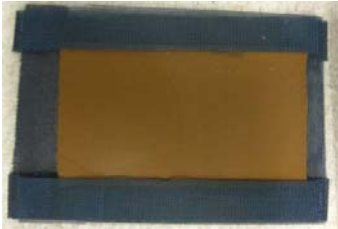




2.3.3 Carbonization






The main role of AM in PANAM copolymer is to generate a milder reaction environment during stabilization stage of high temperature treatment. As shown in Fig. 2-14(b), the rapid and surge amount of heat generation of PAN at high temperature could potentially damage the fibre [15, 20]. The chain cyclization for PAN is mainly initiated by free radical mechanism, which occurs at higher temperature with fast reaction rate and large exotherm. Incorporation of comonomer, in this case AM, initiates cyclization at lower temperature with the introduction of ionic mechanism [19, 30]. In Fig. 2-14(b), the two DSC peaks for PANAM at ca. 200 and 250°C are believed to be contributed from ionic and free radical mechanisms, respectively. Addition of more AM increase the amount

contribution from ionic mechanism, which increases the relative exothermic peak height at 200°C of the DSC curve.

Samples with tensions at different time frames were examined, as shown in Table 2-1. Experiment done with sample holders kept on for the entire carbonization process caused significant fibre breakage. Only the first method, where the tension was removed during carbonization, produces flat CNF films without uneven shrinkage or partial breakage. Therefore, the first method was used for the subsequent experiments. Expulsion of various gases during carbonization produced carbon fibres with 92 ± 2 % carbon content as determined by DEX. Increasing carbonization temperature tends to improve the graphitic structure (precisely should be “pseudo-graphitic” structure since the interplanar distance of turbostratic carbon, 0.34 – 0.35 nm, is always greater than that of pure graphite, 0.3354 nm [50]) of carbon fibre; however, due to the furnace temperature limitation, the fibres were only treated at 1100°C. CNF derived from PANAM copolymer showed good scalability and flexibility, which will be quantified by flexural rigidity test as discussed in section 2.3.6. Fig. 2-16 shows the SEM images of the CNF pyrolyzed from different precursors. The average diameters for PAN, PANAM (0.9 wt% AM), and PANAM (1.8 wt% AM) are $3.3\pm 0.7\times 10^2$, $4.0\pm 0.5\times 10^2$, and $3.9\pm 0.5\times 10^2$ nm, respectively.

Table 2-1 Methods of using sample holders during carbonization.

Method Description	Resulting CNF
<p>1. Sample holders + clamps during oxidation in air. Everything was removed afterwards. The steel mesh was used to prevent direct contact between nanofibre mat and the furnace glass.</p>  	 <p>CNF remained intact with no curling or uneven shrinkage.</p>
<p>2. Sample holders were not removed at all time.</p> 	  <p>The result was inconsistent. Some samples shrank more and had wavy folds and some samples remained intact.</p>

<p>3. Sample holders were used with screws on with enhanced tensions and were not removed at all time.</p> 	 <p>The final CNF sample broke into two pieces and curled up.</p>
<p>4. Sample holders were used with clamps during oxidation in air. Clamps were removed after oxidation in air but the sample holders were kept on at all time. (the difference between methods 1 and 4 is that sample holders were removed in method 1 during carbonization)</p>  	 <p>CNF remained in one piece but curled up and shrank unevenly.</p>

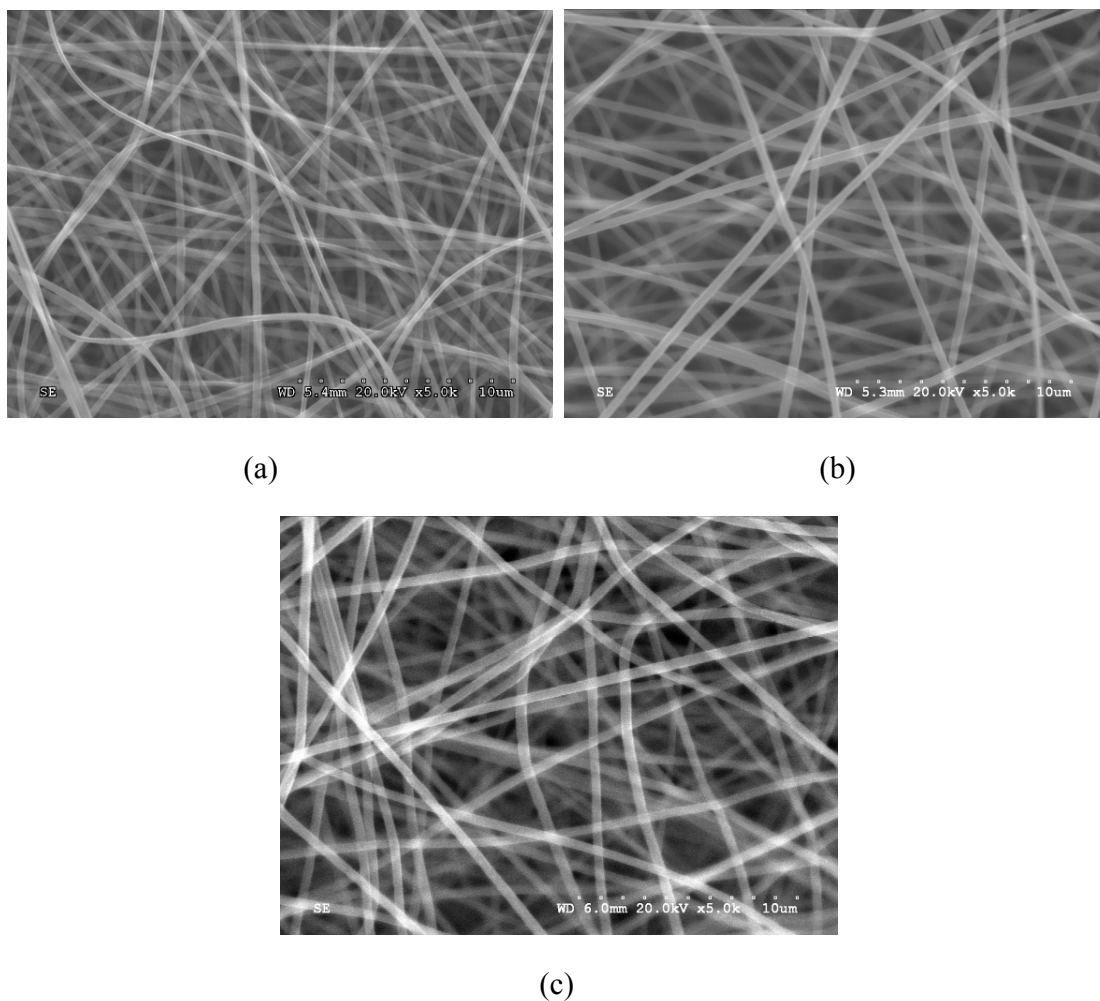


Fig. 2-16 SEM of carbon nanofibres pyrolyzed from PAN (a), PANAM (0.9 wt% AM) (b), and PANAM (1.8 wt% AM) (c).

2.3.4 Raman Spectroscopy

Raman scattering was known to be very sensitive to carbon polymorphs. Two signature peaks for disordered carbon films are the D and G peaks centered at ca. 1355 cm^{-1} and 1580 cm^{-1} , respectively, using an excitation wavelength of 514 nm [51, 52]. Peak D is the vibration mode from amorphous carbon, and its intensity is only related to the presence of sixfold aromatic ring. Peak G is the vibration mode from all sp^2 carbons. The position and sharpness of peak G also dictates the morphology of carbons. A single

crystal graphite possess a sharp single peak at 1580 cm^{-1} . As the peak G broadens and shifts between 1580 to 1600 cm^{-1} , the morphology of carbon changes from single graphite to nanocrystalline graphite or turbostratic carbon. In the mean time, peak D appears with the disordering of graphite and ordering of amorphous carbon. As the peak G shifts even further to ca. 1520 cm^{-1} , carbon becomes completely disordered, amorphous, and possess large amount of defects with reduced crystal size. This is accompanied by the reduced peak D intensity as the number of ordered rings decreases [53].

The intensity ratio of the two peaks, denoted as I_D and I_G , is often used to verify the amount graphitization and the alignment of carbon planes. For the case of carbonizing acrylic fibres, increasing the carbonization temperature increases the molecular order of the carbon film and subsequently decreases the I_D/I_G ratio [52-56]. Fig. 2-17 is the representative Raman spectra of CNF film pyrolyzed from pristine PAN, PANAM (0.9 wt% AM), and PANAM (1.8 wt% AM). Table 2-2 is the peak position summary and the intensity ratio calculated from Gaussian curve fitting. The D and G peaks from all three CNF films were located at approximately 1320 and 1585 cm^{-1} , indicating the presence of carbon. The shift in peak D position from 1355 to 1320 cm^{-1} was mainly due to the longer excitation wavelength used in this experiment. The position of peak G in contrast was not very sensitive to the excitation wavelength [51]. Since acrylic fibres are not graphitizable due to the presence of sp^3 bond[15], the presence of both peaks D and G for all samples indicates the formation of turbostratic carbon.

The average I_D/I_G for carbons pyrolyzed from different precursors are shown in Table 2-2. The ratios are mostly between 1.60 and 1.70, which are lower than previously reported values (1.95 and 2.45) using electrospun PAN carbonized at $900 - 1100^\circ\text{C}$ [54, 56]. I_D/I_G

ratios here for carbons from all polymer precursors were fairly close. The limited improvement of carbon chain ordering by using copolymers might be a result of two reasons. First is the limited polymer chain ordering during electrospinning due to the fast evaporation of solvents. Second is the potential defects developed during copolymer synthesis, which reduces the resultant carbon quality.

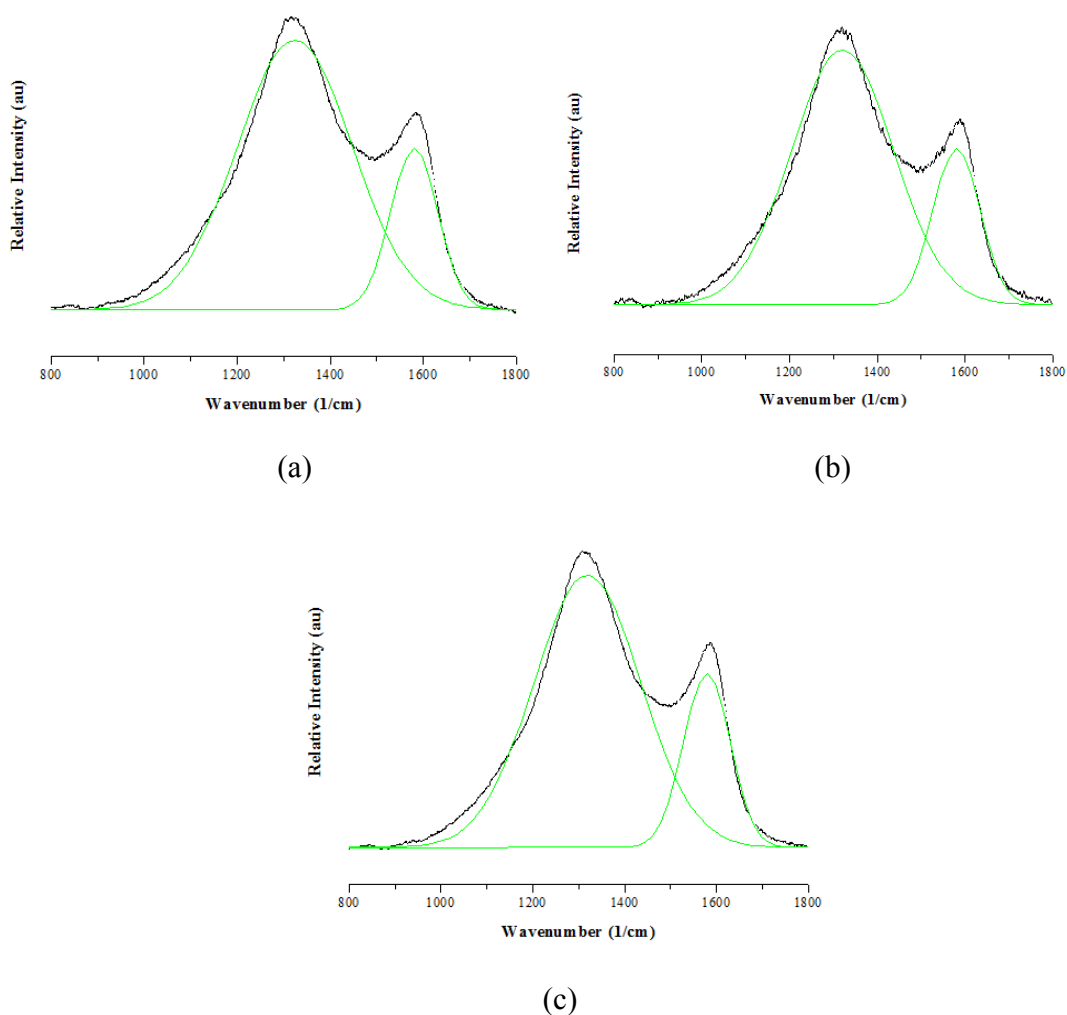


Fig. 2-17 Representative Raman spectra of CNF pyrolyzed from PAN (a), PANAM (0.9 wt% AM) (b), and PANAM (1.8 wt% AM) (c).

Table 2-2 D and G peak positions and their intensity ratios from CNF pyrolyzed from different polymer precursors.

Polymer Precursor	Peak D position (cm ⁻¹)	Peak G position (cm ⁻¹)	I _D /I _G	Average I _D /I _G
PAN	1323.66	1587.62	1.70	1.68 ± 0.01
	1317.91	1588.44	1.67	
	1323.66	1584.06	1.67	
	1315.18	1582.69	1.69	
PANAM (0.9 wt% AM)	1312.17	1581.87	1.56	1.60 ± 0.04
	1315.18	1584.88	1.64	
	1317.91	1590.63	1.63	
	1323.66	1590.63	1.57	
PANAM (1.8 wt% AM)	1309.43	1587.62	1.56	1.61 ± 0.04
	1303.69	1587.62	1.61	
	1303.69	1587.62	1.61	
	1297.94	1587.62	1.68	

2.3.5 Conductivity Measurement

The average conductivities (S/cm), CNF volume density, and weight loss of nanofibres after carbonization are shown in Table 2-3. The measured conductivities of CNF pyrolyzed from both PAN and PANAM (0.9 wt% AM) are 17±1 and 18±1 S/cm, respectively, while that from PANAM (1.8 wt% AM) is only 9±1 S/cm. The weight loss for most samples ranged between 40 – 50 wt%. The conductivity of electrospun CNF derived from PAN agreed with the results reported previously [55, 57]. Some post-spinning treatment might be required to further align the molecular chain to achieve higher conductivities for both PAN and PANAM (0.9 wt% AM). The low conductivity of PANAM (1.8 wt% AM) might be due to the addition of too much AM comonomer, which creates more defects in the polymer chain and slows down the chain cyclization

during stabilization process. Electrospun PANAM (0.9 wt% AM) was selected to carbonize into larger samples to compare its flexural rigidity with pure PAN.

Table 2-3 Conductivities of CNF pyrolyzed from different polymer precursors.

Precursor	Polymer Weight Loss After Carbonization (%)	Volume Density (mg/cm ³)	Conductivity (S/cm)	Average Conductivity (S/cm)
PAN	47±3	160±10	1.8±0.2×10 ¹	17±1
	48±3	180±20	1.7±0.2×10 ¹	
	45±3	140±10	1.7±0.2×10 ¹	
	44±3	160±10	1.7±0.3×10 ¹	
PANAM (0.9wt% AM)	46±6	160±30	1.8±0.2×10 ¹	18±1
	47±5	160±20	1.7±0.2×10 ¹	
	45±5	170±20	2.0±0.3×10 ¹	
	47±4	160±20	1.8±0.4×10 ¹	
PANAM (1.8wt% AM)	59±5	110±10	0.9±0.1×10 ¹	9±1
	40±2	120±10	1.0±0.1×10 ¹	
	60±7	80±10	0.8±0.1×10 ¹	
	40±3	130±10	1.0±0.1×10 ¹	

2.3.6 Flexural Rigidity

Both electrospun PAN and PANAM (0.9 wt% AM) nanofibres were carbonized in a stainless steel sample holder with outer dimensions of 30.00±0.05 cm × 5.50±0.05 cm. At a smaller sample size, PAN can be carbonized in one piece with no breakage. However, when the sample size is increased, the electrospun PAN film tends to break apart after stabilization, as shown in Fig. 2-18(a). The crack mostly appears close to the center of the sample, making it difficult to keep the sample intact and obtain a sample size large enough for the flexural rigidity test. The crease on the sample, as shown in Fig. 2-18(a), also implies that stabilization reaction might happen too rapidly. As a result, the film shrinks too fast with uneven shrinkage throughout the length. In contrast,

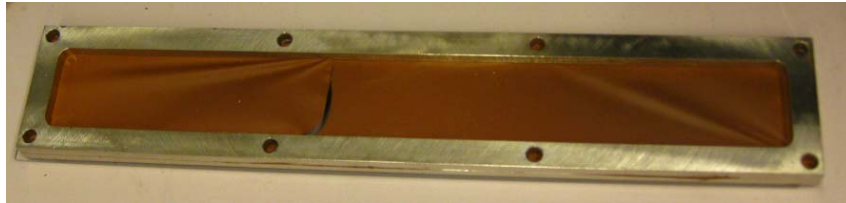
electrospun PANAM (0.9 wt% AM) was able to remain intact after stabilization with no crease formation throughout the film and was able to carbonize into long carbon fibre samples, as shown in Fig. 2-18(b) and Fig. 2-19. The dimension of the CNF was $23.00 \pm 0.05 \text{ cm} \times 2.50 \pm 0.05 \text{ cm}$. This result has a significant impact on the scale-up capability of electrospun CNF. The addition of AM comonomer could produce not only a more flexible carbon sample, but also produce samples without size limit. Due to the breakage of PAN sample during stabilization, it could not be made into CNF films long enough for the flexural rigidity test.

Flexural rigidity test is a measure of a membrane or a fabric's ability to bend on its own weight. The flexural rigidity of PANAM (0.9 wt%) was measured by a cantilever bending tester constructed in our laboratory according to ASTM , as shown in Fig. 2-20. The CNF mat was slid along the edge of the slope with a ruler until the end of the mat overhang touches the 41.5° slope. The length of the overhang or bending length of the mat was measured and the flexural rigidity was calculated from the following equation,

$$G = 1.421 \times 10^{-5} \times W \times c^3$$

where G is the flexural rigidity ($\mu\text{joule/m}$), W is the areal density of the carbon fibre (g/cm^2), and c is the bending length (mm). The areal density of the carbon fibre was $5.6 \pm 0.2 \times 10^{-4} \text{ g/cm}^2$. The bending length is half length of the ruler protrusion, which is $53.8 \pm 0.5 \text{ mm}$. G is therefore $1.24 \pm 0.05 \times 10^{-3} \mu\text{joule/m}$. Flexural rigidity is a method of characterizing the fabric stiffness. In general, the stiffer the fibre, the longer is the bending length. The stiffness of the fibre is also directly proportional to the areal density of the fabrics [58]. It is unfair to compare the flexural rigidity of CNF directly with other

fabrics since areal densities varies with different experiments. However, it can be concluded from this study that electrospun CNF mat possesses certain degree of flexibility since it is able to bend under its own weight.



(a)



(b)

Fig. 2-18 Stabilized electrospun PAN (a) and PANAM (0.9 wt% AM) (b).

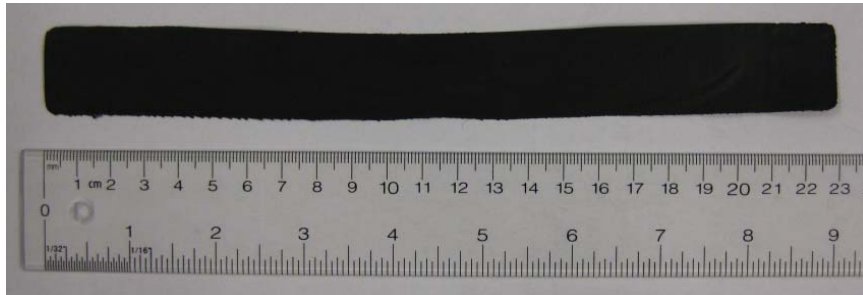


Fig. 2-19 Carbonized electrospun PANAM (0.9 wt% AM) sample.

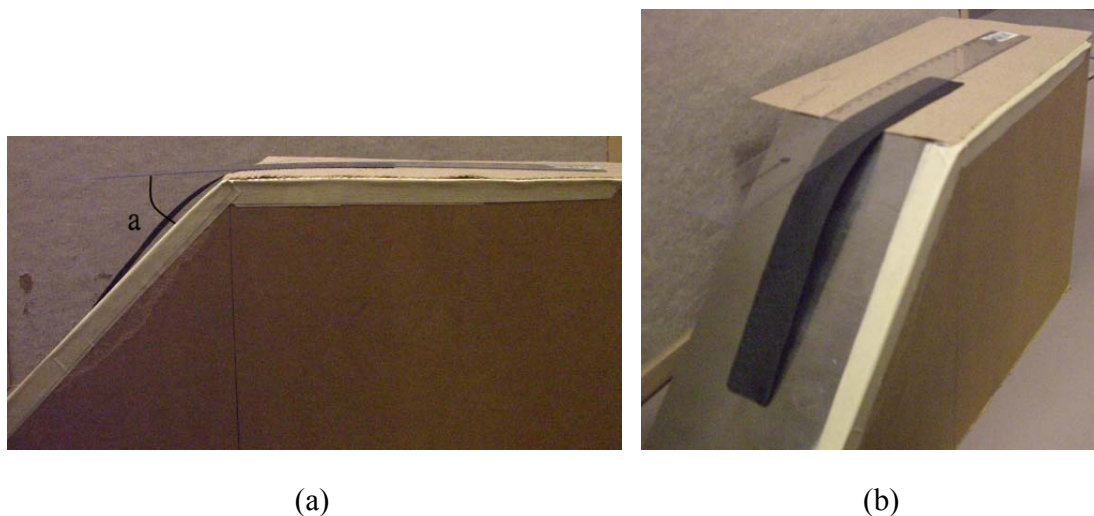


Fig. 2-20 Side view indicating angle $a = 41.5^\circ$ (a) and top view (b) of the home-made cantilever bending tester with the carbonized electrospun PANAM (0.9 wt% AM).

2.4 Conclusion

Copolymer PANAM with 0.9 and 1.8 wt% of AM were successfully synthesized, electrospun, and carbonized into non-woven CNF mats with $4.0 \pm 0.5 \times 10^2$ and $3.9 \pm 0.5 \times 10^2$ nm in CNF diameter, respectively. Among all, PANAM (0.9 wt% AM) carbon possess a conductivity of 18 ± 1 S/cm, which is similar to electrospun PAN carbon but higher than electrospun PANAM (1.8 wt% AM) carbon. PANAM (0.9 wt% AM) also proves to possess a superior scale-up capability due to a milder and smaller amount of exothermic heat generation during pyrolysis. The milder heat reaction stabilizes nanofibres and significantly reduces the chance of chain scission and fibre breakage. PANAM (0.9 wt% AM) was able to be fabricated into large CNF film and the flexural rigidity test shows that the CNF film is a flexible membrane material. Some post-spinning processes, such as hot stretching of nanofibers, might be required for polymer nanofibre precursors to improve the fiber chain alignment and thus the CNF conductivity.

3 Supercapacitor

3.1 Introduction to Supercapacitor

Supercapacitors are also known as electrochemical double layer capacitors (EDLC), ultracapacitors, and gold capacitors. Supercapacitors store and release energy rapidly like conventional capacitors but possess much higher specific energy, hence deriving the name “super” and “ultra.” One important feature for supercapacitors is that they fill in the energy and power gap between conventional capacitors and batteries, as shown in the Ragone plot in Fig. 3-1 [59]. Being able to provide pulse of powers with high energy, in which traditional capacitors are unable to store, supercapacitors are versatile as a single energy supply or as a hybrid system with batteries or fuel cells. At present, they are mostly used for backup power supply, engine starters, forklifts, cell phones, and hybrid electric vehicles. However, the specific energy (5 – 7 Wh/kg) is still low to be considered as a long term energy supply (80 – 100 Wh/kg) [11].

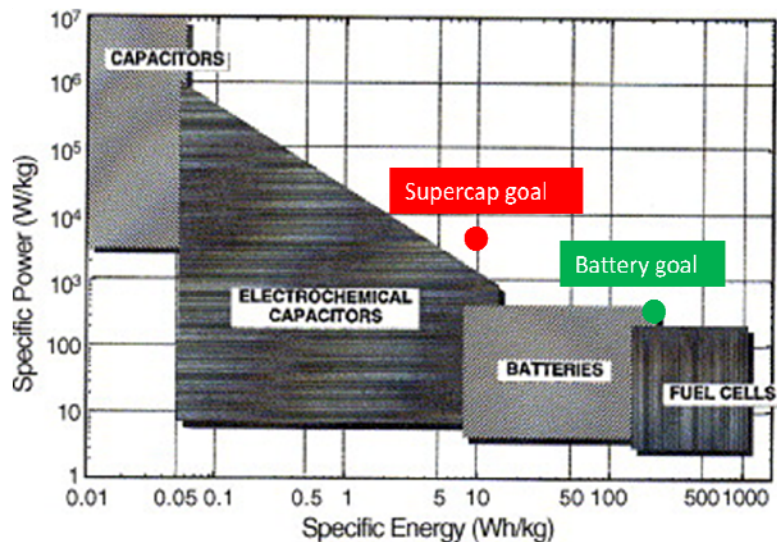


Fig. 3-1 Ragone plot of various energy storage devices [59]. Reproduced with permission from Elsevier Science Ltd.

Supercapacitors compensate the power deficiencies of batteries and fuel cells. Batteries, although can store large amount of energy (40 – 100 Wh/kg), are poor at delivering surge of power (few hundred W/kg) [10]. Their cycle life is short (few thousand cycles) due to the self-discharge, chemical reactions occurring in the cell, and mechanical failure of electrodes induced by cycling[60-63]. In contrast, supercapacitors can be charged/discharged rapidly with a high power density over 1 kW/kg. The cycle life as high as 500,000 has also been reported [64]. Their quick response to sudden changes in power interruption or load helps to maintain the system stability and power quality. One example is the combination of supercapacitor with other fuel sources for hybrid electric vehicles. Supercapacitors mitigate the short-comings of long term fuel sources by handling burst of power during accelerating, breaking, and engine starting. This not only conserves the energy of the long term fuel supply but also prolongs its lifetime.

3.1.1 Principles of Supercapacitors

Similar to batteries, supercapacitors mainly consist of an anode and a cathode separated by a porous separator in an electrolyte. Depending on their charge storage mechanisms, supercapacitors can be classified into two types: (i) electrochemical double layer capacitors (EDLC) and (ii) redox supercapacitors. Type (i) mainly involves in the use of porous carbon as electrodes and type (ii) involves in the use of metal oxides and conducting polymers [11].

The charge storage for EDLC is governed by charge separation, which is similar to traditional capacitors. As shown in Fig. 3-2, when the carbon electrode is charged, counterions from the solution diffuse to the surface of the electrode to neutralize these

charges. Counterions are stored through electrostatic force at the interface of the electrode and the solution, hence the term “double layer.” Because the distance of charge separation is very small (\AA scale comparing to μm scale of traditional capacitors), more charges can be stored at the interface and results in higher specific energy. The storage and the release of energy is inherently rapid with the fast ionic movement between the interface and the bulk solution. Increasing the surface area per volume of the carbon electrode allows greater counterion accumulation. This is often achieved by using different forms of carbon, such as porous activated carbon, graphite carbon powder, carbon nanofibres, and carbon nanotubes [11, 65, 66].

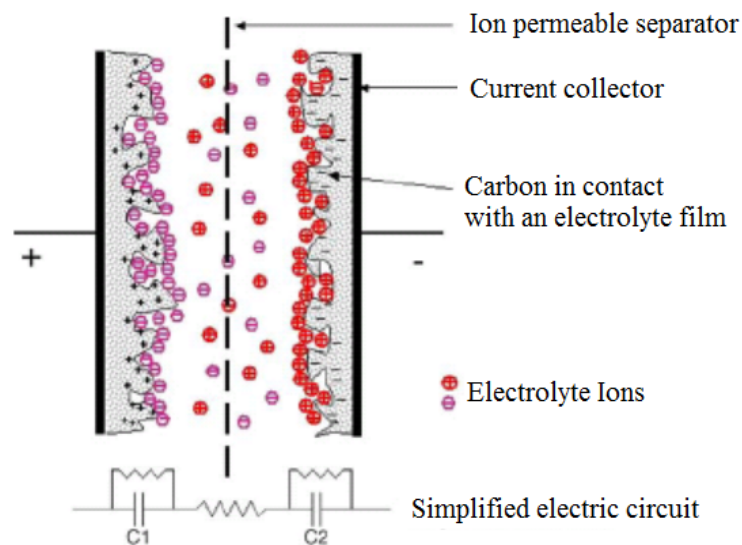


Fig. 3-2 Schematic representation of EDLC and the charge accumulation at the electrode/electrolyte interface upon charging the electrode [11]. Reproduced with permission from Elsevier Science Ltd.

In contrast, the charge storage mechanism for type (ii) redox supercapacitors mainly depends on the reversible Faradaic current flow. The electrode is either reduced or oxidized upon charging. Faradaic reaction occurs with the transfer of charges across the

interface to neutralize charges on the electrode film. For the case of metal oxide, such as RuO_2 , cathodic polarization will cause the intercalation of positive ions; depolarization will cause the deintercalation of positive ions. For the case of conducting polymers, the films are p-doped when charged positively and n-doped when charged negatively. Electrolyte counterions will diffuse into the film to neutralize the charge imbalance. The capacitance developed is called “pseudocapacitance.” When the film is discharged, or “de-doped,” ions diffuse out of the electrode film [11, 67].

As shown in Fig. 3-2, each electrode-electrolyte interface can be thought as one capacitor. A supercapacitor cell is therefore consisted of two pairs of capacitor plates connected in series. The cell capacitance (C_{cell}) can be expressed as

$$\frac{1}{C_{\text{cell}}} = \frac{1}{C_1} + \frac{1}{C_2} \quad (1)$$

where C_1 and C_2 represent the capacitance of the two electrodes. For the case of EDLC, C_1 and C_2 can be calculated from the double layer capacitance (C_{dl}), which is proportional to the surface area (A) of the electrode, the electrolyte permittivity (ϵ), and inversely proportional to the charge separation distance (d).

$$C_{\text{dl}} = \frac{\epsilon A}{d} \quad (2)$$

For the case of redox supercapacitor, the average capacitance (C_{av}) is related to the total charge transferred (Q_{tot}) and the operating voltage (V).

$$C_{\text{av}} = \frac{Q_{\text{tot}}}{V} \quad (3)$$

The energy (E) and power (P) of supercapacitors are calculated as follows:

$$E = \frac{1}{2} CV^2 \quad (4)$$

$$P = \frac{V^2}{4R_s} \quad (5)$$

where C is the capacitance in Farads, and R_s is the equivalent series resistance (ESR) in ohms [10, 11, 65], assuming that capacitance is independent of voltage in Eq.(4).

3.1.2 Electrolyte Solution

The optimum operating voltage of supercapacitors is mostly determined by the breakdown voltage of the electrolyte solution. Common electrolytes used include aqueous electrolyte, organic electrolyte, and ionic liquid. The advantage of using aqueous electrolyte is its high conductivity, low cost, and less stringent purification process [59]. Common acid and basic electrolytes used include H_2SO_4 and KOH. Because of their high dielectric constant and high conductivity (up to ~ 1 S/cm), a very high specific capacitance (F/g) can be obtained comparing to other non-aqueous solutions [11]. The small sized ions also allow fast diffusion through electrode materials. However, the breakdown voltage is ~ 1 V, which significantly restricts the amount of energy storage according to Eq.(4). A much higher capacitance is often required in order to achieve a certain amount of energy density. In contrast, the maximum operating voltage for organic electrolyte can reach ca. 2.5V. The energy stored using such system is at least five times larger than that using aqueous electrolyte [11]. However, the main drawback for organic electrolyte is its lower conductivity, namely higher resistivity. The resistivity of aqueous electrolyte is 1 – 2 Ω cm, while that of organic electrolyte is 20 – 60

Ωcm (propylene carbonate or acetonitrile based electrolyte) [10]. The high resistivity significantly reduces the power generation according to Eq.(5). An electrode with larger pore size (15 – 20 Å comparing to pore size of 5 – 10 Å required for aqueous electrolyte) is often required for the larger organic electrolyte to penetrate through. The lower dielectric constant of organic electrolyte also reduces capacitance per volume storage [65, 68]. Common organic electrolyte used include acetonitrile or propylene carbonate containing tetraethylammonium tetrafluoroborate or other salts. Ionic liquid, which is also known as the room temperature molten salt, was developed to possess higher thermal stability and negligible vapour pressure. Although the operating voltage can be extended to 4 – 6 V, the high viscosity, poor wetting ability, and low conductivity (1.5 mS/cm at 25°C) prevents the wide-spread application of ionic liquid. Fig. 3-3 is a plot summary of the specific energy with respect to the operating voltage using different types of electrolytes [69].

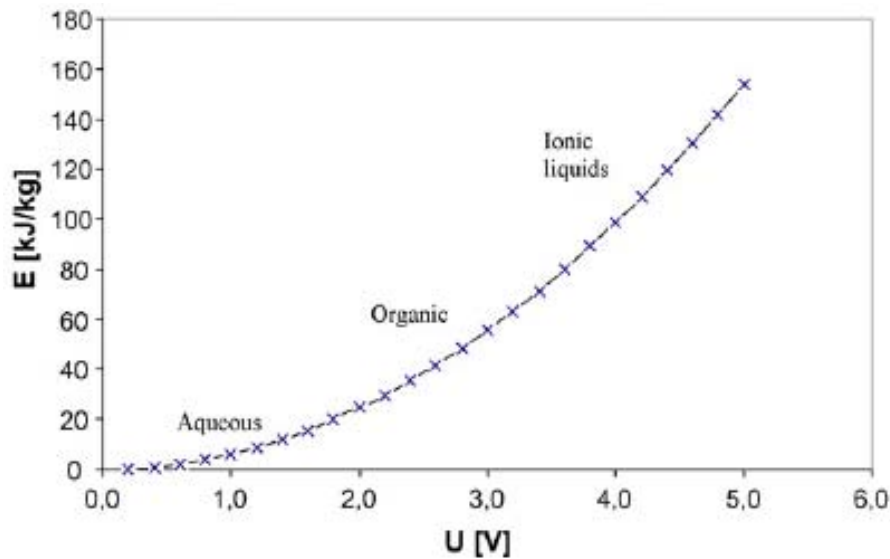


Fig. 3-3 Plot of specific energy vs. operating voltage by using aqueous, organic, and ionic liquid electrolytes [69]. Reproduced with permission from Elsevier Science Ltd.

3.1.3 Electrode Materials

Today, most of the commercially available supercapacitor electrodes are made of activated carbons due to their reasonable performance and low price. The capacitance per carbon electrode is 75 – 175 F/g with aqueous electrolyte but drops to 40 – 100 F/g with organic electrolyte. This is due to the reduced diffusion capability of large-sized organic electrolyte ions through mesopores of carbon. Although carbon can be made with surface area as high as 1000 m²/g, most of the surface pores are not effectively used due to the presence of small size, closed, or isolated pores [10, 11, 70]. The performance of commercial supercapacitor electrodes based on carbon black or activated carbon has been optimized already. Other carbon forms (aerogel carbon, glassy carbon, or templated carbon from silica) often suffer from high cost, complicated preparation method, or limited capacitance performance [65]. Alternative materials have been sought for enhanced energy and power capacity.

Metal oxides, including RuO₂ and IrO₂, have demonstrated an enhanced capacitance and the highest recorded for RuO₂ is 750 F/g. A 95% discharging efficiency can provide a specific power over 1 kW/kg. They also possess low resistance and high surface area. However, both RuO₂ and IrO₂ are very expensive. They are mostly used in military or aerospace applications [59, 71]. Other metal oxide such as magnesium oxide or nickel oxide is investigated for substitution, but their performance is not as satisfactory [72].

Electrically conductive polymers (ECP) possess both plastic properties and metallic conductivities. The ECP capacitance ranges from few hundreds to over a thousand F/g depending on the type of electrolyte used. Upon doping, charges are stored within the

volume of the polymer electrode, which results in higher capacitance than carbon electrode. The compatibility of conducting polymers with organic electrolyte also permits higher energy storage. The slow transport of electrolyte ions into and out of the polymer film is a major limitation of high power generation. This is often adjusted by reducing the thickness or increasing the surface area of the film. One other issue is the long term stability of the electrode as a result of degradation upon cycling. However, due to the low cost, ease of synthesis, and high capacitance, conducting polymers still possess a high potential as a supercapacitor electrode [10, 11, 59, 73, 74]. The mostly investigated conducting polymers today include polyaniline (PANI), polypyrrole (PPy), and (derivatives of) polythiophene (PT). Among all, PPy is chosen for this study due to its good conductivity and high specific capacitance comparing to other conducting polymers [12], and our familiarity with this material.

3.1.4 Polypyrrole

As shown in Fig. 3-4, PPy is a conjugated polymer that possesses π bonds for electron delocalization and conduction. However, like most ECP, PPy is an insulator at reduced (undoped) state due to Peierls distortion. It has a filled valence band and an empty conduction band separated by an energy gap. In a supercapacitor device, doping PPy involves the removal of electrons (p-doped, oxidation) from the valence band to produce mobile charge carriers including polarons and bipolarons to increase the electrical conductivity. Bipolarons have been shown to play a major role in electron conduction through its positive charge carriers in ECP. Charges can be transported either along the polymer chain or via inter-chain hopping. The mobility and the number of charge carriers determine the electrical conductivity of PPy. PPy (and ECP in general) can be

doped at a fairly high level to reduce the energy bandgap and to increase the conductivity [75, 76].

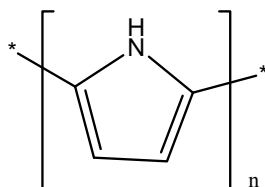


Fig. 3-4 Chemical Structure of PPy.

The conductivity of PPy is a function of its oxidation state, as shown in Fig. 3-5 [77]. When oxidized with a more positive potential, PPy becomes highly conductive (few hundred S/cm) and counterions are taken up to maintain the electroneutrality. PPy chains expand with the insertion of counterions. As the potential scans sufficiently negative, PPy becomes an insulator with the expulsion of counterions and the contraction of the polymer chain. The schematic is shown in Fig. 3-6 [78].

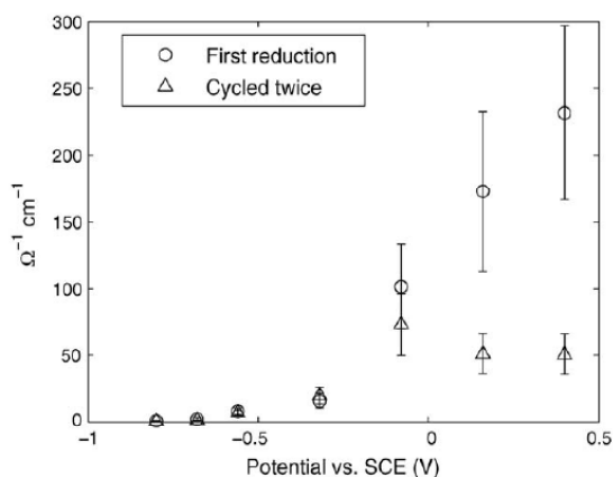


Fig. 3-5 The conductivity of the as-grown PPy film vs. potentials (circle) and the conductivity of the PPy film after cycled twice with a potentiostatic square wave (triangle) [77].

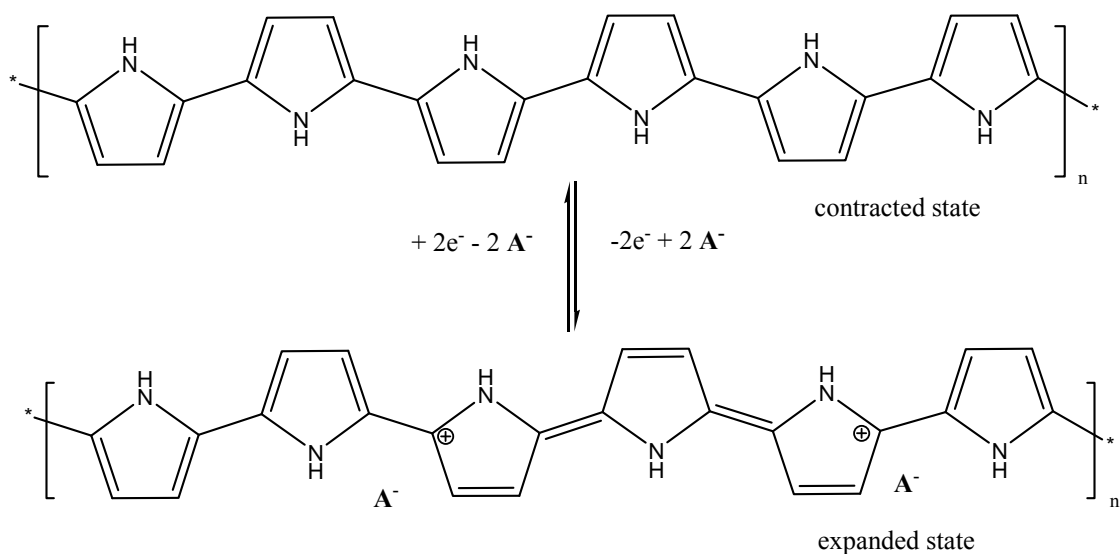


Fig. 3-6 Electrochemical redox reactions of PPy with the insertion and extraction of counterions. A^- is the counterion and e^- is the electron [78].

Various electrode morphologies, such as whisker-like, nanosphere, nanorod, nanotube, or porous surface, can be achieved by different synthetic methods. Electrochemical deposition is most often used for polymerization since it has a better control of the mass of the deposited material over chemical synthesis [80]. It has also been demonstrated in general that conducting polymers with rod-like structure possess higher capacitance than those with sphere-like or filmed structures. This is due to the large surface area and the less compact structure of nanorod for the easy access of electrolyte and the fast redox reaction. Wang *et al.* reported that the rod-like composite electrode of poly(3,4-ethylenedioxythiophene)(PEDOT)/PPy possess higher specific capacitance than the sphere-like composite electrode [81, 82]. PPy nanofibres synthesized by Van Dyke *et al.* also demonstrated an enhanced charge transport rate comparing to the film formation [83].

3.1.5 ECP/Carbon Composite Electrodes

The use of ECP as active electrode materials with carbon as a support or growth substrate has been intensively investigated today. During charge/discharge, ECP swells and shrinks due to the ion insertion and removal. The induced mechanical stress often enhances the degradation rate of the polymer film [12, 68]. Incorporation of relatively inert carbon can reduce the mechanical stress and degradation problem. The good conductivity of carbon can serve as a current collector without inducing significant IR drop; the high surface area and porosity of various carbon forms permit the greater ion transport rate of the electrolyte. Types of carbons including single walled carbon nanotubes, graphite, vapour grown carbon nanofibres, and carbon aerogels have been reported to composite with PPy. The specific capacitance ranges between 300 – 500 F/g in aqueous electrolyte with a scan rate of 10 – 200 mV/s [70, 84-86].

3.2 Experimental

In this section, a composite of electrospun nanofibrous CNF/PPy supercapacitor electrode was fabricated. The advantage of electrospinning is the generation of continuous nanofibres with high aspect ratio, which forms a continuous conductive network without the addition of binders. Since a thinner layer of conductive polymer can facilitate the ion diffusion throughout the polymer volume, it is proposed to deposit a thin layer of PPy on the surface of electrospun carbon nanofibre. Organic electrolyte was used to increase the specific energy of the electrode.

3.2.1 Polypyrrole Synthesis

A solution mixture of 0.060 M pyrrole, 0.05 M tetrabutyl ammonium hexafluorophosphate (TBAP), propylene carbonate (PC), and water (PC:water, 100:1 v:v) was prepared and purged with nitrogen for 10 min. CNF, the working electrode (WE), was placed in between two copper counter electrode (CE) sheets. PPy was then galvanostatically deposited onto the surface of CNF pyrolyzed from PANAM (0.9 wt% AM) by applying a current density of 0.125 mA/cm^2 for 4 and 8 hours. The dimension of CNF used for 4 and 8 hour deposition were $1.30 \pm 0.05 \text{ cm} \times 1.30 \pm 0.05 \text{ cm} \times 33 \pm 2 \text{ }\mu\text{m}$ and $1.30 \pm 0.05 \text{ cm} \times 1.50 \pm 0.05 \text{ cm} \times 44 \pm 2 \text{ }\mu\text{m}$, respectively. The deposition was carried out in an ethylene glycol bath set to -30°C . The current was applied using an AMEL Model 7050 potentiationstat[87]. Pure PPy film was also synthesized to compare the effect of different PPy morphology on the ion transport. Pure PPy film was deposited onto one surface of SIGRADUR® glassy carbon (GC) disk with $2.50 \pm 0.05 \text{ cm}$ diameter using one copper sheet as the CE with the same experimental parameters described above. The SIGRADUR® GC was purchased from HTW Germany. The synthesized PPy samples were washed with PC to remove impurities and residual pyrrole monomers before used for characterization. CNF/PPy with 4 and 8 hours of PPy deposition is denoted as CNF/PPy-4 and CNF/PPy-8, respectively. GC/PPy with 4 and 8 hours of PPy deposition is denoted as GC/PPy-4 and GC/PPy-8, respectively.

3.2.2 Characterization

A Hitachi S-3000 Scanning Electron Microscopy (SEM) was used to characterize the surface morphology and average fibre diameters of the CNF/PPy composite. The

working distance was set at ca. 6 mm with an accelerating voltage of 20 kV. SEM images were taken at $\times 600$ and $\times 5k$ magnifications. The electrochemical properties of the CNF/PPy and GC/PPy composite were characterized by cyclic voltammetry (CV) and galvanostatic charge/discharge using an AMEL Model 7050 potentiostat. Testing was performed in a three-electrode cell setup with CNF/PPy or GC/PPy as a WE, carbon as a CE, and 0.1 M TBAP in PC as the electrolyte solution. A non-aqueous Ag/AgNO₃ electrode (from Bioanalytical Systems) was used as a reference electrode (RE) and was placed approximately 9.0 ± 2.5 mm away (from the center of the RE) from the WE. Samples were cycled twice with CV at 1, 5, 10, and 20 mV/s rates from -0.8 to 0.6 V (vs. Ag/AgNO₃). Samples were also cycled twice with galvanostatic charge/discharge tests by applying ± 0.3 , 0.45, 0.6, 0.9, 2, and 3 mA currents from -0.8 to 0.6 V (vs. Ag/AgNO₃). PPy samples were air dried after testing. The thickness and the weight of PPy deposited were measured.

3.3 Results and Discussions

3.3.1 CNF/PPy Characterization

Fig. 3-7 shows the SEM images of the CNF/PPy composite film. The average fibre diameters for 4 and 8 hours of depositions are $5.4 \pm 0.6 \times 10^2$ nm and $6.0 \pm 0.9 \times 10^2$ nm, which are $1.5 \pm 0.8 \times 10^2$ nm and $2 \pm 1 \times 10^2$ nm larger than that of the pristine CNF, respectively. The image also shows that PPy was evenly deposited onto CNF.

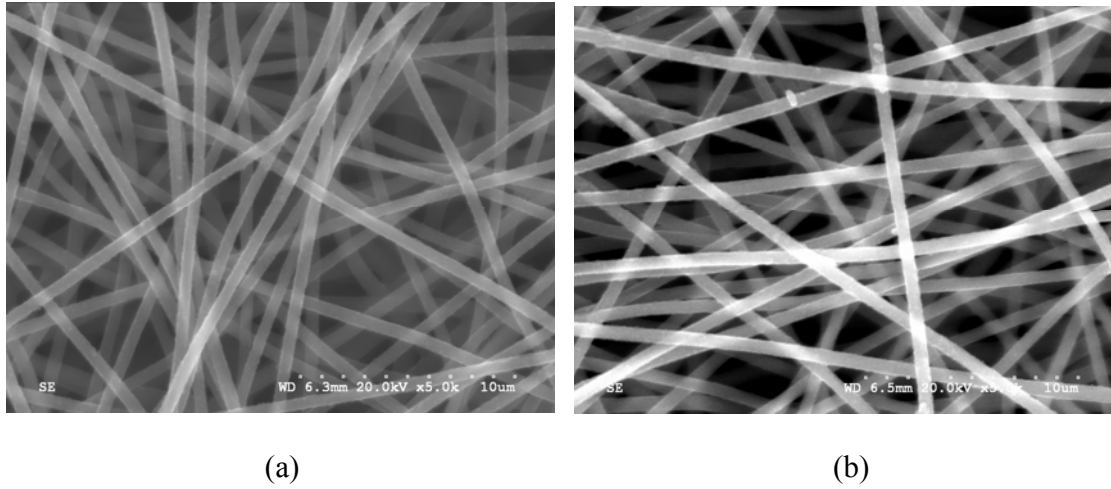


Fig. 3-7 SEM images of CNF/PPy-4 (a) and CNF/PPy-8 (b).

The total amount of PPy deposited onto CNF after 4 and 8 hours are 4.5 ± 0.6 and 7.6 ± 0.8 mg, respectively. The thickness of the CNF before 4 and 8 hours of depositions were 33 ± 2 and 44 ± 2 μm , respectively. The thickness of CNF/PPy-4 and CNF/PPy-8 became 58 ± 1 and 80 ± 10 μm , respectively. Fig. 3-8(a) and (b) are the CV curves of pure CNF and its comparison with that of CNF/PPy-4 cycled at 1 mV/s, respectively. With the addition of PPy, the specific capacitance increased dramatically. The specific capacitance of pure CNF approximated from Fig. 3-8(a) is calculated as follows:

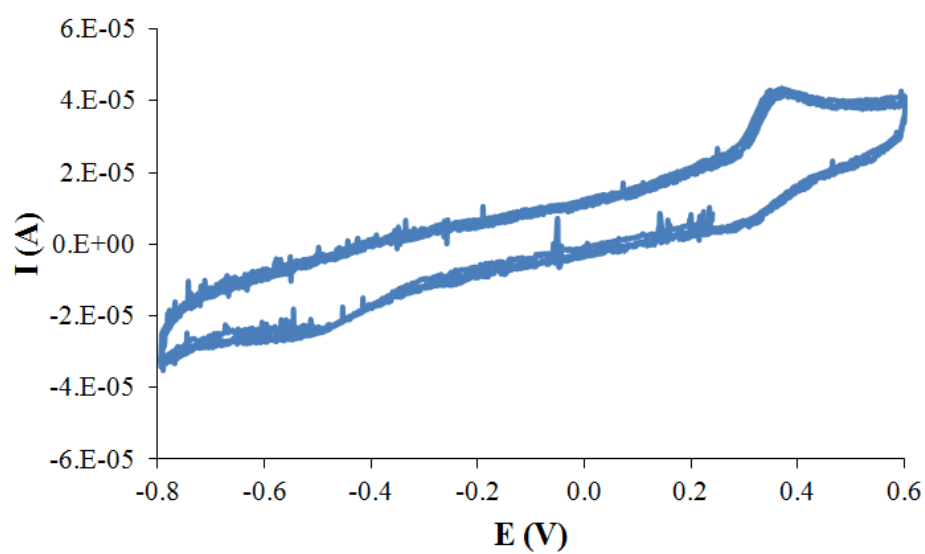
$$\text{Specific Capacitance} = (1 \times 10^{-5} \text{ A}) * (s/1 \times 10^{-3} \text{ V}) / (2.1 \pm 0.2 \times 10^{-3} \text{ g}) = 4.8 \pm 0.5 \text{ F/g}$$

The specific capacitance of CNF/PPy-4 approximated from Fig. 3-8(b) is calculated as follows:

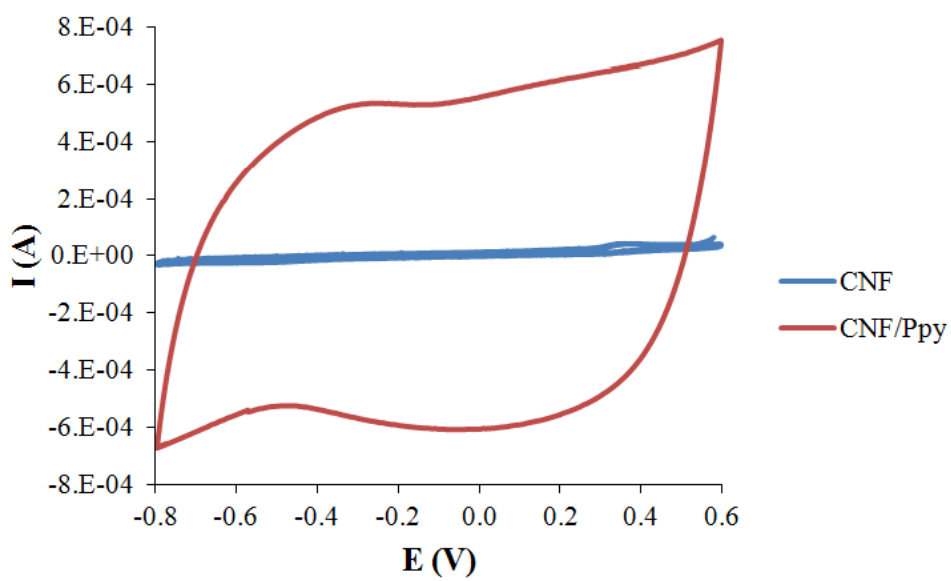
$$\text{Specific Capacitance} = (6 \times 10^{-4} \text{ A}) * (s/1 \times 10^{-3} \text{ V}) / (4.5 \pm 0.6 \times 10^{-3} \text{ g}) = 1.6 \pm 0.2 \times 10^2 \text{ F/g}$$

The errors were estimated using error propagation method assuming 5 % uncertainty for the capacitance and 10 % uncertainty for the electrode mass (residual salt and solvent). The small capacitance of pure CNF is a result of low surface area. In order to use CNF

alone as a supercapacitor electrode, activation process is necessary to generate surface pores for higher energy storage. It was reported that PAN samples activated between 700 and 800°C possess a surface area of 850 – 1230 m²/g. At a discharge current density of 10 mA/g, the electrodes possess highest specific capacitances of 150 – 180 F/g with aqueous electrolyte [88].



(a)

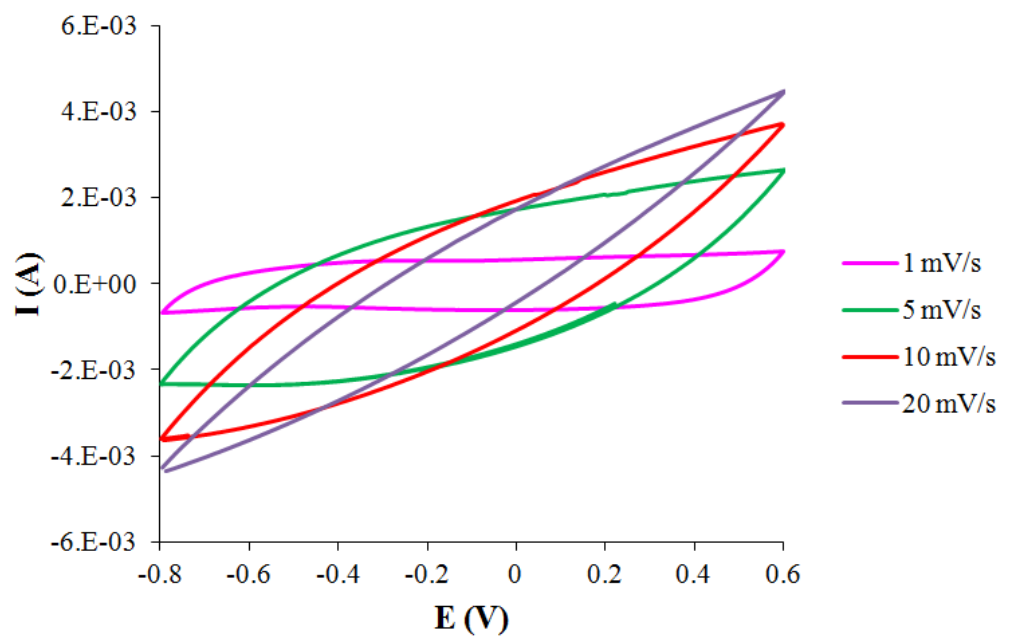


(b)

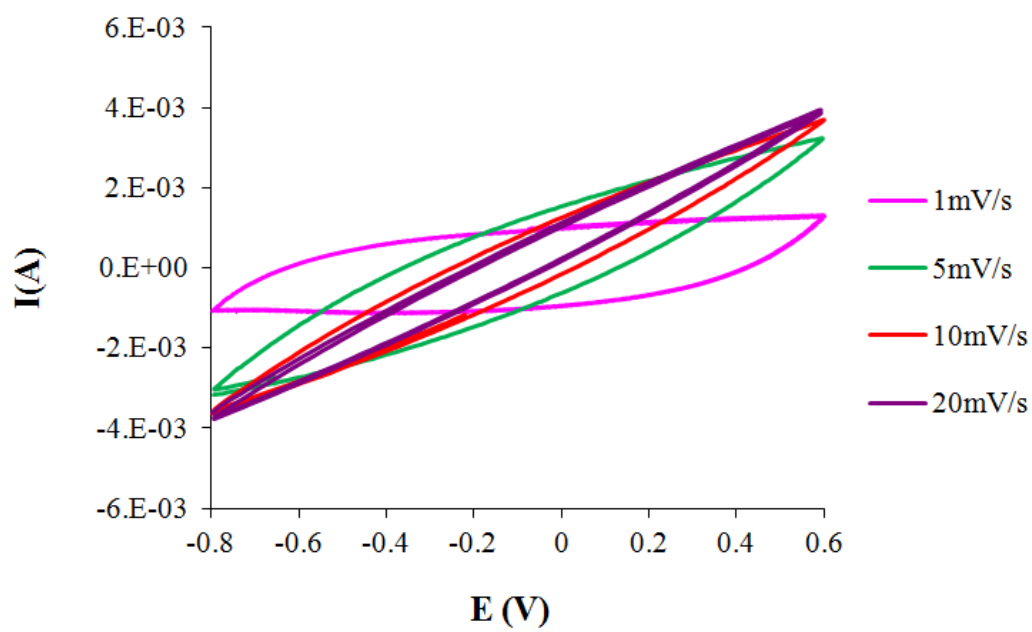
Fig. 3-8 CV curves of pure CNF (a) vs. CNF/PPy-4 (b) at 1mV/s cycle rate.

The goal for using CNF/PPy electrode is to improve the rate of ion insertion/removal with the support of conductive CNF and to enhance the specific capacitance of the electrode with PPy. It is believed that the conductive CNF could facilitate the charge transfer of PPy at its less conductive state and act as a robust backbone to absorb the mechanical stress generated from constant swelling/shrinkage of PPy upon charging/discharging. The high porosity of CNF films allows easier access of the electrolyte to interact with PPy nanofibres. The light weight characteristic of CNF further reduces its impact on the specific capacitance (normalized by weight). PPy, on the other hand, is used to enhance the amount of energy storage with its advantage of high capacitance, better compatibility with organic solvent, low cost, and simple fabrication. The deposition of PPy film on a glassy carbon disk was used to compare the charging speed of PPy at different morphology.

Fig. 3-9 is the CV analysis of CNF/PPy-4 and CNF/PPy-8 composite electrodes. The electrodes were cycled at 1, 5, 10, and 20 mV/s. Both electrodes maintained more capacitive behavior at lower scan rates, represented by more rectangular shaped curves. When the scan rate increased, the CV curves became sloped, indicating the resistive nature of the electrochemical environment, which reduced the rate at which current reaches its maximum value. The series resistance affecting the charge/discharge at higher rates can be estimated from the inverse slope of the IV curve. The slope of 20 mV/s curve, with the most resistive response, is calculated using the voltage range of 1.4 V (-0.8 – 0.6 V) with the corresponding current at -0.8 and 0.6 V. The estimated resistances for CNF/PPy-4 and CNF/PPy-8 are 160 and 180 Ω , respectively.



(a)



(b)

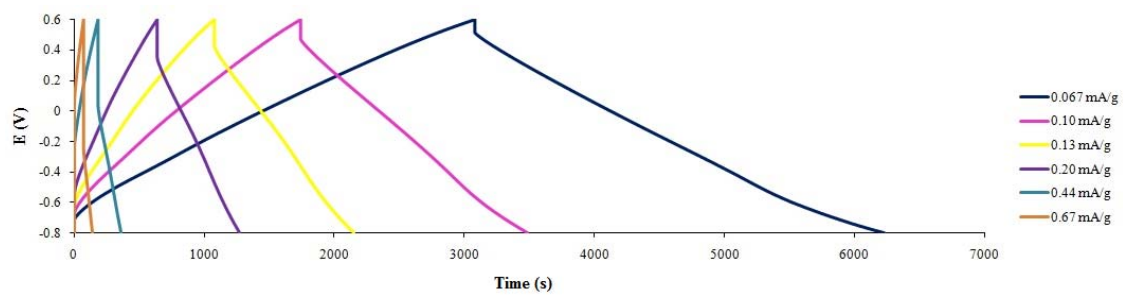
Fig. 3-9 CV of CNF/PPy capacitance at 4 (a) and 8 (b) hours of PPy deposition.

The galvanostatic cycling results for CNF/PPy-4 and CNF/PPy-8 are shown in Fig. 3-10(a) and Fig. 3-11(a). The specific capacitance of CNF/PPy electrodes are calculated from these graphs, as shown below:

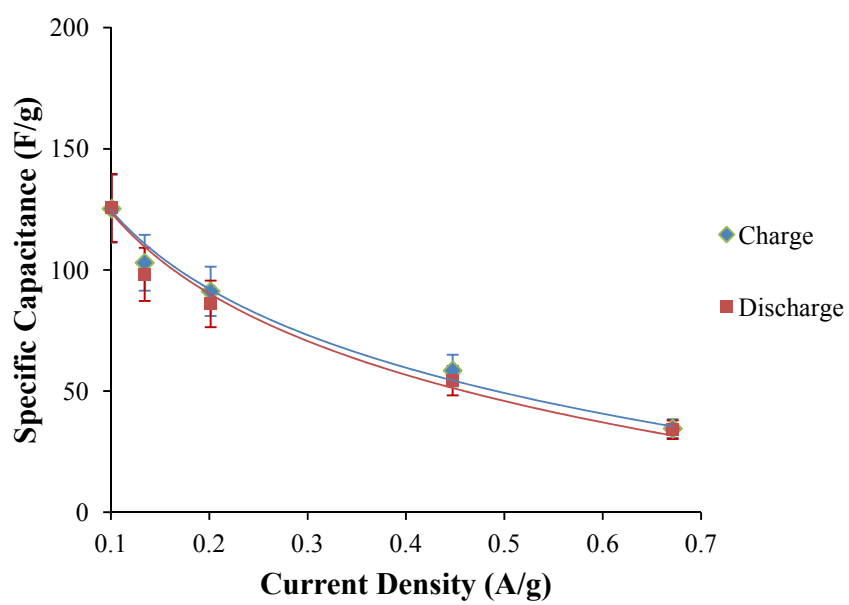
$$\text{Specific Capacitance (F/g)} = dQ / dE / m = I \times dt / dE / m,$$

where I is the current applied (A), dt/dE is the total change in time with respect to the change in voltage range (1.4 V), and m is the mass of PPy (g). Charge/discharge capacitances and Coulombic efficiencies of both electrodes at different current densities are summarized in Fig. 3-10(b), (c) and Fig. 3-11(b), (c). These capacitances are high compared to previous studies that incorporated PPy with single-walled carbon nanotubes, for which a capacitance of 130 – 200 F/g was achieved in aqueous electrolytes [84, 89]. The capacitance at slow cycle rates are also comparable to those of commercially available carbon electrodes.

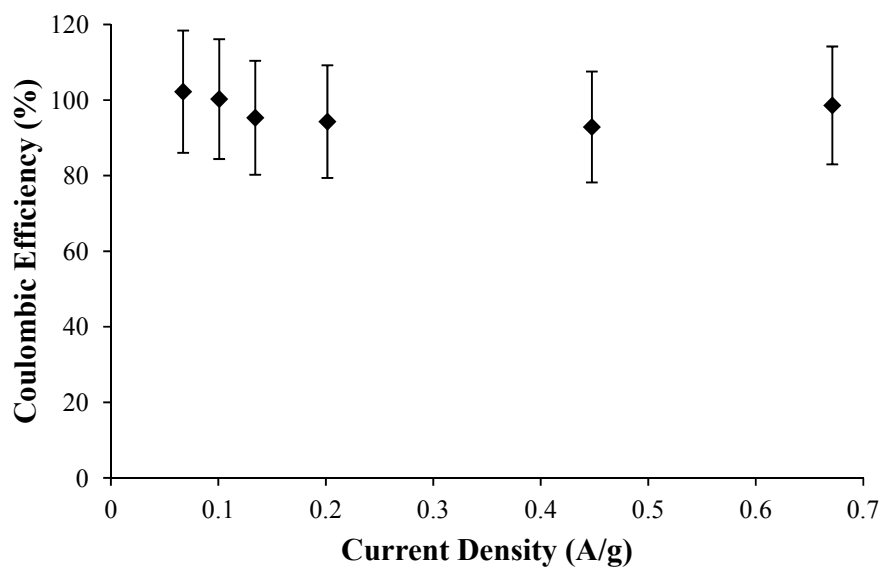
For both electrodes, as the current densities increased, the voltage drop increased, which is an indication of the uncompensated resistance, as shown in Fig. 3-10(a) and Fig. 3-11(a). This results in lower capacitance at higher cycling rates. Over 50% of the capacity was lost as the current density increased 10 times higher. The Coulombic efficiency of CNF/PPy-8 decreased from ca. 100% to 80%, indicating the inability of the electrodes to extract all the charges at higher cycling rates.



(a)

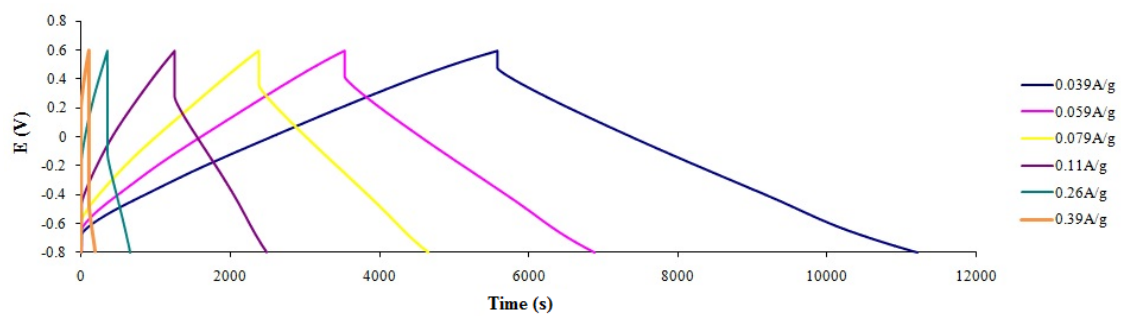


(b)

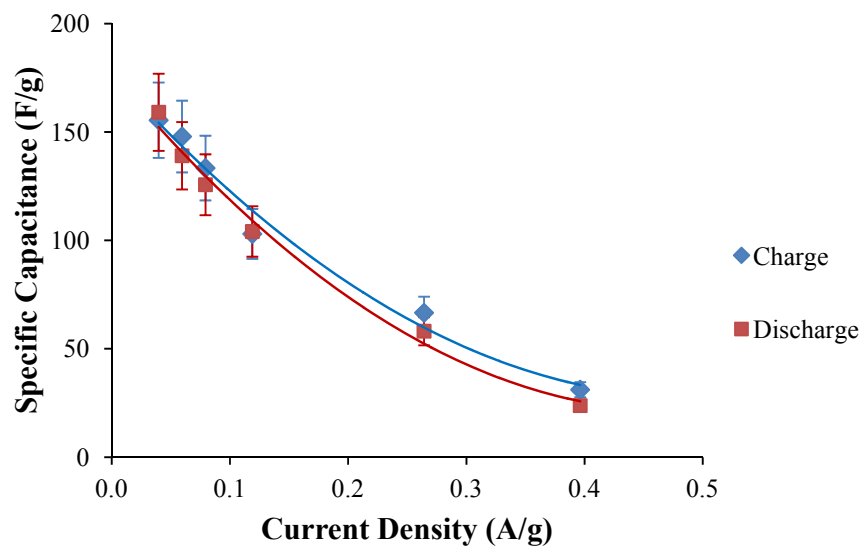


(c)

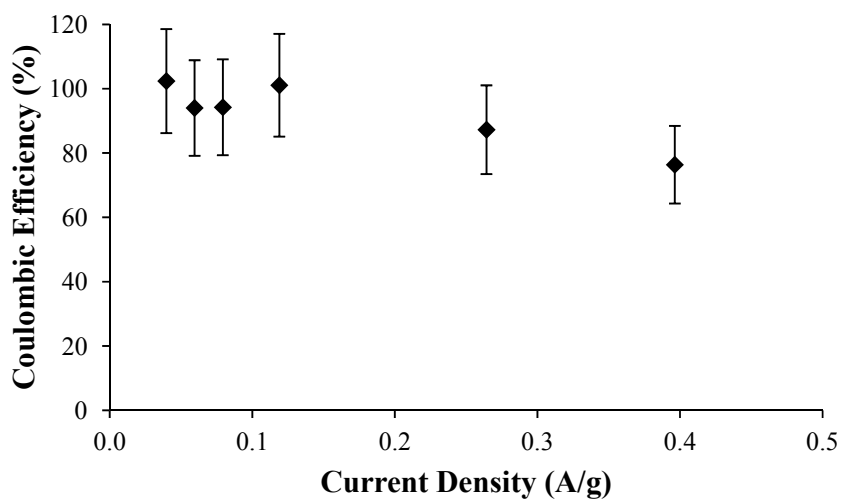
Fig. 3-10 Galvanostatic cycling of CNF/PPy-4 (a), its charge/discharge capacitance (b), and Coulombic efficiency (c) at different current densities.



(a)



(b)

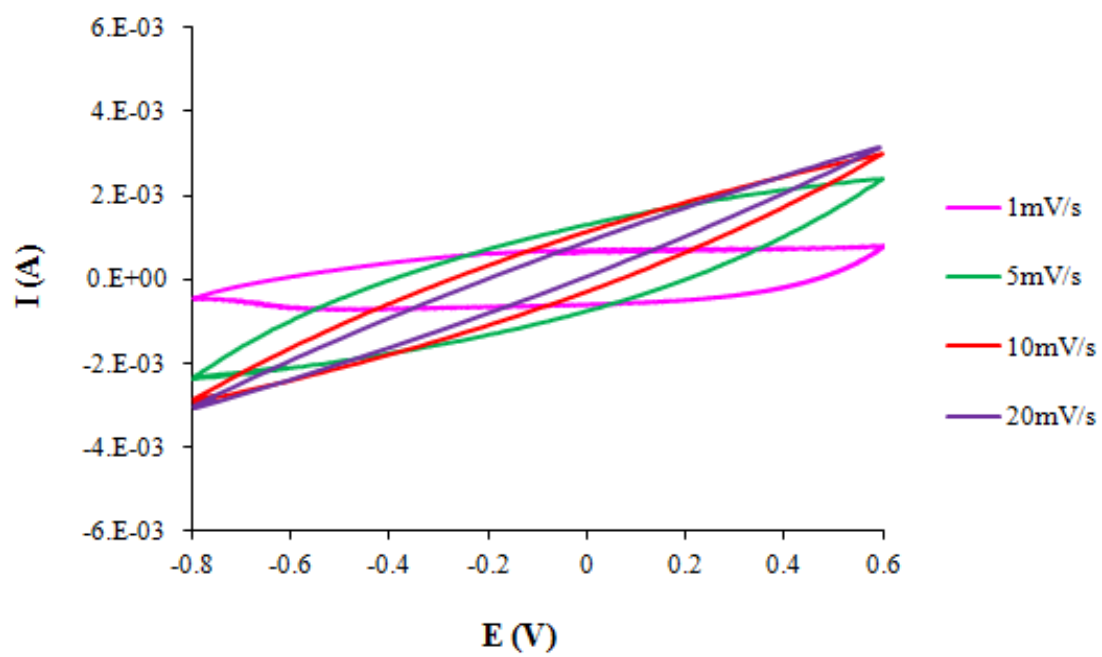


(c)

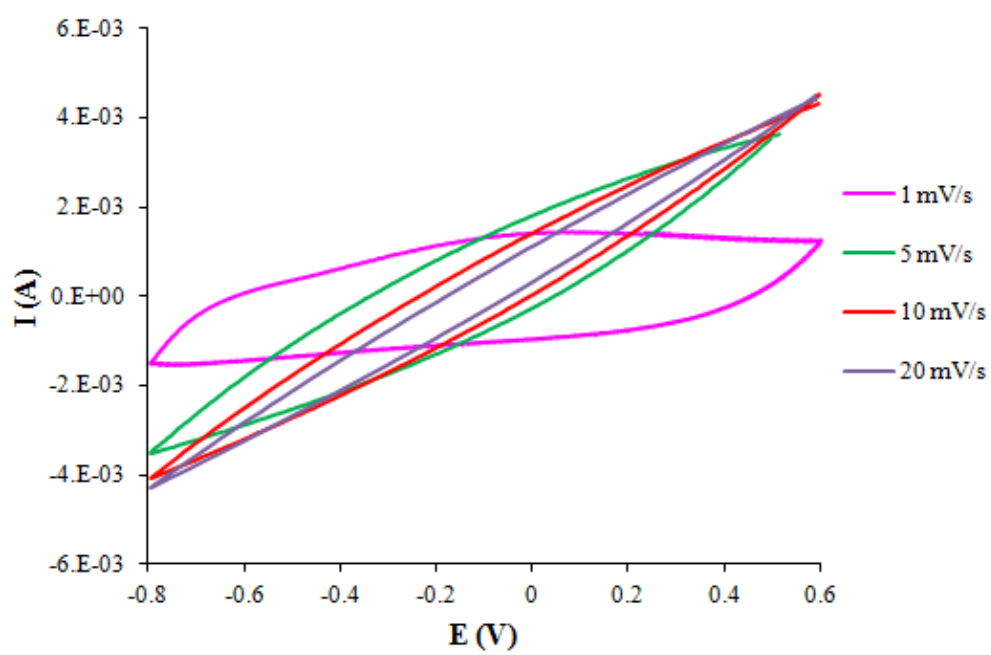
Fig. 3-11 Galvanostatic cycling of CNF/PPy-8 (a), its charge/discharge capacitance (b), and Coulombic efficiency (c) at different current densities.

3.3.2 GC/PPy Characterization

The total amount of PPy deposited onto GC after 4 and 8 hours are 4.4 ± 0.4 and 7.1 ± 0.7 mg, with 17 ± 3 and 45 ± 3 μm thickness, respectively. Fig. 3-12(a) and (b) are the CV analyses of the electrodes with 4 and 8 hours of PPy deposition, respectively. The resistive nature of the PPy also prevents quick charging and discharging of the film at higher cycling rates, which resulted in less-squared curves and reduced capacitance. The series resistance are also estimated from 20 mV/s cycle rate. The resistance for GC/PPy-4 and GC/PPy-8 are ca. 230 and 160 Ω , respectively.



(a)



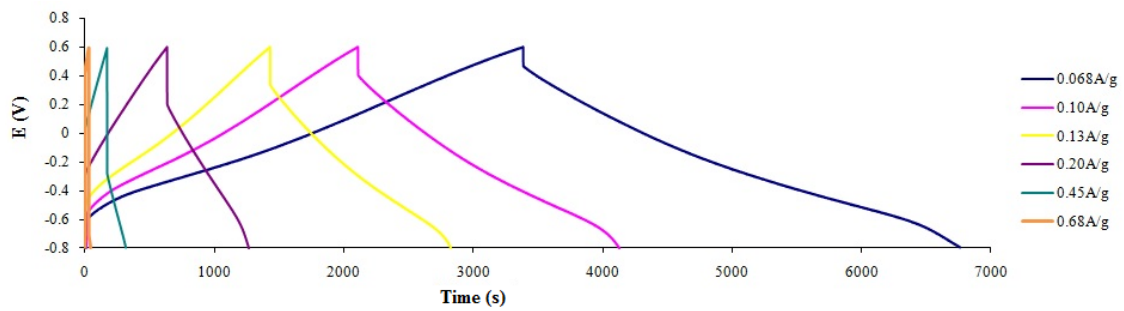
(b)

Fig. 3-12 CV of GC/PPy-4 (a) and GC/PPy-8 (b).

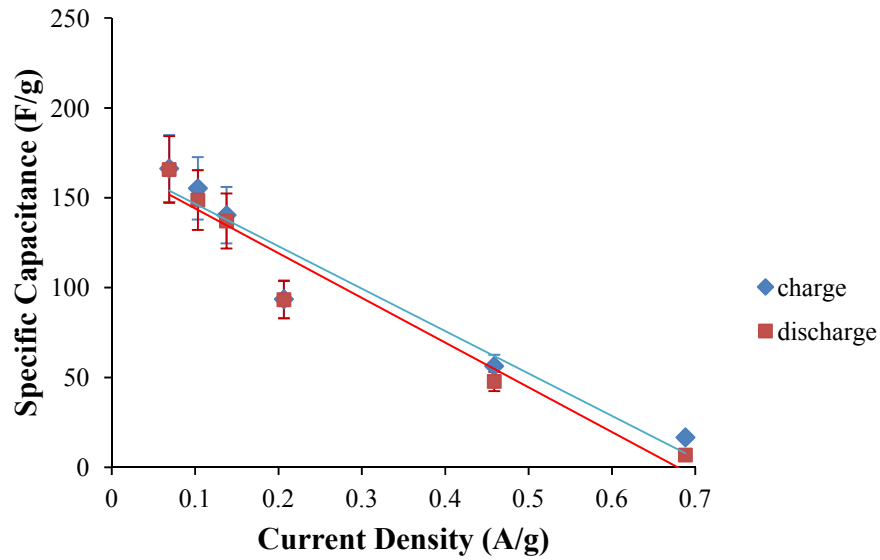
The galvanostatic cycling results of GC/PPy-4 and GC/PPy-8 are shown in Fig. 3-13(a) and Fig. 3-14 (a), respectively. The charge/discharge capacitances and the Coulombic efficiencies of both electrodes at different current densities are summarized in Fig. 3-13(b), (c) and Fig. 3-14(b), (c). In Fig. 3-13(a) and Fig. 3-14(a), both electrodes show an enhanced voltage drop also caused by uncompensated resistance at higher current densities. In contrast to CNF/PPy samples where voltage drop only occurred at the beginning of each charge/discharge curve, GC/PPy shows an additional voltage drop at the end of each discharge curve. The inflection point where PPy switches from a conductive to a non-conductive state is -0.1 V vs. SCE (corresponds to ca. -0.3 V vs. Ag/AgNO₃), as shown in Fig. 3-5 [77]. Below -0.3 V vs. Ag/AgNO₃, little change in conductivity occurs. As observed in Fig. 3-13(a) and Fig. 3-14(a), the additional voltage drop occurs at -0.6 – -0.8 V, which is away from the inflection voltage. In addition, the voltage drop of GC/PPy-8 was more significant than that of GC/PPy-4. This might mainly be a result of an increased diffusion time constant as the PPy film grows thicker. As reported by C. H. Tso *et al*, the time constant is $\tau_{RC} = R_{total}C_{total} = a^2C_v/\sigma$, where a is the thickness of the film, C_v is the volumetric capacitance, and σ is the ionic conductivity within the film [90]. The thickness of the PPy film, a , becomes the limiting factor as the film grows thicker. The ionic conductivity, σ , reduces as PPy film becomes more reduced [91] or grows thicker[92]. Both a and σ likely increase R_{total} and contribute to the additional voltage drop of GC/PPy. The effect become more significant in GC/PPy-8 with its greater film thickness.

Over 50% of the capacity was lost as the current density increased 10 times higher. The Coulombic efficiencies of GC/PPy-4 and GC/PPy-8 decreased from ca. 100% to 41% and

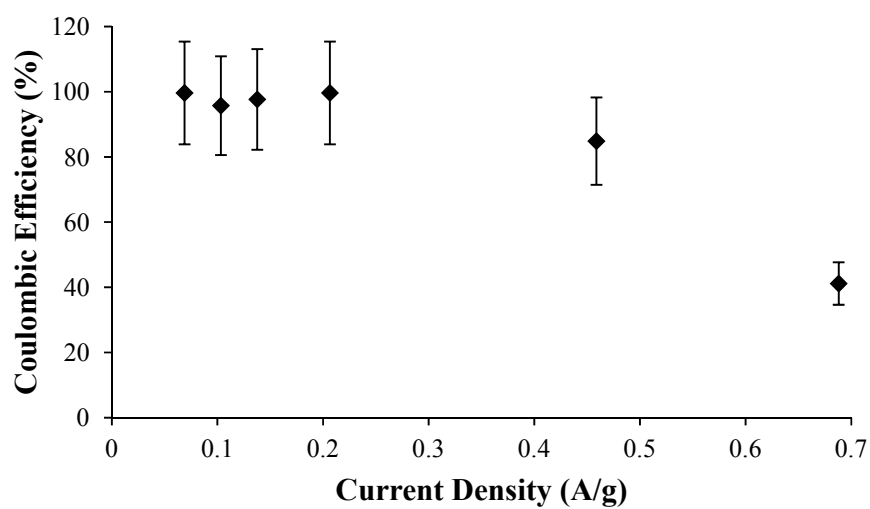
80%, respectively, indicating the inability of the electrodes to extract all the charges at higher cycling rates. At a current density of ca. 0.7 A/g, the Coulombic efficiency of GC/PPy-4 decreased drastically to 40 %. In contrast, CNF/PPy-4 maintained the efficiency over 90 %. This enhanced efficiency is likely a result of porous nanofibre structure, which increases the ion diffusion rate to the fibrous matrix. This effect will be further discussed in section 3.3.3.



(a)

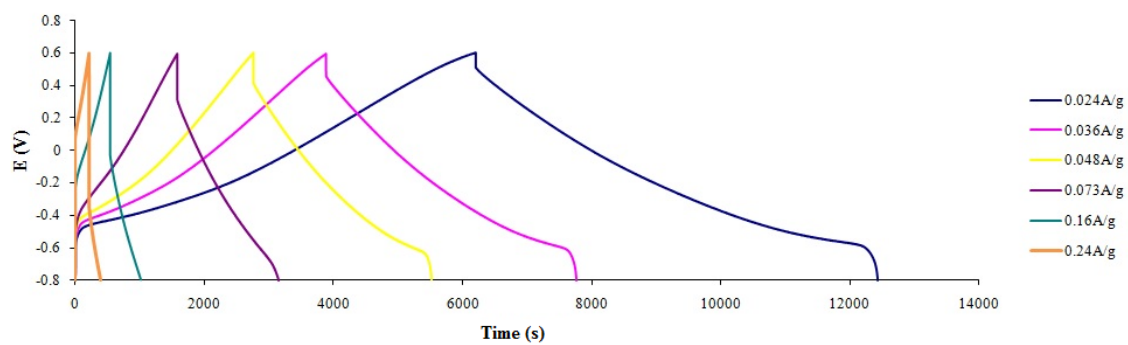


(b)

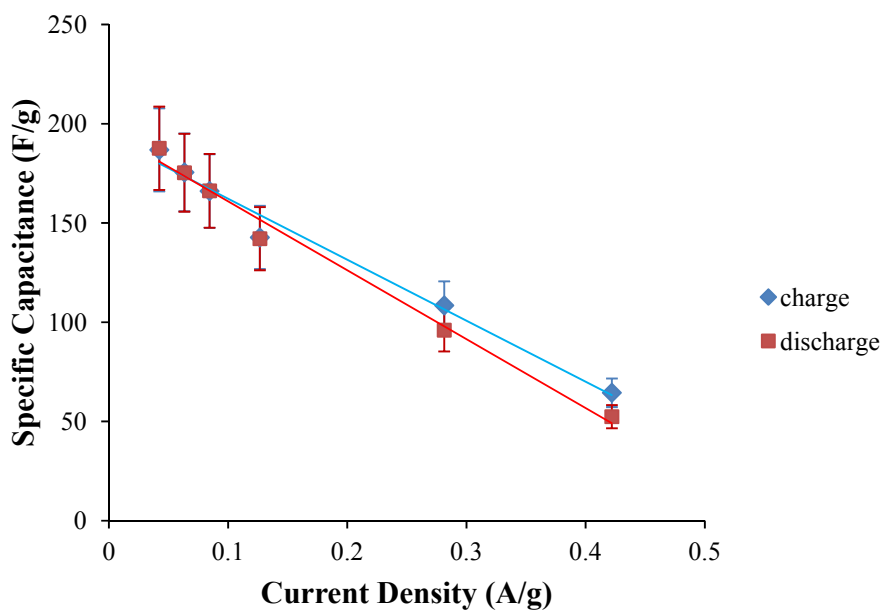


(c)

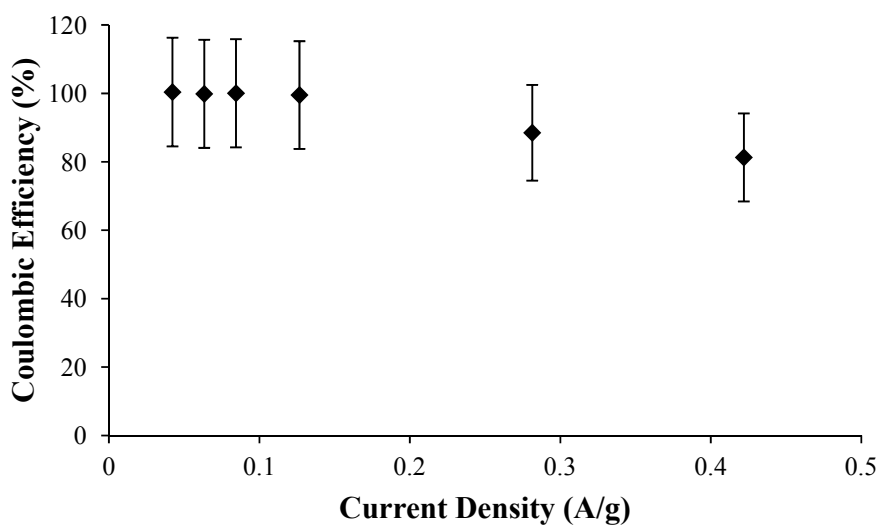
Fig. 3-13 Galvanostatic cycling of GC/PPy-4 (a), its charge/discharge capacitance (b), and Coulombic efficiency (c) at different current densities.



(a)



(b)



(c)

Fig. 3-14 Galvanostatic cycling of GC/PPy-8 (a), its charge/discharge capacitance (b), and Coulombic efficiency (c) at different current densities

3.3.3 Resistance Analysis

The slow charge and discharge rate of PPy samples were contributed from various resistances in the electrochemical system. The total resistance (R_{total}) of the system is expected to result from electronic resistance (R_{elec}), ionic resistance (R_{ionic}), and solution resistance (R_{sol}), as shown in the equivalent circuit model of PPy in Fig. 3-15. When PF_6^- ions diffuse from solution to the solution/electrode interface, a time delay occurs with R_{sol} . The time delay τ can be calculated from $\tau = R_{\text{sol}}C$, where C is the PPy capacitance. As ions diffuse into the volume of PPy, another time delay occurs, which is proportional to the PPy thickness. In a pure PPy film, R_{elec} is assumed negligible due to the high conductivity of PPy upon doping. The time delay is therefore determined from $\tau = a^2 / D_{\text{eff}}$, where a is the film thickness and D_{eff} is the effective diffusion coefficient. D_{eff} can be used to determine the ionic conductivity (σ_{ionic}) of PPy by $D_{\text{eff}} = \sigma_{\text{ionic}} / C_v$, where C_v is the volumetric capacitance of PPy [91]. The time delay for the ion diffusion into PPy is determined differently for the porous system. For the CNF/PPy composite, the highest R_{elec} was assumed from the resistance of the pure CNF film. R_{ionic} is determined from $R_{\text{ionic}} = L / \sigma_{\text{electrolyte}} \cdot A$, where $\sigma_{\text{electrolyte}}$ is the electrolyte conductivity, A is the area of CNF/PPy film, and L is the thickness of the CNF/PPy film.

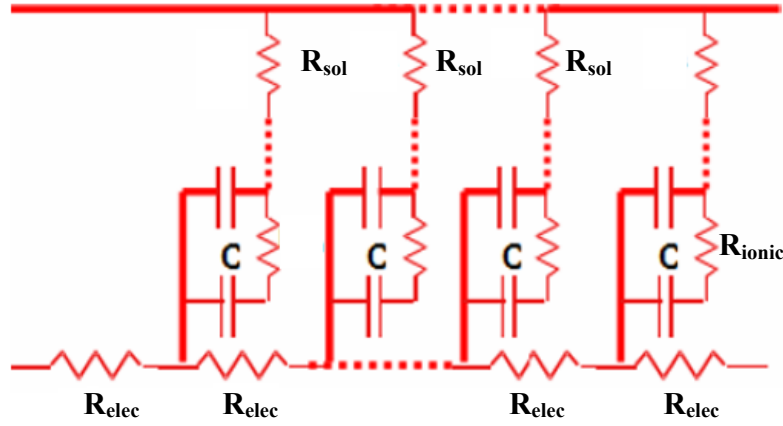


Fig. 3-15 Equivalent circuit model of ion diffusion into the PPy electrode, adapted from [93].

R_{elec} of CNF was used to estimate the R_{elec} of CNF/PPy electrode. The R_{elec} of the film was back calculated from the electronic conductivity of CNF (σ_{CNF}). Taken a CNF film with dimensions of $1.30 \pm 0.05 \text{ cm} \times 1.30 \pm 0.05 \text{ cm} \times 33 \pm 2 \text{ }\mu\text{m}$,

$$R_{elec} = L / \sigma_{CNF}A = (1.30 \text{ cm}) / (22 \pm 2 \text{ S/cm} \times 1.30 \text{ cm} \times 33 \text{ }\mu\text{m}) = \mathbf{14 \pm 2 \text{ }\Omega}$$

(L here is the length of the film and A is the area of width \times thickness)

The R_{ionic} of the CNF/PPy was estimated from its dimension ($1.30 \text{ cm} \times 1.30 \text{ cm} \times 33 \text{ }\mu\text{m}$) and $\sigma_{electrolyte}$,

$$R_{ionic} = L / \sigma_{electrolyte}A = (33 \text{ }\mu\text{m}) / (0.00184 \text{ S/cm} \times 1.30^2 \text{ cm}^2 \times 0.47 \pm 0.05) = \mathbf{2.3 \pm 0.3 \text{ }\Omega}$$

where 0.47 is the volume fraction of CNF/PPy estimated from ImageJ Program [48].

The uncompensated resistance causing the voltage drop in galvanostatic curves was calculated using $R = dE/(2I)$, where dE is the voltage drop from galvanostatic curves at close to 0 second and at where the current switches directions, and I is the current applied. The presented value of uncompensated resistance was the average resistance derived

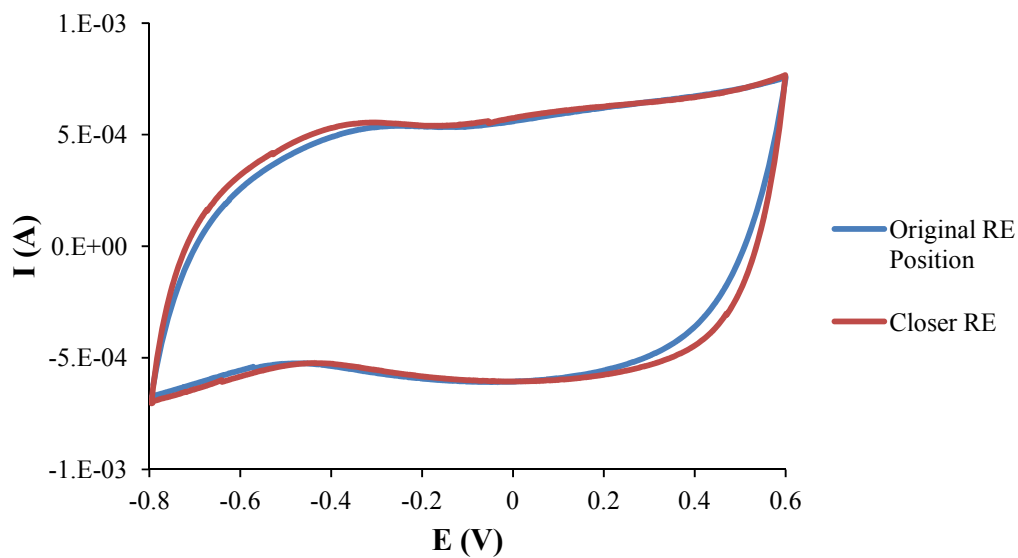
from all galvanostatic curves. It is assumed to be R_{total} here to verify the high contribution of R_{sol} to the electrochemical system. R_{sol} was calculated from the subtraction of R_{total} with R_{elec} and R_{ionic} . R_{total} , R_{elec} , R_{ionic} , and R_{sol} from CNF/PPy-4 and CNF/PPy-8 are summarized in Table 3-1. This assumption is valid since the calculated result is comparable with R_{sol} derived from $R_{\text{sol}} = \rho l/A$, where ρ is the resistivity of the electrolyte (1/0.00184 S/cm), l is the distance between WE and RE (9.0±2.5 mm), and A is the area of WE (1.30±0.05 × 1.50±0.05 cm² or 1.30±0.05 × 1.30±0.05 cm²). R_{sol} estimated from this method is 290±80 Ω for CNF/PPy-4 and 250±70 Ω for CNF/PPy-8.

Table 3-1 Resistance summary of CNF/PPy.

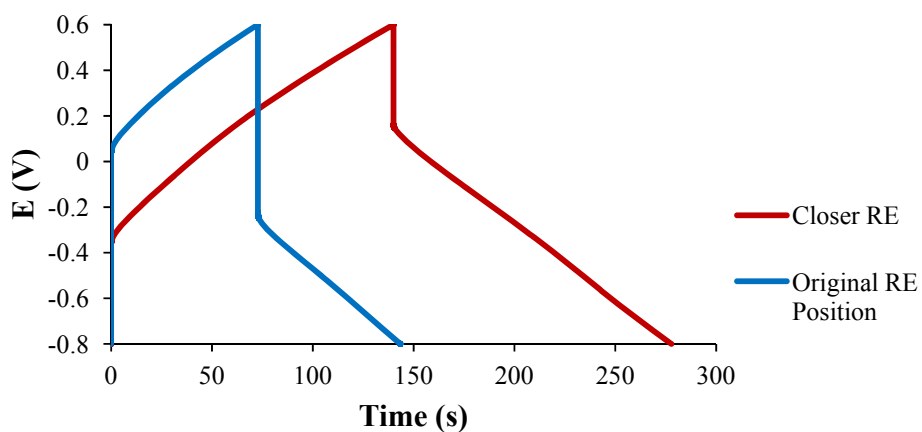
CNF/PPy	R_{total} (Ω)	R_{elec} (Ω)	R_{ionic} (Ω)	R_{sol} (Ω)	C (F)	C_v (F/m ³)	RC (τ)
CNF/PPy-4 charge	139 ±2	14 ±2	2.3 ±0.3	123 ±3	0.65 ±0.03	6.6±0.5×10 ⁷	9.0±0.4×10 ¹
CNF/PPy-4 discharge	137 ±2	14 ±2	2.3 ±0.3	122 ±3	0.67 ±0.03	6.8±0.5×10 ⁷	9.2±0.5×10 ¹
CNF/PPy-8 charge	190 ±20	12 ±2	3.0 ±0.4	180 ±20	1.17 ±0.05	9±1×10 ⁷	2.2±0.2×10 ²
CNF/PPy-8 discharge	190 ±10	12 ±2	3.0 ±0.4	180 ±10	1.20 ±0.06	9±1×10 ⁷	2.3±0.2×10 ²

As shown in Table 3-1, the RC constants of CNF/PPy-4 and CNF/PPy-8 were estimated to be ca. 90 and 200 seconds, with no significant difference between charge and discharge constants. The RC estimation was comparable to the time required to charge the CV curve (1mV/s) to its maximum current, confirming resistances in the system mainly caused the slow charge/discharge rate of PPy. Among all, R_{sol} dominates. R_{sol} could be reduced by moving the RE closer to the WE. A quick experiment demonstrating this effect was done by reducing the RE and WE distance from the original 9.0±2.5 mm

to 4.0 ± 2.5 mm. The difference in charge/discharge time CNF/PPy-4 is shown in Fig. 3-16. In Fig. 3-16(a), at closer RE position (red curve), the CV current reached the plateau slightly faster than that at the original RE position (blue curve). Since the difference in CV shape was very small, galvanostatic charge/discharge of CNF/PPy-4 at 0.67 A/g was done, as shown in Fig. 3-16(b), to further investigate the difference in R_{sol} . It is evident that at reduced RE distance, the potential drop significantly reduced from ca. 0.80 to 0.40 V, namely the uncompensated resistance was reduced by half. In order to reduce the effect of R_{sol} , it is necessary to re-design the cell setup to obtain better CNF/PPy performance at higher charge/discharge rates.



(a)



(b)

Fig. 3-16 The effect of R_{sol} at different RE positions. The effect is demonstrated using CV at 1 mV/s cycle rate (a) and galvanostatic charge/discharge at 0.67 A/g cycle rate (b) on the CNF/PPy-4 sample.

For the GC/PPy sample, the major resistances consist of R_{ionic} and R_{sol} . R_{elec} is ignored here assuming the high conductivity of PPy. The time constant τ of R_{ionic} is calculated from $\tau = a^2/D_{eff}$. The estimated D_{eff} value used here is $2.1 \pm 0.7 \times 10^{-12} \text{ m}^2/\text{s}$ as previously

published [78]. The values of D_{eff} , τ , C_v , σ_{ionic} , and R_{ionic} of GC/PPy are summarized in Table 3-2. σ_{ionic} estimated is about 20 times higher than previously published result [92], which is likely due to the higher D_{eff} value used. C_v estimated from GC/PPy system decreased from $1.0 \pm 0.2 \times 10^8$ to $6.0 \pm 0.5 \times 10^7$ F/m³ with increased PPy deposition time. In contrast, C_v of CNF/PPy system increased from ca. 7×10^7 to 9×10^7 F/m³ with increased PPy deposition time, indicating the volume of nanofibrous PPy was effectively interacting with PF₆⁻ ions. As the amount of PPy increases, its volume ratio to pure CNF increases, thus increasing C_v .

The lower C_v of GC/PPy-8 comparing to GC/PPy-4 was mainly affected by the lower PPy density, hence a much thicker film, at extended deposition time. The σ_{ionic} from both GC/PPy were much lower than their electronic conductivity, implying that the resistive nature and slow charging time of the non-porous PPy film is largely affected by σ_{ionic} . R_{sol} resistance was calculated from galvanostatic curves in Fig. 3-13(a) and Fig. 3-14(a). Average charge and discharge R_{sol} , C , and τ of GC/PPy-4 and GC/PPy-8 are summarized in Table 3-3. τ from charging curves in general are higher than that from discharging curves, indicating the value of R_{sol} might be partially contributed from R_{ionic} . The high τ from R_{ionic} is likely due to lower anionic conductivity of PPy in the reduced state [90, 94]. τ (from R_{sol}) of GC/PPy-8 at lower charging current densities ($3.6 \pm 0.7 \times 10^2$ sec) was much higher than that at higher charging current densities ($2.0 \pm 0.2 \times 10^2$ sec). One explanation could be that at higher rates, PPy film is not able to reach equilibrium and remains in a state effectively higher in voltage during charging and lower in voltage during discharging. It is also suspected that the PPy film resistance at reduced state might still be very high at first few galvanostatic cycles (the film was cycled from low to

high current densities). The film gradually stabilized afterwards and exhibited similar resistance to the discharge cycles. This effect can be clearly observed in Fig. 3-17, where R_{sol} of GC/PPy-4 and GC/PPy-8 at charge and discharge current densities are summarized. For both samples, R_{sol} reaches a plateau as the cycling proceeds towards higher current densities. Since R_{sol} should not be affected by the variation of PPy internal resistance at different oxidation state or the number of cycles, the actual R_{sol} could be estimated from the lowest number of R_{sol} . For GC/PPy-4, R_{sol} is estimated to be 201 Ω and for GC/PPy-8, R_{sol} is estimated to be 141 Ω . The difference between R_{sol} and the highest resistance in Fig. 3-17 are estimated to be ca. 70 Ω and 200 Ω for GC/PPy-4 and GC/PPy-8, respectively, which are lower than R_{ionic} (assuming the rest of the resistance is contributed from R_{ionic} only) calculated from Table 3-2. It is suspected that PPy films are not fully interacting with PF_6^- ions due to their dense structure and high film thickness.

As shown in the 1 mV/s rate of CV curves in Fig. 3-12 (a) and (b), the time required to charge PPy to the maximum current is ca. 500 and 800 sec for GC/PPy-4 and GC/PPy-8, respectively. In contrast, the time required to discharge PPy to minimum current was ca. 300 and 400 sec for GC/PPy-4 and GC/PPy-8, respectively. For GC/PPy-4, the sum of τ from R_{ionic} and R_{sol} is close to the CV approximation. However, for GC/PPy-8, τ from R_{ionic} alone dominated τ estimated from CV during charging but exceeded that during discharging. The increased τ could be correlated with a combination of increased film thickness and reduced anionic conductivity, where ion diffusion was slowed down. In contrast, during discharging, the higher oxidation state of PPy at positive potential possessed high conductivity and facilitated faster anion extraction. The actual D_{eff} of GC/PPy-8 during discharging might be larger than $2.1 \pm 0.7 \times 10^{-12} \text{ m}^2/\text{s}$.

Table 3-2 Table summary of D_{eff} , τ (ionic), C_v , σ_{ionic} , and R_{ionic} of GC/PPy-4 and GC/PPy-8.

PPy Film	Assumed D_{eff} (m^2/s)	$^1\tau$ (s)	C_v (F/m^3)	$^2\sigma_{\text{ionic}}$ (S/m)	$^3R_{\text{ionic}}$ (Ω)
GC/PPy-4	$2.1 \pm 0.7 \times 10^{-12}$	$1.4 \pm 0.6 \times 10^2$	$1.0 \pm 0.2 \times 10^8$	$1.8 \pm 0.7 \times 10^{-4}$	$1.9 \pm 0.8 \times 10^2$
GC/PPy-8	$2.1 \pm 0.7 \times 10^{-12}$	$1.0 \pm 0.3 \times 10^3$	$6.0 \pm 0.5 \times 10^7$	$1.3 \pm 0.4 \times 10^{-4}$	$7.0 \pm 2.2 \times 10^2$

1 Derived from $\tau = a^2 / D_{\text{eff}}$

2 Derived from $\sigma_{\text{ionic}} = D_{\text{eff}} C_v$

3 Derived from $R_{\text{ionic}} = L / \sigma_{\text{ionic}} A$, where L = thickness of the PPy film and A is the area of GC disk

Table 3-3 Table summary of R_{sol} , C , and RC (solution) of GC/PPy-4 and GC/PPy-8.

GC/PPy	R_{sol} (Ω)	C (F)	RC (τ)
GC/PPy-4 charge	$2.4 \pm 0.3 \times 10^2$	0.73 ± 0.04	$1.8 \pm 0.2 \times 10^2$
GC/PPy-4 discharge	$2.2 \pm 0.1 \times 10^2$	0.72 ± 0.04	$1.6 \pm 0.1 \times 10^2$
GC/PPy-8 charge	$^1 2.7 \pm 0.5 \times 10^2$	1.3 ± 0.1	$3.6 \pm 0.7 \times 10^2$
	$^2 1.5 \pm 0.1 \times 10^2$	1.3 ± 0.1	$2.0 \pm 0.2 \times 10^2$
GC/PPy-8 discharge	$1.6 \pm 0.1 \times 10^2$	1.3 ± 0.1	$2.0 \pm 0.2 \times 10^2$

1 Average R_{sol} of GC/PPy-8 from the three lower charging current densities

2 Average R_{sol} of GC/PPy-8 from the three higher charging current densities

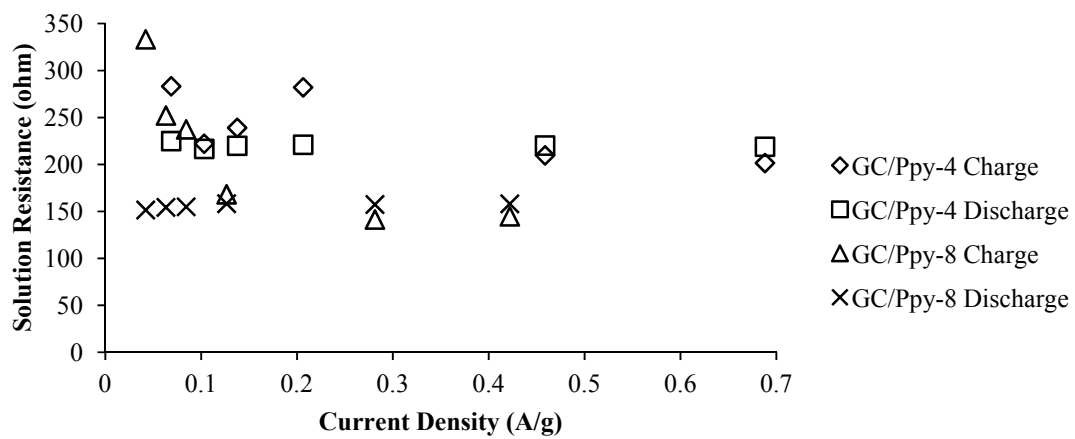
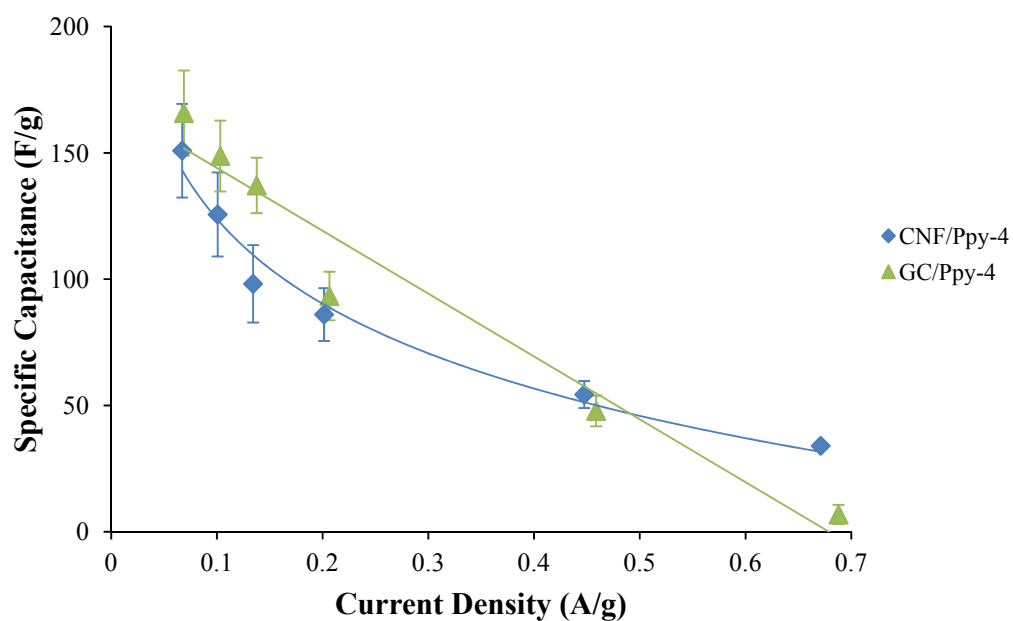


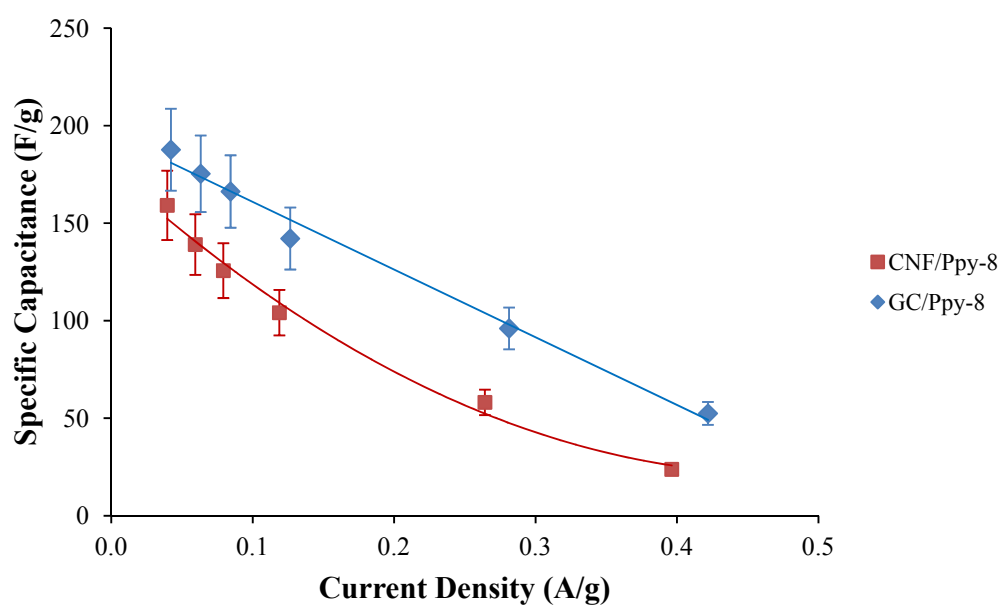
Fig. 3-17 R_{sol} of GC/PPy-4 and GC/PPy-8 at different charge and discharge current densities.

Fig. 3-18 (a) and (b) are the specific capacitance comparison between CNF/PPy and GC/PPy at 4 and 8 hours of deposition, respectively. The capacitances of CNF/PPy cycled at different current densities are comparable to that of GC/PPy but with no significant difference. R_{sol} contributed highly to the capacitance drop for all samples but R_{ionic} contributes more significantly in GC/PPy samples. CNF/PPy in theory could achieve better performance than GC/PPy at higher cycle rate given that τ from the sum of R_{elec} and R_{ionic} of CNF/PPy are lower than τ from R_{ionic} of GC/PPy. However, in order to accurately measure the capacitance of PPy at higher cycle rates, a better electrode setup needs to be designed to reduce the resistance drop between RE and WE.

The specific capacitance and specific energy of a supercapacitor device using CNF/PPy electrode can be estimated with Equation (1) and (4), assuming both cathode and anode consist of CNF/PPy. By using a capacitance of 150 F/g per CNF/PPy electrode, the specific capacitance of the cell is 37.5 F/g (4× smaller than a single electrode [92]). Specific energy of a cell estimated using an operating voltage (V) of 1.4 V from this study is ca. 10 Wh/kg. Using the CNF/PPy composite electrode improves the energy performance of commercial carbon (ca. 100 F/g in organic electrolyte) by about 1.5×. However, improvement in the power performance is necessary since most commercial supercapacitors discharge within just a few minutes.



(a)



(b)

Fig. 3-18 Discharge capacitance comparison between CNF/PPy-4 and GC/PPy-4 (a) and CNF/PPy-8 and GC/PPy-8 (b)

3.4 Conclusion

CNF/PPy and GC/PPy at 4 and 8 hours of PPy deposition time were fabricated and characterized. Both electrodes possess an intrinsic capacitance of ca. 150 F/g. It was found that with the porous nanofibrous system, R_{ionic} of pure PPy film could be significantly reduced at highly reduced state, as compared with a sudden voltage drop at slow cycle rate during discharge and higher charging R_{ionic} of GC/PPy. However, the long time constant from R_{sol} still results in a long charge/discharge time measurement of the porous CNF/PPy electrode. An improved electrochemical cell setup is necessary to accurately measure the cycling performance excluding the effect of solution resistance.

4 Rechargeable Lithium Ion Batteries (LIB)

4.1 Introduction to LIB

Consumers today are demanding for smaller, lighter, cleaner, and cheaper batteries for portable electronics and telecommunication equipment. The rapid advancement in mobile devices and the emphasis of wireless connections with multiple functionalities exerts high expectations in batteries with greater power. Common rechargeable batteries today include lead-acid, nickel-cadmium, nickel metal hydride (NiMH), and LIB. Some of their properties are summarized in Table 4-1 [95]. Among all, nickel-based batteries dominated the portable, rechargeable battery market until the development of LIB in 1990s [96-98]. As shown in Table 4-1, LIB can be operated at a much higher voltage of 4.0 V, which requires fewer cells to deliver high energy density and, consequently, reduces the weight of the device. A LIB is able to reduce the weight of nickel-based batteries by 50% and the volume by 20-50% [99]. LIB also possess the advantage of low discharge rate, low maintenance issues, and miniaturizing capabilities compared to nickel-based batteries. Known for light weight, high energy density, and high voltage capacity per cell, LIB make up the highest market share of 91.8% in mobile IT and 78.8% in communication devices today [100]. As shown in Fig. 4-1, LIB possess both superior volumetric and gravimetric energy densities comparing to other rechargeable devices. Although LIB is still more expensive than other types of rechargeable batteries due to the complex processing conditions and the requirement of highly purified non-aqueous electrolyte, it is believed that the cost could be significantly reduced once the production process is optimized [100]. Because of its superior energy and power density, Li-ion technology is promising for heavy duty hybrid electric vehicles, aerospace, and military

applications [101, 102]. A further increase in energy densities (approximately 2× higher in Wh/kg) is necessary.

Table 4-1. Properties of common rechargeable batteries [95, 103].

	Nominal Voltage (V)	Operating Temperature (°C)	Specific Energy (Wh/kg)	Energy Density (Wh/L)	Power Density (W/kg)	Cycle Life (cycles)	Price (USD/kWh)
Lead-acid	2.0	-40 – 50	10 – 35	50 – 90	150 – 300	200 – 700	300 – 120
NiCd	1.2	-55 – 60	20 – 40	40 – 100	260	500 – 10,000	300 – 1400
NiMH	1.2	-20 – 50	35 – 50	80 – 175	180 – 220	300 – 600	350 – 550
Li Ion (LiCoO ₂ /C)	4.0	-20 – 50	150	400	200 – 300	1000	200 – 1000

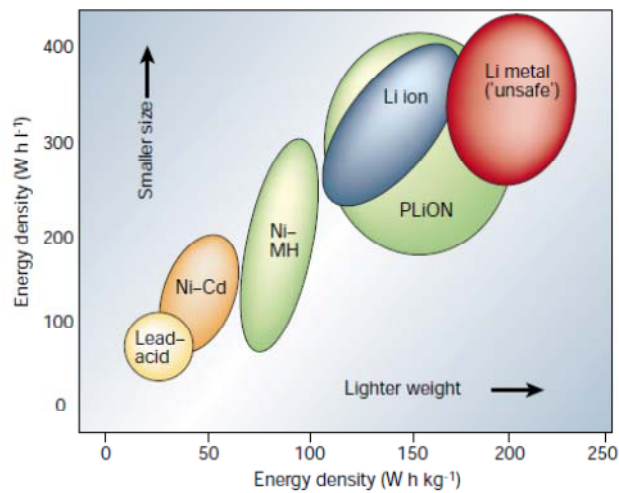
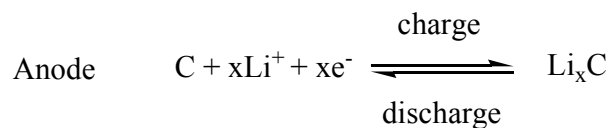
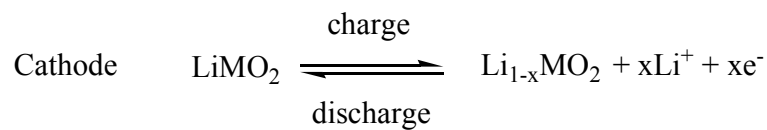


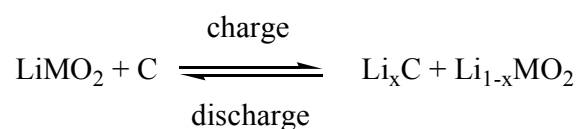
Fig. 4-1 Volumetric and gravimetric energy density summary of common rechargeable batteries. PLiON is a type of flexible LIB developed by Bellcore [98]. Reproduced with permission from Nature Publishing Group.

4.1.1 Principles of LIB

A LIB mainly consists of an anode, a cathode, and the electrolyte. The electrodes are usually attached to a metal current collector through a binder, commonly a mixture of polyvinylidene fluoride (PVDF) and carbon black. Lithiated metal oxides with layered or tunnelled structures are mostly used for cathode materials, including layered oxides (ex. LiCoO_2), transition metal phosphates (ex. LiFePO_4), and spinels (ex. LiMn_2O_4). Among all, LiCoO_2 is most widely used commercially due to its easy preparation, good safety, and reduced sensitivity to moisture and preparation process [104]. Lithium metal was mainly used as the anode material when LIB was first developed in the 1970s. Because Li is the lightest and most electropositive metal (reduction potential of -3.04 V vs. standard hydrogen electrode), it possesses a very high specific energy density and impressive performance. However, explosions can occur with the growth of dendritic Li after cycling [98]. Carbon and graphite replace Li metal for commercial anodes today due to their stable, safe, consistent morphology upon cycling, and high Li ion insertion density. The liquid electrolyte is often a mixture of Li-salts (LiPF_6 , LiBF_4 , or LiClO_4) with aprotic organic solvents (carbonates, amides, imides, or their mixtures) [105]. The ionic conductivity of the electrolyte is at most 2×10^{-2} S/cm with the salt concentration between 1 – 1.5 M [95]. Besides the high ionic conductivity, the electrolyte also possesses high thermal, chemical, and electrochemical stability [95]. Fig. 4-2 is a schematic representation of conventional Li-ion batteries. During charging, Li ions deintercalate out of the cathode and intercalate into the anode. The reverse reaction occurs during discharging. The electrodes reactions are summarized as follows (adapted from [104]):



The overall reaction can be summarized as



The capacity of a LIB is proportional to the number of Li ions reacted with the electrodes. The overall capacity is normalized by weight or volume. Due to our experience with carbon production, application of electrospun CNF in LIB anode will be investigated in this study.

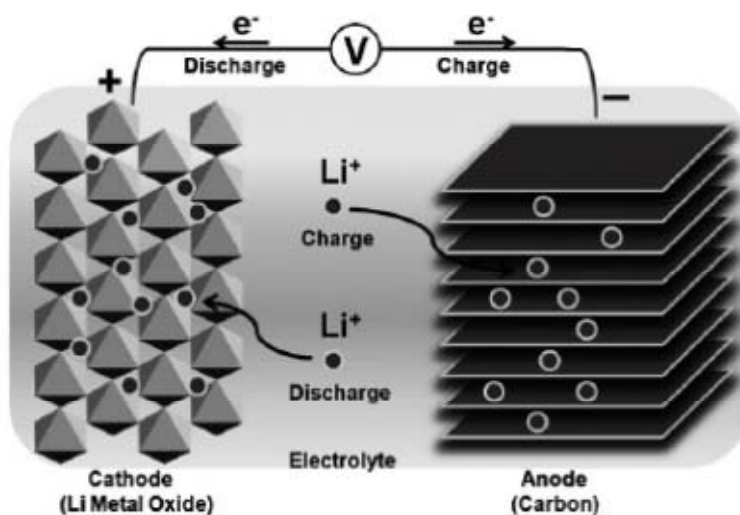


Fig. 4-2 Schematic representation of a conventional rechargeable Li-ion battery [105]. Reproduced with permission from John Wiley and Sons.

4.1.2 Role of Carbon in LIB Anode

Among all types of carbon materials used for LIB anode, graphite has become the standard material in industry due to its low discharge potential and long plateau at 0.1 V versus Li metal, as shown in Fig. 4-3(a) [99, 106]. The plateau is a desirable feature for Li ion cells to possess a flat voltage output and maximized energy density [107]. However, the maximum capacity of graphite is limited to a theoretical capacity of 372 mAh/g, corresponding to LiC_6 composition under ambient atmosphere. When intercalated, Li ion occupies the next nearest site (4.25\AA apart) within the van der Waals space between two graphene sheets and transfers most of its 2s electron density to carbon. Due to the large repulsion between adjacent Li ions, greater numbers of Li ion intercalation were only achieved under high pressure [106].

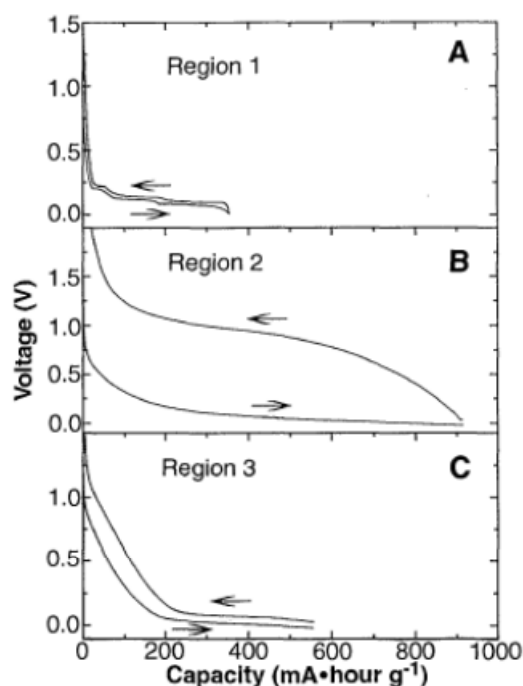


Fig. 4-3 Charge/discharge profile of graphite (a), soft carbon (b), and hard carbon (c) [106]. Reproduced with permission from the American Association for the Advancement of Science.

Other types of carbons, including soft and hard carbons, have been continuously investigated to improve the capacity of carbon anode. Soft carbons possess parallel-stacked graphene crystallites that can evolve towards graphitic structure upon high temperature treatment above 2000°C. Soft carbon heat treated between 500 and 1000°C can reach a reversible capacity of 700 mAh/g. When treated below 700°C, a signature discharge potential plateau appears at 1.0 V, as shown in Fig. 4-3(b), due to the presence of hydrogen atoms. The high discharge potential will cause the voltage loss of LIB and result in the operating voltage below 3 V [99, 108]. Hard carbons have no parallel-stacked crystals and are not graphitizable even heated to 3000°C. They are usually treated at 1100°C and the reversible capacity could reach 600 mAh/g, with small irreversible capacity and hysteresis in the voltage profile, as shown in Fig. 4-3(c) [97, 99]. Mesocarbon microbeads (MCMB) derived from soft carbon heat treated at 3000°C, natural graphite, and hard carbon are mainly used for LIB electrodes commercially. The capacity of these graphite and hard carbon are 310 and 400 mAh/g, respectively[104]. Graphite often possess a more consistent discharge profile and hard carbon often possess a sloping discharge behavior, as shown in the schematics of Fig. 4-4. Graphite is suitable for small electronics such as cell phone due to its high energy density per volume and constant discharge profile. Hard carbon, in contrast, is more suitable in larger-sized electric vehicles due to its high power and durability [109].

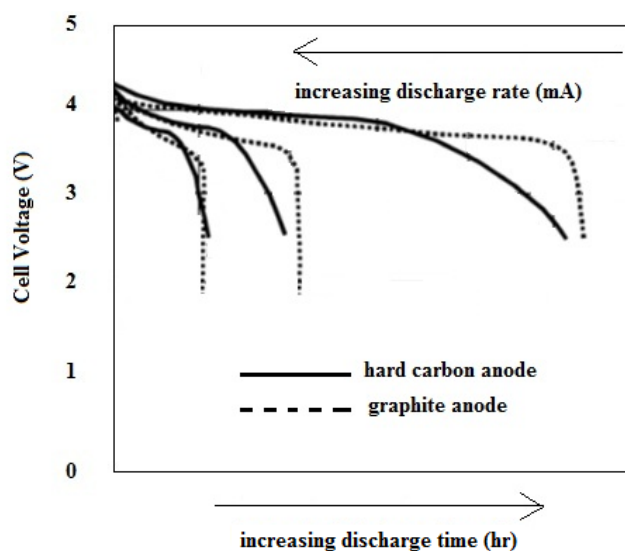
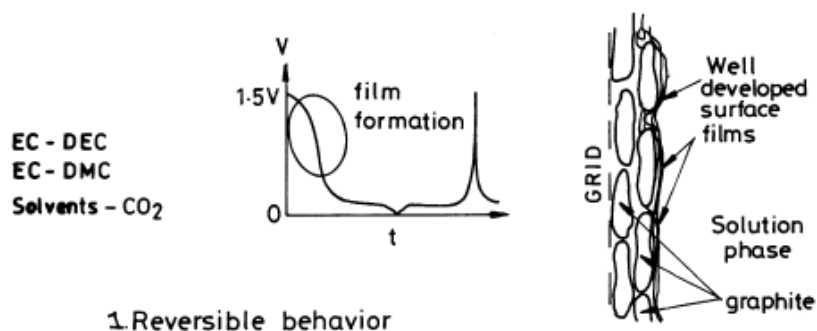


Fig. 4-4 Discharge profile of hard carbon and graphite, adapted from [110].

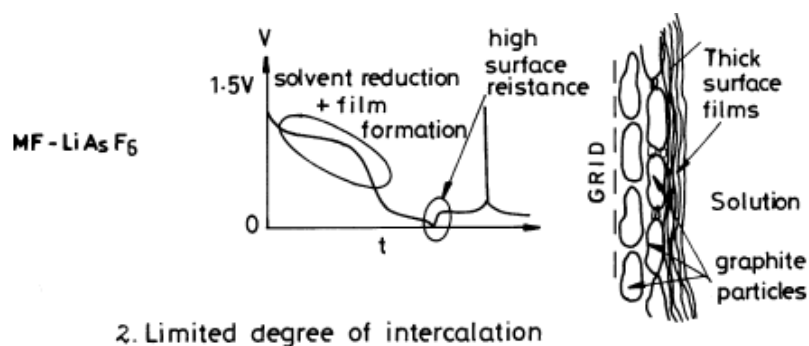
4.1.3 Solid Electrolyte Interface

A passivating layer called the solid electrolyte interface (SEI) is often formed on carbon at 0.8 – 0.9 V vs. Li^+/Li during the first charge cycle. The layer is formed through reduction and decomposition of electrolyte and mainly consists of lithium carbonate and lithium alkyl carbonates [111-114]. It is permeable to Li^+ but impermeable to other electrolyte species, which protects carbon from electrolyte insertion and further degradation on the carbon structure. One exception with graphite is using propylene carbonate (PC) as the only solvent. When the Li^+ concentration in carbon is low, the formation of the ternary compound, $\text{Li}(\text{solv})_y\text{C}_n$, is favored over the formation of LiC_n [115]. Further reduction causes the decomposition of the ternary compound and produces propylene gas, which exfoliates graphene sheets. The irreversible capacity is dramatically increased due to the low useable reversible capacity, the reduced electrical contact, and the increased surface area of graphite after exfoliation, as shown in Fig.

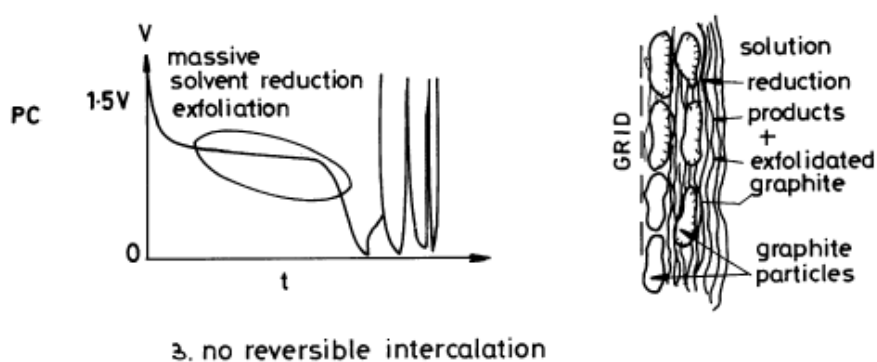
4-5(c). Alternative electrolytes have been sought to reduce the formation of ternary compound. Ethylene carbonate (EC) has been proven to form a thin and stable SEI layer with small capacity loss. Because EC is solid at room temperature, it is often mixed with other solvents with lower melting temperature, such as diethyl carbonate (DEC) or dimethyl carbonate (DMC) [111, 116, 117]. As shown in Fig. 4-5, the EC solvent mixture forms the least amount of SEI, the highest reversible capacity, and the lowest surface resistance among electrolytes investigated.



(a)



(b)



(c)

Fig. 4-5 Schematic view of various types of SEI and their effect on the electrode capacity: (a) high reversible capacity (b) low reversible capacity, and (c) no reversible capacity[118]. Reproduced with permission from Springer.

4.1.4 Carbon Structure vs. Capacity

Natural graphite is rarely used by itself as commercial anode because the large crystal size and spacially packed graphene layers limits the accessibility and the penetration of Li ions. Modified graphite materials, including mesocarbon microbead (MCMB), graphite fibres, or reduced particle size of graphite by ball milling, have been attempted [102]. The structural advantage of MCMB is the presence of turbostratic disordered regions, which serves as more efficient charge/discharge sites. The low surface area of these spherical particles also reduces the amount of SEI formation and the irreversible capacity [119]. As for graphitic carbon fibres, both mechanical strength and crystal orientation play an important role in Li ion intercalation. It was shown that the radial texture with zig-zag layers is favoured over concentric (onion-like) structures and exhibits least amount of graphite exfoliation even using PC. Although the concentric structure hinders the diffusion of Li ions, it was observed that smaller graphite crystal size significantly reduced the effect of this crystal orientation [120]. Same analogy was applied to graphite powders produced from ball milling. By proper control of powder size from milling, the graphite crystal is small enough to enhance Li ion diffusion but not producing a large amount of irreversible capacity with the increased surface area. Milling could also expand the interlayer space of graphene sheets to facilitate more efficient Li ion intercalation/deintercalation [121].

On the other hand, hard carbon also attracted much attention after the successful commercialization of LIB by Sony Corporation using hard carbon as the anode material [122]. Hard carbons usually possess cross-linked groups, which prevent the formation of graphitic structure [117]. The electrochemical performance of various hard carbons heat

treated between 500 and 1100°C have been studied, including pitch coke, petroleum coke, pyrolyzed polymers of PAN, poly(vinylchloride) (PVC), poly(vinylidene fluoride) (PVDF), poly(phenylene sulfide) (PPS), and phenolic resins [123-130]. They in general possess high reversible capacity, high irreversible capacity at the first cycle, and large hysteresis at 1.0 V when the pyrolysis temperature is low [117]. At low pyrolysis temperature, impurities such as oxygen, hydrogen, or sulphur, are often found in the carbon matrix depending on the precursor used. The presence of these heteroatoms has been shown to reduce the reversible capacity of carbon. It was also proposed that Li could bind to the hydrogen-terminated edges of carbon fragment, which changes the carbon-carbon bonding from sp^2 to sp^3 and leads to hysteresis. If reformation of sp^2 orbital during discharging is slow, the battery cell would suffer from capacity decay upon cycling [106].

Several reasons contribute to the high irreversible capacity of hard carbon. With the presence of micropores, the capacity loss with the formation of SEI could increase if electrolyte was able to diffuse through the pores and form additional passivating layer [131]. Reaction of Li ions with the active sites, including hydroxyl groups or carbon radicals, on carbon could also result in large irreversible capacity [132]. The performance of hard carbon could be improved dramatically with the elimination of impurities, the advantage of low crystallinity, and large porosity to achieve electrochemical performance similar to Fig. 4-3(c). The presence of numerous micro- and nanopores provides easier accessibility of Li ions to the carbon layer [133]. Because hard carbons are not graphitizable, they are composed of many randomly aligned single carbon layers with interlayer distance (0.523 nm) higher than that of graphite (0.3354 nm)

[108]. Li ions could be adsorbed on both surfaces of these layers in contrast to the single layer intercalation of graphite, as shown in Fig. 4-6. This could potentially lead to a maximum theoretical capacity of 740 mAh/g with Li_2C_6 composition. Because Li ions are loosely bounded on those disordered layers, a flat voltage plateau could be achieved with fast charge/discharge, as shown in Fig. 4-3(c) [106, 134].

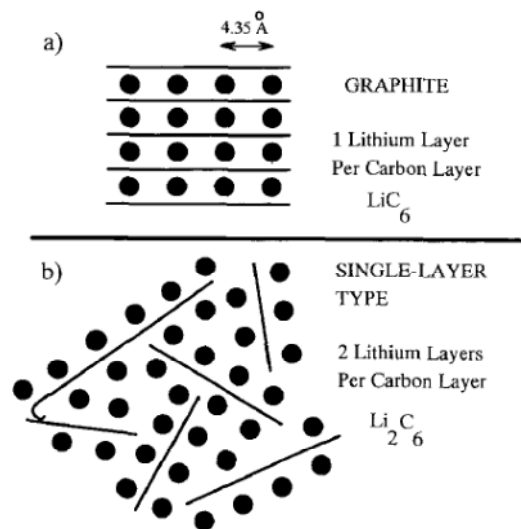


Fig. 4-6 Schematic representation of lithium intercalation into layered graphite (a) and single-layered hard carbon (b) [134]. Reproduced with permission from Elsevier Science Ltd.

4.1.5 Role of Silicon in LIB Anode

LIB cathodes with 160-200 mAh/g capacities can be achieved today; however, it is difficult to develop new cathode materials with enhanced capacity [101]. A considerably higher anode capacity than that of carbon or graphite is necessary to increase the total capacity of the LIB. Calculations have shown that increasing the anode capacity slowly increases the total capacity, but the overall capacity reaches a plateau when the anode capacity reaches 1000-1200 mAh/g [135]. Intercalation capacities of various metals (Sn,

Pb, Al, Au, Pt, Zn, Cd, Ag, Si, Mg, and Si) with Li were investigated for their substitution with carbon. Among all, Si is known to possess the highest theoretical specific capacity of 4200 mAh/g, where each Si atom alloys with 4.4 Li atoms to form $\text{Li}_{22}\text{Si}_5$ alloy [136-138]. Besides its outstanding capacity, Si is also the second most abundant element on earth. Its charge/discharge profile within a narrow potential range of 0.0 and 0.4 V is advantageous to be used as a LIB anode. However, formation of the alloy induces 400% volume expansion of the Si lattice and often results in cracking, disintegration, and detachment of the electrode from the current collector. The poor electrical contact often leads to the capacity fade of the electrode [101].

Studies on pure Si electrode have shown that the electrical conductivity of Si-Li alloy increases during Li intercalation, in contrast to the low conductivity of pure Si. However, deintercalation of Li increases the contact resistance and charge transfer resistance of the electrode with volume contraction and pulverization of Si [139]. Conductive fillers such as carbon black or graphite flakes have been added to improve the electrical contact among Si particles and to reduce particle agglomeration [140]. Si nanoparticles (SiNP) have also been used to reduce the amount of volume expansion [141, 142]. The use of SiNP has demonstrated the improved cyclability with a discharge capacity of 1729 mAh/g after 10th cycle with 17.5% capacity fade [142]. Inactive metal matrices is one other method used to incorporate with Si. Metal compounds including TiN, SiC, and TiC were homogeneously mixed with Si to act as a strong mechanical support, to provide electrical conductivity, and to buffer the volume change of Si [143-145]. Although the inactive matrices demonstrated the mechanical stability after galvanostatic cycling, the cycling capacity was only 300-400 mAh/g in 15 cycles, which is lower than the

theoretical value of 700-900 mAh/g. The low capacity was likely due to the poor diffusivity of Li ions through the inactive matrix [146]. The diffusivity was later improved by the incorporation of the active matrix, either graphite or carbon. The cycle life and the capacity retention of the composite, including Fe/Si, Ba/Fe/Si, and Ni/Si, were significantly improved with the active matrix coating [147-149]. Among all, Ni/Si/Graphite composites possessed the best performance, where constant capacities between 700 and 800 mAh/g for 50 cycles were achieved with different graphite ratios [149].

Besides providing better diffusivity of Li ion, carbon is also known for light weight, compliance, and good electrical conductivity. Much effort has been focused on developing Si/C composite to further reduce the capacity fade of Si upon cycling. In 1990s, many polymer precursors were pyrolyzed at temperatures between 700 – 900°C to produce Si/C composites. Precursors used include siloxane polymers, epoxysilanes, polysilanes, and mixtures of carbon copolymer precursor with silanes [150-153]. It was generally found that the presence of oxygen increases the irreversible capacity and the discharge potential (an additional plateau between 0.6 and 0.8 V). The presence of sulfur also traps Li ions and increases the irreversible capacity. Although pyrolyzing polymer precursors at high temperatures eliminates oxygen, at above 1300°C, the formation of silicon carbide is inactive to Li ions. The reversible capacity of these composite electrodes are mostly between 400 – 700 mAh/g.

In recent years, nano Si/carbon composite has been highly investigated by many research groups. Holzapfel *et al.* deposited 10-20 nm-sized Si nanoparticles on Timcal KS-6 graphite through thermal vapor deposition of silane [154]. Nano-Si adheres tightly on the

graphite surface and the charge/discharge capacity of this electrode showed superior performance in 100 cycles at a rate of 74 mA/g. The initial discharge capacity was 1000 mAh/g and remained over 900 mAh/g after 100 cycles. The 26% irreversible capacity was contributed from the formation of SEI on the high surface area nano-Si and graphite. The improved capacity retention by carbon was also explained by Liu *et al.* [155]. The rate of capacity fade for Si/C composite was a lot slower than that of pure Si electrode because carbon was able to preserve the conductive network even after the fracture of Si particles. Kim *et al.* pyrolyzed nano-Si, pitch, and graphite together at 900°C and produced a porous electrode structure, which improved the capacity retention and helped to release the mechanical stress of volume change [156]. Carbon coating was also found to reduce the chance of contacts between nano-Si. Another form of carbon, carbon aerogel, was fabricated by Wang *et al.* to disperse nano-Si and a constant discharge capacity of 1400 mAh/g was obtained for 50 cycles at C/10 rate [157].

Core-shell structured Si/C composite electrode was used by Gao *et al.* and demonstrated cycling stability. Polymer poly(cyclotriphosphazene-4,4'-sulfonyldiphenol) was chosen to encapsulate nano-Si simply by ultrasonication, followed by carbonization to obtain carbon coated nano-Si [158]. The size of the nanoparticle was distributed from 70 to 120 nm with *ca.* 10 nm carbon coating. The electrode was able to retain a constant discharge capacity of 1350 mAh/g at 0.5C rate for 40 cycles. However, as the rate increased to 1C, the discharge capacity reduced to 650 mAh/g. One approach done by Martin *et al.* was to graft nano-Si onto graphite through a phenyl bridge [159]. This covalent bonding provided stronger contact between Si and graphite. In contrast to samples with no grafting, Si grafted graphite retained greater capacity after 50 cycles at 25 mA/g rate.

Simple Si/graphite mixture only possessed a total capacity of 325 mAh/g after 50 cycles, it corresponds to utilizing 6% of the theoretical capacity of Si. On the other hand, Si grafted graphite retained a higher capacity of 540 mAh/g, corresponding to the utilization of 42% of the theoretical capacity of Si. One method used by Ji *et al.* was to electrospin PAN with Si nanoparticles, followed by carbonization at 700°C to produce a Si/C nanocomposite [13]. The electrode showed a stable capacity at different rates with 15 wt% nano-Si (with respect to PAN). However, more significant capacity drop occurred after 50 cycles as the Si content increased to 30 and 50 wt%. At 30 and 50 wt% Si, the initial electrode discharge capacity achieved over 1000 mAh/g; however, the agglomeration of Si after cycling resulted in less than 15% capacity retention after 50 cycles.

4.2 Experimental

Based on our experience with electrospinning and carbon fibre fabrication, the method of using core-shell electrospinning to generate carbon fibres containing SiNP is proposed. Instead of exposing SiNP on the surface of CNF as previously done by Ji *et al.* [13], it is believed that the inclusion of SiNP within CNF could reduce the capacitance fading upon cycling.

4.2.1 Determination of Optimum Processing Parameters for Core-Shell Electrospinning Using PAN/SiNP Composite Nanofibres

SiNP was purchased from Nanostructured and Amorphous Materials, Inc. Triton X-100 (TX100), polyvinylpyrrolidone (PVP), PAN, and DMF were purchased from Sigma Aldrich. A solution mixture of 5 wt% SiNP (with respect to PAN), 5 wt% TX100 or PVP (with respect to PAN), and DMF was sonicated at 20 Watt power, 30 sec pulse on,

and 30 sec pulse off for 20 hours. 10 wt% PAN was then added and the solution was stirred at 76 – 80°C for 20 hours. The solution mixture was then electrospun using NANON at 15 kV, 1.0 ml/hr flow rate, 13 cm distance between needle tip and the drum collector, and 100 rpm rotating speed using the drum collector. Nanofibres collected on the aluminium foil covering the drum collector were then carbonized at 700, 900, and 1100°C using the parameter for PAN described earlier.

PAN/SiNP samples were characterized with SEM and TEM. SEM and TEM images were taken with $\times 5k$ and $\times 30k$ magnifications, respectively. CNF/SiNP samples were characterized with conductivity and EDX measurements. The instrument parameters used were the same as described in Chapter 2. The conductivity of CNF/SiNP was the average measurement from two samples and the atomic concentration was the average from four EDX measurements. In addition, X-ray diffraction (XRD) was used to characterize the presence of SiNP or other Si-containing impurities in CNF/SiNP. A Rigaku X-ray diffractometer, Multiflex 2kW was used for the sample analysis. The X-ray source was Cu K α ($\lambda = 1.54 \text{ \AA}$). $10^\circ - 130^\circ$ of the 2θ axis was scanned at a rate of $2^\circ/\text{min}$. The operating voltage was 40 kV and the current was 20 mA. The sampling width was 0.020° . The software MDI Jade 7[160] was used to analyze the peak data.

A three electrode cell was assembled in the glove box with Ar atmosphere using Li metal as both RE and CE. The CNF/SiNP fibre mat was used as the WE. The assembly was tightly sealed and immersed in the electrolyte solution with 1:1 (v/v) mixture of ethylene carbonate (EC) and propylene carbonate (PC) containing 1 M of LiPF₆ salt purchased from UBE Chemicals (EC forms a stable SEI layer and prevents the exfoliation of electrode by PC). A schematic of the setup is shown in Fig. 4-7. Each cell was cycled

between 2.5 and 0.01 V at 113.6 mA/g rate for three cycles using an AMEL Model 7050 potentiostat. This slow rate (113.6 mA/g) was chosen to evaluate the intrinsic cycling behaviour of CNF/SiNP electrode.

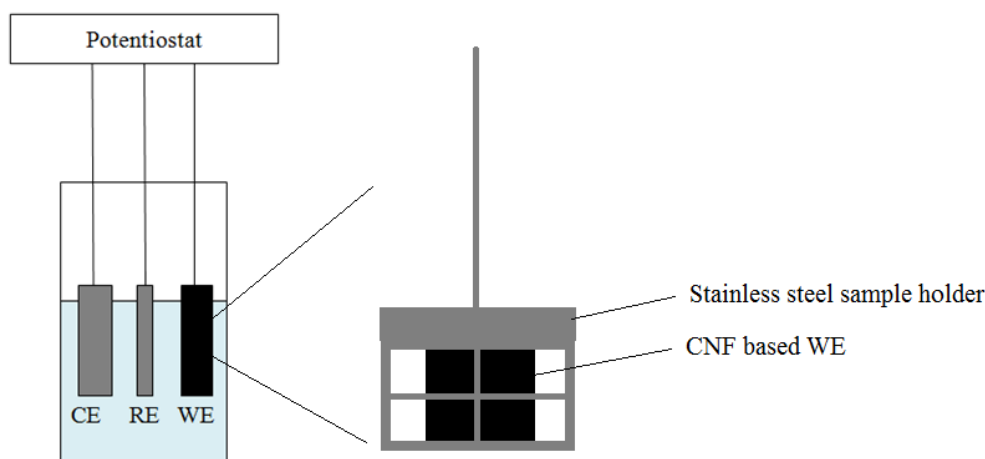


Fig. 4-7 Schematic representation of the three electrode cell setup for CNF/SiNP electrode testing.

4.2.2 Preparation of Core-Shell CNF/SiNP Composite Electrode with Different Concentrations of SiNP Using PANAM as Carbon Precursor

Core solutions were prepared by sonicating a solution mixture of 15, 30, 50, and 80 wt% SiNP (with respect to PANAM) with 15, 30, 50, and 80 wt% TX100, respectively, in DMF at 20 Watt power, 30 sec pulse on, and 30 sec pulse off for 20 hours. 8.5 or 8 wt% PANAM was then added and the solution was stirred at 80°C for 20 hours. Shell solution was prepared by heating a solution mixture of 8.5 or 9 wt% PANAM in DMF at 76 – 80°C for 20 hours. Viscosity measurement using Viscomate Model VM-10A was conducted to correlate the optimum spinning condition in relation to the solution viscosity in core and shell solutions. The viscosities of 9, 8.5, and 8 wt% PANAM in

DMF and the viscosities of 9, 8.5, and 8 wt% PANAM with 15, 30, 50, and 80 wt% SiNP in DMF were measured.

Core-shell electrospinning was conducting using NANON at 13 – 15 kV, 1.0 – 1.4 ml/hr flow rate with the flow rate of shell solution 0.2 ml/hr higher than that of the core solution, 13 cm distance between needle tip and the drum collector, and 100 rpm rotating rate for the drum collector. Nanofibres collected on the aluminium foil covering the drum collector were then carbonized at 900°C using the parameter for PANAM described earlier. Polymer core-shell nanofibres derived from 15, 30, 50, and 80 wt% SiNP in the core solution will be denoted as PANAM/Si-15, PANAM/Si-30, PANAM/Si-50, and PANAM/Si-80, respectively. The CNF/Si samples derived from each will be CNF/Si-15, CNF/Si-30, CNF/Si-50, and CNF/Si-80. Fig. 4-8 is a schematic of the experimental process.

Non-core-shell nanofibres were also prepared by electrospinning a DMF solution consisted of 30 wt% SiNP, 30 wt% TX100 (with respect to PANAM) and 9 wt% PANAM. It was then carbonized into CNF/SiNP composite using the same furnace parameter as the core-shell sample. The non-core-shell polymer precursor and its carbon derivatives are denoted as n-PANAM/Si and n-CNF/Si, respectively.

PANAM/SiNP and CNF/SiNP samples were characterized with SEM and TEM. SEM images of both samples were taken at $\times 600$ and $\times 5k$ magnifications. TEM images of PANAM/SiNP and CNF/SiNP were taken at $\times 30k$ and $\times 50k$ magnifications, respectively. CNF/SiNP was also characterized with XRD, EDX, and conductivity measurement. The conductivity of CNF/SiNP was the average measurement from two samples and the

atomic concentration was the average from four EDX measurements. CNF/SiNP and pure CNF carbonized at 900°C were also characterized with Raman to investigate the change in carbon structure with the addition of SiNP. The calculated peak ratio was derived from the average of four Raman measurements. All the instrumental parameters used were the same as described in Chapter 2.

Seven samples from CNF/Si-80 and seven samples from n-CNF/Si were prepared for tensile test. Thin strips of samples with dimensions of 5 cm × 5 mm were sandwiched between a folded paper frame with outer dimensions of 5 cm × 5 cm and inner dimensions of 4 cm × 4 cm. A KES-G1 Tensile Tester from KATO TECH CO., LTD was used for tensile testing. Load cells of 40 and 200 g were used for CNF/Si-80 and n-CNF/Si samples, respectively. A deformation rate of 0.02 cm/s was used for both samples.

The galvanostatic charge/discharge performance of CNF/Si-80 and n-CNF/Si were tested with the three electrode cell setup as described earlier. Both samples were cycled at 100, 200, 400, and 600 mA/g rates between 2.5 and 0.01 V for 20 cycles using an AMEL Model 7050 potentiationstat. The cycled nanofibres were then washed with PC, air dried, and characterized with SEM. SEM images were taken with ×600 and ×3k magnifications.

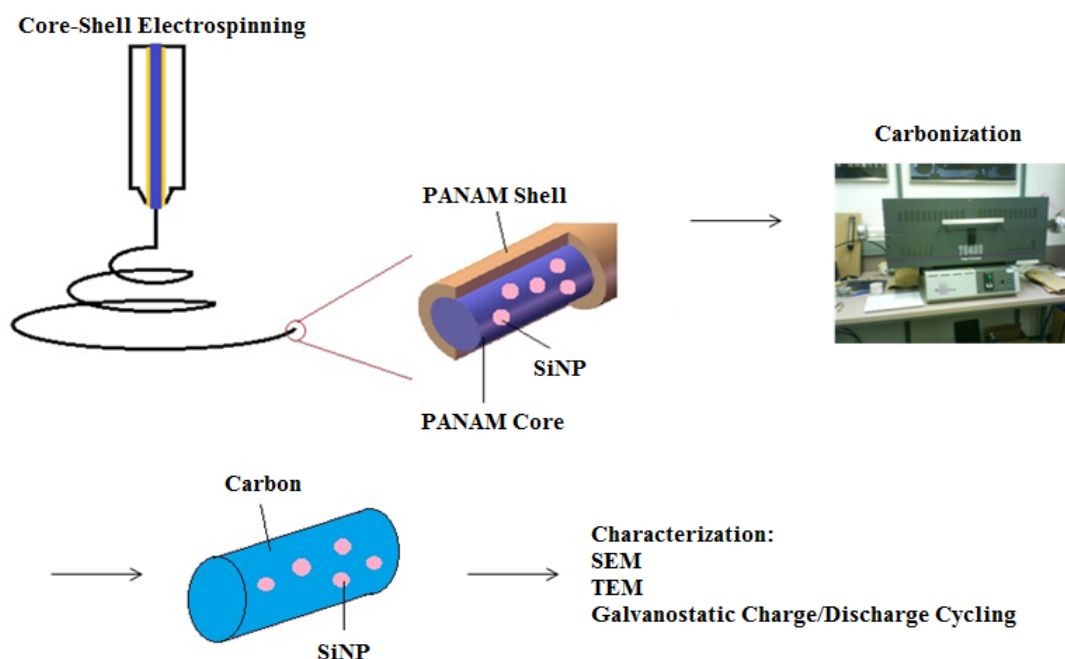


Fig. 4-8 Schematic representation of fabricating CNF/SiNP composite electrode through core-shell electrospinning.

4.3 Results and Discussions

4.3.1 Determination of Solution Properties Using PAN/SiNP Prior to Core-Shell

Electrospinning

The dispersion properties of both TX100 and PVP for SiNP in PAN nanofibres were analyzed by TEM and SEM, as shown in Fig. 4-9 and Fig. 4-10. In the TEM figures, it is apparent that SiNP were dispersed more homogeneously within the PAN nanofibre matrix using TX100, while that using PVP showed more extensive particle agglomeration on the surface of nanofibres. In the SEM figures, nanoparticle dispersion using TX100 showed a smoother fibre surface, while that using PVP showed uneven lumps resulted from nanoparticle agglomeration. Therefore, TX100 was chosen as the surfactant of dispersion for the consequent experiments. Surfactant characteristics, including the type

of surfactant (ionic vs. non-ionic), hydrophilicity, chain length of the non-polar groups, and the area of the head groups could affect the type of chemical for dispersion and the packing properties. TX100 and PVP are both non-ionic surfactants with a polar and a non-polar group. The major difference is that TX100 possess a very long oxyethylene block (typically 9 – 10 oxyethylene units), while PVP only possess an oxygen as the polar group. It was previously reported by Douglas *et al.* that longer oxyethylene groups creates greater steric stability and reduces the size of nanoparticles to a greater extent [161]. The steric effect of TX100 might be a major contribution for better SiNP dispersion.

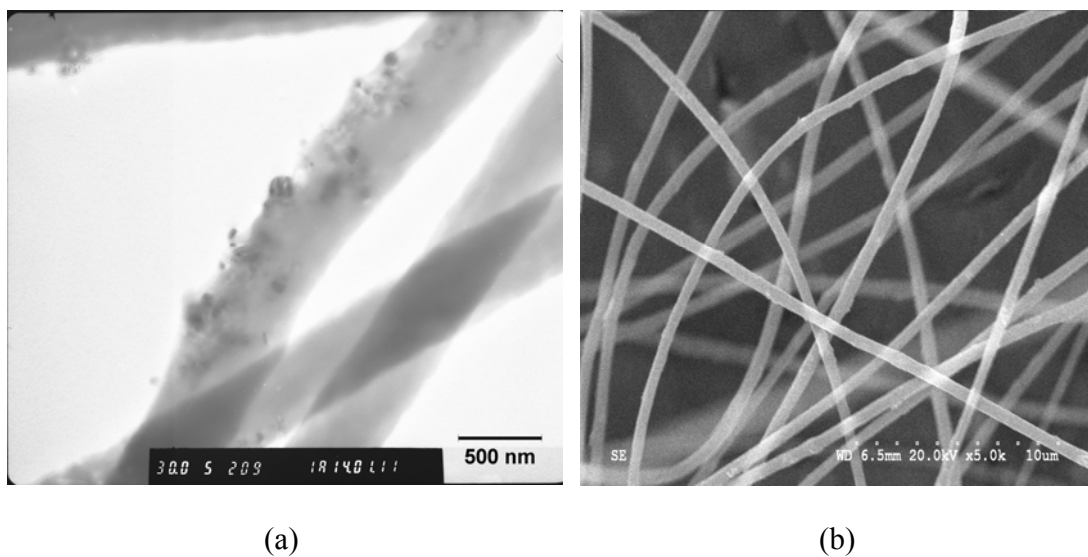


Fig. 4-9 TEM (a) and SEM (b) of PAN/SiNP using TX100 as the surfactant.

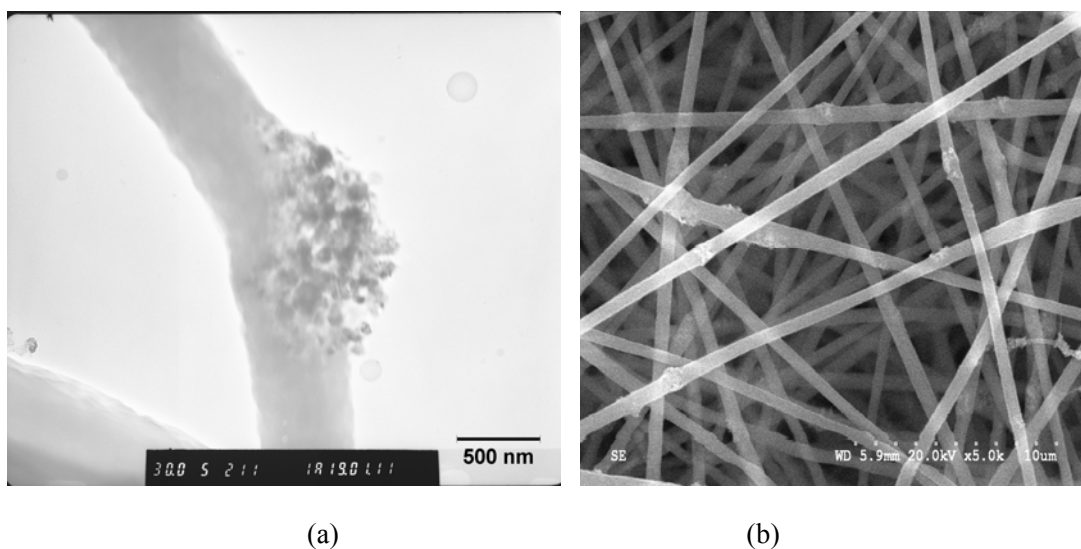


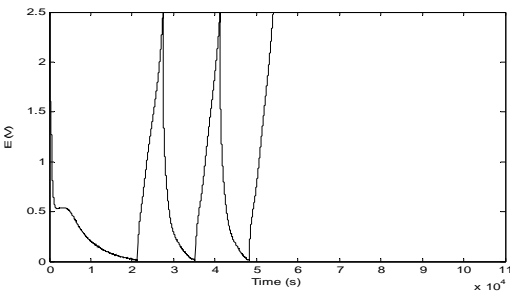
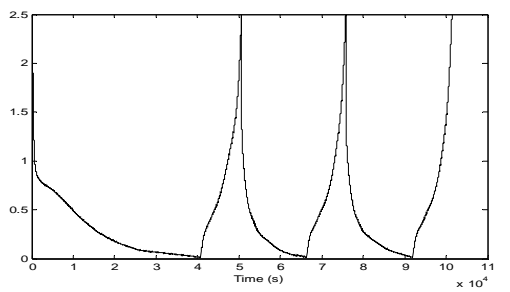
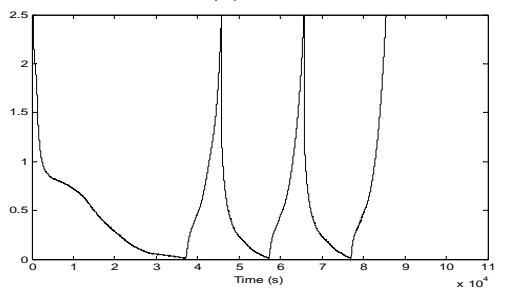
Fig. 4-10 TEM (a) and SEM (b) of PAN/SiNP using PVP as the surfactant.

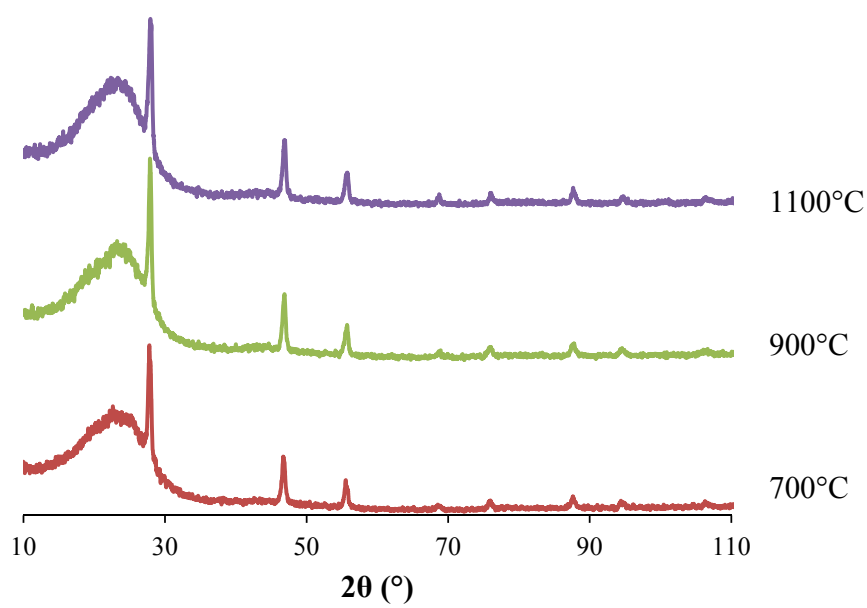
Approximately 2.5 mg of CNF/SiNP composite electrodes carbonized at 700, 900, and 1100°C were cycled galvanostatically at 113.6 mA/g and the capacity is summarized in Table 4-2. The capacity errors were estimated using error propagation method with uncertainties from electrode weight measurements. CNF/SiNP pyrolyzed at 700°C possesses the lowest capacity below 200 mAh/g. Highest capacity of over 300 mAh/g is obtained with CNF/SiNP pyrolyzed at 900°C. The conductivities for samples carbonized at 700, 900, and 1100°C are 1 ± 1 , 5 ± 2 , and 7 ± 1 S/cm. At such slow cycle rate, the conductivity effect is unlikely the main contribution for samples carbonized at 700°C to possess low capacitance. A slight capacity decrease was observed when the carbonization temperature increases from 900 to 1100°C. It is unlikely due to the generation of silicon carbide since the XRD result in Fig. 4-11 showed no presence of the strong SiC peak at 35.5 and 60° [162].

Fig. 4-11 (a) and (b) are the XRD comparison between CNF/SiNP composite and pure Si. The diffraction peaks of Si in CNF/SiNP is similar to that of pure SiNP, which are located at 28.40°, 47.26 °, 56.02 °, 68.94 °, 76.26 °, 87.84 °, 94.76 °, and 106.44 °, which correspond to (111), (220), (311), (400), (331), (422), (511), and (440) of Si crystal planes, respectively [163]. The broad peak at 20 – 30° is the carbon diffraction peak. Comparing to pure graphite, which exhibit a sharp peak at 26.6°, the peak broadening of the electrospun CNF implied the disordered carbon crystallite [13, 54].

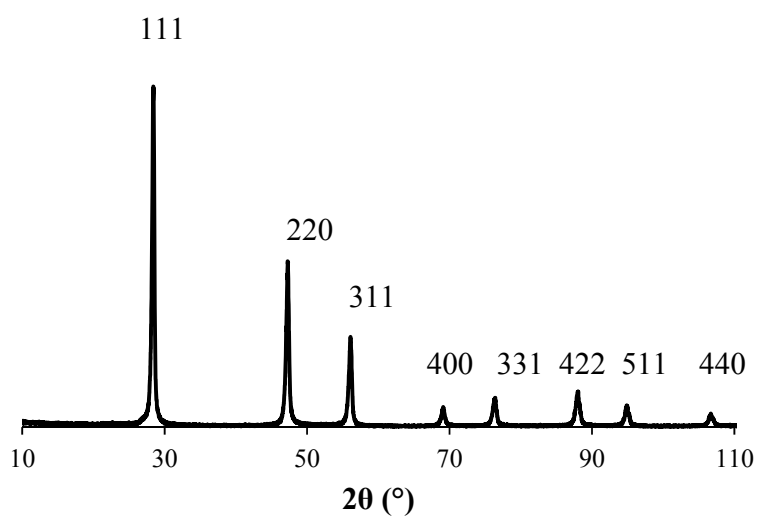
The slightly lowered capacitance for CNF/SiNP carbonized at 1100°C is likely a result of higher amount oxygen in the sample, as shown in Table 4-3, a summary of carbon, oxygen, and silicon concentration in the CNF/Si NP sample. Carbonization at 1100°C seemed to cause a greater extent of carbon degradation, which resulted in relatively higher amount of oxygen concentration. On the other hand, at carbonization temperature of 700°C, a large amount of nitrogen remained in the final product, which contributed to impurities lowering the cycling performance [164].

Table 4-2 Discharge capacity summary of CNF/SiNP carbonized at 700 (a), 900 (b), and 1100°C (c).

<p>(a) 700°C</p> 	Discharge Cycle	CNF Weight (mg)	Capacity (mAh/g)
	1	2.79±0.01	188±1
	2	2.79±0.01	183±1
	3	2.79±0.01	178±1
<p>(b) 900°C</p> 	Discharge Cycle	CNF wt (mg)	Capacity (mAh/g)
	1	2.64±0.01	348±1
	2	2.64±0.01	362±1
	3	2.64±0.01	365±1
<p>(c) 1100°C</p> 	Discharge Cycle	CNF wt (mg)	Capacity (mAh/g)
	1	2.20±0.01	264±1
	2	2.20±0.01	261±1
	3	2.20±0.01	264±1



(a)



(b)

Fig. 4-11 XRD of CNF/SiNP carbonized at 700, 900, and 1100°C (a) and pure SiNP (b).

Table 4-3 Atomic concentrations of CNF/SiNP carboized at 700, 900, and 1100°C.

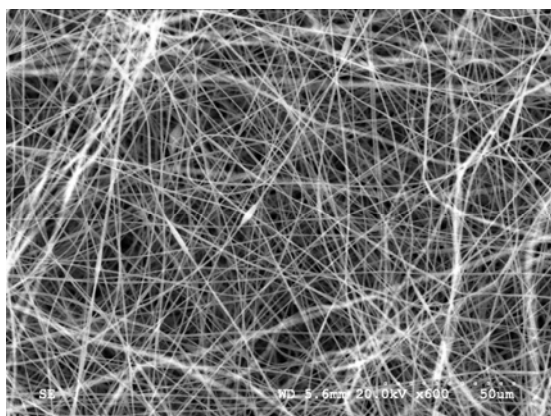
Carbonization Temperature (°C)	Atomic Concentration (wt%)			
	Carbon	Oxygen	Nitrogen	Silicon
700	66±1	6±1	21±1	7±1
900	83±1	8±1	-	9±1
1100	78±2	12±1	-	9±1

4.3.2 Core-Shell Electrospinning

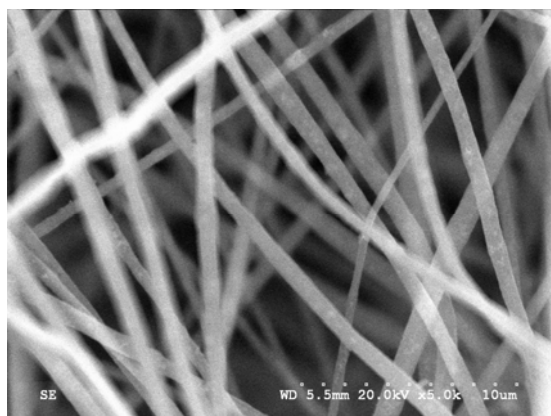
4.3.2.1 Characterization of PANAM/SiNP Nanofibres

Fig. 4-12 and Fig. 4-13 are the SEM and TEM figures of PANAM/SiNP nanofibres electrospun from core solutions with different weight concentrations of SiNP. The amount of SiNP was gradually increased in each spinning to optimize the amount of SiNP incorporation without deteriorating the fibre morphology. Nanofibres electrospun from 15, 30, 50, and 80 wt% of SiNP in core solutions possess average diameters of $6.5 \pm 2.1 \times 10^2$, $9.7 \pm 1.5 \times 10^2$, $9.7 \pm 1.5 \times 10^2$, and $13.2 \pm 2.1 \times 10^2$ nm, respectively. The fibres have even diameters with very few beads, which implies the high stability of spinning dope even at high concentrations of SiNP. The increased fibre diameter is a result of increasing SiNP concentration but not the solution viscosity. Fig. 4-14 is a summary of solution viscosity at different PANAM and SiNP concentration. The solution viscosity in general increases with increasing polymer concentration due to the increased polymer chain entanglement. However, with the addition of SiNP concentrations, the measured solution viscosity was mostly lower than that of the pure polymer solution. This could be explained by the non-Einstein-like phenomenon discovered in recent years. Einstein stated that the volume fraction of particles suspended in liquid is proportional to the solution viscosity [165]. Suspension of particles in polymer solution shows a similar

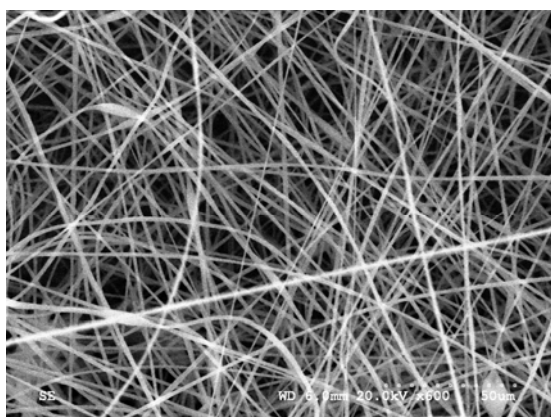
trend [166]. However, viscosity reduction was observed by Hawker *et al.* when small polystyrene (PS) nanoparticles were suspended in PS melt with high molecular weight, which entangle and confine nanoparticles [166, 167]. This effect holds even with nanoparticle volume fraction as high as 50%. This was explained by increased free volume (inversely proportional to the particle radius) and significant change in the entanglement structure of PS with the incorporation of nanoparticles. At larger particle size or nanoparticle agglomeration, the viscosity of polymer melt increases. Same analogy could be applied to the viscosity behavior in this study. The lower solution viscosity at most SiNP concentrations indicates a good dispersion of SiNP. At 80 wt% SiNP concentration, slight nanoparticle agglomeration might occur, which resulted in slightly higher solution viscosity comparing to that of the pure PANAM solution. Core-shell spinning is most stable at 8.5 wt% PANAM concentration for both core and shell solutions due to the closer viscosity for both solutions and the ease of high-concentration nanoparticle dispersion. The 8 wt% PANAM solution concentration was too low to form a stable spinning jet. The size of SiNP could be estimated from TEM images in Fig. 4-13. They were mostly distributed homogeneously within the polymer matrix with an average particle diameter of 50 – 70 nm.



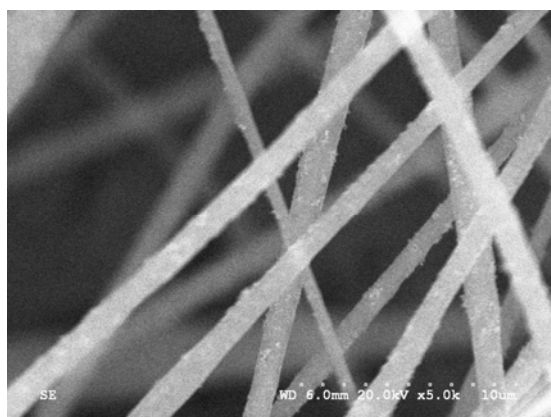
(a)



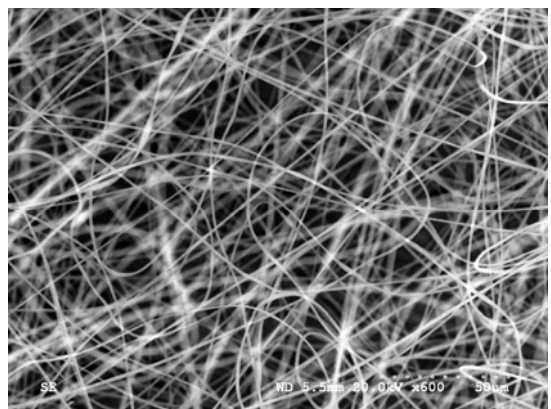
(b)



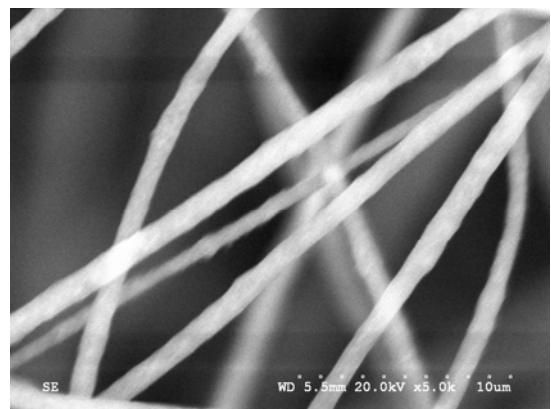
(c)



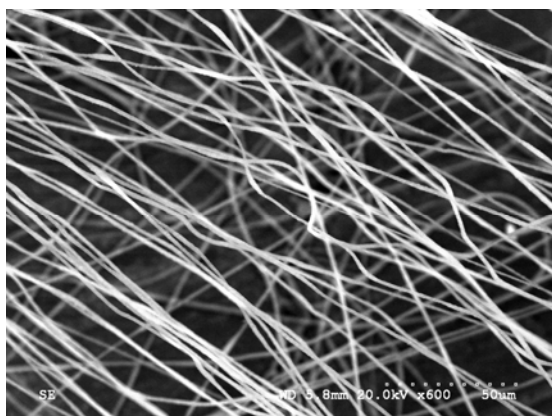
(d)



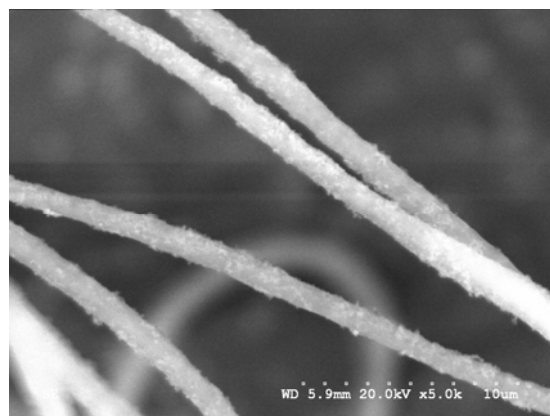
(e)



(f)

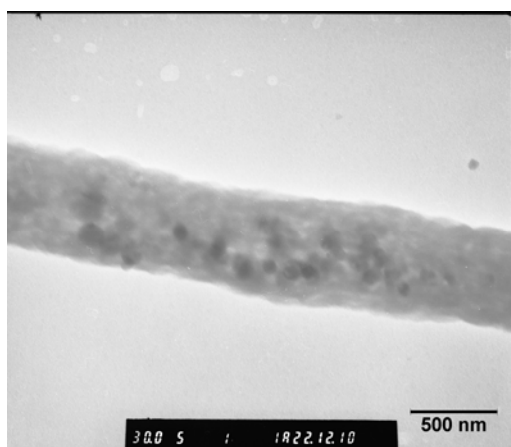


(g)

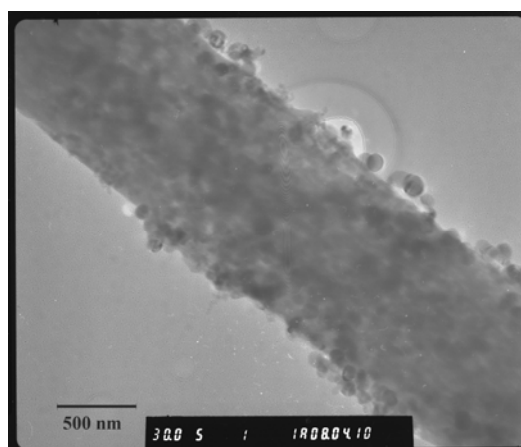


(h)

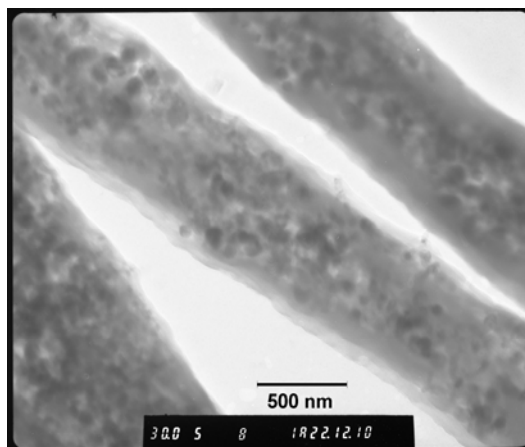
Fig. 4-12 SEM of core-shell PANAM/Si-15 at $\times 600$ (a) and $\times 5k$ (b) magnification, PANAM/Si-30 at $\times 600$ (c) and $\times 5k$ (d) magnification, PANAM/SiNP-50 at $\times 600$ (e) and $\times 5k$ (f) magnification, and PANAM/SiNP-80 at $\times 600$ (g) and $\times 5k$ (h) magnification.



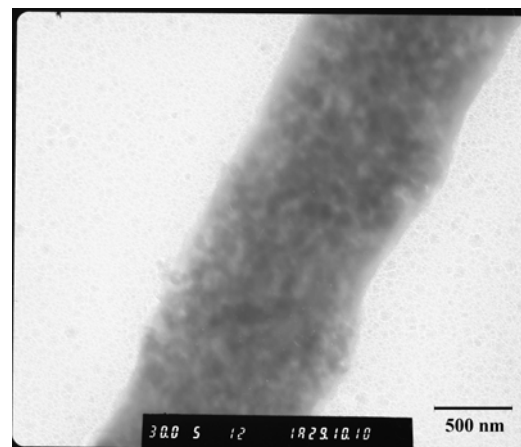
(a)



(b)



(c)



(d)

Fig. 4-13 TEM of core-shell PANAM/SiNP-15 (a), PANAM/SiNP-30 (b), PANAM/SiNP-50 (c), and PANAM/SiNP-80 (d) at $\times 30k$ magnification.

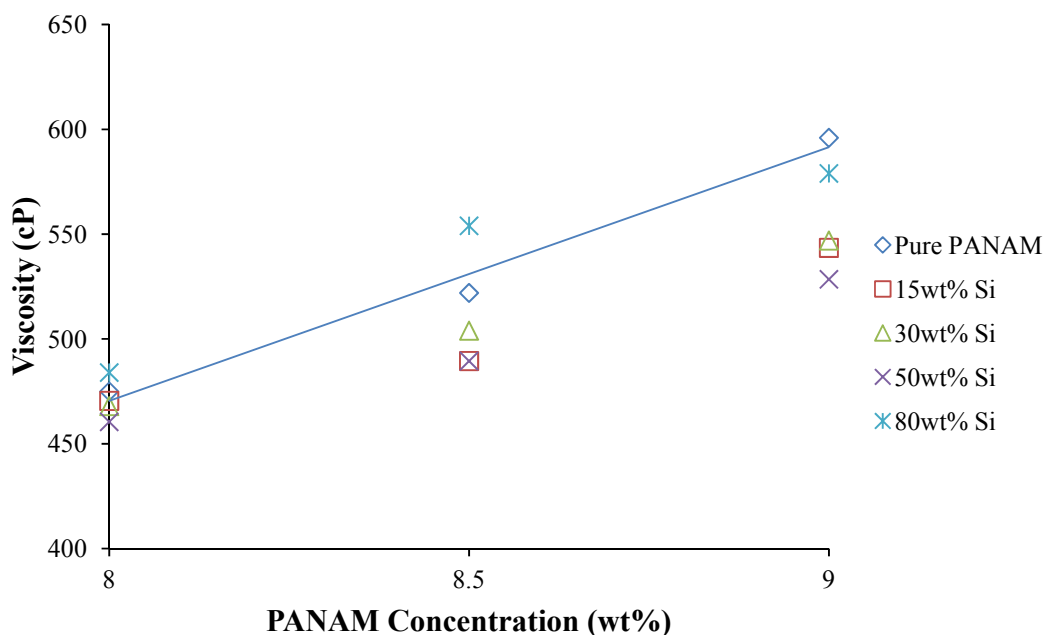
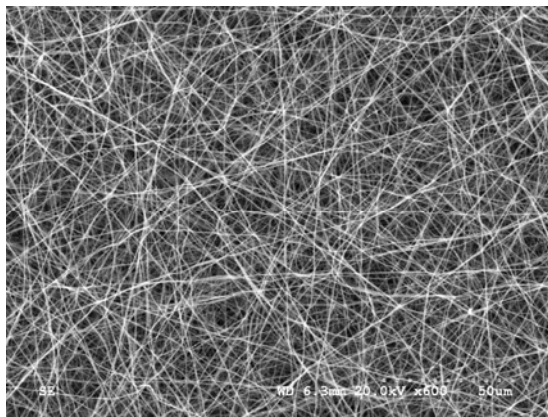


Fig. 4-14 Viscosity measurement of pure PANAM and PANAM/SiNP solutions with various SiNP concentrations.

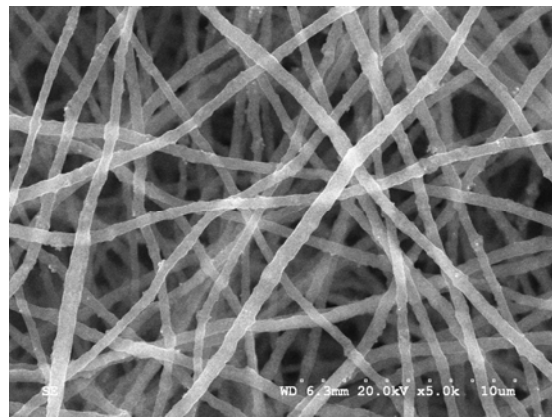
4.3.2.2 Characterization of Core-Shell CNF/SiNP Nanofibres

The morphology of carbonized PANAM/SiNP nanofibres were shown in SEM and TEM of Fig. 4-15 and Fig. 4-16. The average fibre diameters for CNF/Si-15, CNF/Si-30, CNF/Si-50, and CNF/Si-80 are $5.2 \pm 1.0 \times 10^2$, $7.3 \pm 1.3 \times 10^2$, $6.4 \pm 1.0 \times 10^2$, and $8.1 \pm 1.5 \times 10^2$ nm, respectively. The brighter spots on the fibre surface in Fig. 4-15 are the presence of SiNP. It is shown that less amount of SiNP are presented on the fibre surface with CNF/Si-15, CNF/Si-50, and CNF/Si-80; however, with CNF/Si-30, more SiNP were exposed to the surface. This is a result of greater extent of solution mixing during electrospinning. Most fibre mats remained intact after carbonization, indicating the presence of Si did not exert too much stress during fibre shrinkage to break the fibre. Fig. 4-16 is the TEM image showing SiNP inside the CNF. SiNP are homogeneously

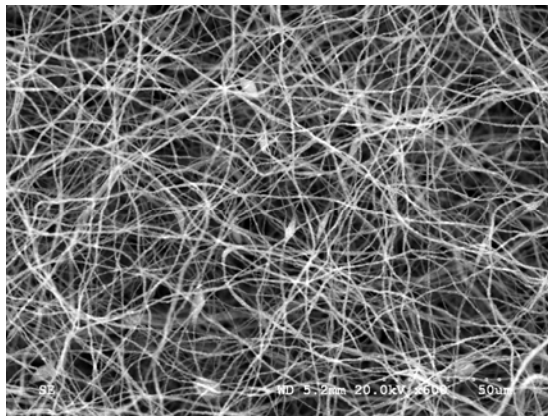
distributed within CNF, with a layer of CNF, estimated 50 nm, covering the outer boundary of SiNP as indicated by the arrows. Because most SiNP are located within the CNF, it is difficult to observe the boundary between individual nanoparticle. The estimated average size for SiNP is 100 nm in diameter. A significant increase in nanoparticle density was observed as the concentration of SiNP increased in the spinning dope.



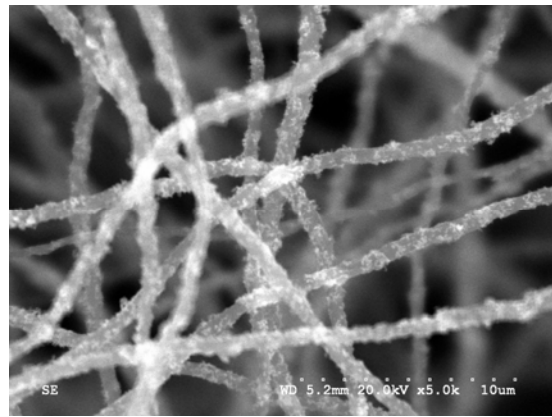
(a)



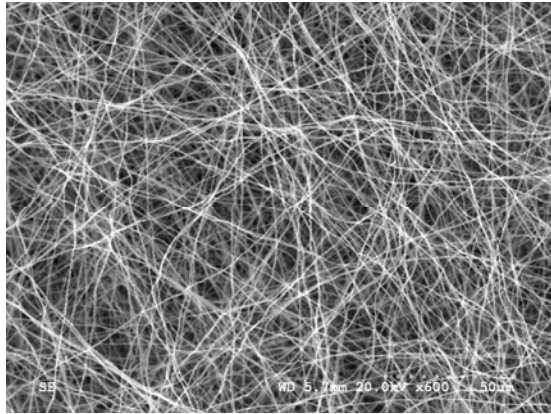
(b)



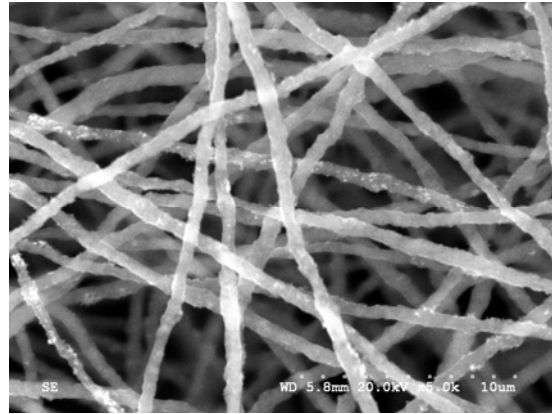
(c)



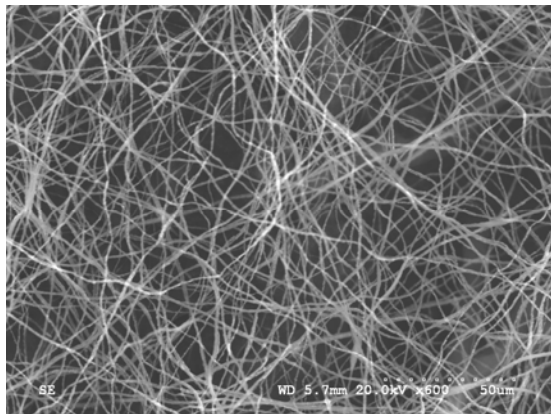
(d)



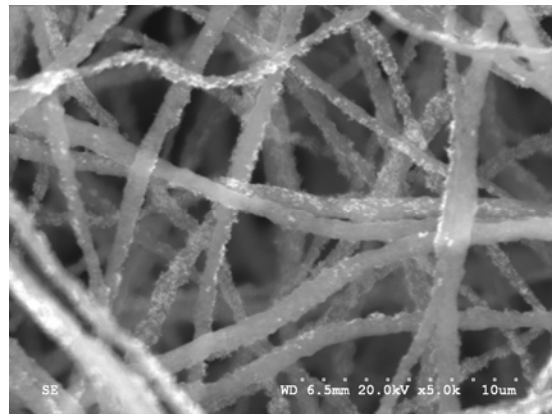
(e)



(f)



(g)



(h)

Fig. 4-15 SEM of core-shell CNF/Si-15 at $\times 600$ (a) and $\times 5k$ (b) magnification, CNF/Si-30 at $\times 600$ (c) and $\times 5k$ (d) magnification, CNF/Si-50 at $\times 600$ (e) and $\times 5k$ (f) magnification, and CNF/Si-80 at $\times 600$ (g) and $\times 5k$ (h) magnification.

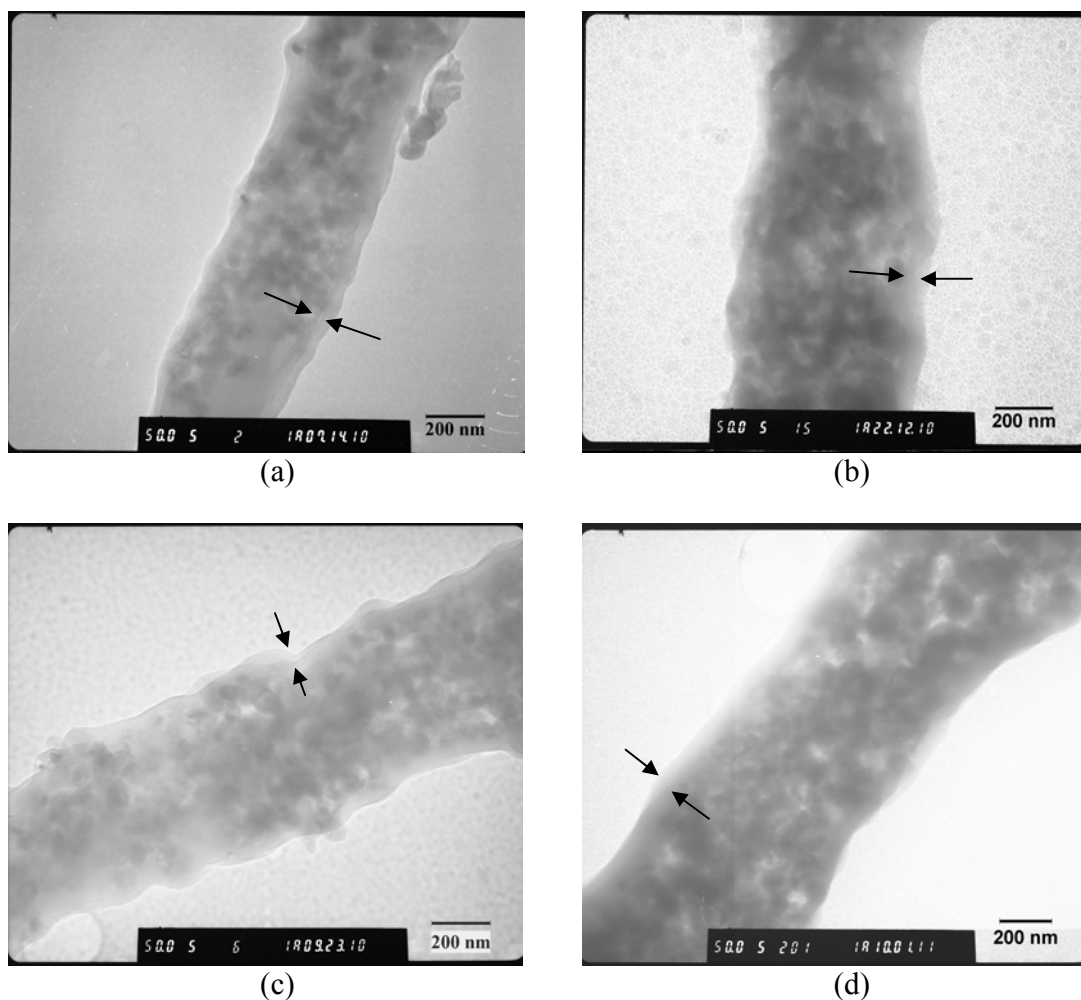


Fig. 4-16 TEM of core-shell CNF/Si-15 (a), CNF/Si-30 (b), CNF/Si-50 (c), and CNF/Si-80 (d) at $\times 50k$ magnification.

4.3.2.3 EDX and XRD Characterization of Core-Shell CNF/SiNP Nanofibres

The concentration of Si, carbon, and oxygen in the final CNF/SiNP composite was characterized by EDX and the result is summarized in Table 4-4. The gradual increase of SiNP concentration in CNF is also shown with the increased Si peak height in the XRD spectrum of Fig. 4-17. Similar to previous XRD result, the broadening of graphite peak at $20 - 30^\circ$ indicates disordered CNF generated from electrospinning. According to Table 4-4, the resulting concentration of Si in CNF is lower than that in the original core

solution. This is mainly due to the addition of shell material. The relationship between the original concentration of SiNP in the core solution and the final concentration of SiNP in CNF is plotted in Fig. 4-18. It is a non-linear relationship with smaller increase of SiNP in CNF at higher Si concentration. The limitation in the concentration of SiNP in CNF is governed by the addition of shell material, and that the flow rate of shell solution is always at least 0.2 ml/hr higher than that of the core solution. In some carbonized samples, the oxygen concentration was fairly low (approximately 10 wt%), which means that the high oxygen concentration could be reduced with a purer supply of nitrogen during carbonization or better furnace seal.

Table 4-4. Atomic concentrations of core-shell CNF/SiNP.

Core-Shell Sample	CNF/Si-15	CNF/Si-30	CNF/Si-50	CNF/Si-80
SiNP (wt%)	11±2	18±3	27±5	32±2
Carbon (wt%)	76±5	65±5	53±8	48±6
Oxygen (wt%)	13±3	18±5	19±4	19±4

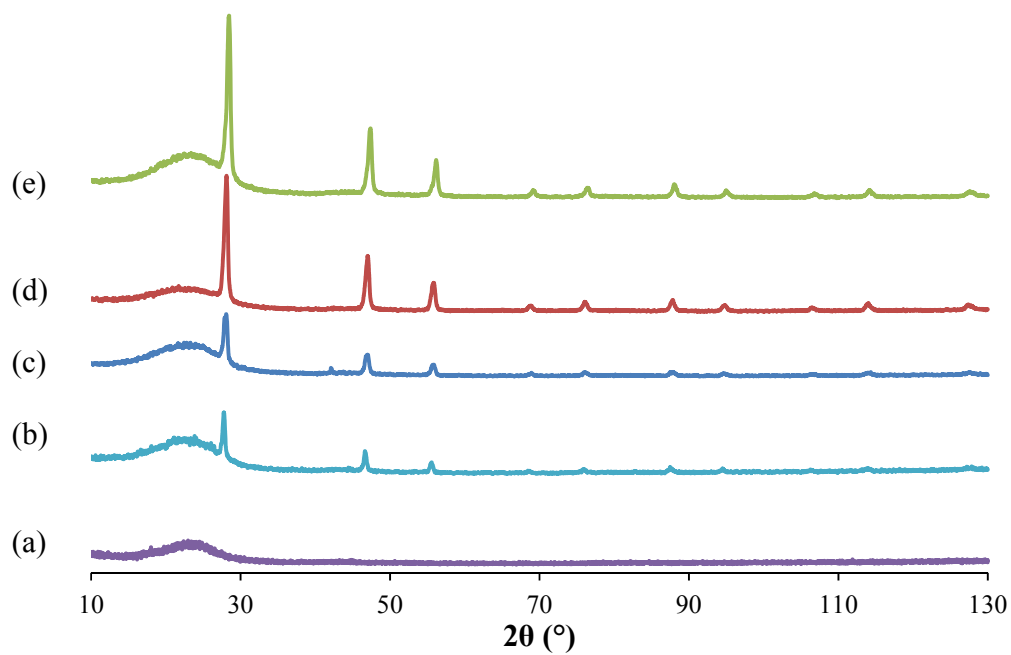


Fig. 4-17 XRD of pure carbon (a), core-shell CNF/Si-15 (b), CNF/Si-30 (c), CNF/Si-50 (d), and CNF/Si-80 (e).

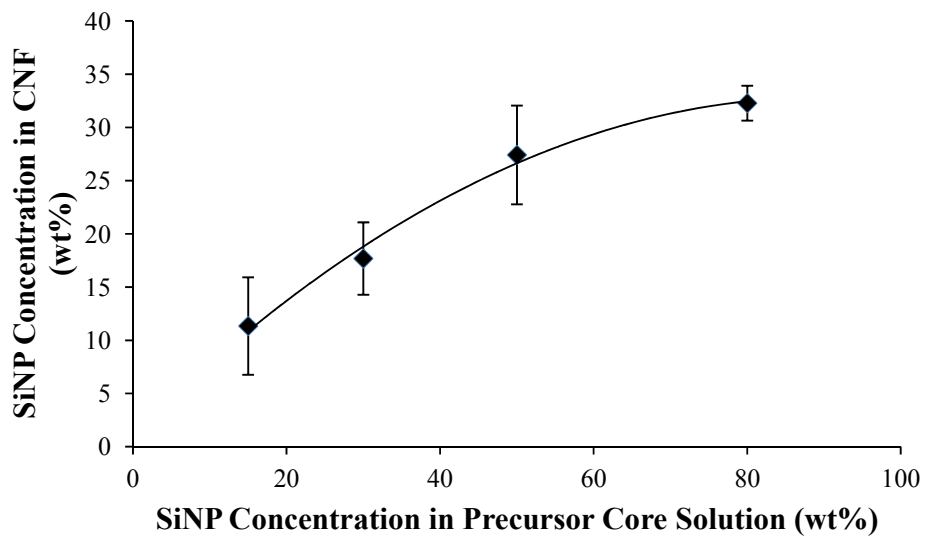


Fig. 4-18 Plot of SiNP concentration in CNF vs. SiNP concentration in the core solution during core-shell electrospinning.

4.3.2.4 Raman Spectroscopy and Electrical Conductivity of Core-Shell CNF/SiNP

Nanofibres

The carbon structure of CNF/SiNP was investigated through Raman and the result is summarized in Fig. 4-19 and Table 4-5. The I_D/I_G ratios of CNF composited with SiNP are between 1.50 – 1.70, which are slightly lower than that of pure CNF carbonized at 900°C (1.89 ± 0.09). The I_D/I_G ratio first experienced a more significant decrease with CNF/Si-15 sample, followed by a smaller decrease with CNF/Si-30 and CNF/Si-50, and finally a slight increase with CNF/Si-80. The decrease in I_D/I_G ratio indicates an improved graphitic structure of CNF. This phenomenon was known to be catalytic graphitization. With the addition of various metal or inorganic elements, alloys, or compounds to the carbon precursor, the crystallinity of carbon can be improved through chemical reactions of non-graphitized carbon with catalytic materials at low temperature ($< 1000^\circ\text{C}$) [168, 169]. Such catalysts often have an atomic number less than 40 and the first ionic potential between 6 and 8 eV [170]. Silicon fits in this criteria and has been proven to graphitize carbon at high temperature ($> 2000^\circ\text{C}$) [170, 171]. The working mechanism of silicon at high temperature ($> 2000^\circ\text{C}$) was known by the diffusion of carbon into silicon or the evaporation followed by reprecipitation of silicon on carbon to produce SiC [168]. For temperatures as low as 900°C, the graphitization effect was not observed previously through XRD and microscopy [170]. The catalyst size effect has also been investigated. If the small sized catalysts (e.g. 20 nm nickel particle) are homogeneously distributed within a non-graphitizable carbon precursor, a turbostratic carbon is formed [168]. Moreover, sp^3 carbons are more readily graphitized than sp^2 carbon [171]. In this study, it is observed that SiNP can help produce more ordered

carbon structure from the sp^3 carbon backbone of PANAM precursor at temperature as low as 900°C, as shown with the decreased I_D/I_G ratio. Because the change in structure is so small, there is no observable changes in the broad carbon peak of XRD.

Although the addition of nanoparticles enhances graphitization, the addition of too many nanoparticles was observed to disrupt the carbon structure, as the CNF film became more difficult to handle. For the CNF/Si-80 sample, I_D/I_G ratio increased to 1.64 ± 0.04 . The amount of ordered carbon structure was reduced as compared to CNF with lower SiNP concentration. Nanoparticles were helpful in local graphitization but were not beneficial to the electrical conductivity of CNF, as shown in Table 4-6. The conductivity of most CNF/SiNP composite is measured below 2 S/cm. The conductivity did not vary too much between samples with different SiNP concentrations but were ten times lower than that of pure CNF. The reduced conductivity of CNF/SiNP could be explained by several reasons. Since SiNP is non-conductive at neutral state, inclusion of non-conductive material reduces the total amount of fibre per volume for electronic conduction, given that the volume density of the CNF/SiNP was similar to that of pure CNF. Moreover, the fragile CNF/SiNP sample implies the disruption by SiNP of the overall carbon structure. Defects are likely to be generated to reduce the CNF conductivity.

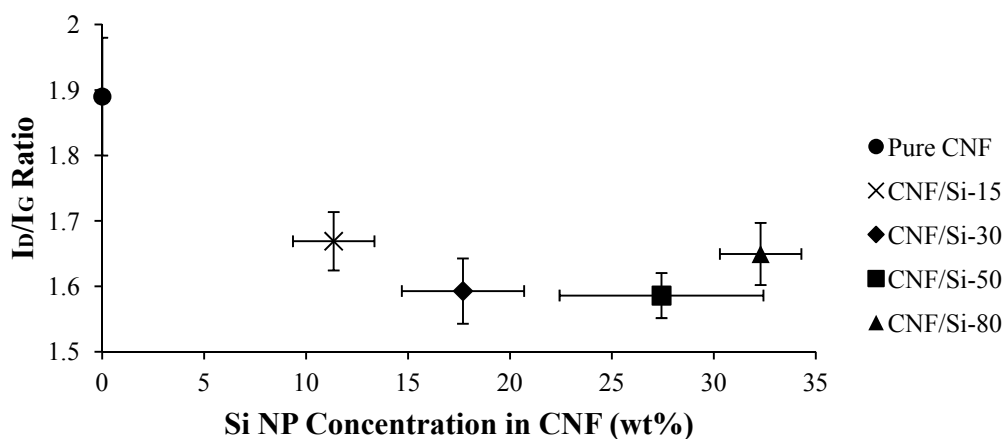


Fig. 4-19 Raman I_D/I_G ratios for core-shell CNF/SiNP samples with different SiNP concentration in the final CNF product.

Table 4-5 Raman peak positions and I_D/I_G ratio summary of pure carbon and core-shell carbon samples.

Sample Type	Peak D position (cm^{-1})	Peak G position (cm^{-1})	I_D/I_G	Average I_D/I_G
Pure CNF (carbonize at 900°C)	1320.92	1599.11	2.02	1.89 ± 0.09
	1316.54	1579.14	1.83	
	1318.73	1581.87	1.84	
	1323.11	1579.68	1.86	
CNF/Si-15	1315.18	1581.87	1.72	1.67 ± 0.04
	1320.92	1581.33	1.61	
	1315.18	1582.69	1.66	
	1315.18	1579.68	1.68	
CNF/Si-30	1315.18	1581.87	1.55	1.59 ± 0.04
	1315.72	1580.51	1.66	
	1315.18	1581.87	1.56	
	1317.36	1581.33	1.60	
CNF/Si-50	1320.92	1584.06	1.55	1.58 ± 0.03
	1312.99	1581.87	1.62	
	1315.72	1580.51	1.57	
	1317.91	1584.88	1.61	
CNF/Si-80	1317.91	1584.88	1.71	1.64 ± 0.04
	1315.18	1581.33	1.64	
	1317.91	1582.69	1.59	
	1315.18	1579.14	1.65	

Table 4-6 Polymer precursor weight loss, conductivity, and volume density of core-shell CNF/SiNP.

Core-Shell Carbon Sample	Polymer Weight Loss After Carbonization (wt%)	Volume Density (mg/cm ³)	Conductivity (S/cm)	Average Conductivity (S/cm)
CNF/Si-15	$1.5 \pm 0.2 \times 10^1$	120 \pm 10	1.7 \pm 0.2	2.7 \pm 1.3
	$0.4 \pm 0.1 \times 10^1$	130 \pm 10	3.6 \pm 0.4	
CNF/Si-30	$1.0 \pm 0.1 \times 10^1$	140 \pm 20	1.5 \pm 0.2	1.4 \pm 0.1
	$2.5 \pm 0.4 \times 10^1$	170 \pm 30	1.3 \pm 0.2	
CNF/Si-50	$2.3 \pm 0.3 \times 10^1$	120 \pm 10	1.7 \pm 0.2	1.7 \pm 0.1
	$3.1 \pm 0.4 \times 10^1$	140 \pm 20	1.7 \pm 0.2	
CNF/Si-80	$3.3 \pm 0.3 \times 10^1$	160 \pm 20	0.7 \pm 0.1	1.0 \pm 0.4
	$2.8 \pm 0.3 \times 10^1$	140 \pm 10	1.3 \pm 0.2	

4.3.2.5 Characterizations of Non-Core-Shell PANAM/Si and Its Pyrolyzed n-CNF/Si

In the mean time, n-PANAM/Si with 30wt% SiNP was electrospun and carbonized to compare its cycling properties with that of core-shell samples. Fig. 4-20(a) – (b) are the SEM of n-PANAM/Si and the average fibre diameter was $6.8 \pm 1.2 \times 10^2$ nm. Fig. 4-20(c) is the TEM of n-PANAM/Si. It is shown that nanoparticles were dispersed homogeneously along the fibre with the particle diameters ranging from 50 – 100 nm. Fig. 4-21(a) – (b) are the SEM of n-CNF/Si. The average fibre diameter calculated was $4.9 \pm 1.3 \times 10^2$ nm. Fig. 4-21(c) is the TEM of the non-core-shell carbon fibre. After the fibre shrinkage, most nanoparticles were agglomerated on the fibre surface. In general, the carbon fibre properties from non-core-shell sample was similar to that from core-shell ones. The electrical conductivity of the non-core-shell carbon fibre was 2 ± 1 S/cm and its Raman I_D/I_G ratio was 1.8 ± 0.8 . The atomic concentration of the carbon fibre consisted as follows: carbon = 56 ± 6 wt%, oxygen = 16 ± 5 wt%, and silicon = 28 ± 1 wt%. Since the

major difference between both fibres were the core-shell and the non-core-shell carbon structure, it is reasonable to compare the cycling properties of both materials.

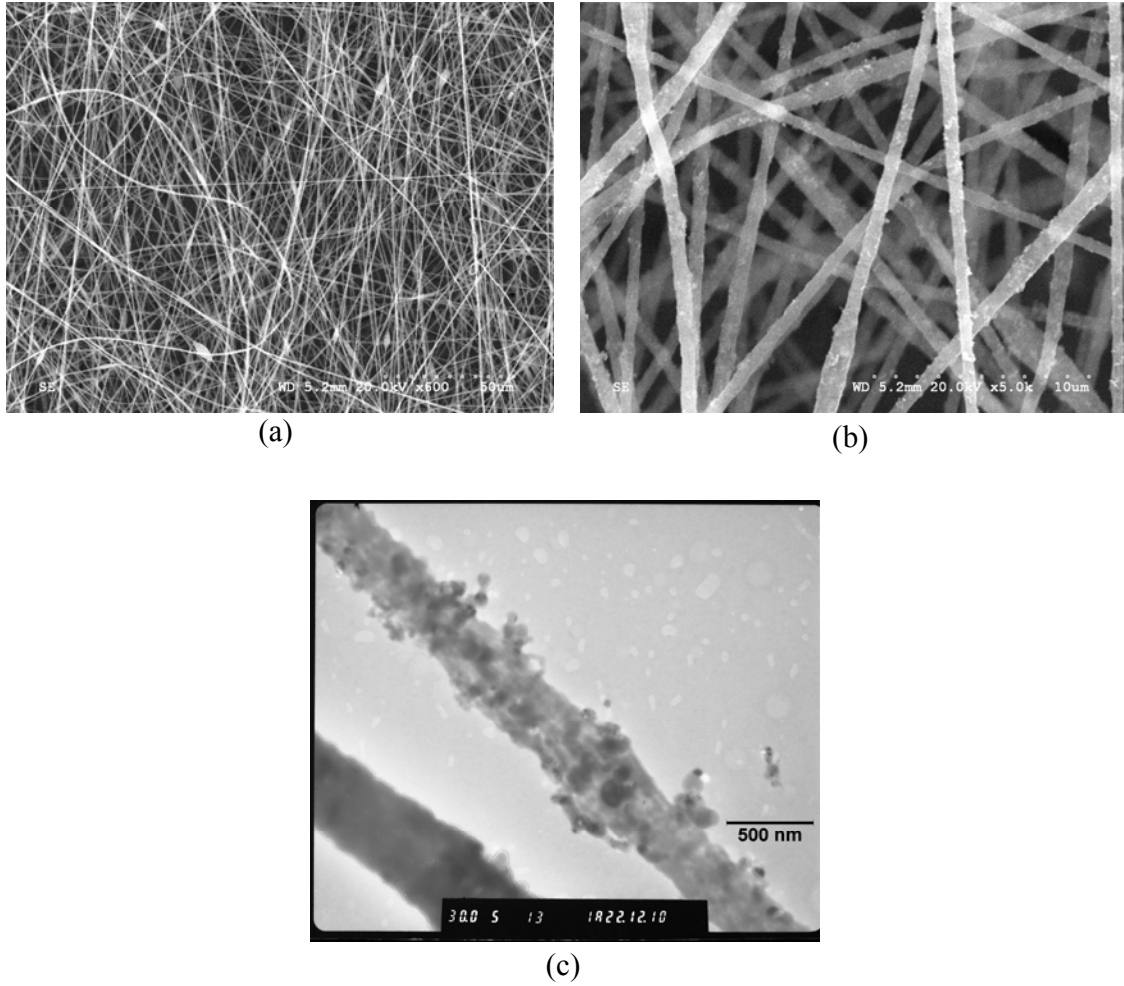


Fig. 4-20 SEM of n-PANAM/Si at $\times 600$ (a) and $\times 5k$ magnification (b), and TEM of n-PANAM/Si at $\times 30k$ magnification (c).

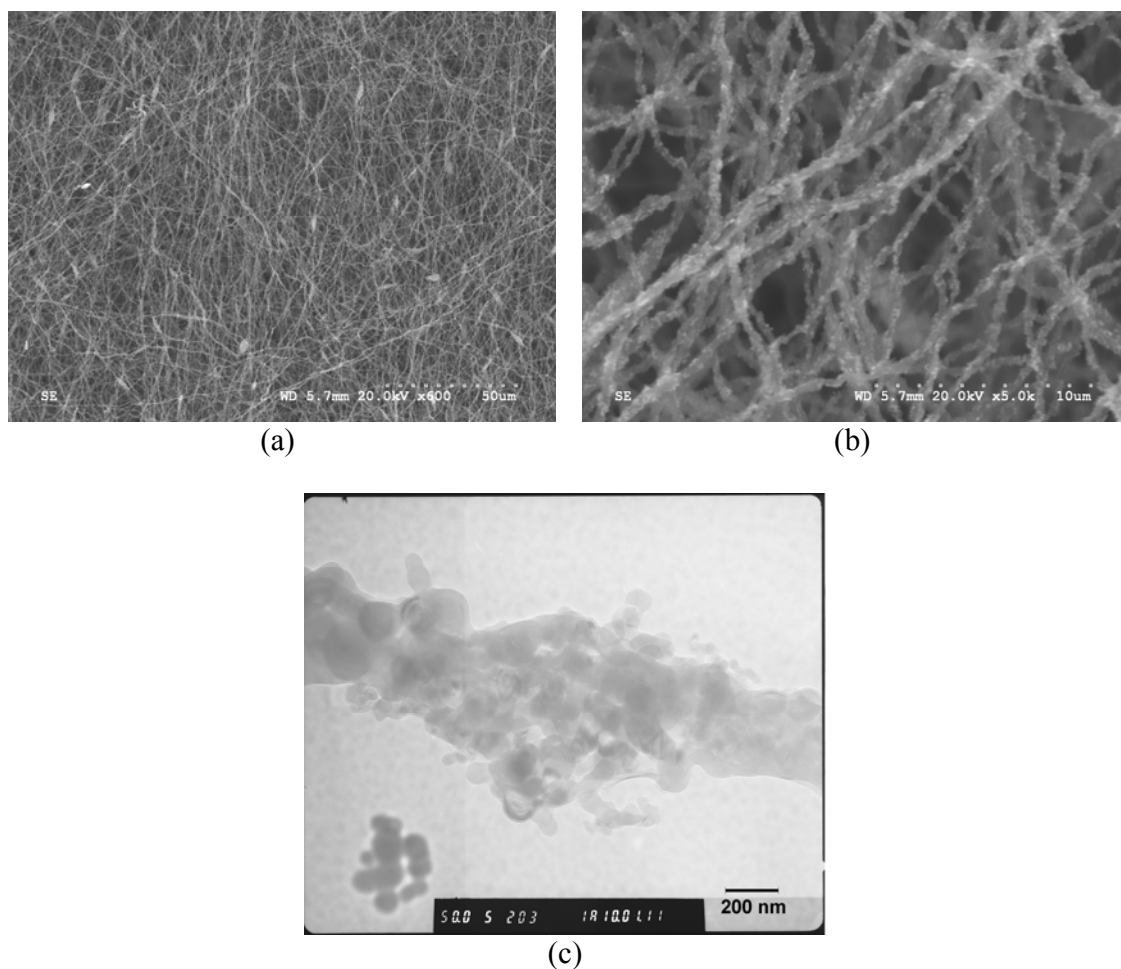


Fig. 4-21 SEM of n-CNF/Si at $\times 600$ (a) and $\times 5k$ magnification (b), and TEM of n-CNF/Si at $\times 50k$ magnification (c).

4.3.2.6 Tensile Test Comparison Between CNF/Si-80 and n-CNF/Si

Tensile test was conducted on both CNF/Si-80 and n-CNF/Si to verify the difference in mechanical properties of CNF with different methods of nanoparticle loading. The stress strain curves of CNF/Si-80 and n-CNF/Si are shown in Fig. 4-22 and Fig. 4-23, respectively. Young's modulus, ultimate tensile strength, and elongation to failure of both CNF/Si-80 and n-CNF/Si were calculated from the average of seven tensile tests. Young's moduli of CNF/Si-80 and n-CNF/Si were 0.21 ± 0.06 and 0.52 ± 0.07 MPa,

respectively. Ultimate tensile strengths of CNF/Si-80 and n-CNF/Si were 0.25 ± 0.02 and 0.41 ± 0.06 MPa, respectively. Elongation to failure of CNF/Si-80 and n-CNF/Si were 1.3 ± 0.2 and 0.8 ± 0.1 %, respectively.

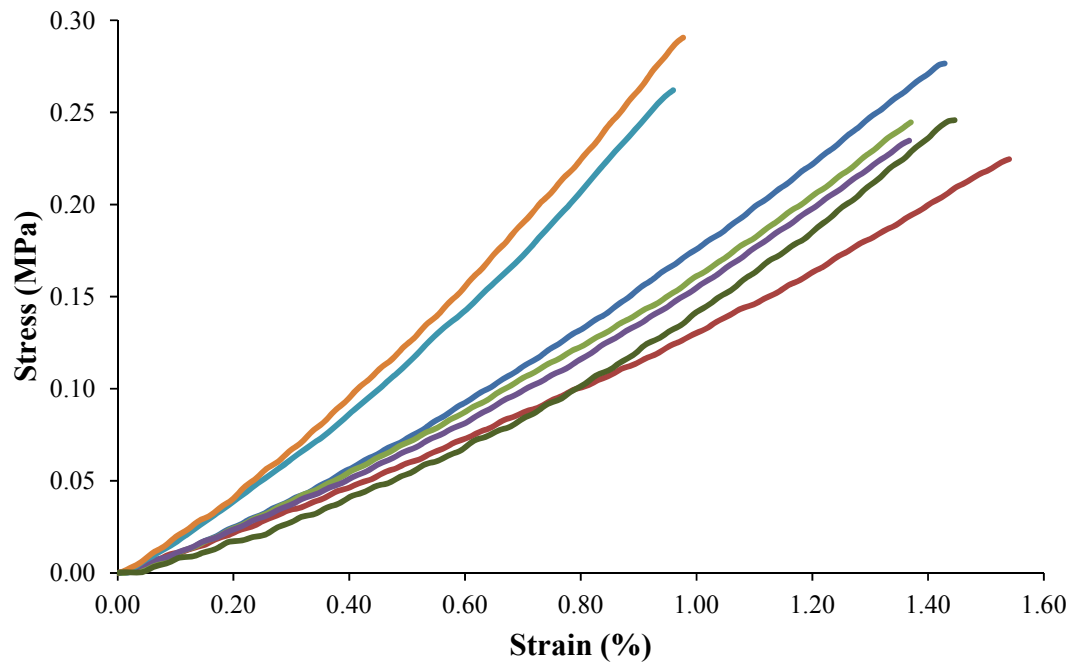


Fig. 4-22 Stress-strain curves of CNF/Si-80.

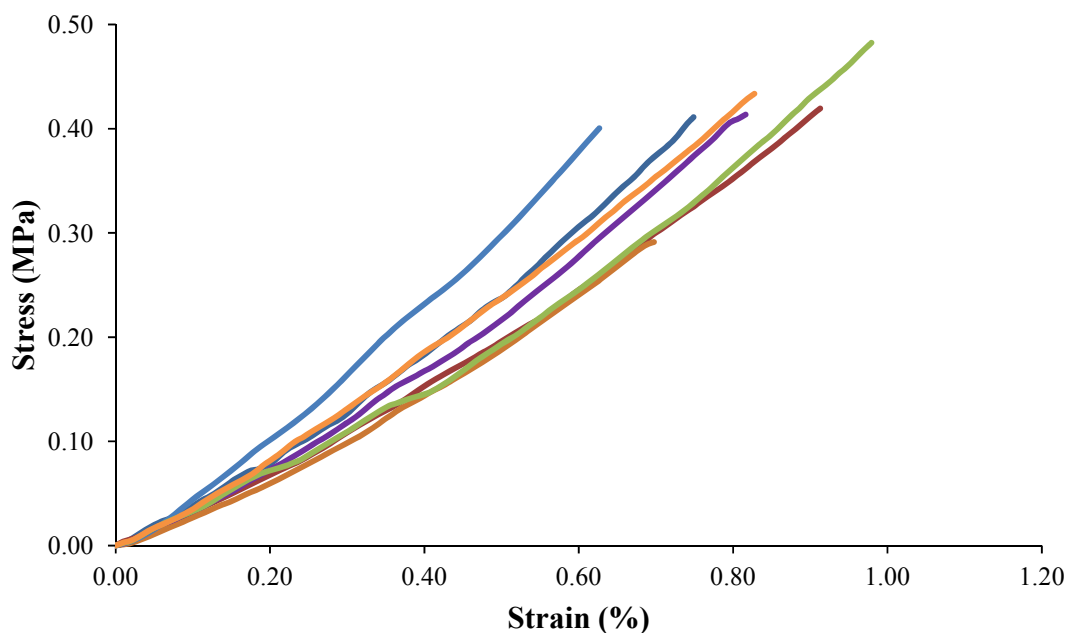


Fig. 4-23 Stress-strain curves of n-CNF/Si.

The average stress-strain curves of the seven samples from n-CNF/Si and five closer samples from CNF/Si-80 (excluding the orange and light blue stress-strain curve samples) were plotted in Fig. 4-24 to directly compare their mechanical properties. The average curves were plotted using the average stress from the selected samples at the same strain value, and the standard deviations of the average stresses were calculated. The point of the highest stress and strain value for both CNF/Si-80 and n-CNF/Si in Fig. 4-24 were calculated by averaging the maximum stresses at the maximum strains of sample curves. Agreeing with values reported earlier, n-CNF/Si is stiffer than CNF/Si-80 with limited amount of fibre elongation. The tensile strength of CNF/Si-80 was reduced but the fibres become softer and more ductile (almost 2× elongation than n-CNF/Si). The improved ductility of CNF is beneficial to retain the fibre morphology and accommodate the constant swelling and shrinkage of SiNP. In contrast, the stiffer CNF of n-CNF/Si is

more susceptible to fibre breakage due to its brittleness and resistive nature to deformation.

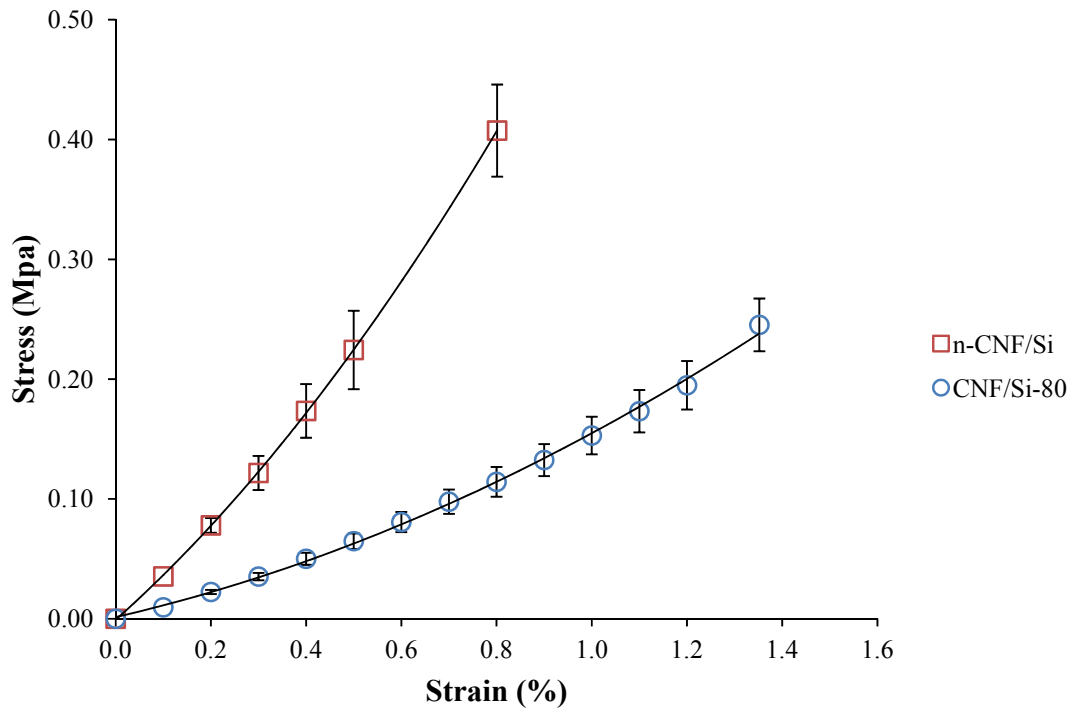


Fig. 4-24 Average stress-strain of CNF/Si-80 and n-CNF/Si.

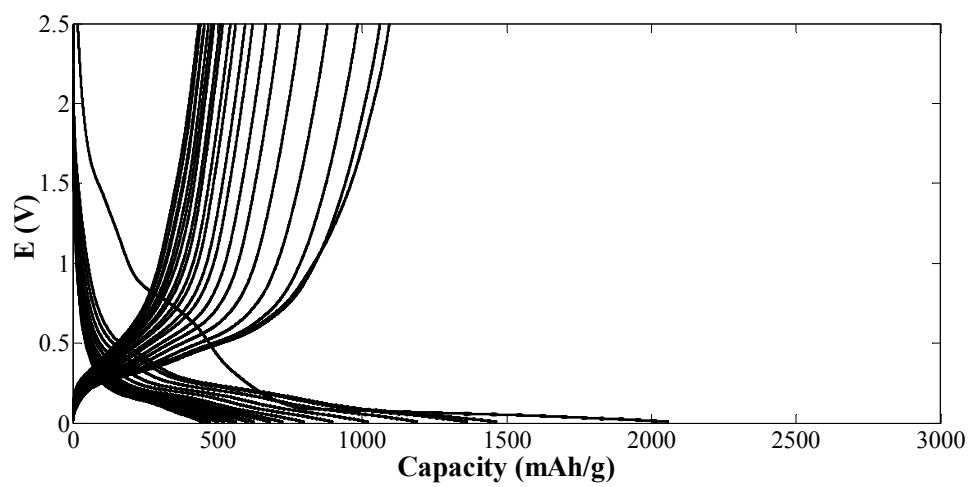
4.3.3 Electrochemical Cycling Characterization

4.3.3.1 Galvanostatic Charge/Discharge Cycling of CNF/Si-80

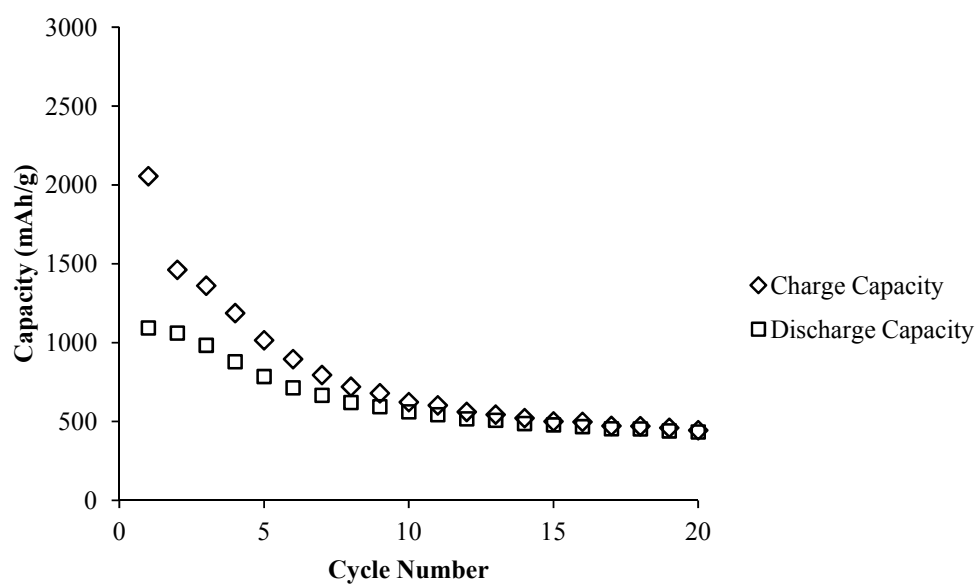
Core-shell CNF/Si-80 was cycled at 100, 200, 400, and 600 mA/g. Its voltage profiles are shown in Fig. 4-25 (a), (c), (e), and (g), and the capacity performance after cycling are shown in Fig. 4-25 (b), (d), (f), and (h). At all cycle rates, SEI layer was formed between 0.5 and 1.0 V at the first charge cycle, as observed in the slow decrease in potential. At 100 mA/g, the initial discharge capacity was 1090 ± 10 mAh/g. The capacity remained 561 ± 6 and 433 ± 4 mAh/g after 10 and 20 cycles, which was 51.4 ± 0.7 and 39.7 ± 0.6 % of

the initial capacity. As shown in Fig. 4-25 (b), both charge and discharge capacity suffered from larger capacity decrease at first 10 cycles. The capacity gradually stabilized afterwards. At 200 mA/g, the initial discharge capacity was 1090 ± 10 mAh/g. The capacity remained 897 ± 9 and 788 ± 8 mAh/g after 10 and 20 cycles, which was 82.0 ± 1.1 and 72.0 ± 1.0 % of the initial capacity. As shown in Fig. 4-25 (d), the CNF/Si sample only suffered from large irreversible capacity at the first cycle. The capacity loss at 200 mA/g was significantly smaller than that at 100 mA/g and the capacity levels off at approximately 780 mAh/g. At 400 mA/g cycle rate, the initial discharge capacity was 1330 ± 10 mAh/g. The capacity remained 848 ± 8 and 678 ± 7 mAh/g after 10 and 20 cycles, which was 63.5 ± 0.9 and 50.8 ± 0.7 % of the initial capacity. At 600 mA/g cycle rate, the highest discharge capacity of 1180 ± 10 mAh/g occurred at the second cycle. The capacity remained 1010 ± 10 and 854 ± 9 mAh/g after 10 and 20 cycles, which was 85.3 ± 1.2 and 72.7 ± 1.0 % of the initial capacity.

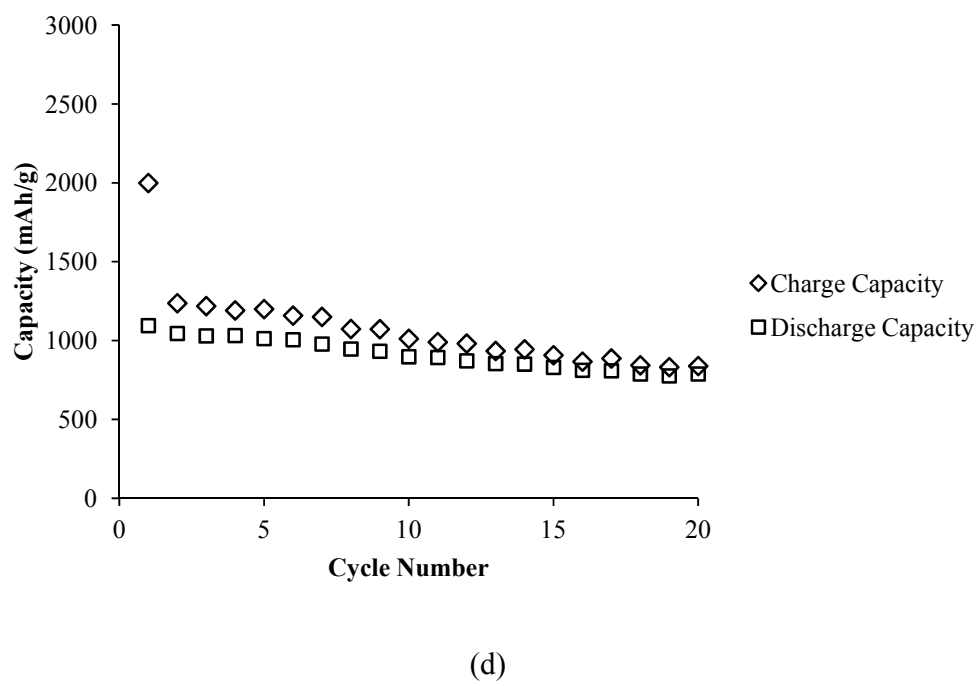
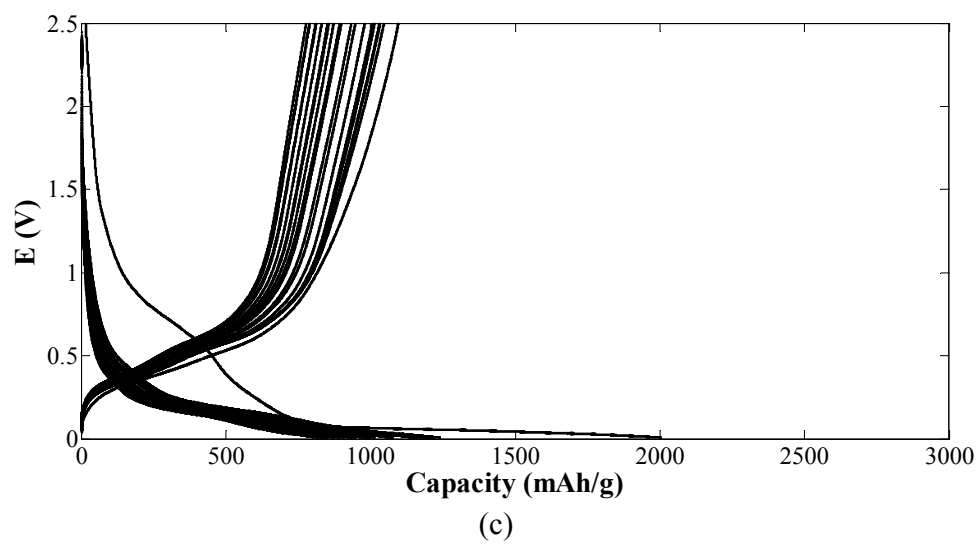
Fig. 4-25 (i) summarizes the Coulombic efficiency of CNF/Si-80 cycled at 100, 200, 400, and 600 mA/g. At the first cycle, all samples possess efficiencies of ca. 53%. The low efficiency is due to the decomposition of electrolyte and SEI formation, which irreversibly consumes Li ions but forms a protective layer to prevent carbon exfoliation. The high irreversible capacity is likely a result of the high surface area of the CNF/SiNP composite. The advantage of the high surface area is to facilitate ion diffusion into the fibre; however, more Li ions could be consumed. Coulombic efficiencies of CNF/Si-80 cycled at all rates gradually recovered to 80 – 90% after 5th cycle with no specific recovery trend, implying the carbon shell did not inhibit Li ion interaction with Si to a significant extend.

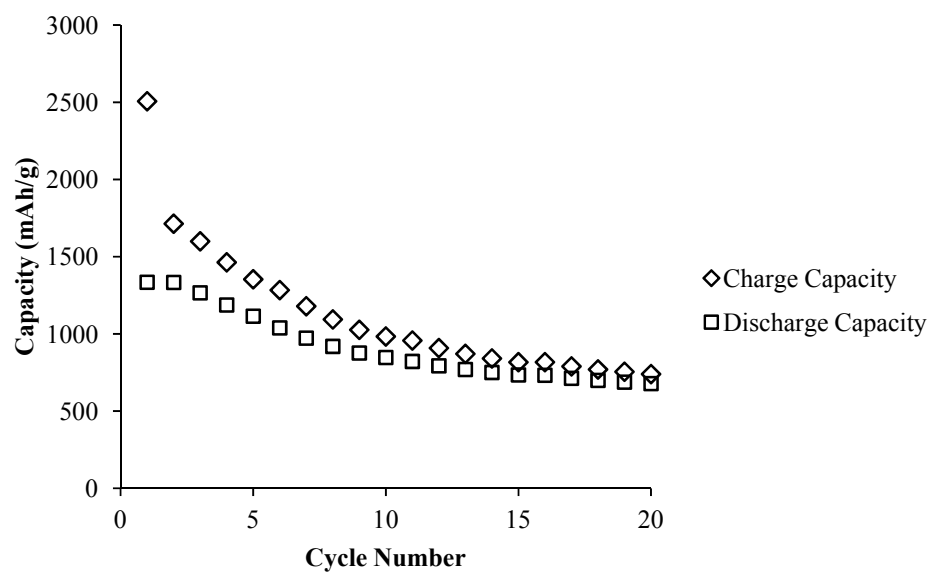
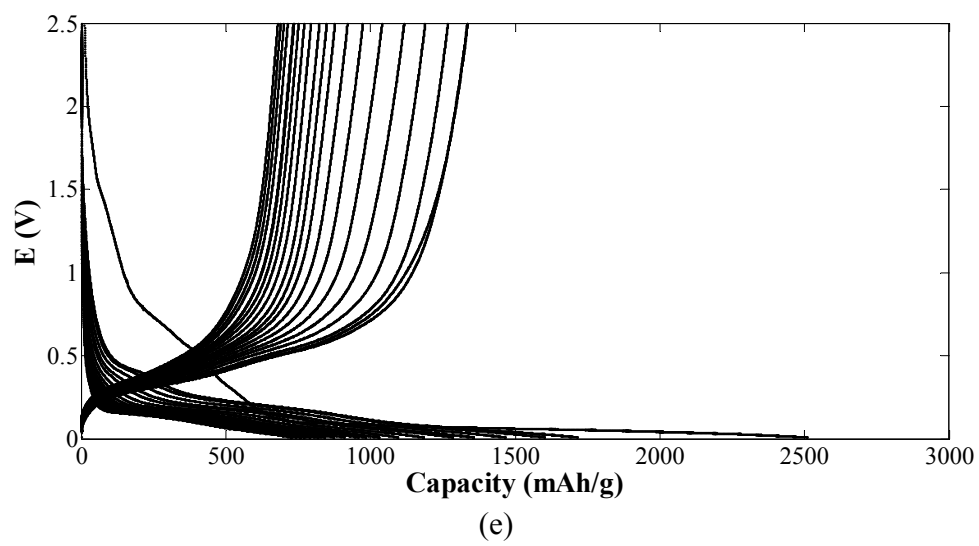


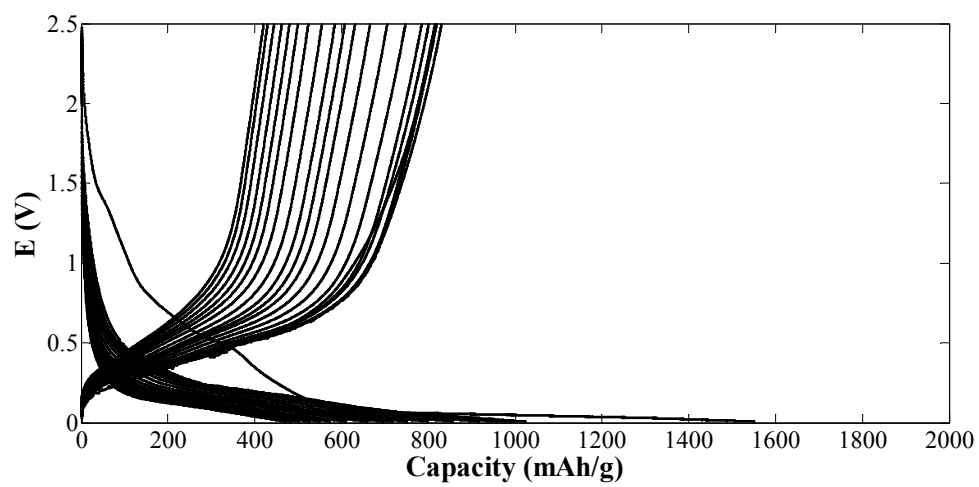
(a)



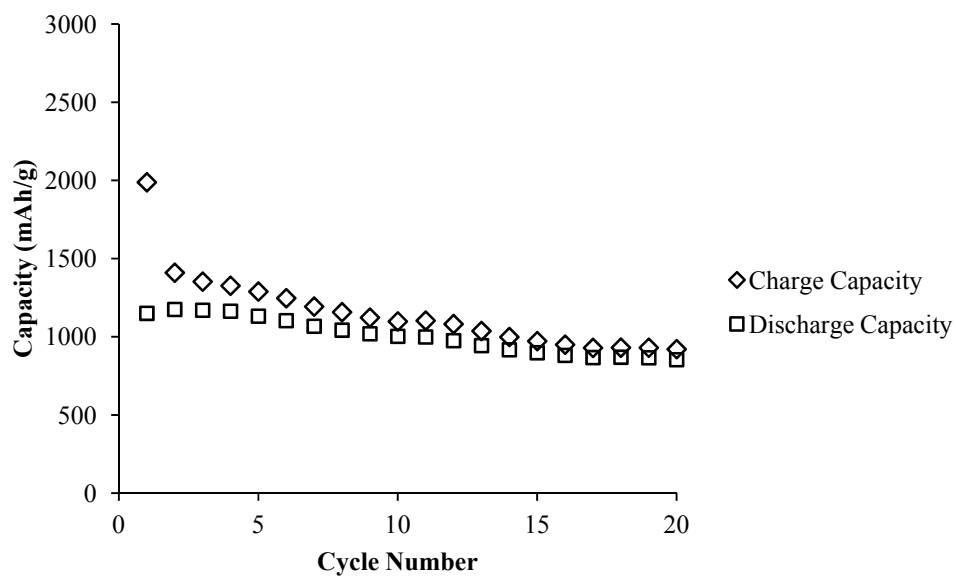
(b)



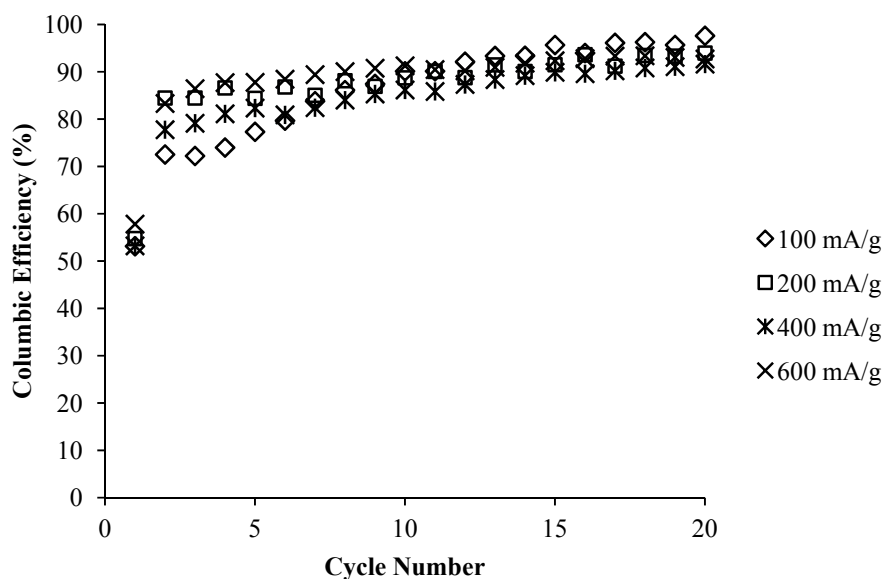




(g)



(h)



(i)

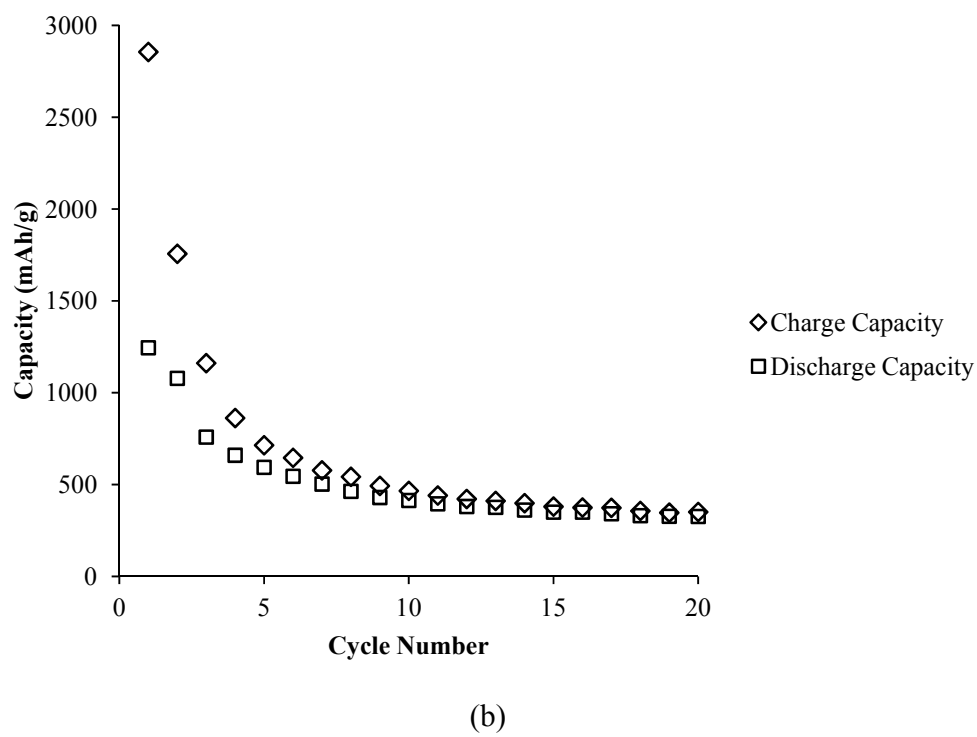
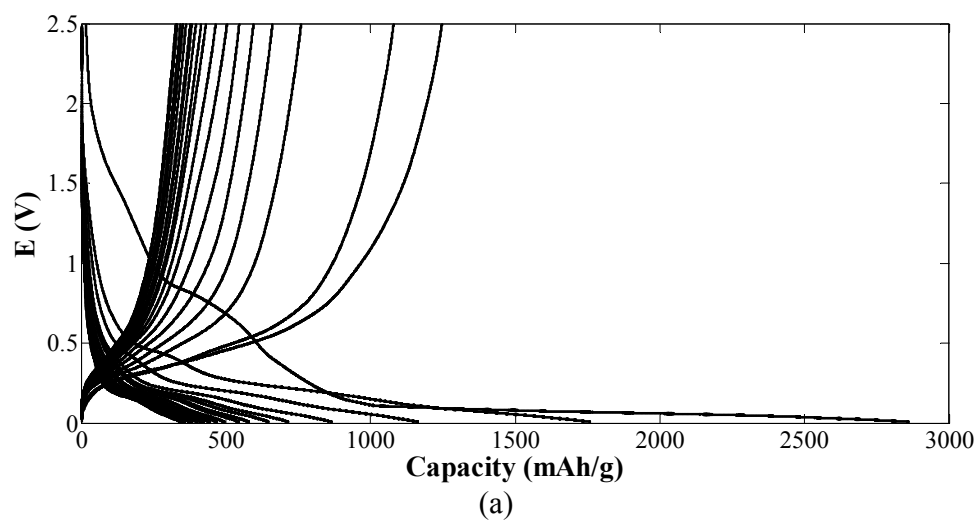
Fig. 4-25 Charge/discharge voltage profile of core-shell CNF/Si-80 cycled at 100 (a), 200 (c), 400 (e), and 600 (g) mA/g; charge/discharge capacity summary of core-shell CNF/Si-80 cycled at 100 (b), 200 (d), 400 (f), and 600 (h) mA/g; the Coulombic efficiency (i) of the sample at each cycling rate.

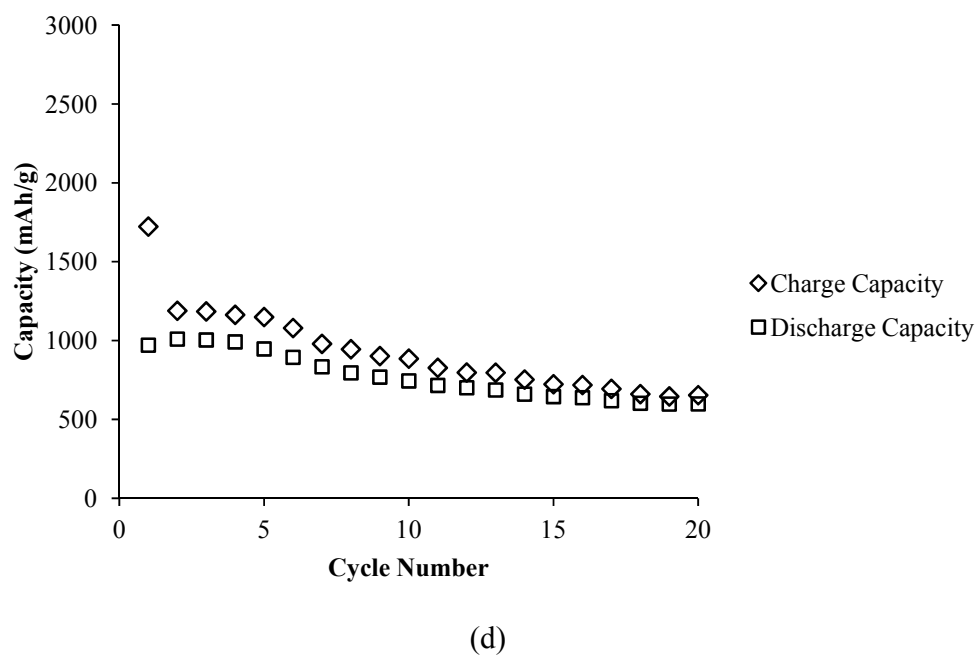
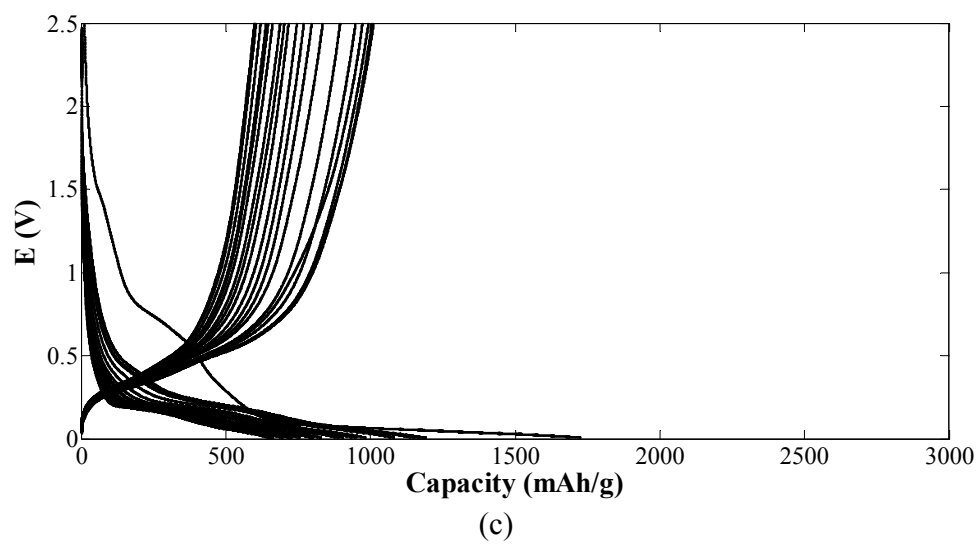
4.3.3.2 Galvanostatic Charge/Discharge Cycling of n-CNF/Si

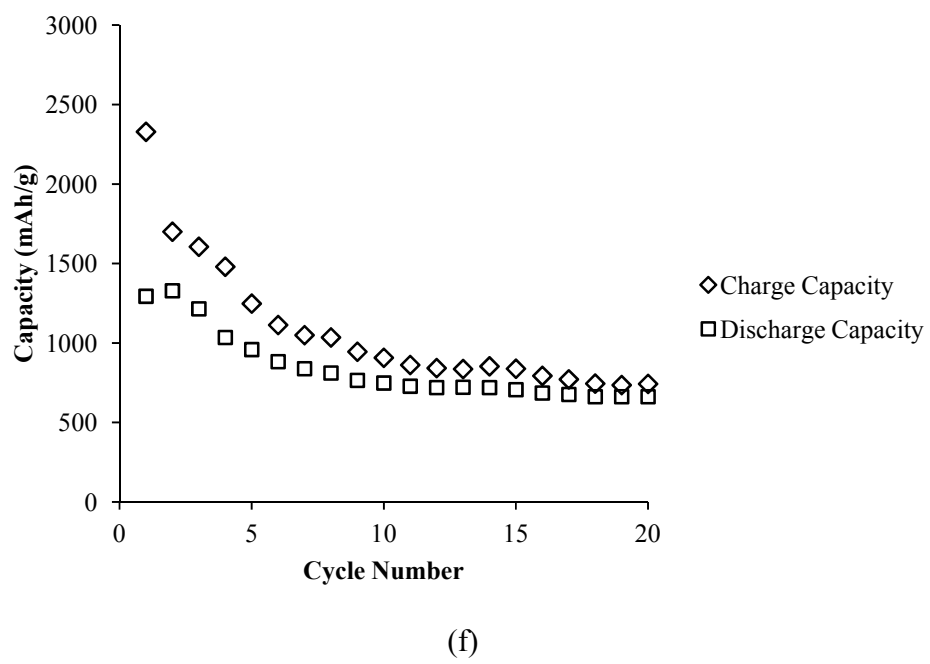
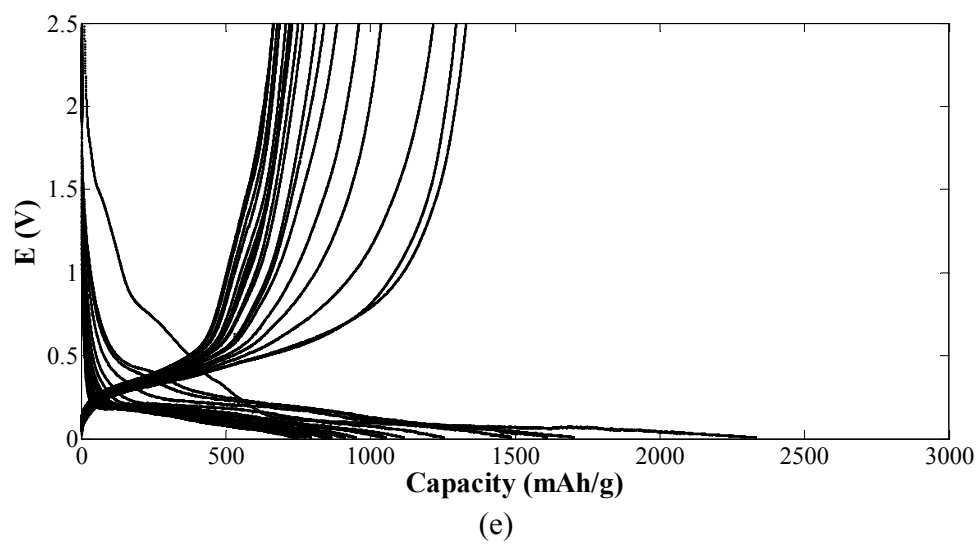
Non-core-shell CNF/Si-80 was cycled at 100, 200, 400, and 600 mA/g. Its voltage profiles are shown in Fig. 4-26 (a), (c), (e), and (g), and the capacity performance after cycling are shown in Fig. 4-26 (b), (d), (f), and (h). At all cycle rates, SEI layer was formed between 0.5 and 1.0 V at the first charge cycle, as observed in the slow decrease in potential. At 100 mA/g, the initial discharge capacity was 1250 ± 10 mAh/g. The capacity remained 413 ± 4 and 326 ± 3 mAh/g after 10 and 20 cycles, which was 33.2 ± 0.5 and 26.2 ± 0.4 % of the initial capacity. As shown in Fig. 4-26 (b), both charge and discharge capacities suffered from larger capacity decrease at first 10 cycles. The capacity leveled off afterwards. At 200 mA/g, the initial discharge capacity was 970

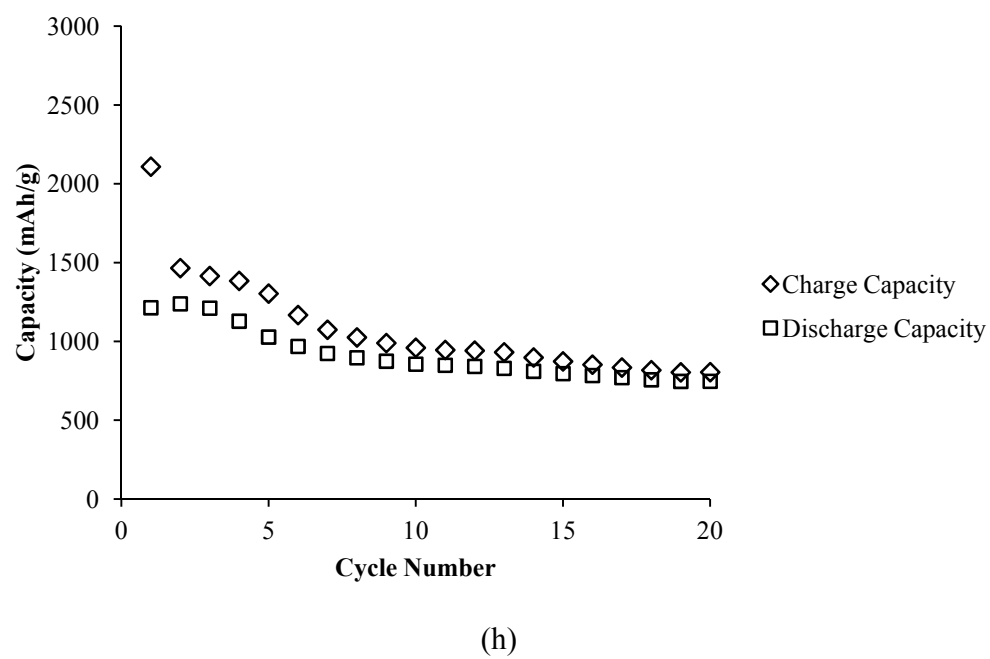
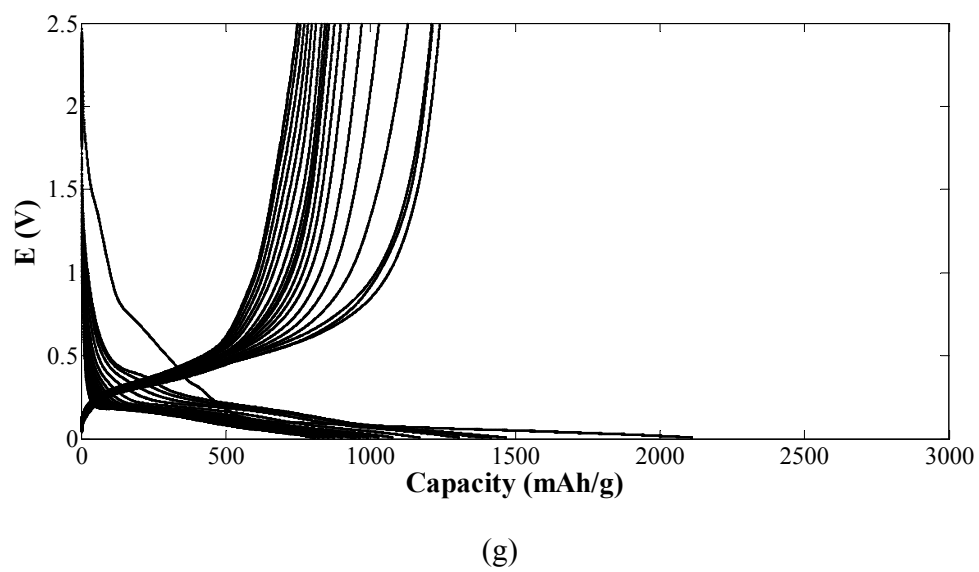
mAh/g and increased to 1010 ± 10 mAh/g at the 2nd cycle. The capacity remained 744 ± 7 and 598 ± 6 mAh/g after 10 and 20 cycles, which was 73.7 ± 1.0 and $59.3 \pm 0.8\%$ of the 2nd cycle capacity (highest capacity). As shown in Fig. 4-26 (d), the capacity loss at 200 mA/g was significantly smaller than that at 100 mA/g and capacity levels off at ca. 600 mAh/g. At 400 mA/g cycle rate, the initial maximum discharge capacity was 1330 ± 10 mAh/g. The capacity remained 749 ± 7 and 662 ± 7 mAh/g after 10 and 20 cycles, which was 56.4 ± 0.8 and $49.8 \pm 0.7\%$ of the maximum capacity. At 600 mA/g cycle rate, the initial maximum discharge capacity was 1240 ± 10 mAh/g. The capacity remained 856 ± 9 and 747 ± 7 mAh/g after 10 and 20 cycles, which was 69.1 ± 1.0 and $60.3 \pm 0.8\%$ of the maximum capacity.

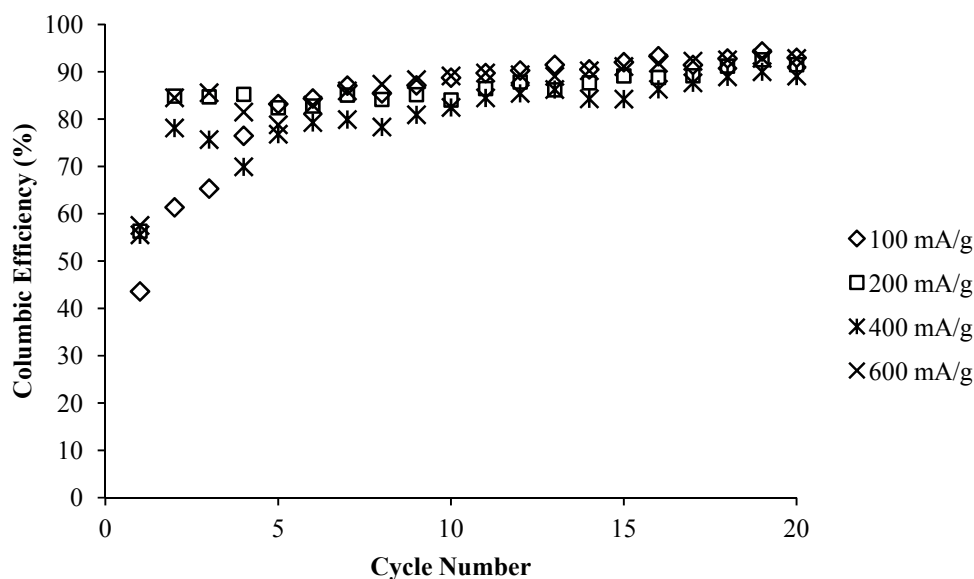
Fig. 4-26 (i) summarizes the Coulombic efficiency of n-CNF/Si cycled at 100, 200, 400, and 600 mA/g. The low efficiencies at first cycles were also due to the decomposition of electrolyte and SEI formation. The high irreversible capacity indicated that n-CNF/Si might also possess high accessible surface area to the electrolyte solution. The Coulombic efficiency of n-CNF/SiNP cycled at all rates recovered to over 80% after the 5th cycle. No specific trend in efficiency recovery was observed, indicating a good rate capability of the electrode was achieved using nanofibrous network.











(i)

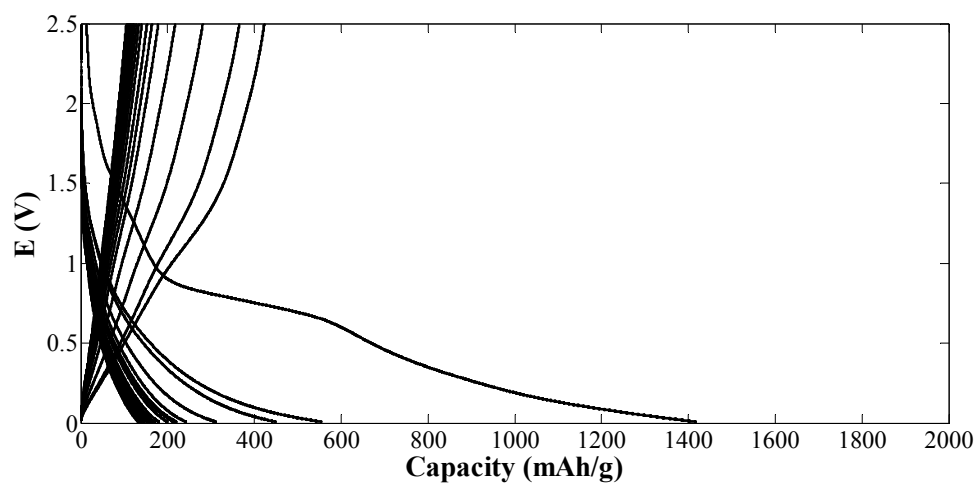
Fig. 4-26 Charge/discharge voltage profile of n-CNF/Si cycled at 100 (a), 200 (c), 400 (e), and 600 (g) mA/g; charge/discharge capacity summary of n-CNF/Si cycled at 100 (b), 200 (d), 400 (f), and 600 (h) mA/g; the Coulombic efficiency (i) of the sample at each cycling rate.

4.3.3.3 Galvanostatic Charge/Discharge Cycling of Pure CNF

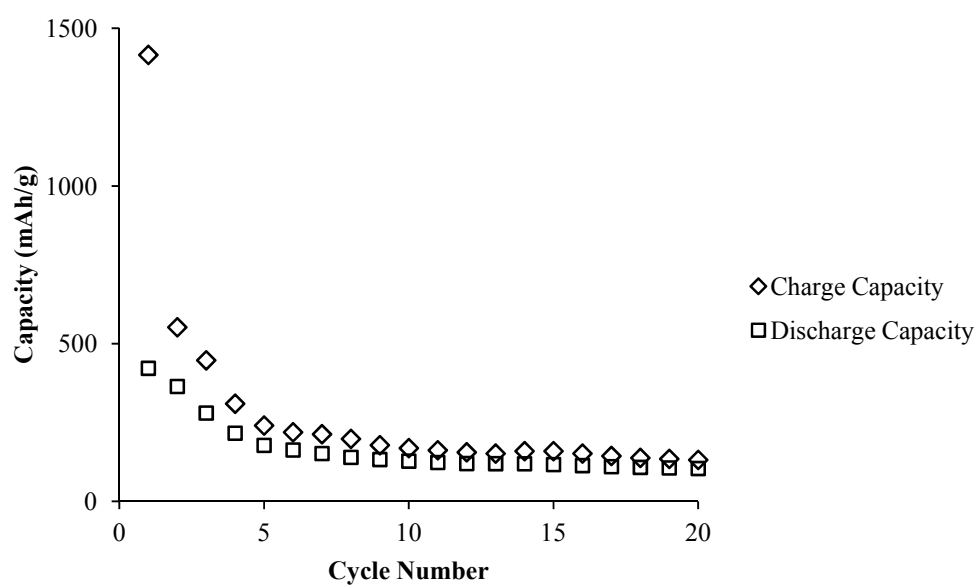
In order to understand the intrinsic capacitive behavior of pure SiNP, the cycling behavior of pure CNF at 100, 200, 400, and 600 mAh/g was also investigated, as shown in Fig. 4-27 (a) – (i). Since it is pure carbon, a long plateau at 0.5 – 1.0 V indicates the formation of SEI, as shown in Fig. 4-27 (a), (c), (e), and (g). At 100 mA/g, the initial discharge capacity was 421 ± 4 mAh/g. The capacity decreased slightly faster at first 5 cycles and gradually stabilized. After 10th and 20th cycles, the capacity remained 127 ± 1 and 104 ± 1 mAh/g, which was 30.2 ± 0.4 and $24.7 \pm 0.3\%$ of the initial capacity. At 200 mA/g, the initial discharge capacity was 404 ± 4 mAh/g. The capacity slowly decreased in the first 10 cycles and stabilized afterwards. After 10th and 20th cycles, the capacity remained 199 ± 2 and 112 ± 1 mAh/g, which was 49.3 ± 0.7 and $27.8 \pm 0.4\%$ of the initial

capacity. At 400 mA/g, the initial discharge capacity was 325 ± 3 mAh/g. The capacity retention was higher at this rate. After 10th and 20th cycles, the capacity remained 224 ± 2 and 202 ± 2 mAh/g, which was 68.9 ± 1.0 and $62.2 \pm 0.9\%$ of the initial capacity. At 600 mA/g, the initial discharge capacity was 306 ± 3 mAh/g. The capacity retention was higher at this rate. After 10th and 20th cycles, the capacity remained 158 ± 2 and 129 ± 1 mAh/g, which was 51.6 ± 0.7 and $42.2 \pm 0.6\%$ of the initial capacity.

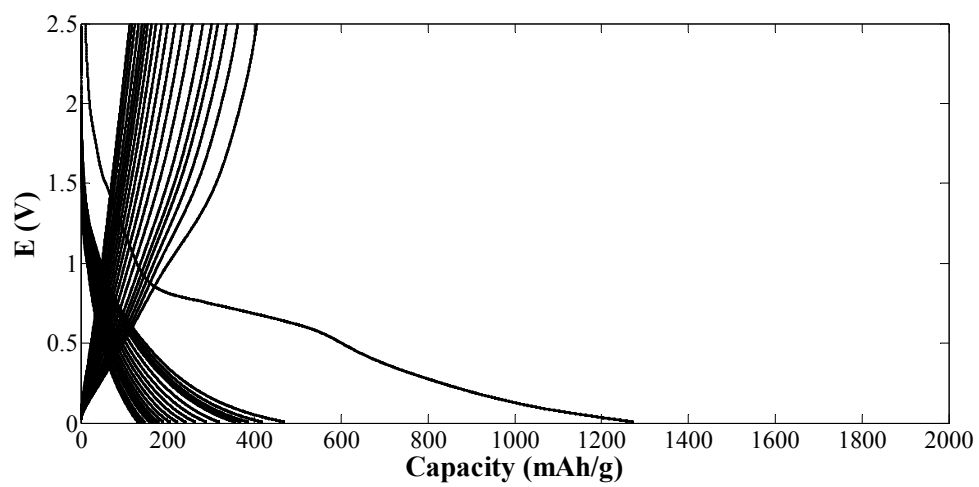
Fig. 4-27 (i) summarizes the Coulombic efficiency of the pure CNF cycled at 100, 200, 400, and 600 mA/g. At the first cycle, CNF cycled at all rates possessed an efficiency of 30%. The increased efficiency (40 – 60%) of the CNF sample with SiNP incorporation implies that majority of the SEI formation occurs on carbon. The high irreversible capacity is a characteristic of electrospun CNF regardless of SiNP. The Coulombic efficiency of CNF samples cycled at different rates are fairly consistent along the cycles. At 100, 200, 400, and 600 mA/g, the efficiency maintained around 70 – 80, 80 – 85, 85 – 90%, and 85 – 90%, respectively. The gradual increase in efficiency at higher cycle rate is opposite to theoretical trend prediction. This phenomenon is most likely due to the generation of thick SEI layer and high resistance, which will be discussed in detail in section 4.3.3.5.



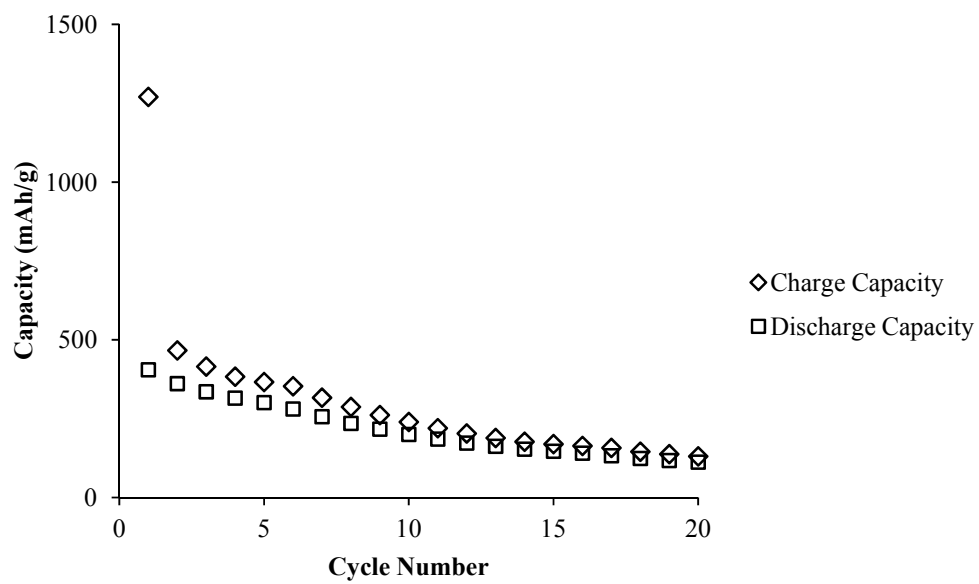
(a)



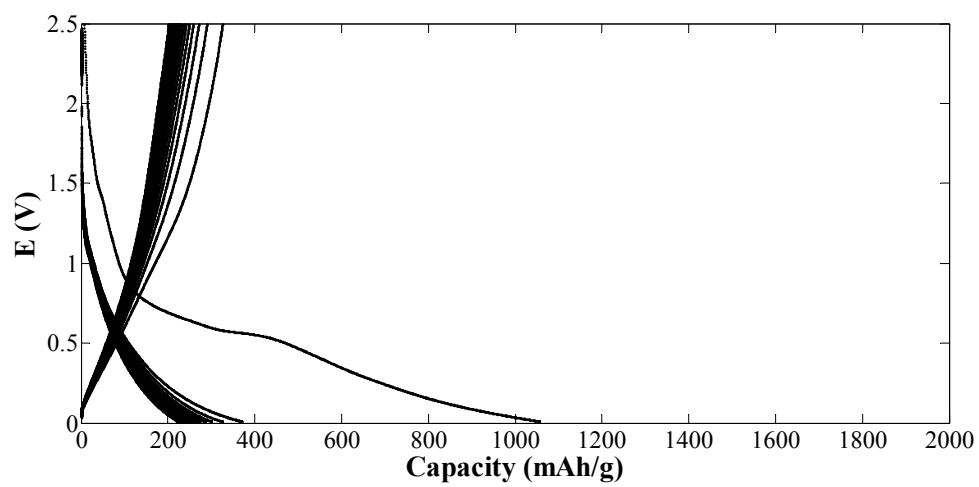
(b)



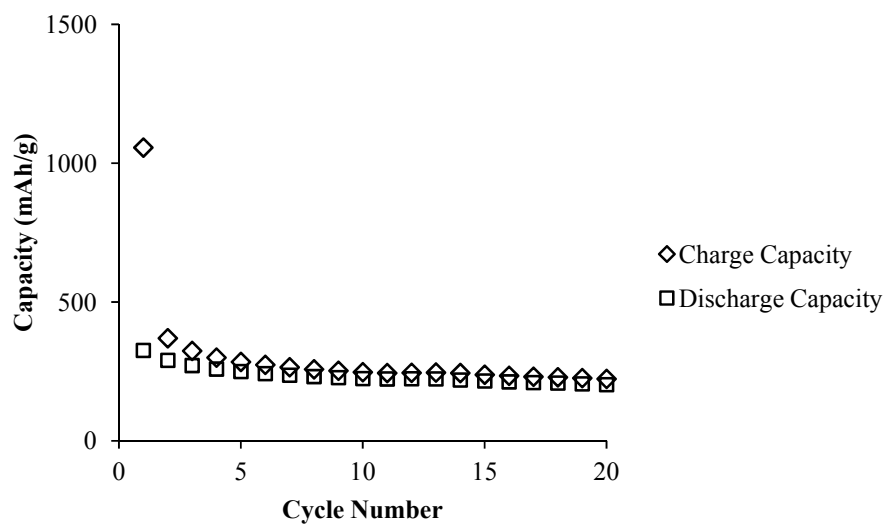
(c)



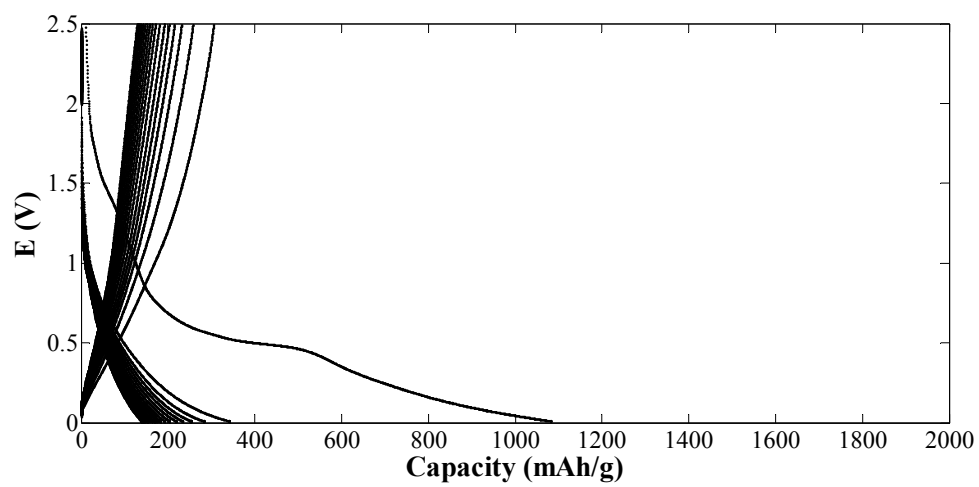
(d)



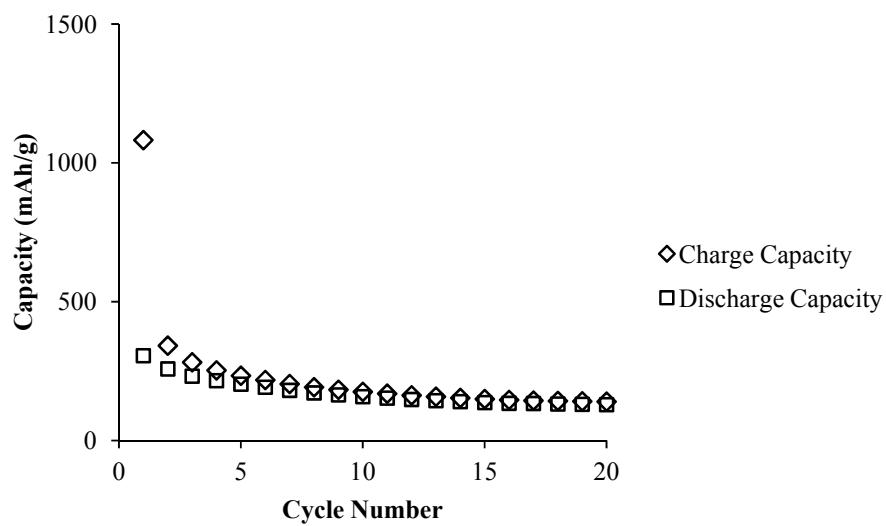
(e)



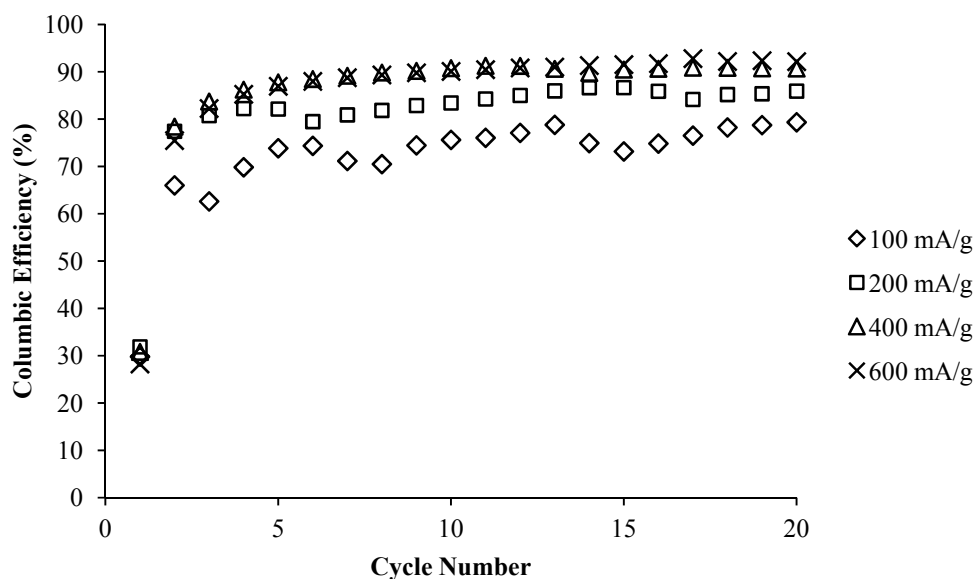
(f)



(g)



(h)



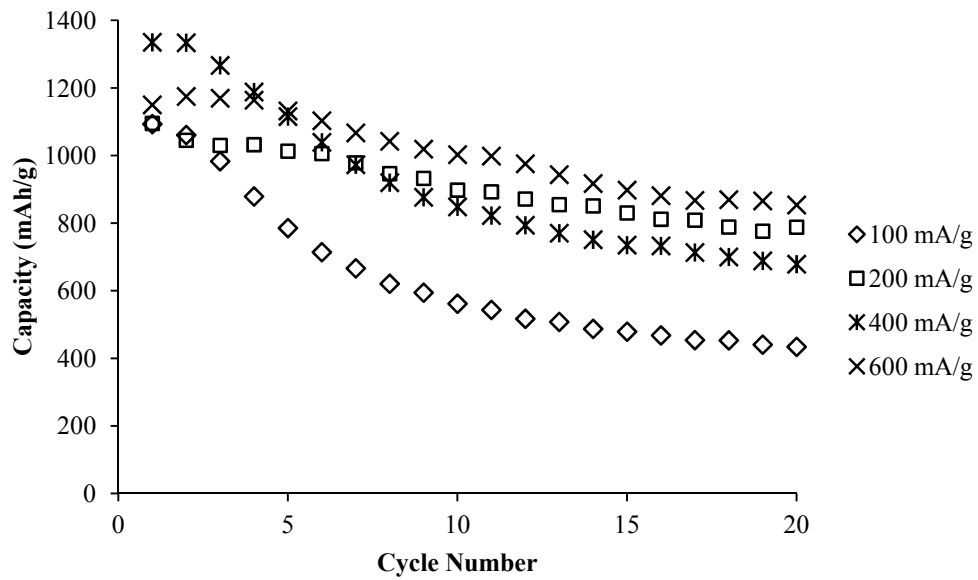
(i)

Fig. 4-27 Charge/discharge voltage profile of pure CNF cycled at 100 (a), 200 (c), 400 (e), and 600 (g) mA/g; charge/discharge capacity summary of pure CNF cycled at 100 (b), 200 (d), 400 (f), and 600 (h) mA/g; the Coulombic efficiency (i) of the sample at each cycling rate.

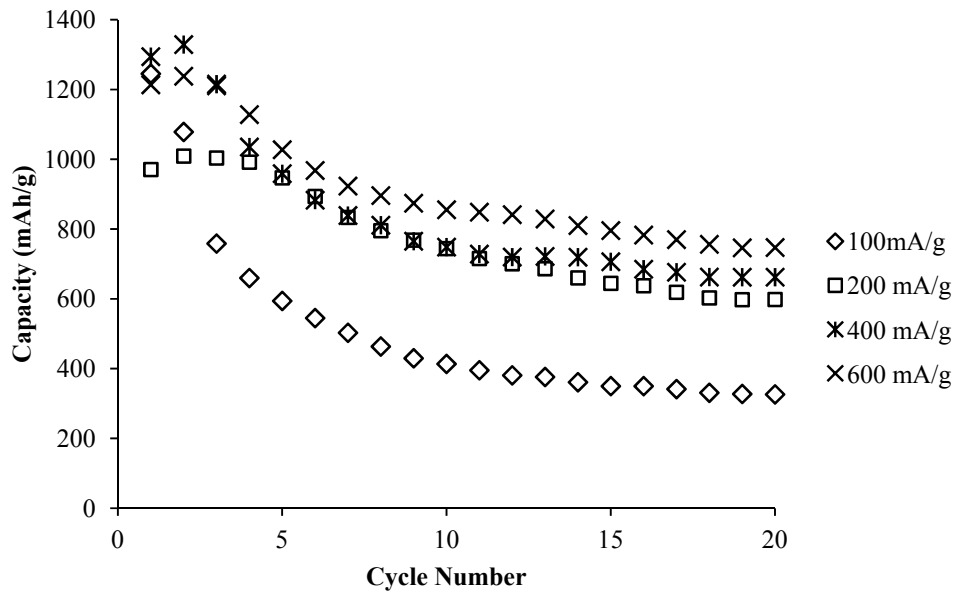
4.3.3.4 Discharge Capacity Comparison

Fig. 4-28 is the discharge capacity summary of CNF/Si-80, n-CNF/Si, and pure CNF cycled at 100, 200, 400, and 600 mA/g. In Fig. 4-28(a), CNF/Si-80 system shows similar trend in capacity retention as the cycle rate increases from 200 to 600 mA/g, indicating the good conductivity and ion accessibility of CNF based electrodes. n-CNF/Si in Fig. 4-28(b) shows a similar behaviour as well. In contrast, both systems suffer from a more significant capacity drop at the first 10 cycles of the slowest rate, 100 mA/g. This could be correlated to the steeper slope of capacity drop in pure carbon cycled at 100 mA/g, as shown in Fig. 4-28(c). Capacity loss of carbon mainly occurs at the first 10 cycles as well. Many reasons, such as inactivation or degradation of the host carbon, or the

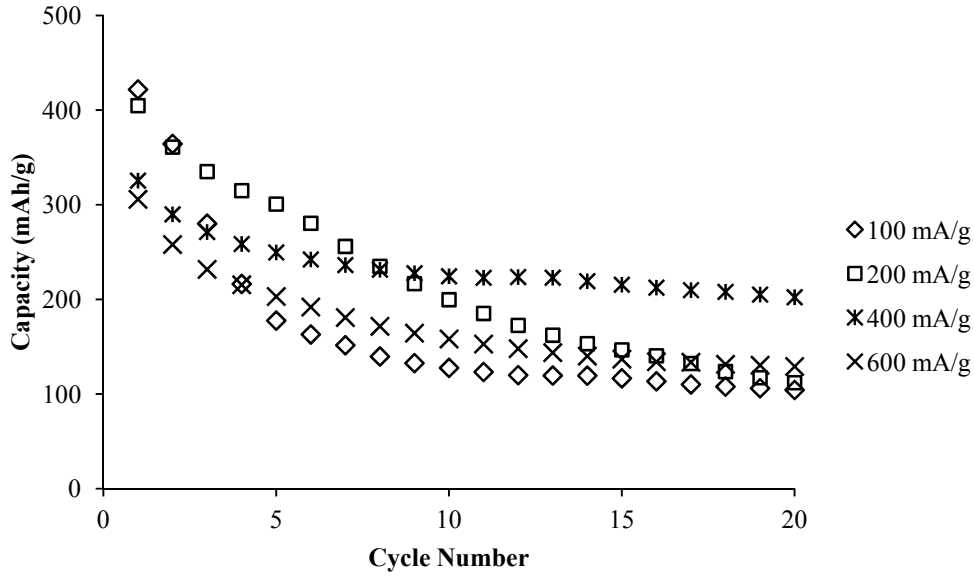
increased film resistance, could affect the SiNP performance. More details are discussed in section 4.3.3.5 to correlate the fibre morphology with the different trend observed in capacity retention.



(a)



(b)



(c)

Fig. 4-28 Discharge capacity summary of CNF/Si-80 (a), n-CNF/Si (b), and pure CNF (c) cycled at 100, 200, 400, and 600 mA/g.

4.3.3.5 Capacity Characterization with Sample Morphology

In order to further understand the advantages and disadvantages of different nanofibre structures, core-shell, non-core-shell, and pure carbon samples cycled at the same rates are plotted in the same graph. The pure SiNP capacity was estimated from the subtraction of core-shell and non-core-shell sample capacity (in mAh/g) by pure carbon capacity (in mAh/g). Fig. 4-29(a) shows the discharge capacities of all three different samples cycled at 100 mA/g. It is shown that with the inclusion of SiNP in the carbon fibre, the capacity drop of CNF/Si-80 was smaller than that of n-CNF/Si. Fig. 4-29(b) shows the estimated capacity contribution from pure SiNP in both CNF/Si-80 and n-CNF/Si samples. It is calculated assuming 30 wt% capacity contribution from SiNP and 70 wt% capacity contribution from carbon. A sample calculation of pure SiNP capacity is shown below:

Using the 1st cycle core-shell electrode capacity = 1090±10 mAh/g and 1st cycle carbon electrode capacity = 421±4 mAh/g in Fig. 4-29(a),

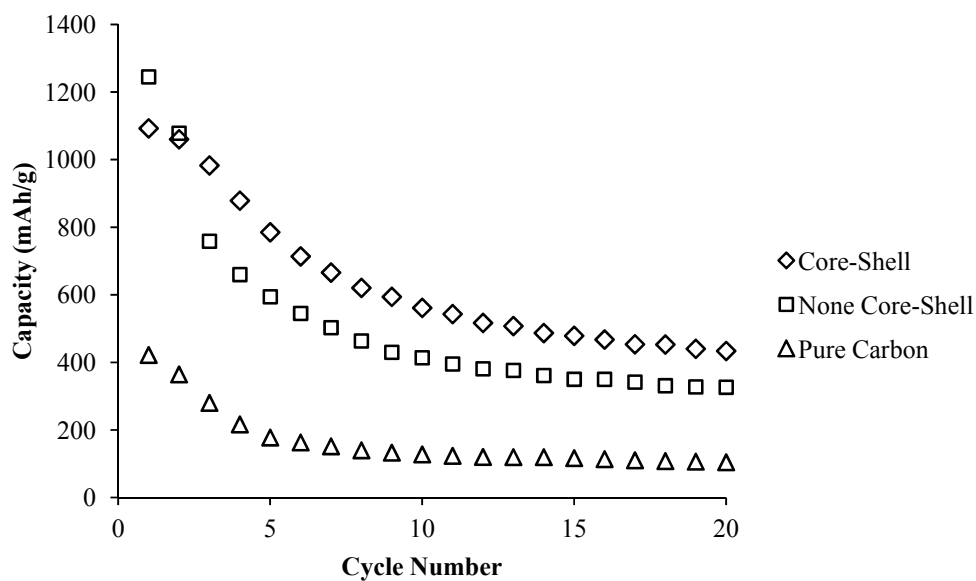
$$\text{SiNP capacity} = (1090 \pm 10 \text{ mAh/g} - 421 \pm 4 \text{ mAh/g} \times 0.7) / 0.3 = 2660 \pm 40 \text{ mAh/g}$$

After normalization, the pure Si capacity in CNF/Si-80 and n-CNF/Si are approximately 2500 – 3200 mAh/g (of silicon) initially, which are 60 – 76 % of the theoretical capacity (4200 mAh/g) of silicon, respectively. The percentage utilization of Si capacity is similar to a previously reported value also using a Si/C composite [159].

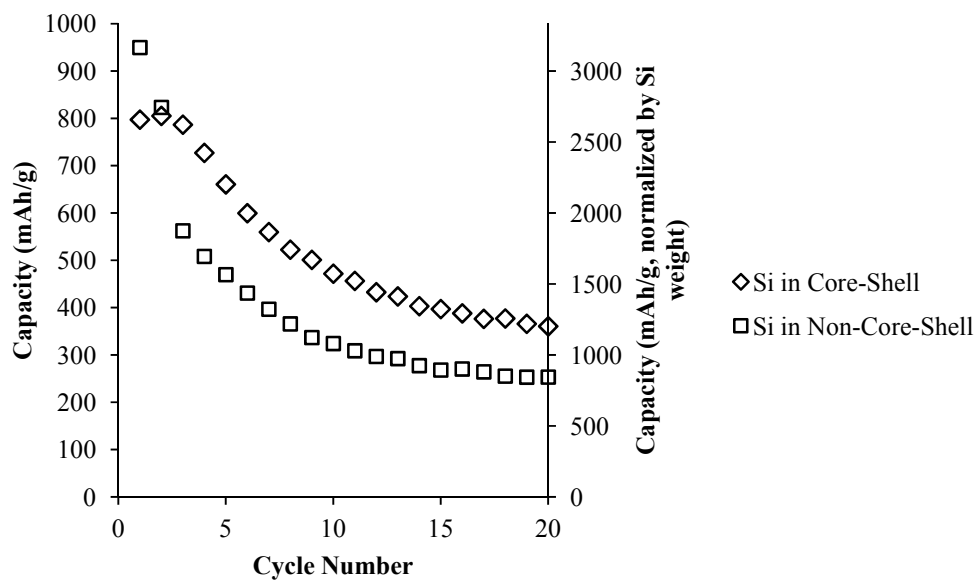
SiNP in n-CNF/Si suffered from significant capacity loss in the first three cycles, which resulted in smaller capacity retention of SiNP. It is common that the capacity fade of SiNP is mainly due to the nanoparticle fusion and breakage during charge/discharge and its loss of contact with electrode matrix [13]. By surrounding SiNP with a CNF matrix, the amount of Si capacity fade, especially in the first three cycles, was significantly reduced. This result is also consistent with the reports of Chan *et al.* on pure Si nanowire, indicating the exposure of Si in electrolyte solution is detrimental to the good cycling performance due to the constant SEI formation and dissolution [172]. The percentage capacity retentions for the last cycle capacity (vs. initial highest cycle capacity) of CNF/Si-80 and n-CNF/Si are 44.8±0.6% and 26.7±0.4%, respectively.

The capacity fade in the subsequent cycles for both CNF/Si-80 and n-CNF/Si was still inevitable. One major reason is the destruction of CNF structure upon constant cycling, where SiNP shrank and expanded during discharge/charge. Both CNF/Si-80 and n-CNF/Si became fragile after cycled at 100 mA/g. As shown in the SEM images of Fig. 4-34(a) and (b), the CNF/Si-80 after being cycled at 100 mA/g, the nanofibre swelled and

broke into short fibres with diameters between 1 – 2 μm . The swollen fibre diameter of n-CNF/Si after 20 cycles, as shown in Fig. 4-35(a) and (b), was slightly smaller ($\sim 1 \mu\text{m}$) due to the smaller pristine fibre diameter. However, fibres appeared to fuse together more through the surface expanded Si granules. The second reason for the capacity fade would be the recurrent growth of SEI layer. Aurbach has indicated that upon cycling, the inorganic SEI layer is susceptible to cracking due to the constant swelling and shrinkage of carbon [173]. The breakage of the SEI opens up more active surface to react with electrolyte on a small scale. The constant breaking and repairing of SEI thickens the surface film, which in turn increases the ionic resistance of the electrode. In order to fully charge and discharge the thickened electrode, a very high overpotential is required to reduce the capacity fade. This effect can be used to explain the observed discharge trend of CNF/SiNP composite shown in Fig. 4-28. At higher current densities, the capacity retention significantly improves after 20 cycles. The thickened SEI layer in this study was likely to build up throughout cycles. However, it is useful to conduct experiments to observe the amount SEI formation (change in fibre diameter) vs. cycle numbers. A schematic of the SEI film thickening is shown in Fig. 4-30 [174].



(a)



(b)

Fig. 4-29 Discharge capacity comparison between CNF/Si-80, n-CNF/Si, and pure CNF cycled at 100 mA/g (a) and the pure SiNP capacity in different nanofibre composite after the subtraction of pure CNF capacity (b).

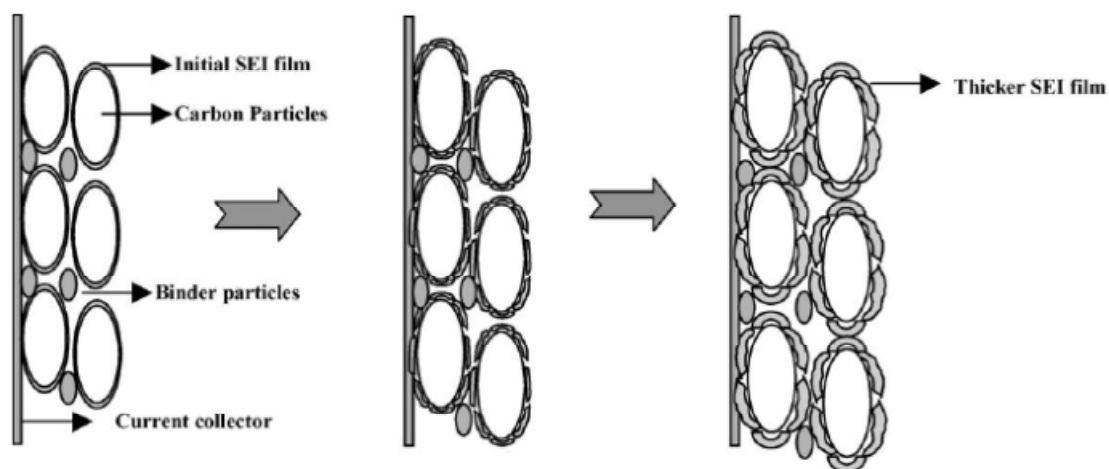
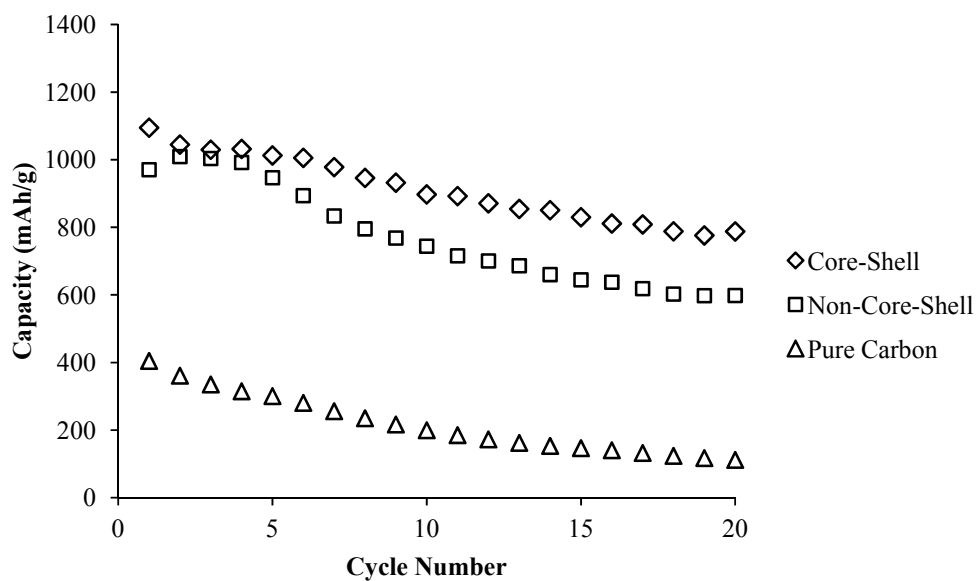


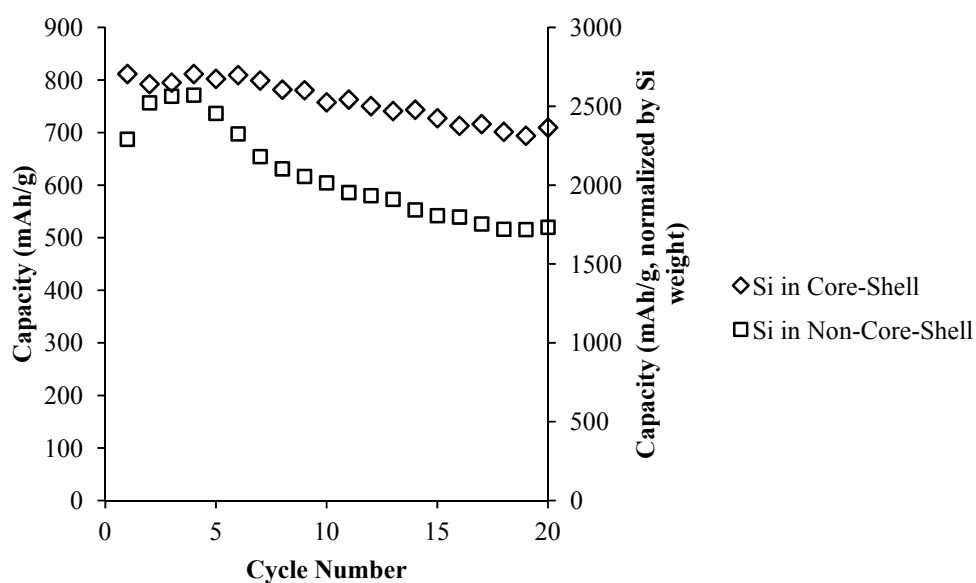
Fig. 4-30 Schematic representation of the SEI film thickening upon cycling [174].

Fig. 4-31(a) are the discharge capacities of all three different carbon samples cycled at 200 mA/g. Towards the end of the cycle, the core-shell sample was able to retain the capacity nearly 200 mAh/g higher than that of the non-core-shell sample. As shown in Fig. 4-31(b), SiNP in CNF/Si-80 successfully retained a constant capacity close to 700 mAh/g (ca. 2300 mAh/g normalized by Si weight), while SiNP in n-CNF/Si experienced a gradual increase in capacity, followed by a constant capacity drop. The capacity retention of SiNP in CNF/Si-80 at the end of the cycle was $87.4 \pm 1.2\%$ but in n-CNF/Si, it was reduced to $67.4 \pm 0.9\%$. This further showed the retention of SiNP capacity through carbon coating. The overall decrease in capacity (Fig. 4-31(a)) of CNF/Si-80 could be concluded to be the result of capacity fading from CNF. Fig. 4-34 (c) and (d) are the SEM images of CNF/Si-80 after cycled at 200 mA/g. Fibres were also broken into short segments with the swelling of fibre diameter to 1 – 2 μm . However, the fibres appeared to be in more discrete structure in contrast to Fig. 4-35(d), where fibres fused together more without clear boundaries. Fig. 4-35(c) and (d) are the SEM images of n-CNF/Si

after being cycled at 200 mA/g. The fibres were swollen with large granules on the surface, which are expanded SiNP. Fibres fused together and interconnected with each other through expanded SiNP. Without the protection of the carbon coating, the expansion and the fusion of SiNP could cause the capacity fading.



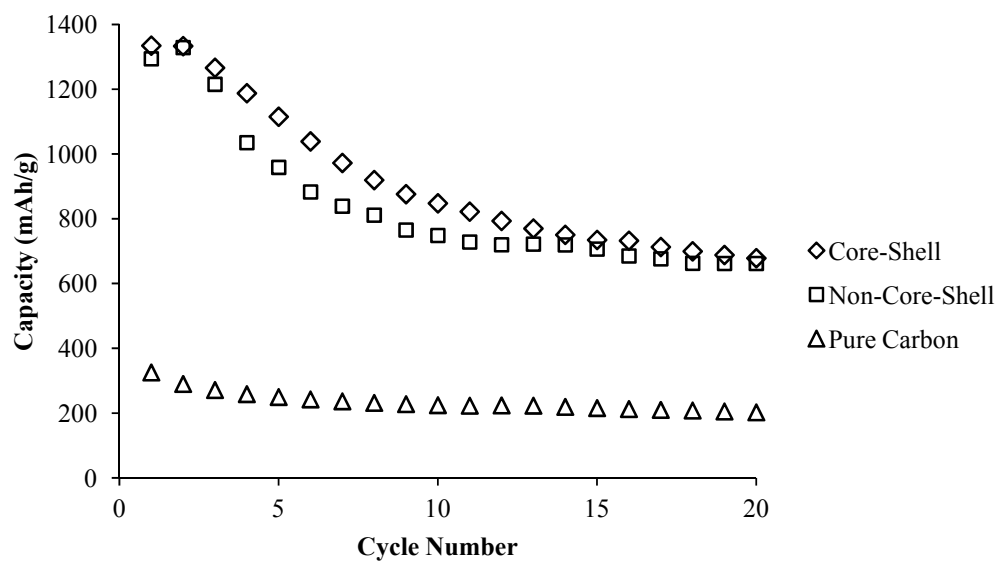
(a)



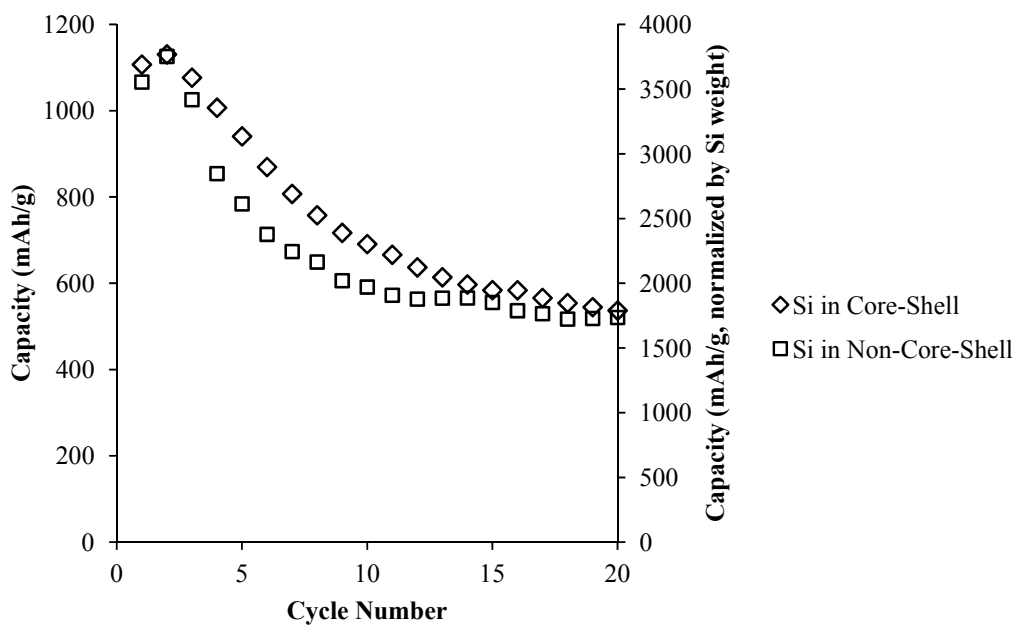
(b)

Fig. 4-31 Discharge capacity comparison between core-shell CNF/Si, non-core-shell CNF/Si, and pure CNF cycled at 200 mA/g (a) and the pure SiNP capacity after the subtraction of pure CNF capacity (b).

Fig. 4-32(a) are the discharge capacity of all three different carbon samples cycled at 400 mA/g. In this case, n-CNF/Si also suffered from a more significant capacity fade between 6th – 10th cycles. However, the capacity levels off towards the end, which merges with that from CNF/Si-80. Since the pure CNF capacity is fairly stable at this cycle rate, the capacity fade of the nanofibrous electrode is mainly a result of Si capacity fade, as shown in Fig. 4-32(b). SEM of CNF/Si-80 and n-CNF/Si after cycling are shown in Fig. 4-34(e), (f) and Fig. 4-35(e), (f), respectively. n-CNF/Si appears to obtain a more intact fibrous structure at 400 mA/g rate comparing to other cycle rates, which explains its comparable cycling performance with that of CNF/Si-80. The SiNP capacity retention for both electrodes are ca. 46 – 47 %. It is unclear at this moment for the reason of greater capacity decrease of CNF/Si-80. More samples need to be tested to confirm the possibility of sample variation.



(a)



(b)

Fig. 4-32 Discharge capacity comparison between CNF/Si-80, n-CNF/Si, and pure CNF cycled at 400 mA/g (a) and the pure SiNP capacity for both samples after the subtraction of pure CNF capacity (b).

Fig. 4-33(a) are the discharge capacities of all three different carbon samples cycled at 600 mA/g. Towards the end of the cycle, the core-shell sample was able to retain a capacity at ca. 100 mAh/g higher than that of the non-core-shell sample. As shown in Fig. 4-33(b), SiNP in CNF/Si-80 successfully retained a capacity at ca. 2500 mAh/g normalized by Si weight, while SiNP in n-CNF/Si experienced a higher initial capacity than CNF/Si-80 but followed by a steep capacity drop from cycle three to seven. The Si capacity retention in CNF/Si-80 is $75.3 \pm 1.1\%$, while that in n-CNF/Si is $62.1 \pm 0.9\%$. This further shows the retention of SiNP capacity through carbon coating. The capacity fade is contributed from both CNF and SiNP; however, the capacity fade of SiNP in n-CNF/Si mainly caused capacity drop. Fig. 4-34(g) and (h) are the SEM images of CNF/Si-80 after cycled at 600 mA/g. Fibres appeared to be in more discrete and intact structure in contrast to Fig. 4-35(g) and (h), the SEM of n-CNF/Si after cycled at the same rate, where fibres fused together more and broke into short segments. Many granules on the surface can be seen in Fig. 4-35(h), which are expanded SiNP.

The specific energy of a LIB with the improved anode capacity can be calculated as follows, assuming 140 mAh/g cathode capacity and 1000 mAh/g anode capacity:

$$\frac{1}{Q_{total}} = \frac{1}{Q_{cathode}} + \frac{1}{Q_{anode}} \quad (6)$$

$$E_{total} = Q_{total} \times V \quad (7)$$

where $Q_{cathode}$ and Q_{anode} are the capacities of cathode and anode, respectively, and Q_{total} is the sum capacity of both electrodes. Q_{total} calculated is 122 mAh/g. The overall specific energy (E_{total} normalized by weight of electrodes only) using operating voltage (V) = 3.7

V is calculated to be 454 Wh/kg. The energy and capacity of this composite anode has significantly improved the LIB performance than using graphite as anode (372 mAh/g). The capacity and energy of a LIB using graphite as anode are calculated to be 102 mAh/g and 376 Wh/kg, respectively.

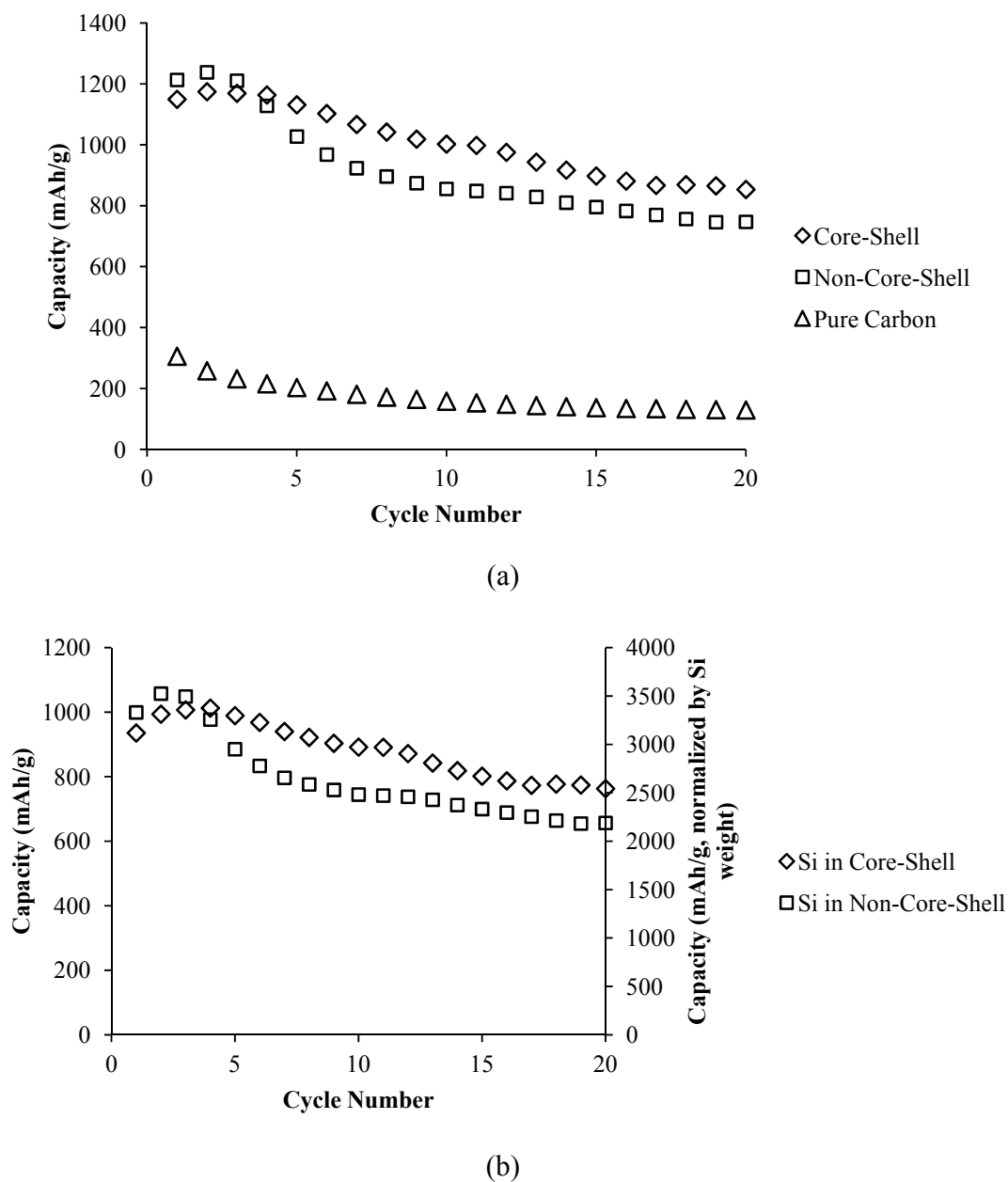
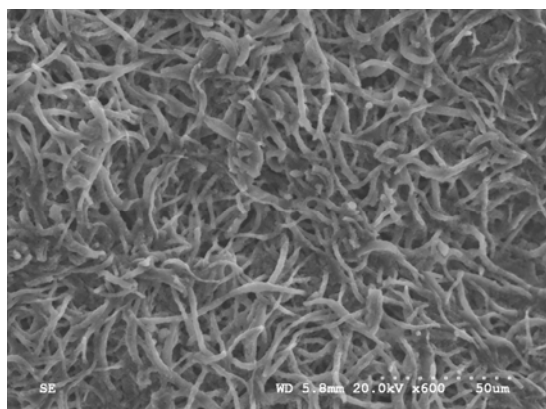
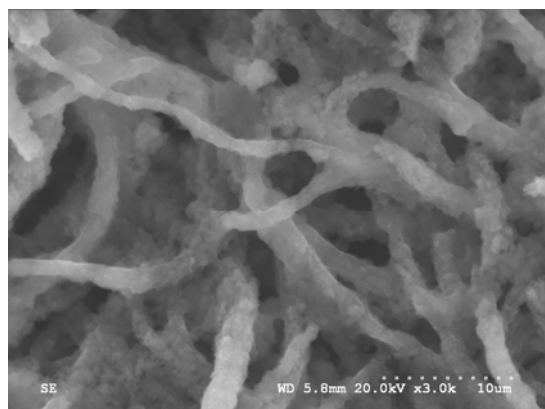


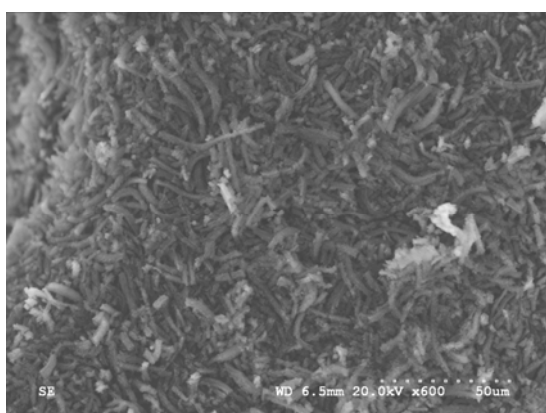
Fig. 4-33 Discharge capacity comparison between CNF/Si-80, n-CNF/Si, and pure CNF cycled at 600 mA/g (a) and the pure SiNP capacity for both samples after the subtraction of pure CNF capacity (b).



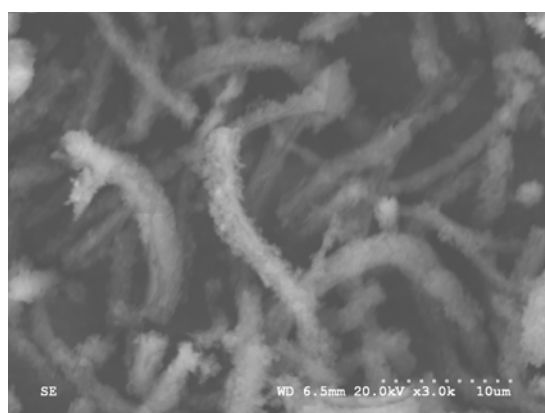
(a)



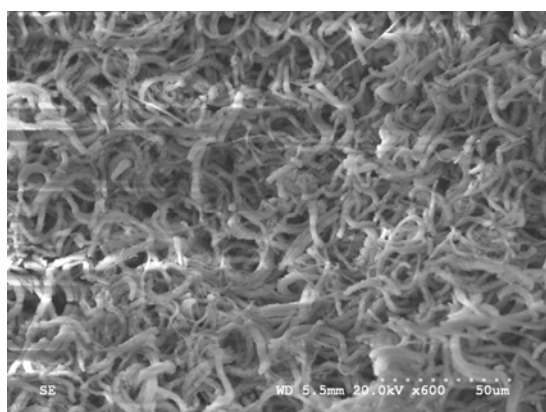
(b)



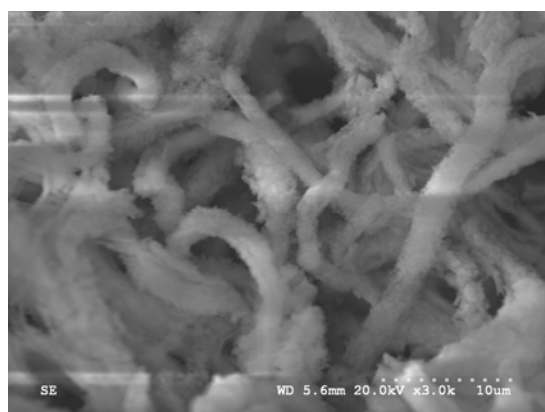
(c)



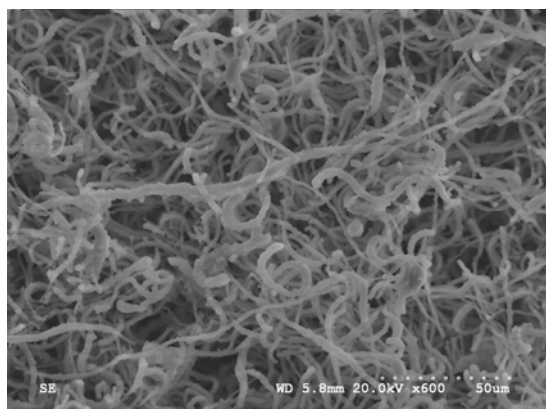
(d)



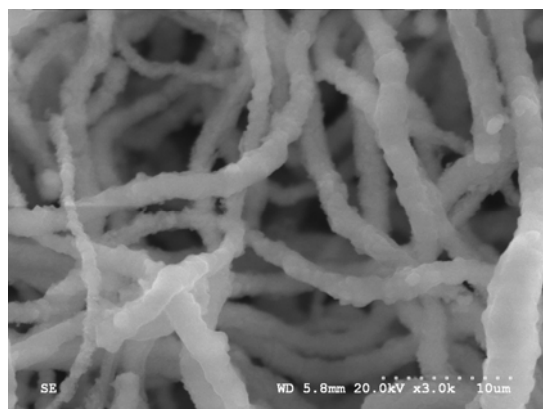
(e)



(f)

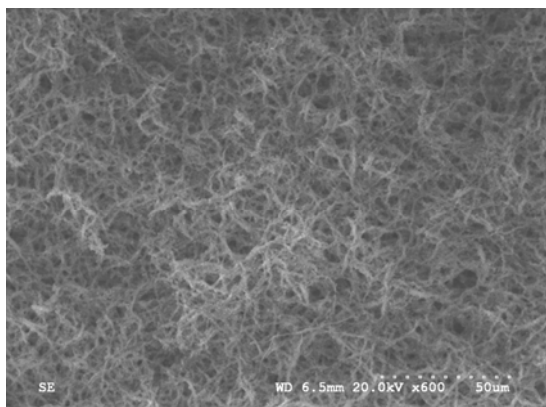


(g)

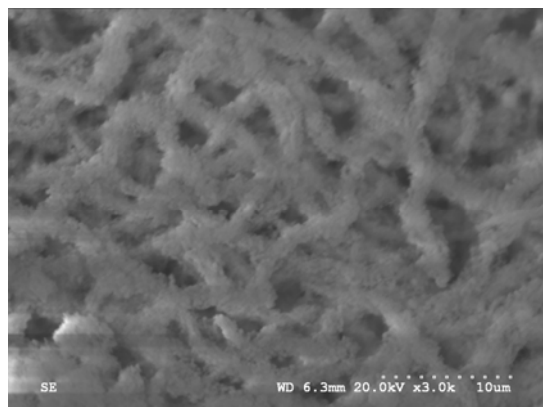


(h)

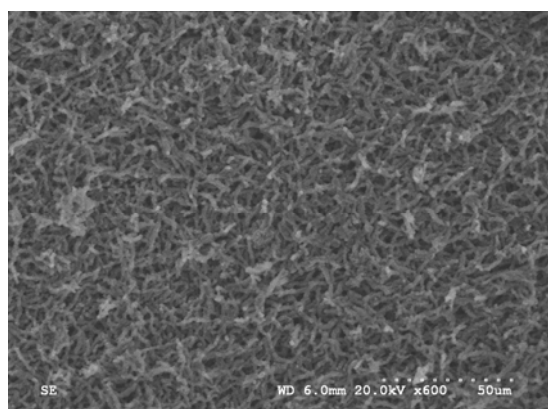
Fig. 4-34 SEM of CNF/Si-80 after cycled at 100 mA/g with $\times 600$ (a) and $\times 3k$ (b) magnifications, after cycled at 200 mA/g with $\times 600$ (c) and $\times 3k$ (d) magnifications, after cycled at 400 mA/g with $\times 600$ (e) and $\times 3k$ (f) magnifications, and after cycled at 600 mA/g with $\times 600$ (g) and $\times 3k$ (h) magnifications.



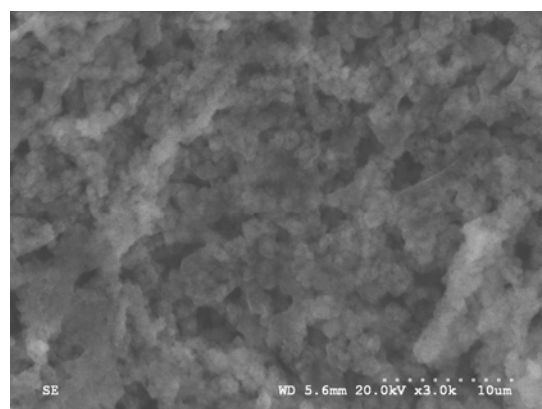
(a)



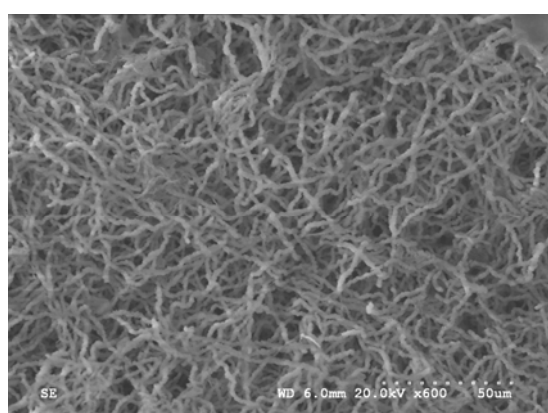
(b)



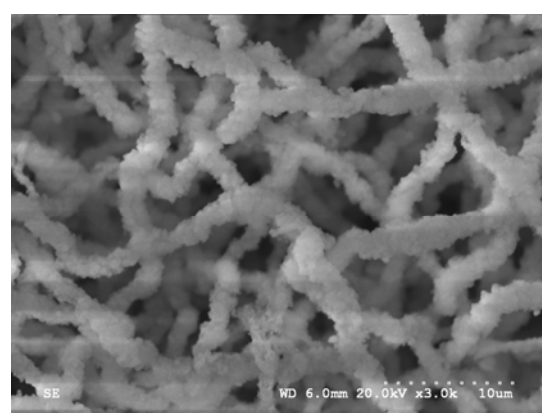
(c)



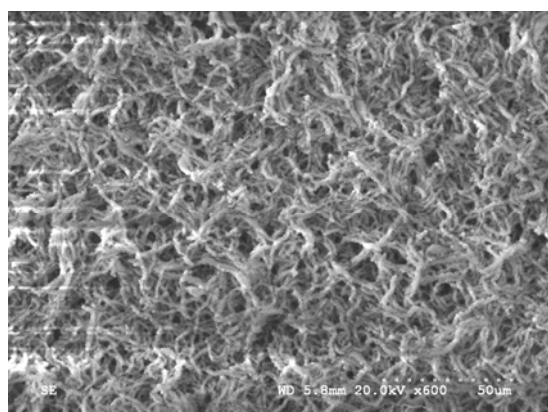
(d)



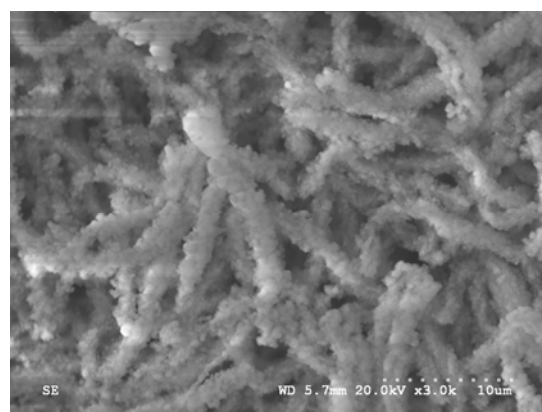
(e)



(f)



(g)



(h)

Fig. 4-35 SEM of n-CNF/Si after cycled at 100 mA/g with $\times 600$ (a) and $\times 3k$ (b) magnifications, after cycled at 200 mA/g with $\times 600$ (c) and $\times 3k$ (d) magnifications, after cycled at 400 mA/g with $\times 600$ (e) and $\times 3k$ (f) magnifications, and after cycled at 600 mA/g with $\times 600$ (g) and $\times 3k$ (h) magnifications.

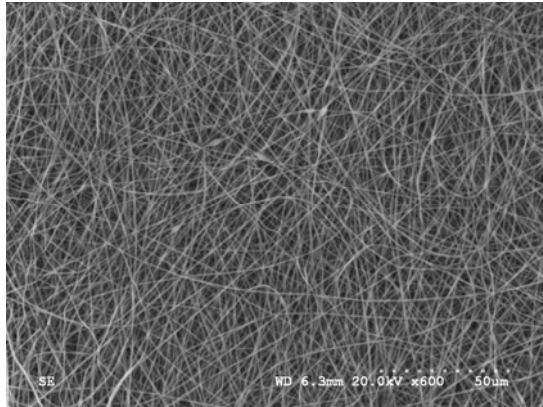
The morphology of pure CNF after 20 cycles at 100, 200, 400, and 600 mA/g was investigated, as shown in Fig. 4-36(a) – (f). At all cycle rates, the pure CNF sample remained intact and easy to handle after experiments, with increase in fibre diameter. The fibre diameters for carbon samples after cycling at 100, 200, 400, and 600 mA/g are $7.9\pm1.0\times10^2$, $7.4\pm1.2\times10^2$, $6.9\pm0.7\times10^2$, and $7.3\pm1.3\times10^2$ nm, respectively, which are $1.75\times$ than the original $4.0\pm0.5\times10^2$ nm. This result confirms that the expansion and contraction of SiNP was the main cause for carbon fibre breakage.

The cycling trend of electrospun CNF behaved differently from conventional carbon samples. Kim *et al.* investigated the cycling performance of natural graphite and aluminum-modified graphite at different rates. The result is shown in Fig. 4-37 [175]. In both cases, the capacity retention was greater at slower cycle rates. Sony US 18650 LIB also experienced the same trend. At the cycle rate of 1C, 2C, and 3C, the capacity fade for the carbon anode was 2.77, 8.30, and 10.59 %, respectively. The capacity fade for the whole cell was 9.50, 13.20, and 16.90 %, respectively [174]. Ning *et al.* claimed that this phenomenon is due to the fast increase in the SEI film thickness at faster rates, which results in the higher electronic resistance of carbon anode. The fast growth of SEI film also generates unstable films, which produces surface cracks more easily upon cycling and induces more SEI formation [174].

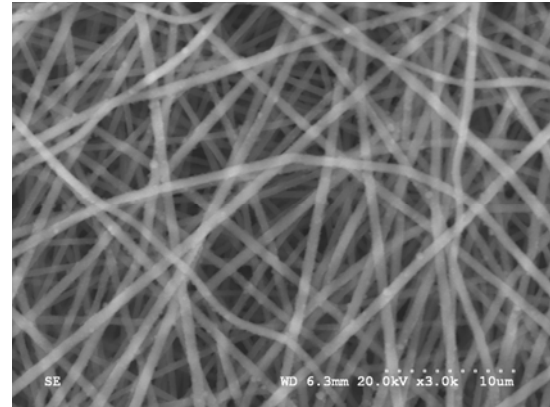
In this experiment, the rates 100, 200, 400, and 600 mA/g used are estimated to be 1/3C, 1/1.5C, 1.3C, and 2C (assume the initial capacity stabilizes at 300 mAh/g). The reversed cycling trend observed, as mentioned in section 4.3.3.5, is likely due to the higher current required to charge/discharge the electrode without significant capacity fade. CNF samples cycled at both 100 mA/g and 200 mA/g show a greater initial discharge capacity

than samples cycled at 400 and 600 mA/g, indicating that a slower rate permits greater amount of Li ions to interact with the electrode. At 200 mA/g rate, although the capacitance drop was slower than that at 100 mA/g, their final capacitance merges at 20 cycles, which is likely due to the extended SEI growth and the requirement of higher current to reduce the capacity fade. 400 and 600 mA/g rate samples, in contrast, show a more stable capacitance retention throughout cycles.

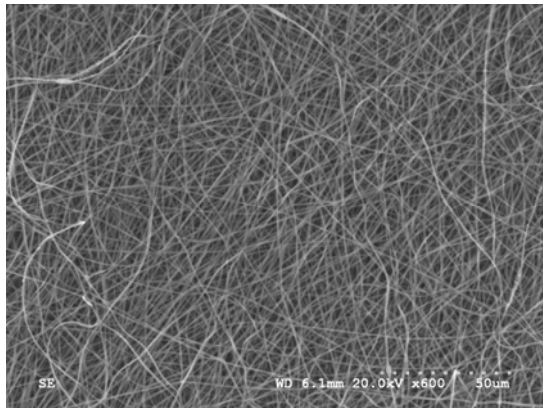
The capacity fade of LIB in general can be attributed to two effects. First is the loss of active material, including the inability of the electrode to host Li ions, dissolution of active material, and the loss of electrical contact between active material and the current collector. Second is the increased resistance, mostly dominated by the electrical resistance of the electrode and the contact resistance between active material and the current collector after cycling [95, 174]. Since Li ions were in excess in our test solution, CNF remained intact without breaking, and an increase in at least $1.75\times$ fibre diameter was observed with SEI growth, the most plausible explanation for the opposite trend observed from electrospun CNF is the increased resistance. The increased resistance can be due to both electrical resistance (thick SEI film) and the contact resistance between CNF (the film was not compacted).



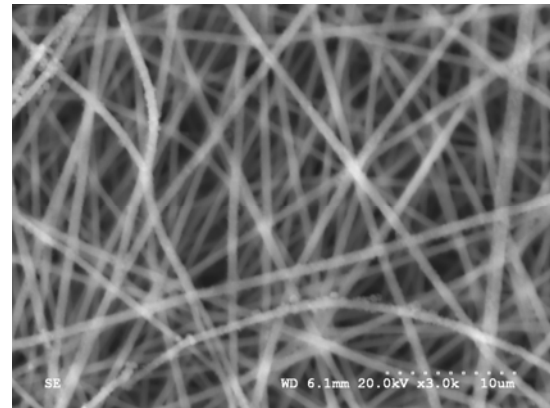
(a)



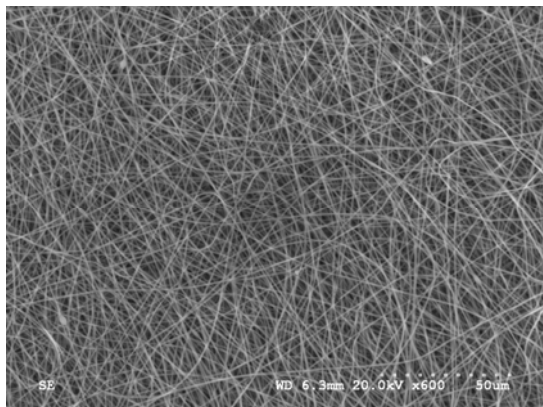
(b)



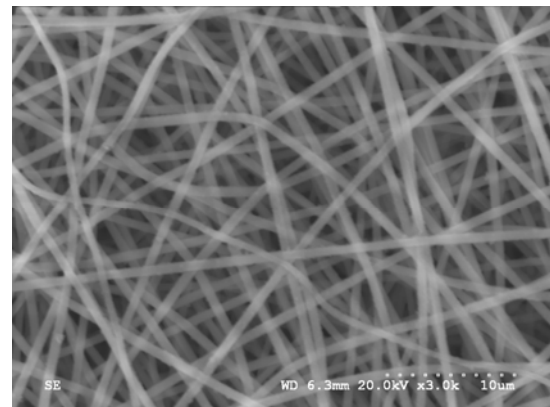
(c)



(d)



(e)



(f)

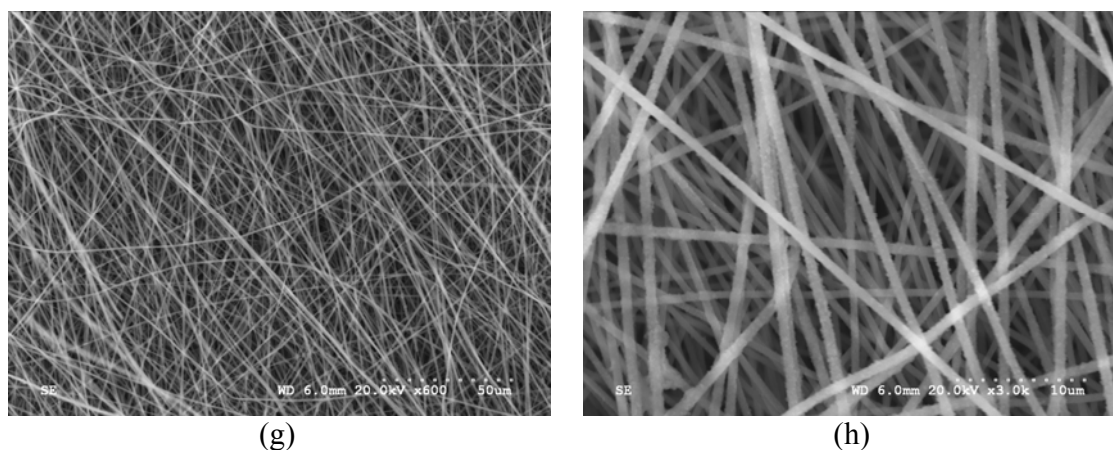


Fig. 4-36 SEM of pure CNF after cycled at 100 mA/g with $\times 600$ (a) and $\times 3k$ (b) magnifications, after cycled at 200 mA/g with $\times 600$ (c) and $\times 3k$ (d) magnifications, after cycled at 400 mA/g with $\times 600$ (e) and $\times 3k$ (f) magnifications, and after cycled at 600 mA/g with $\times 600$ (g) and $\times 3k$ (h) magnifications.

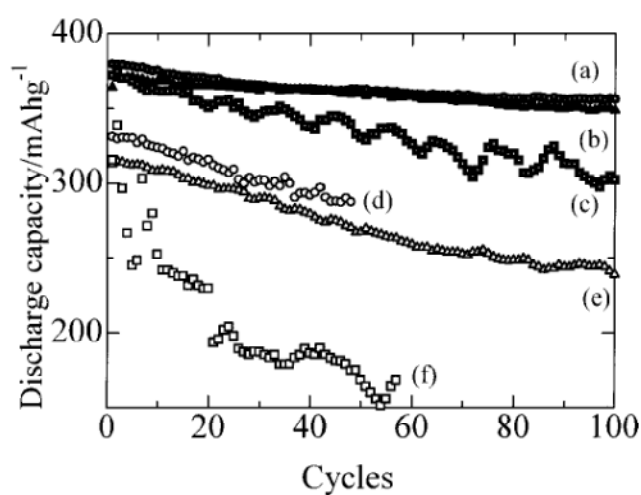


Fig. 4-37 Curves (a), (b), and (c) are Al-treated natural graphite cycled at 0.2, 0.5, and 1.0 C rate, respectively, and curves (d), (e), and (f) are natural graphite cycled at 0.2, 0.5, and 1.0C rate, respectively [175]. Reproduced with permission from the Electrochemical Society.

4.3.4 Comparison with Published Results

The cycling performance of our CNF/Si-80 is compared with the published results and the commercially available LIB cells as described below.

4.3.4.1 Comparison with C/Si Composite

This work demonstrates that the addition of SiNP greatly improves the capacity of pure carbon. Kim *et al.* cycled the pure electrospun CNF at slow rates (< 100 mA/g) and obtained the initial nanofibre capacity of at most 450 mAh/g with nanofibres carbonized at 1100°C [57]. We were able to fabricate pure electrospun CNF with comparable capacities at much higher rates. With the addition of SiNP, the CNF morphology is retained with minimal fibre breakage. The capacity of CNF/SiNP composite doubles the capacity of pure CNF and improves the first cycle Coulombic efficiency.

This electrospinning method has also proven to be more effective to fabricate composite lithium anodes as compared to the graphite-grafted silicon nanocomposite, as previously published by Martin *et al* [159]. The advantage of Martin's method is that the covalent linkage between Si and carbon retained a greater Si capacity compared to mixtures of graphite and Si. The initial discharge capacity was 1503 mAh/g; however, the capacity dropped to ca. 700 mAh/g at the 20th cycle at a slow rate of 25 mA/g. The reason for the capacity fade was not clearly described. In contrast, our sample shows a good cycling range and is able to maintain a comparable discharge capacity at much higher rates. Further work can be done to reduce repeated SEI formation and the capacity fade for samples cycled at lower rate.

Ji *et al.* previously demonstrated the cycling performance of electrospun CNF/SiNP derived from carbonizing PAN at 700°C [13]. The samples with different amount of SiNP loadings were cycled between 50 – 200 mA/g. At 30 wt% SiNP loading, their sample is comparable to our CNF/Si-80. As shown in Fig. 4-38, at 100 and 200 mA/g cycle rate, Ji's CNF/SiNP composite electrode showed a discharge capacity retention of ca. 61 and 34 % after 20 cycles, with initial capacities of ca. 1250 and 1000 mAh/g, respectively. Our CNF/Si-80 presents enhanced capacity retention of 72 % at 200 mA/g but reduced capacity retention of 39 % at 100 mA/g. Our n-CNF/Si also showed a lower capacity retention at 100 mA/g rate. As mentioned earlier, this is likely a result of thick SEI formation and increased electrode resistance. However, the core-shell structure in general shows the advantage of enhanced capacity retention capability with reduced capacity drop both initially and throughout the cycles.

There are several advantages of our electrode fabrication comparing to many published result and the past experience of using PAN as carbon precursor [13, 176-178]. By using PANAM copolymer as carbon precursor, the stabilization time is greatly reduced, which reduces the amount of time that SiNP is exposed to the high temperature, oxygenated environment. This can subsequently eliminate the chance of SiO₂ formation, which is known as an electrode contamination and a factor of capacity degradation [101]. One other advantage of this electrode fabrication method is the use of higher carbonization temperature. By increasing the carbonization temperature to 900°C instead of conventional 700°C, the conductivity of CNF/Si composite is increased by at least 10 times, which facilitates faster Li ion interaction with SiNP. A greater amount of nitrogen, which is considered as contamination, can also be eliminated at temperatures over 700°C

[35]. The enhanced cycling stability of CNF/Si composite electrode is demonstrated with a broader range of cycling rate (100 – 600 mA/g) using the electrode fabrication method presented in this study.

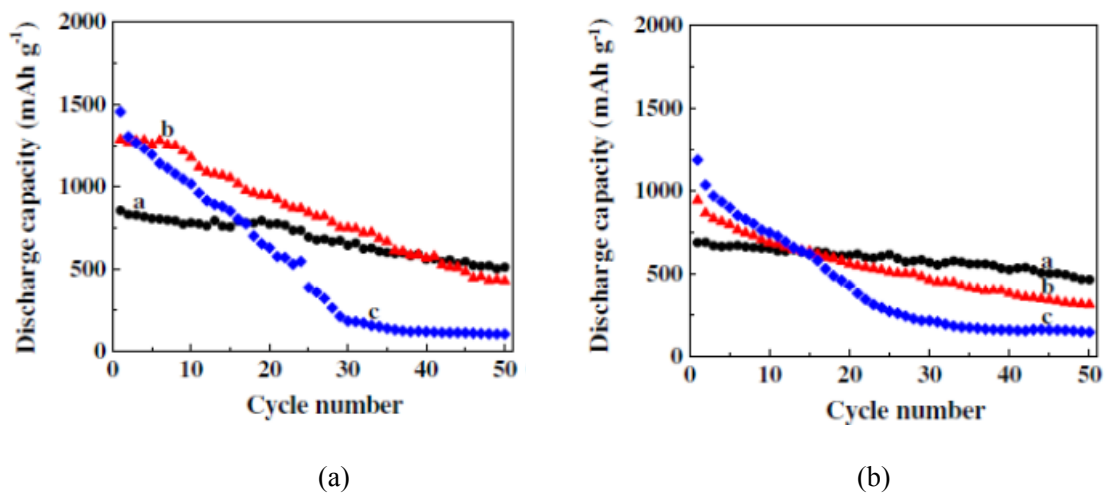


Fig. 4-38 Curve a, b, and c are the 15, 30, and 50 wt% SiNP loading, respectively, in PAN CNF cycled at 100 mA/g in (a) and curve a, b, and c are the 15, 30, and 50 wt% SiNP loading, respectively, in PAN CNF cycled at 200 mA/g in (b). Curve b in both figures are comparable to our CNF/SiNP samples [13]. Reproduced with permission from Elsevier Science Ltd.

One other Si/C nanocomposite approach was to coat the SiNP (50 –100 nm diameter) with microporous carbon, as previously mentioned in the literature review [158]. The discharge capacity was stable at 0.5 C rate and maintained at ca. 1250 mAh/g for 40 cycles. Park *et al.* fabricated Si nanotubes with a thin carbon coating on the tube surface and demonstrated a high capacity retention of 89 % after 200 cycles [179]. The main advantage of these methods are the thin protective coating (≤ 10 nm) of carbon on SiNP, but binder and conductive carbon black are required to assemble the electrode. The main advantage of electrospun CNF/SiNP is that electrode film is ready to use without the addition of binding and conductive materials. However, the morphology of CNF/Si-80

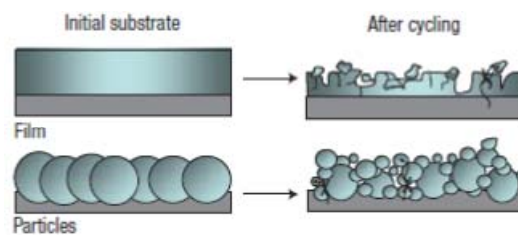
can be redesigned and optimized (ex. reducing fibre diameter) to minimize the thickness of carbon coating and increase the accessibility of SiNP to electrolyte ions. Compacting the nanofibre film will also help to reduce the contact resistance between fibres and potentially improve the capacity retention at higher cycle rates.

4.3.4.2 Comparison with Pure Si Nanowire

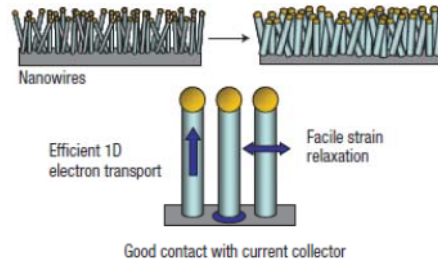
Besides the C/Si nanocomposite approach, some have investigated the performance of pure Si nanowire (SiNW). Chan *et al.* [180] found that nanowire-shaped Si is less susceptible to breakage than bulk film or micron-sized Si particles and maintains more of its original shape after electrochemical cycling, as shown in the schematics in Fig. 4-39. Fig. 4-39(a) shows that Si in both bulk film and micron-sized particles tend to experience more pulverization and loss electrical contact with the current collector; in contrast, nanowires swell evenly in diameter and retained good electrical contact with the current collector after cycling, as shown in Fig. 4-39(b). Fig. 4-40(a) and (b) are the voltage profile and charge/discharge capacity, respectively, of Si nanowires cycled at C/20 rate. Although a theoretical Si capacity of 4200 mAh/g is achieved at first charge cycle, as shown in Fig. 4-40(a), the first charge cycle shows no development of SEI layer with the sharp decrease of voltage from 2.0 to ca. 0.2 V. Although SiNW shows over 3000 mAh/g discharge capacity over the first 10 cycles, it is questionable whether Si can maintain its morphology and capacity for further cycles without any nanowire fusion/breakage.

Cui *et al.* have used chemical vapor deposition (CVD) method to produce crystalline-amorphous core-shell SiNW [181]. Because crystalline Si reacts with Li ions at lower potential (~120 mV) than amorphous Si (~220 mV), SiNW were designed to mainly be

cycled at a higher cut off potential (150 mV was used in the paper). The unreacted, pristine crystalline Si core could then be used as a mechanical support. At a cut off potential of 10 mV, the discharge capacity dropped $\sim 17\%$ after 30 cycles. Although the SiNW capacity was stable at a cut off potential of 150 mV, the total discharge capacity was reduced by ca. 50 %. Once incorporated into the LIB cell, the high cut off potential is likely to lead to a reduction of the total capacity and energy of the cell.



(a)



(b)

Fig. 4-39 Schematic of Si film and micron-sized particle pulverization after cycling (a) and the preservation of SiNW morphology after cycling (nanowires grown directly on the current collector) (b) [180]. Reproduced with permission from Nature Publishing Group.

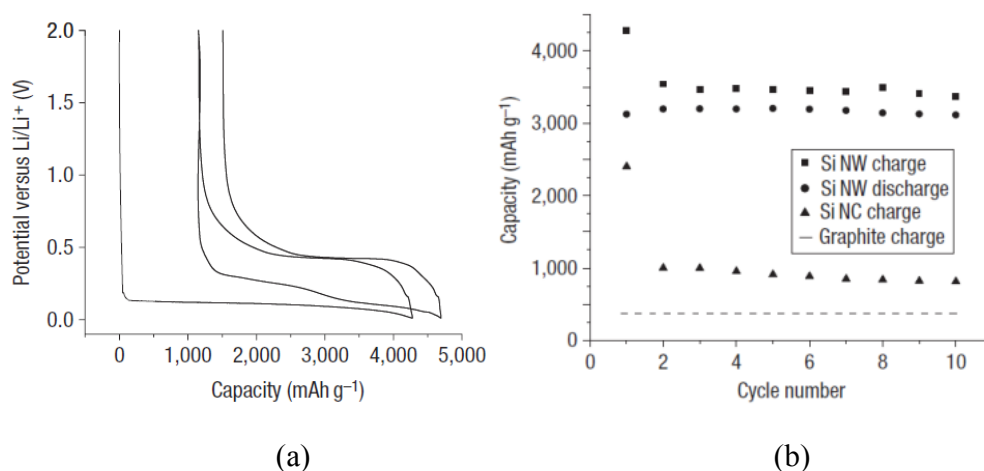


Fig. 4-40 Potential profile of the first two cycles for SiNW cycled at C/20 rate (a) and the charge/discharge capacity (squared and circled dots) of SiNW cycled at C/20 rate (b) [180]. Reproduced with permission from Nature Publishing Group.

4.3.4.3 Comparison with the State-of-the-Art Commercial LIB Cell

Although most conventional LIB still use graphite anodes, some have incorporated inorganic materials for improved performance. In year 2005, Sony developed the Nexelion battery, which used tin-based amorphous Sn-Co-C alloy as anode and LiCoO_2 / $\text{Li}(\text{Co}_y\text{Ni}_{1.7x}\text{Mn}_x)\text{O}_2$ mixture as cathode, and claimed the performance of this battery improved 30 % in capacity (910 mAh vs. 710 mAh of conventional LIB) [182]. Fan *et al.* analyzed the anode alone at 1 mA/cm^2 ($\sim 50 \text{ mA/g}$) and the result is shown in Fig. 4-41 [183]. Fig. 4-41(a) is the charge/discharge capacity of the anode and Fig. 4-41(b) is the percentage of the capacity left after cycling. The 100 % capacity is 543 mAh/g. The capacity suffered from a 25 % drop initially and stabilized at 350 – 400 mAh/g. Our CNF/Si-80 system has shown an improved capacity performance and stability at higher cycle rates. Stability at low cycle rate (100 mA/g) needs further improvement.

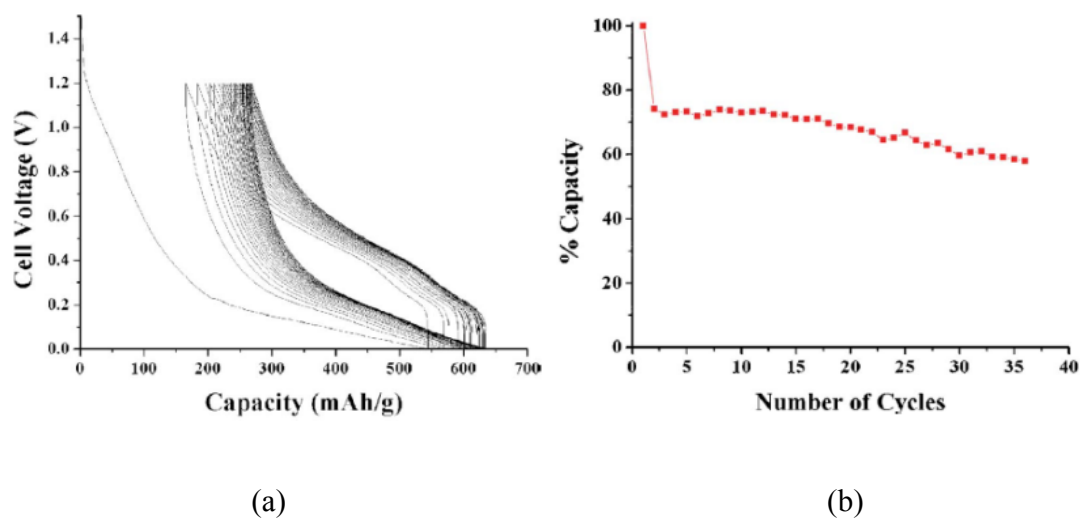


Fig. 4-41 Capacity of Sony's Sn-Co-C alloy anode (a) and the percentage capacity retention upon cycling. The 100 % capacity is 543 mAh/g (b) [183]. Reproduced with permission from the Electrochemical Society.

3M also has developed a Si-based nanocrystalline alloy, which is claimed to improve the energy density of the conventional LIB by 20 % and reduce the cost of raw material of Sn-based anode by 4 times [184]. A low volume expansion coating material was formulated, such that even at 115% of Si-alloy volume expansion, the coating material only expanded 50 %. Fig. 4-42 is the capacity performance and Coulombic efficiency of the Si-based anode. The capacity is very stable at ca. 680 mAh/g for 60 cycles. The advantage of our CNF/Si-80 electrode is its high discharge capacity of 1000 mAh/g. However, the problem of capacity fade needs to be resolved in order to compete with commercial products.

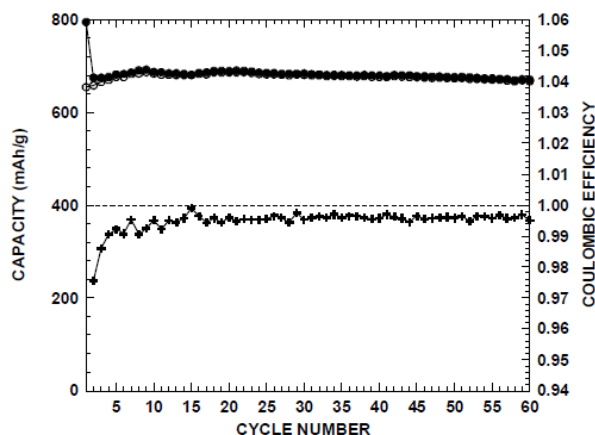


Fig. 4-42 Capacity performance of 3M's Si-alloy anode (upper) and its Coulombic efficiency after cycling (lower) [184]. Reproduced with permission from the Electrochemical Society.

4.4 Summary

The core-shell and non-core-shell CNF/SiNP composites were successfully fabricated. Ganvanostatic charge/discharge tests for both samples were conducted at 100, 200, 400, and 600 mA/g rates. The results indicated that core-shell samples enhanced the capacity retention at most rates through the enclosure and separation of SiNP with carbon fibre coating. The nanofibre coating does not hinder the interaction of SiNP with electrolyte ions significantly comparing to the non-core-shell CNF/SiNP. In general, the capacity decrease of CNF/SiNP composites can be summarized with the following reasons:

1. Based on the experimental result, it is hypothesized that the accumulation and thickening of SEI could increase the resistance of ion diffusion through fibres, hence a higher current is required to reduce capacitance drop.
2. Based on the cycling performance and SEM images, it is hypothesized that the thickened SEI could also reduce the porosity of nanofibre, hence reduce the rate

of ion diffusion into the fibre to interact with SiNP. Further experiments need to be conducted to observe the porosity change of the nanofibre after cycling.

3. The destruction of CNF (in the CNF/SiNP) after continuous SiNP swelling and shrinkage reduces the capacity retention.

5 Conclusion

The purpose of this work is to fabricate high performance CNF from PAN copolymer precursor and to demonstrate its application in electronics. In contrast to the violent heat reaction of pure PAN, PANAM was successfully synthesized and its heat profile from DSC has shown a milder stabilization reaction by introducing ionic cyclization mechanism. PANAM is also more suitable for the large scale fabrication of CNF.

Electrospun CNF in general possess an electrical conductivity of 18 – 20 S/cm. Its composite with polypyrrole coating has shown an improved ionic conductivity and charging speed especially at more reduced state of PPy. However, it is suspected that due to the large solution resistance, the improvement was not significant on the specific capacitance of PPy at different cycling rate. At a low cycle rate of 0.06 A/g, both CNF/PPy and GC/PPy possess a PPy specific capacitance in the range of 150 – 180 F/g. As the cycle rate increased 5× higher, the capacitance dropped 50 % of the original value.

CNF was also composited with SiNP to form a core-shell structured nanofibre with SiNP in the core for LIB anode. At 30 wt% SiNP loading, the capacitance could reach 1000 mAh/g. It is shown that at 100 – 600 mA/g cycle rate, the core-shell nanofibres demonstrate the advantage of protecting and separating SiNP from electrolyte with a layer of ca. 50 nm thick carbon coating. In most cases, the capacity of SiNP in the core-shell sample was retained ca. 10 – 20 % higher than that in the non-core-shell sample. However, further optimization is required to reduce material degradation and capacity fade upon constant cycling.

6 Future Work

Improvement on Carbon Nanofibre Fabrication

The electrical conductivity of carbonized PAN fibres fabricated from conventional spinning methods could reach at least 200 S/cm [185]. The low conductivity of electrospun CNF might mainly be a result of insufficient fibre drawing and chain alignment during electrospinning. The conductivity of electrospun CNF could be improved by modifying electrospinning or incorporating post spinning processes. Possible method includes stretching the fibre in a warm temperature (ca. 50°C) after electrospinning to align the polymer chain.

Improvement on CNF/PPy Composite

The setup of the electrochemical cell could be improved to reduce the influence of solution resistance. For example, the distance between WE and RE could be further reduced or using lugging capillary as RE. The electrical conductivity of CNF could further be improved to improve the charge/discharge rate of CNF/PPy system. The parasitic reaction and contamination could be reduced by a more stringent experimental setup.

Improvement on Core-Shell CNF/SiNP Composite

The experimental result demonstrated that core-shell structured nanofibre preserves the charge storage capacity of SiNP. A thinner surface coating on SiNP or a smaller fibre diameter can potentially improve its power extraction. Different approaches could be pursued to improve the electrochemical performance of the CNF/SiNP composite as described below:

1. Instead of core-shell electrospinning, single-solution (non-core-shell) electrospinning could be conducted first to produce CNF/SiNP, followed by a thin layer of surface coating or deposition with other materials. The preferred material would be conductive, permeable, but not reactive to Li ions.
2. Using smaller SiNP to reduce the possibility of nanoparticle agglomeration and amount expansion during electrochemical cycling.
3. Using CNF polymer precursor with smaller molecular weight to reduce the resulting CNF fibre diameter.
4. Substituting SiNP with SiNW or Si nanotube to compare the difference in capacity retention. It is hypothesized that SiNW and nanotubes might be able to reduce the amount of capacity fade since cylindrical-shaped Si is likely to expand evenly onto the length of CNF.
5. Using different electrochemical testing setup. As shown in Fig. 4-7, a large area of the CNF/SiNP film is exposed to the solution with very little support from the conductive holder. The setup could be modified such that the working electrode could obtain more mechanical support to prevent enhanced SEI thickening. Using coin-type half cell is one example for this.

References

- [1] Dong, Z., Kennedy, S. J., Wu, Y. (2011). Electrospinning Materials for Energy-Related Applications and Devices. *Journal of Power Sources*. 196(11): 4886-4904.
- [2] Kiehl, J. T.&Trenberth, K. E. (1997). Earth's Annual Global Mean Energy Budget. *Bulletin of the American Meteorological Society*. 78(2): 197-208.
- [3] Li, D.&Xia, Y. (2004). Electrospinning of Nanofibers: Reinventing the Wheel? *Advanced Materials*. 16(14): 1151-1170.
- [4] Martin, C. R. (1994). Nanomaterials: A Membrane-Based Synthetic Approach. *Science*. 266(5194): 1961-1966.
- [5] Zhang, Y., Lim, C., Ramakrishna, S., et al. (2005). Recent Development of Polymer Nanofibers for Biomedical and Biotechnological Applications. *Journal of Materials Science: Materials in Medicine*. 16(10): 933-946.
- [6] Qiu, H., Wan, M., Matthews, B., et al. (2001). Conducting Polyaniline Nanotubes by Template-Free Polymerization. *Macromolecules*. 34(4): 675-677.
- [7] Huang, J., Virji, S., Weiller, B. H., et al. (2004). Nanostructured Polyaniline Sensors. *Chemistry. A European Journal*. 10(6): 1314-1319.
- [8] Burger, C., Hsiao, B. S., Chu, B. (2006). Nanofibrous Materials and their Applications. *Annual Review of Materials Research*. 36(1): 333-368.
- [9] Huang, Z., Zhang, Y. -, Kotaki, M., et al. (2003). A Review on Polymer Nanofibers by Electrospinning and their Applications in Nanocomposites. *Composites Science and Technology*. 63(15): 2223-2253.
- [10] Burke, A. (2000). Ultracapacitors: Why, How, and Where Is the Technology. *Journal of Power Sources*. 91(1): 37-50.
- [11] Pandolfo, A. G.&Hollenkamp, A. F. (2006). Carbon Properties and their Role in Supercapacitors. *Journal of Power Sources*. 157(1): 11-27.
- [12] Snook, G. A., Kao, P., Best, A. S. (2011). Conducting-Polymer-Based Supercapacitor Devices and Electrodes. *Journal of Power Sources*. 196(1): 1-12.
- [13] Ji, L.&Zhang, X. (2009). Electrospun Carbon Nanofibers Containing Silicon Particles as an Energy-Storage Medium. *Carbon*. 47(14): 3219-3226.
- [14] Chand, S. (2000). Review Carbon Fibers for Composites. *Journal of Materials Science*. 35(6): 1303-1313.

- [15] Morgan, P. (2005). *Carbon Fibers and Their Composites*, Cambridgeshire, UK: CRC Press, pp. 121-859.
- [16] Rahaman, M. S. A., Ismail, A. F., Mustafa, A. (2007). A Review of Heat Treatment on Polyacrylonitrile Fiber. *Polymer Degradation and Stability*. 92(8): 1421-1432.
- [17] Sutasinpromprae, J., Jitjaicham, S., Nithitanakul, M., et al. (2006). Preparation and Characterization of Ultrafine Electrospun Polyacrylonitrile Fibers and their Subsequent Pyrolysis to Carbon Fibers. *Polymer International*. 55(8): 825-833.
- [18] Wang, Y., Wang, C., Wu, J., et al. (2007). High-Temperature DSC Study of Polyacrylonitrile Precursors during their Conversion to Carbon Fibers. *Journal of Applied Polymer Science*. 106(3): 1787-1792.
- [19] Wangxi, Z., Jie, L., Gang, W. (2003). Evolution of Structure and Properties of PAN Precursors during their Conversion to Carbon Fibers. *Carbon*. 41(14): 2805-2812.
- [20] Henrici-Olivé, G. & Olivé, S. (1983). The Chemistry of Carbon Fiber Formation from Polyacrylonitrile. *Advances in Polymer Science*. 51: 1-60.
- [21] Zhang, W. & Li, M. (2005). DSC Study on the Polyacrylonitrile Precursors for Carbon Fibers. *Journal of Materials Science and Technology*. 21(4): 581-584.
- [22] Chung, D. L. (1994). "Part I - Carbon Fiber." *Carbon Fiber Composites*, Massachusetts, USA: Butterworth-Heinemann: Boston, pp. 3-65.
- [23] Yu, M., Wang, C., Bai, Y., et al. (2006). Evolution of Tension during the Thermal Stabilization of Polyacrylonitrile Fibers Under Different Parameters. *Journal of Applied Polymer Science*. 102(6): 5500-5506.
- [24] Subbiah, T., Bhat, G. S., Tock, R. W., et al. (2005). Electrospinning of Nanofibers. *Journal of Applied Polymer Science*. 96(2): 557-569.
- [25] Li, D. & Xia, Y. (2004). Direct Fabrication of Composite and Ceramic Hollow Nanofibers by Electrospinning. *Nano Letters*. 4(5): 933-938.
- [26] Grassie, N. & Hay, J. N. (1962). Thermal Coloration and Insolubilization in Polyacrylonitrile. *Journal of Polymer Science*. 56(163): 189-202.
- [27] Grassie, N. & McNeill, I. C. (1958). Thermal Degradation of Polymethacrylonitrile. Part II. the Coloration Reaction. *Journal of Polymer Science*. 27(115): 207-218.
- [28] Simitzis, J. & Soulis, S. (2007). Correlation of Chemical Shrinkage of Polyacrylonitrile Fibres with Kinetics of Cyclization. *Polymer International*. 57(1): 99-105.

- [29] Grassie, N. & McGuchan, P. (1970). Pyrolysis of Polyacrylonitrile and Related Polymers—I. Thermal Analysis of Polyacrylonitrile. *European Polymer Journal*. 6(9): 1277-1291.
- [30] Sivy, G. T. & Coleman, M. M. (1981). Fourier Transform IR Studies of the Degradation of Polyacrylonitrile copolymers—IV: Acrylonitrile/acrylamide Copolymers. *Carbon*. 19(2): 137-139.
- [31] Donnet, J. B., Wang, T. K., Peng, J. C. M., Rebouillat, S. (1998). *Carbon Fiber*. Marcel Dekker Inc.
- [32] Riggs, D. M., Shuford, R. J., Lewis, R. W. (1987). *Handbook of Composites*, New York: Van Nostrand Reinhold.
- [33] Houtz, R. C. (1950). Orlan Acrylic Fibre: Chemistry and Properties. *Textile Research Journal*. 20: 786-801.
- [34] Wu, G., Lu, C., Liang, L. (2005). Influence of Tension on the Oxidative Stabilization Process of Polyacrylonitrile Fibers. *Journal of Applied Polymer Science*. 96(4): 1029-1034.
- [35] Goodhew, P. J., Clarke, A. J., Bailey, J. E. (1975). Review of Fabrication and Properties of Carbon-Fibers. *Materials Science and Engineering*. 17(11): 3-30.
- [36] Hoffman, W. P., Hurley, W. C., Liu, P. M., et al. (1991). The Surface Topology of Non-Shear Treated Pitch and PAN Carbon Fibers as Viewed by STM. *Journal of Materials Research*. 6(8): 1685-1694.
- [37] Fiedler, A. K., Fitzer, E., Rozploch, F. (1973). PAN Pyrolysis Studied by Gas- and ESR-Analyses. *Carbon*. 11(4): 426-428.
- [38] Minus, M. & Kumar, S. (2005). The Processing, Properties, and Structure of Carbon Fibers. *JOM Journal of the Minerals, Metals and Materials Society*. 57(2): 52-58.
- [39] Huang, X. (2009). Fabrication and Properties of Carbon Fibers. *Materials*. 2(4): 2369-2403.
- [40] U.S. Food and Drug Administration.
<http://www.fda.gov/RegulatoryInformation/Guidances/ucm257698.htm#rationale>.
- [41] Shea, C. M. (2005). Future Management Research Directions Innanotechnology: A Case Study. *Journal of Engineering and Technology Management*. 22(): 185-200.
- [42] Yao, Z., Postma, H. W. C., Balents, L., et al. (1999). Carbon Nanotube Intramolecular Junctions. *Nature (London)*. 402(6759): 6759-276.

- [43] Nabet, B., Castro, F., Anwar, A., et al. (2000). Heterodimensional Contacts and Optical Detection. *International Journal of High Speed Electronics and Systems*. 10(1): 375-386.
- [44] Zucchelli, A., Focarete, M. L., Gualandi, C., et al. (2011). Electrospun Nanofibers for Enhancing Structural Performance of Composite Materials. *Polymers for Advanced Technologies*. 22(3): 339-349.
- [45] Bal, S. (2010). Experimental Study of Mechanical and Electrical Properties of Carbon nanofiber/epoxy Composites. *Journal of Materials and Design*. 31(5): 2406-2413.
- [46] Kim, C. (2005). Electrochemical Characterization of Electrospun Activated Carbon Nanofibres as an Electrode in Supercapacitors. *Journal of Power Sources*. 142(1-2): 382-388.
- [47] Brandup, J., Immergut, E. (1989). " " *Polymer Handbook*, New York: John Wiley & Sons, pp. 8.
- [48] Image J. <http://rsbweb.nih.gov/ij/>.
- [49] Han, N., Zhang, X. X., Wang, X. C. (2007). Synthesis and Properties of Acrylonitrile /Acrylamide Copolymer. *Journal of Materials Science & Engineering*. 25(1): 71-74.
- [50] Saito, Y., Yoshikawa, T., Inagaki, M., et al. (1993). Growth and Structure of Graphitic Tubules and Polyhedral Particles in Arc-Discharge. *Chemical Physics Letters*. 204(3-4): 277-282.
- [51] Ferrari, A. C. (2007). Raman Spectroscopy of Graphene and Graphite: Disorder, electron-phonon Coupling, Doping and Nonadiabatic Effects. *Solid State Communications*. 143(1-2): 47-57.
- [52] Schwan, J., Ulrich, S., Batori, V., et al. (1996). Raman Spectroscopy on Amorphous Carbon Films. *Journal of Applied Physics*. 80(1): 440-447.
- [53] Ferrari, A. C. & Robertson, J. (1999). Interpretation of Raman Spectra of Disordered and Amorphous Carbon. *Physical Review B*. 61(20): 14095-14107.
- [54] Kim, C., Park, S., Cho, J., et al. (2004). Raman Spectroscopic Evaluation of Polyacrylonitrile-Based Carbon Nanofibers Prepared by Electrospinning. *Journal of Raman Spectroscopy*. 35(11): 928-933.
- [55] Wang, Y., Santiago-Aviles, J. J., Furlan, R., et al. (2003). Pyrolysis Temperature and Time Dependence of Electrical Conductivity Evolution for Electrostatically Generated Carbon Nanofibers. *Nanotechnology, IEEE Transactions on*. 2(1): 39-43.

- [56] Wang, Y., Serrano, S., Santiago-Avilés, J. J. (2003). Raman Characterization of Carbon Nanofibers Prepared using Electrospinning. *Synthetic Metals*. 138(3): 423-427.
- [57] Kim, C., Yang, K. S., Kojima, M., et al. (2006). Fabrication of Electrospinning-Derived Carbon Nanofiber Webs for the Anode Material of Lithium-Ion Secondary Batteries. *Advanced Functional Materials*. 16(18): 2393-2397.
- [58] Salam, M. A., Farouqui, F. I., Mondal, M. I. H. (2007). A Study on Sulphonated Jute-Cotton Blended Yarn and Fabrics and their Characteristics. *Journal of Scientific and Industrial Research*. 42(3): 281-286.
- [59] Kotz, R. & Carlen, M. (2000). Principles and Applications of Electrochemical Capacitors. *Electrochimica Acta*. 45(15-16): 2483-2498.
- [60] Bäuerlein, P., Antonius, C., Löffler, J., et al. (2008). Progress in High-Power Nickel–Metal Hydride Batteries. *Journal of Power Sources*. 176(2): 547-554.
- [61] Vetter, J., Novák, P., Wagner, M. R., et al. (2005). Ageing Mechanisms in Lithium-Ion Batteries. *Journal of Power Sources*. 147(1-2): 269-281.
- [62] Rongeat, C., Grosjean, M., Ruggeri, S., et al. (2006). Evaluation of Different Approaches for Improving the Cycle Life of MgNi-Based Electrodes for Ni-MH Batteries. *Journal of Power Sources*. 158(1): 747-753.
- [63] Ruetschi, P. (2004). Aging Mechanisms and Service Life of Lead–Acid Batteries. *Journal of Power Sources*. 127(1-2): 33-44.
- [64] Andrieu, X. (2000). *Energy Storage Systems for Electronics: New Trends in Electrochemical Technology 1*: 521.
- [65] Frackowiak, E. (2007). Carbon Materials for Supercapacitor Application. *Physical Chemistry Chemical Physics*. 9: 1774.
- [66] Frackowiak, E. & Beguin, F. (2001). Carbon Materials for the Electrochemical Storage of Energy in Capacitors. *Carbon*. 39(6): 937-950.
- [67] Laforgue, A., Simon, P., Fauvarque, J. F., et al. (2003). Activated Carbon/Conducting Polymer Hybrid Supercapacitors. *Journal of the Electrochemical Society*. 150(5): A645-A651.
- [68] Zhang, L. L. & Zhao, X. S. (2009). Carbon-Based Materials as Supercapacitor Electrodes. *Chemical Society Reviews*. 38(9): 2520-2531.

- [69] Lewandowski, A. & Galinski, M. (2007). Practical and Theoretical Limits for Electrochemical Double-Layer Capacitors. *Journal of Power Sources*. 173(2): 822-828.
- [70] Park, J. H., Ko, J. M., Park, O. O., et al. (2002). Capacitance Properties of Graphite/Polypyrrole Composite Electrode Prepared by Chemical Polymerization of Pyrrole on Graphite Fiber. *Journal of Power Sources*. 105(1): 20-25.
- [71] Staiti, P. & Lufrano, F. (2007). A Study of the Electrochemical Behaviour of Electrodes in Operating Solid-State Supercapacitors. *Electrochimica Acta*. 53(2): 710-719.
- [72] Gao, B., Yuan, C. Z., Su, L. H., et al. (2009). Nickel Oxide Coated on Ultrasonically Pretreated Carbon Nanotubes for Supercapacitor. *Journal of Solid State Electrochemistry*. 13(8): 1251-1257.
- [73] Cho, S. I. & Lee, S. B. (2008). Fast Electrochemistry of Conductive Polymer Nanotubes: Synthesis, Mechanism, and Application. *Accounts of Chemical Research*. 41(6): 699-707.
- [74] Mastragostino, M., Arbizzani, C., Soavi, F. (2001). Polymer-Based Supercapacitors. *Journal of Power Sources*. 97-98: 812-815.
- [75] Ansari, R. (2006). Polypyrrole Conducting Electroactive Polymers: Synthesis and Stability Studies. *E-Journal of Chemistry*. 3(13): 186-201.
- [76] Bakhshi, A. (1995). Electrically Conducting Polymers: From Fundamental to Applied Research. *Bulletin of Materials Science*. 18(5): 469-495.
- [77] Warren, M. R. & Madden, J. D. (2006). A Structural, Electronic and Electrochemical Study of Polypyrrole as a Function of Oxidation State. *Synthetic Metals*. 156(9-10): 724-730.
- [78] J. D. W., M. (2000). Conducting Polymer Actuators. Massachusetts Institute of Technology.
- [79] Ismail, Y. A., Chang, J., Shin, S. R., et al. (2009). Hydrogel-Assisted Polyaniline Microfiber as Controllable Electrochemical Actuatable Supercapacitor. *Journal of the Electrochemical Society*. 156(4): A313-A317.
- [80] Fan, L. & Maier, J. (2006). High-Performance Polypyrrole Electrode Materials for Redox Supercapacitors. *Electrochemistry Communications*. 8(6): 937-940.
- [81] Wang, J., Xu, Y., Chen, X., et al. (2007). Electrochemical Supercapacitor Electrode Material Based on Poly(3,4-Ethylenedioxythiophene)/Polypyrrole Composite. *Journal of Power Sources*. 163(2): 1120-1125.

- [82] Xu, Y., Wang, J., Sun, W., et al. (2006). Capacitance Properties of Poly(3,4-Ethylenedioxythiophene)/Polypyrrole Composites. *Journal of Power Sources*. 159(1): 370-373.
- [83] Van Dyke, L. S. & Martin, C. R. (1990). Electrochemical Investigations of Electronically Conductive Polymers. *Langmuir*. 6(6): 1118-1123.
- [84] Wang, J., Xu, Y., Chen, X., et al. (2007). Capacitance Properties of Single Wall Carbon Nanotube/Polypyrrole Composite Films. *Composites Science and Technology*. 67(14): 2981-2985.
- [85] Kim, J., Sharma, A. K., Lee, Y. (2006). Synthesis of Polypyrrole and Carbon Nano-Fiber Composite for the Electrode of Electrochemical Capacitors. *Materials Letters*. 60(13-14): 1697-1701.
- [86] An, H., Wang, Y., Wang, X., et al. (2010). Polypyrrole/Carbon Aerogel Composite Materials for Supercapacitor. *Journal of Power Sources*. 195(19): 6964-6969.
- [87] AMEL Electrochemistry.
<http://www.amelchem.com/product/electrochem/index.html>.
- [88] Kim, C. & Yang, K. S. (2003). Electrochemical Properties of Carbon Nanofiber Web as an Electrode for Supercapacitor Prepared by Electrospinning. *Applied Physics Letters*. 83(6): 1216-1218.
- [89] Oh, J., Kozlov, M. E., Kim, B. G., et al. (2008). Preparation and Electrochemical Characterization of Porous SWNT-PPy Nanocomposite Sheets for Supercapacitor Applications. *Synthetic Metals*. 158(15): 638-641.
- [90] Tso, C., Madden, J. D., Michal, C. A. (2007). An NMR Study of PF_6^- Ions in Polypyrrole. *Synthetic Metals*. 157(10-12): 460-466.
- [91] Shoa, T., Madden, J., D., Fok, C. E., et al. (2009). Rate Limits in Conducting Polymers. *Advances in Science and Technology*. 61: 26-33.
- [92] Fekri, N. (2011). Influence of Porosity on Charging Speed of Polypyrrole Supercapacitors. The University of British Columbia.
- [93] Shoa, T., Madden, J. D., Munce, N. R., et al. (2010). Analytical Modeling of a Conducting Polymer-Driven Catheter. *Polymer International*. 59(3): 343-351.
- [94] Jüttner, K. & Ehrenbeck, C. (1998). Electrochemical Measurements of the Ion Conductivity, Permselectivity and Transference Numbers of Polypyrrole and Polypyrrole Derivatives. *Journal of Solid State Electrochemistry*. 2(2): 60-66.

- [95] Zhou, J. (2007). Lithium Metal Microreference Electrodes and their Applications to Li-Ion Batteries. Library Eindhoven University of Technology.
- [96] Kang, B. & Ceder, G. (2009). Battery Materials for Ultrafast Charging and Discharging. *Nature*. 458(7235): 190-193.
- [97] Takeuchi, K. J., Marschilok, A. C., Lau, G. C., et al. (2006). Carbon Structure/Function Relationships: Characterization and Electrochemistry of Carbon Nanofibers. *Journal of Power Sources*. 157(1): 543-549.
- [98] Tarascon, J. & Armand, M. (2001). Issues and Challenges Facing Rechargeable Lithium Batteries. *Nature*. 414(6861): 359-367.
- [99] Endo, M., Kim, C., Nishimura, K., et al. (2000). Recent Development of Carbon Materials for Li Ion Batteries. *Carbon*. 38(2): 183-197.
- [100] Bradford, S. M. (March 2004). *Battery Power Products & Technology Magazine*.
- [101] Kasavajjula, U., Wang, C., Appleby, A. J. (2007). Nano- and Bulk-Silicon-Based Insertion Anodes for Lithium-Ion Secondary Cells. *Journal of Power Sources*. 163(2): 1003-1039.
- [102] Noel, M. & Suryanarayanan, V. (2002). Role of Carbon Host Lattices in Li-Ion intercalation/de-Intercalation Processes. *Journal of Power Sources*. 111(2): 193-209.
- [103] Linden, D. (1995). *Handbook of Batteries*, 2nd. McGraw-Hill,
- [104] Linden, D. & Reddy, T. B. (2002). *Handbook of Batteries (3rd Edition)*, 3rd. McGraw-Hill,
- [105] Teki, R., Datta, M. K., Krishnan, R., et al. (2009). Nanostructured Silicon Anodes for Lithium Ion Rechargeable Batteries. *Small*. 5(20): 2236-2242.
- [106] Dahn, J. R., Zheng, T., Liu, Y., et al. (1995). Mechanisms for Lithium Insertion in Carbonaceous Materials. *Science*. 270(5236): 590-593.
- [107] Shi, H. (1998). Coke Vs. Graphite as Anodes for Lithium-Ion Batteries. *Journal of Power Sources*. 75(1): 64-72.
- [108] Azuma, H., Imoto, H., Yamada, S., et al. (1999). Advanced Carbon Anode Materials for Lithium Ion Cells. *Journal of Power Sources*. 81-82: 1-7.
- [109] Gotoh, K., Maeda, M., Nagai, A., et al. (2006). Properties of a Novel Hard-Carbon Optimized to Large Size Li Ion Secondary Battery Studied by ⁷Li NMR. *Journal of Power Sources*. 162(2): 1322-1328.

- [110] Sony's Catalog, Lithium Ion Rechargeable Battery, ACG-4012-N-9707-P3-002, 1997.
- [111] Fong, R., von Sacken, U., Dahn, J. R. (1990). Studies of Lithium Intercalation into Carbons Using Nonaqueous Electrochemical Cells. *Journal of the Electrochemical Society*. 137(7): 2009-2013.
- [112] Takei, K., Kumai, K., Kobayashi, Y., et al. (1995). an X-Ray Photoelectron Spectroscopy Study on the Surface Film on Carbon Black Anode in Lithium Secondary Cells. *Journal of Power Sources*. 54(2): 171-174.
- [113] Naji, A., Ghanbaja, J., Humbert, B., et al. (1996). Electroreduction of Graphite in LiClO₄-Ethylene Carbonate Electrolyte. Characterization of the Passivating Layer by Transmission Electron Microscopy and Fourier-Transform Infrared Spectroscopy. *Journal of Power Sources*. 63(1): 33-39.
- [114] Naji, A., Ghanbaja, J., Willmann, P., et al. (1997). Electrochemical Reduction of Graphite in LiClO₄-Propylene Carbonate Electrolyte: Influence of the Nature of the Surface Protective Layer. *Carbon*. 35(6): 845-852.
- [115] Besenhard, J. O. (1976). the Electrochemical Preparation and Properties of Ionic Alkali Metal-and NR₄-Graphite Intercalation Compounds in Organic Electrolytes. *Carbon*. 14(2): 111-115.
- [116] Ohzuku, T., Iwakoshi, Y., Sawai, K. (1993). Formation of Lithium-Graphite Intercalation Compounds in Nonaqueous Electrolytes and their Application as a Negative Electrode for a Lithium Ion (Shuttlecock) Cell. *Journal of the Electrochemical Society*. 140(9): 2490-2497.
- [117] Flandrois, S. & Simon, B. (1999). Carbon Materials for Lithium-Ion Rechargeable Batteries. *Carbon*. 37(2): 165-180.
- [118] Aurbach, D., (1990). Nonaqueous Electrochemistry , Ed., New York: Marcel Dekker. (Distributed by Springer at *Russian Journal of Electrochemistry*. 37(8): 871-872)
- [119] Yuqin, C., Hong, L., Lie, W., et al. (1997). Irreversible Capacity Loss of Graphite Electrode in Lithium-Ion Batteries. *Journal of Power Sources*. 68(2): 187-190.
- [120] Imanishi, N., Kashiwagi, H., Ichikawa, T., et al. (1993). Charge-Discharge Characteristics of Mesophase-Pitch-Based Carbon Fibers for Lithium Cells. *Journal of the Electrochemical Society*. 140(2): 315-320.
- [121] Disma, F., Aymard, L., Dupont, L., et al. (1996). Effect of Mechanical Grinding on the Lithium Intercalation Process in Graphites and Soft Carbons. *Journal of the Electrochemical Society*. 143(12): 3959-3972.

- [122] Nagura, T. & Tozawa, K. (1990). Lithium Ion Rechargeable Battery. *Progress Batteries and Solar Cells*. 9: 209-216.
- [123] Yazami, R. & Deschamps, M. (1995). *Mater. Res. Soc. Symp. Proc.* 369: 165.
- [124] Mori, Y., Iriyama, T., Hashimoto, T., et al. (1995). Lithium doping/undoping in Disordered Coke Carbons. *Journal of Power Sources*. 56(2): 205-208.
- [125] Zheng, T., Liu, Y., Fuller, E. W., et al. (1995). Lithium Insertion in High Capacity Carbonaceous Materials. *Journal of the Electrochemical Society*. 142: 2581-2590.
- [126] Zheng, T., Zhong, Q., Dahn, J. R. (1995). High-Capacity Carbons Prepared from Phenolic Resin for Anodes of Lithium-Ion Batteries. *Journal of the Electrochemical Society*. 142(11): L211-L214.
- [127] Verbrugge, M. W. & Koch, B. J. (1996). Lithium Intercalation of Carbon-Fiber Microelectrodes. *Journal of the Electrochemical Society*. 143(1): 24-31.
- [128] Jung, Y., Suh, M. C., Lee, H., et al. (1997). Electrochemical Insertion of Lithium into Polyacrylonitrile-Based Disordered Carbons. *Journal of the Electrochemical Society*. 144(12): 4279-4284.
- [129] Yata, S., Kinoshita, H., Komori, M., et al. (1994). Structure and Properties of Deeply Li-Doped Polyacenic Semiconductor Materials Beyond C₆Li Stage. *Synthetic Metals*. 62(2): 153-158.
- [130] Xing, W., Xue, J. S., Zheng, T., et al. (1996). Correlation between Lithium Intercalation Capacity and Microstructure in Hard Carbons. *Journal of the Electrochemical Society*. 143(11): 3482-3491.
- [131] Matsumura, Y., Wang, S., Mondori, J. (1995). Mechanism Leading to Irreversible Capacity Loss in Li Ion Rechargeable Batteries. *Journal of the Electrochemical Society*. 142(9): 2914-2918.
- [132] Puri, B. R. (1970). *Chemistry and Physics of Carbon*, New York: Marcel Dekker, pp. 191.
- [133] Hoinkis, E. (1997). *Chemistry and Physics of Carbon*, New York: Marcel Dekker, pp. 71.
- [134] Liu, Y., Xue, J. S., Zheng, T., et al. (1996). Mechanism of Lithium Insertion in Hard Carbons Prepared by Pyrolysis of Epoxy Resins. *Carbon*. 34(2): 193-200.
- [135] Yoshio, M., Tsumura, T., Dimov, N. (2005). Electrochemical Behaviors of Silicon Based Anode Material. *Journal of Power Sources*. 146(1-2): 10-14.

- [136] Dey, A. N. (1971). Electrochemical Alloying of Lithium in Organic Electrolytes. *Journal of the Electrochemical Society*. 118(10): 1547-1549.
- [137] Sharma, R. A. & Seefurth, R. N. (1976). Thermodynamic Properties of the Lithium-Silicon System. *Journal of the Electrochemical Society*. 123(12): 1763-1768.
- [138] Boukamp, B. A., Lesh, G. C., Huggins, R. A. (1981). All-Solid Lithium Electrodes with Mixed-Conductor Matrix. *Journal of the Electrochemical Society*. 128(4): 725-729.
- [139] Ryu, J. H., Kim J. W. Sung, Y. E., Oh, S. M. (2004). Failure Modes of Silicon Powder Negative Electrode in Lithium Secondary Batteries. *Electrochemical and Solid-State Letters*. 7(10): A306-A309.
- [140] Liu, W. R., Guo, Z. Z., Young, W. S., et al. (2005). Effect of Electrode Structure on Performance of Si Anode in Li-Ion Batteries: Si Particle Size and Conductive Additive. *Journal of Power Sources*. 140(1): 139-144.
- [141] Li, H., Huang, X., Chen, L., et al. (1999). A High Capacity Nano-Si Composite Anode Material for Lithium Rechargeable Batteries. *Electrochemical and Solid-State Letters*. 2(11): 547-549.
- [142] Guo, Z. P., Wang, J. Z., Liu, H. K., et al. (2005). Study of Silicon/Polypyrrole Composite as Anode Materials for Li-Ion Batteries. *Journal of Power Sources*. 146(1-2): 448-451.
- [143] Kim, I., Kumta, P. N., Blomgren, G. E. (2000). Si/TiN Nanocomposites Novel Anode Materials for Li-Ion Batteries. *Electrochemical and Solid-State Letters*. 3(11): 493-496.
- [144] Kim, I., Blomgren, G. E., Kumta, P. N. (2004). Si-SiC Nanocomposite Anodes Synthesized using High-Energy Mechanical Milling. *Journal of Power Sources*. 130(1-2): 275-280.
- [145] Patel, P., Kim, I., Kumta, P. N. (2005). Nanocomposites of silicon/titanium Carbide Synthesized using High-Energy Mechanical Milling for use as Anodes in Lithium-Ion Batteries. *Mater. Sci. Eng. B-Solid*. 116(3): 347-352.
- [146] Guo, Z. P., Zhao, Z. W., Liu, H. K., et al. (2005). Lithium Insertion in Si-TiC Nanocomposite Materials Produced by High-Energy Mechanical Milling. *Journal of Power Sources*. 146(1-2): 190-194.
- [147] Dong, H., Feng, R. X., Ai, X. P., et al. (2004). Structural and Electrochemical Characterization of Fe-Si/C Composite Anodes for Li-Ion Batteries Synthesized by Mechanical Alloying. *Electrochimica Acta*. 49(28): 5217-5222.

- [148] Dong, H., Ai, X. P., Yang, H. X. (2003). Carbon/Ba-Fe-Si Alloy Composite as High Capacity Anode Materials for Li-Ion Batteries. *Electrochemistry Communications*. 5(11): 952-957.
- [149] Park, M. S., Lee, Y. J., Rajendran, S., et al. (2005). Electrochemical Properties of Si/Ni Alloy-Graphite Composite as an Anode Material for Li-Ion Batteries. *Electrochimica Acta*. 50(28): 5561-5567.
- [150] Wilson, A. M., Reimers, J. N., Fuller, E. W., et al. (1994). Lithium Insertion in Pyrolyzed Siloxane Polymers. *Solid State Ionics*. 74(3-4): 249-254.
- [151] Xue, J. S., Myrtle, K., Dahn, J. R. (1995). an Epoxy-Silane Approach to Prepare Anode Materials for Rechargeable Lithium Ion Batteries. *Journal of the Electrochemical Society*. 142(9): 2927-2935.
- [152] Wilson, A. M., Zank, G., Eguchi, K., et al. (1997). Pyrolysed Silicon-Containing Polymers as High Capacity Anodes for Lithium-Ion Batteries. *Journal of Power Sources*. 68(2): 195-200.
- [153] Hayes, S. E., Eckert, H., Even, W. R., et al. (1999). Structural and Electrochemical Characterization of Glassy Carbon Prepared from Silicon-Doped Polymethacrylonitrile/Divinylbenzene Copolymer. *Journal of the Electrochemical Society*. 146(7): 2435-2442.
- [154] Holzapfel, M., Buqa, H., Scheifele, W., et al. (2005). A New Type of Nano-Sized silicon/carbon Composite Electrode for Reversible Lithium Insertion. *Chemical Communications*. (12): 1566-1568.
- [155] Liu, W. R., Wang, J. H., Wu, H. C., et al. (2005). Electrochemical Characterizations on Si and C-Coated Si Particle Electrodes for Lithium-Ion Batteries. *Journal of the Electrochemical Society*. 152(9): A1719-A1725.
- [156] Kim, B. C., Uono, H., Sato, T., et al. (2004). Li-Ion Battery Anode Properties of Si-Carbon Nanocomposites Fabricated by High Energy Multiring-Type Mill. *Solid State Ionics*. 172(1-4): 33-37.
- [157] Wang, G. X., Ahn, J. H., Yao, J., et al. (2004). Nanostructured Si-C Composite Anodes for Lithium-Ion Batteries. *Electrochemistry Communications*. 69(7): 689-692.
- [158] Gao, P., Fu, J., Yang, J., et al. (2009). Microporous Carbon Coated Silicon Core-Shell Nanocomposite Via in Situ Polymerization for Advanced Li-Ion Battery Anode Material. *Physical Chemistry Chemical Physics*. 11(47): 11101-11105.

- [159] Martin, C., Alias, M., Christien, F., et al. (2009). Graphite-Grafted Silicon Nanocomposite as a Negative Electrode for Lithium-Ion Batteries. *Advanced Materials*. 21(46): 4735-4741.
- [160] MDI Materials Data. <http://www.materialsdata.com/>.
- [161] Douglas, S. J., Illum, L., Davis, S. S. (1985). Particle Size and Size Distribution of Poly(Butyl 2-Cyanoacrylate) Nanoparticles. II. Influence of Stabilizers. *Journal of Colloid and Interface Science*. 103(1): 154-163.
- [162] Jin, G.&Guo, X. (2003). Synthesis and Characterization of Mesoporous Silicon Carbide. *Microporous and Mesoporous Materials*. 60(1-3): 207-212.
- [163] Yu, D. P., Bai, Z. G., Ding, Y., et al. (1998). Nanoscale Silicon Wires Synthesized using Simple Physical Evaporation. *Appl. Phys. Lett.* 72(26): 3458-3461.
- [164] Bandosz, T., J. (2006). "Surface Chemistry of Activated Carbons and Its Characterization." *Activated Carbon Surfaces in Environmental Remediation*. Academic Press, pp. 174-174.
- [165] Namburu, P. K., Kulkarni, D. P., Misra, D., et al. (2007). Viscosity of Copper Oxide Nanoparticles Dispersed in Ethylene Glycol and Water Mixture. *Experimental Thermal and Fluid Science*. 32(2): 397-402.
- [166] Mackay, M. E., Dao, T. T., Tuteja, A., et al. (2003). Nanoscale Effects Leading to Non-Einstein-Like Decrease in Viscosity. *Nature Materials*. 2(11): 762-766.
- [167] Tuteja, A., Mackay, M. E., Hawker, C. J., et al. (2005). Effect of Ideal, Organic Nanoparticles on the Flow Properties of Linear Polymers: Non-Einstein-Like Behavior. *Macromolecules*. 38(19): 8000-8011.
- [168] Ōya, A. & Marsh, H. (1982). Phenomena of Catalytic Graphitization. *Journal of Materials Science*. 17(2): 309-322.
- [169] Yudasaka, M., Tasaka, K., Kikuchi, R., et al. (1997). Influence of Chemical Bond of Carbon on Ni Catalyzed Graphitization. *Journal of Applied Physics*. 81(11): 7623-7629.
- [170] Ōya, A.&Ōtani, S. (1979). Catalytic Graphitization of Carbons by various Metals. *Carbon*. 17(2): 131-137.
- [171] Ōya, A.&Ōtani, S. (1981). Influences of Particle Size of Metal on Catalytic Graphitization of Non-Graphitizing Carbons. *Carbon*. 19(5): 391-400.

- [172] Chan, C. K., Ruffo, R., Hong, S. S., et al. (2009). Surface Chemistry and Morphology of the Solid Electrolyte Interphase on Silicon Nanowire Lithium-Ion Battery Anodes. *Journal of Power Sources*. 189(2): 1132-1140.
- [173] Aurbach, D. (2000). Review of Selected electrode–solution Interactions which Determine the Performance of Li and Li Ion Batteries. *Journal of Power Sources*. 89(2): 206-218.
- [174] Ning, G., Haran, B., Popov, B. N. (2003). Capacity Fade Study of Lithium-Ion Batteries Cycled at High Discharge Rates. *Journal of Power Sources*. 117(1-2): 160-169.
- [175] Kim, S., Kadoma, Y., Ikuta, H., et al. (2001). Electrochemical Performance of Natural Graphite by Surface Modification using Aluminum. *Electrochemical and Solid-State Letters*. 4(8): A109-A112.
- [176] Wang, L., Ding, C. X., Zhang, L. C., et al. (2010). A Novel Carbon–Silicon Composite Nanofiber Prepared Via Electrospinning as Anode Material for High Energy-Density Lithium Ion Batteries. *Journal of Power Sources*. 195(15): 5052-5056.
- [177] Fan, X., Zou, L., Zheng, Y., et al. (2009). Electrospinning Preparation of Nanosilicon/Disordered Carbon Composite as Anode Materials in Li-Ion Battery. *Electrochemical and Solid-State Letters*. 12(10): A199-A201.
- [178] Ji, L., Jung, K., Medford, A. J., et al. (2009). Electrospun Polyacrylonitrile Fibers with Dispersed Si Nanoparticles and their Electrochemical Behaviors After Carbonization. *J.Mater.Chem*. 19(28): 4992-4997.
- [179] Park, M., Kim, M. G., Joo, J., et al. (2009). Silicon Nanotube Battery Anodes. *Nano Letters*. 9(11): 3844-3847.
- [180] Chan, C. K., Peng, H., Liu, G. (2008). High-Performance Lithium Battery Anodes using Silicon Nanowires. *Nature Nanotechnology*. 3(1): 31-35.
- [181] Cui, L., Ruffo, R., Chan, C. K., et al. (2009). Crystalline-Amorphous Core-Shell Silicon Nanowires for High Capacity and High Current Battery Electrodes. *Nano Letters*. 9(1): 491-495.
- [182] Foster, D., Wolfenstine, J., Read, J., et al. (2008). Performance of Sony's Alloy Based Li-Ion Battery.
- [183] Fan, Q., Chupas, P. J., Whittingham, M. S. (2007). Characterization of Amorphous and Crystalline Tin--Cobalt Anodes. *Electrochemical and Solid-State Letters*. 10(12): A274-A278.

- [184] Obrovac, M. N., Christensen, L., Lea, D. B., et al. (2009). New Alloy Anodes for Commercial Lithium Ion Cells. *ECS Meeting Abstracts*. (8): 542-542.
- [185] Chae, H. G. (2008). Polyacrylonitrile / Carbon Nanotube Composite Fibers: Reinforcement Efficiency and Carbonization Studies. Georgia Institute of Technology.